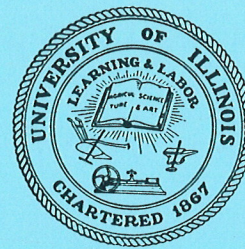


**Metal Process Simulation Laboratory
Department of Mechanical and Industrial Engineering
University of Illinois at Urbana-Champaign
Urbana, IL 61801**



Thermo-Mechanical Model of Steel Shell Behavior in Continuous Slab Casting

Avijit Moitra

**PhD Thesis
1993**

Submitted to

**ARMCO Inc.
Inland Steel
LTV
BHP**

August 18, 1993

THERMO-MECHANICAL MODEL OF STEEL SHELL BEHAVIOR
IN CONTINUOUS SLAB CASTING

BY

AVIJIT MOITRA

B.Tech., Indian Institute of Technology, 1985
M.S., University of Alabama, 1989

THESIS

Submitted in partial fulfillment of the requirements
for the degree of Doctor of Philosophy in Mechanical Engineering
in the Graduate College of the
University of Illinois at Urbana-Champaign, 1993

Urbana, Illinois

© Copyright by Avijit Moitra, 1993

ABSTRACT

The behavior of the solidifying shell in the early stages of solidification has an important influence on the final quality of continuously-cast steel slabs. In order to understand the thermal and mechanical behavior of the shell, a two-dimensional transient stepwise-coupled finite-element model has been developed. The model simulates a transverse section of the slab as it moves down through the mold and below and incorporates the effects of heat conduction, solidification, shrinkage, non-uniform superheat dissipation due to turbulent fluid flow, thermal distortion of the mold and the visco-plastic mechanical behavior of the steel. Coupling between the thermal and the mechanical portions of the model are based on the mutual dependence of heat transfer across the interface between the shell and the mold and the size of the gap. The effects of mold distortion and taper on the gap size are also included. The effect of fluid flow has been incorporated via a heat flux imposed at the solid-liquid interface, which is obtained from a separate fluid flow model. The high temperature creep and plasticity of the steel is incorporated through a unified constitutive law defining the inelastic strain rates as a function of temperature, composition, accumulated plastic strain and the stress state. The model has been successfully verified with analytical solutions and measurements of temperature and shell thickness on an operating caster. Non-uniform dissipation of superheat caused by asymmetrical fluid flow has been found to have a critical influence on shell growth in the mold, in places where the interfacial gap size is significant. Model results suggest that a simple linear taper necessary to compensate for the slab shrinkage is not sufficient for low carbon steels because of the non-linear shrinkage associated with the δ - γ phase transformation. Model simulations extending below the mold suggest that bulging of the shell between rollers is responsible for the formation of off-corner depressions when the off-corner region of the shell leaving the mold is relatively thinner than other places. The model developed in this work is an effective tool and can be judiciously used to understand the formation mechanisms of various defects in continuous slab casting.

ACKNOWLEDGMENTS

I would like to express my deep sense of gratitude to Dr. Brian G. Thomas for his guidance, support and encouragement through out this work. I feel fortunate for receiving the opportunity to work with him. I have learned a great deal from him both technically and personally. I would also like to take this opportunity to thank Dr. Jon Dantzig, Dr. Jyoti Mazumder and Dr. Robert E. Miller for their consent to serve on my dissertation committee. Additionally, I am indebted to them for their advice and assistance with my research over the past few years.

I would like to thank William Storkman for the initial contributions to this research, Hong Zhu for his contribution during the model development, Bryant Ho, Xiaoqing Huang, Gowe Li for the results of other models that are used in this research and David Lui for help with the measurements on the breakout shell.

I would like to thank Mr. William R. Emling, Mr. George Lawson and Mr. Lee Hendrix of LTV Steel Research, for their help with the breakout shell and the related plant data and various other helpful discussions to understand the formation of the breakout.

I would like to express my sincere and deepest appreciation to my wife Chitra, whose love, encouragement, counsel and friendship gave me the energy to continue and complete this work. I am also very grateful to my parents whose encouragement has always been an unwavering source of support and inspiration for me, and I will never be able to repay them for this. I thank them.

Naturally, I owe a lot to my office-mates, both past and present, Xiaoqing, Don, Guowei, Zhu, Bryant, Pat, Robert and David. Their company, camaraderie, geniality, helpfulness and industry served both to inspire me and help me relax, just a little. I will remember them fondly.

Finally, I would like to acknowledge the financial support of the University of Illinois Steel Consortium consisting of Armco Inc., Inland Steel, LTV Steel and BHP, Australia, and National Science Foundation to finish this work and National Center for Supercomputing Applications for time on the Cray-2 and the Convex-C3 super computers.

TABLE OF CONTENTS

| | Page |
|---|------|
| LIST OF TABLES | x |
| LIST OF FIGURES | xi |
| NOMENCLATURE..... | xvi |
| CHAPTER 1. INTRODUCTION..... | 1 |
| 1.1 PROCESS OVERVIEW | 2 |
| 1.2 THE PROBLEM | 5 |
| 1.3 MOTIVATION..... | 6 |
| 1.4 REFERENCES..... | 9 |
| CHAPTER 2. PREVIOUS MATHEMATICAL MODELS..... | 10 |
| 2.1 SOLIDIFICATION HEAT TRANSFER MODELS | 10 |
| 2.2 THERMAL STRESS MODELS OF THE SHELL..... | 12 |
| 2.2.1 2-D SLICE MODELS | 12 |
| 2.2.1.1 BILLET CASTING | 13 |
| 2.2.1.2 SLAB CATING | 14 |
| 2.2.2 SLAB BULGING BELOW MOLD | 16 |
| 2.3 STEADY STATE MODELS | 16 |
| 2.4 REFERENCES..... | 18 |
| CHAPTER 3. MODEL DESCRIPTION | 23 |
| 3.1 ASSUMPTIONS..... | 23 |
| 3.2 HEAT TRANSFER MODEL FORMULATION..... | 24 |
| 3.2.1 HEAT FLOW BOUNDARY CONDITIONS..... | 27 |
| 3.2.1.1 INTERFACE HEAT TRANSFER MODEL..... | 28 |
| 3.2.1.2 SUPER HEAT FLUX..... | 33 |
| 3.2.1.3 SPRAY ZONE BOUNDARY CONDITION | 36 |
| 3.3 MECHANICAL MODEL FORMULATION | 37 |
| 3.3.1 THERMAL STRAIN | 40 |

| | | |
|------------|--|----|
| 3.3.2 | INELASTIC STRAIN..... | 41 |
| 3.3.2.1 | EXPLICIT METHOD..... | 42 |
| 3.3.2.2 | IMPLICIT METHOD..... | 42 |
| 3.3.3 | MECHANICAL BOUNDARY CONDITIONS..... | 44 |
| 3.3.3.1 | FERROSTATIC PRESSURE..... | 45 |
| 3.3.3.2 | SHELL/MOLD CONTACT..... | 46 |
| 3.3.3.3 | CONSTRAINT FOR BULGING BELOW MOLD..... | 49 |
| 3.4 | INITIAL CONDITIONS..... | 51 |
| 3.5 | TREATMENT OF LIQUID..... | 52 |
| 3.6 | THERMO-MECHANICAL PROPERTY DATA..... | 53 |
| 3.6.1 | THERMAL CONDUCTIVITY..... | 53 |
| 3.6.2 | ENTHALPY..... | 53 |
| 3.6.3 | THERMAL LINEAR EXPANSION..... | 53 |
| 3.6.4 | ELASTIC MODULUS..... | 56 |
| 3.6.5 | CONSTITUTIVE BEHAVIOR..... | 57 |
| 3.6.6 | CONSTANT PROPERTIES..... | 58 |
| 3.7 | REFERENCES..... | 59 |
| CHAPTER 4. | MOLD DISTORTION..... | 67 |
| 4.1 | INTRODUCTION..... | 67 |
| 4.2 | PREVIOUS WORK..... | 68 |
| 4.3 | MOLD CONSTRUCTION..... | 69 |
| 4.4 | MODEL FORMULATION..... | 72 |
| 4.4.1 | HEAT TRANSFER MODEL..... | 72 |
| 4.4.1.1 | 2D MODEL..... | 73 |
| 4.4.1.2 | BOUNDARY CONDITIONS..... | 73 |
| 4.4.1.3 | 3D MODEL..... | 75 |
| 4.4.1.4 | BOUNDARY CONDITIONS..... | 76 |

| | | |
|------------|--|-----|
| 4.4.2 | STRESS MODEL..... | 77 |
| 4.4.2.1 | 2D MODEL..... | 77 |
| 4.4.2.2 | BOUNDARY CONDITIONS..... | 78 |
| 4.4.2.3 | 3D MODEL..... | 78 |
| 4.4.2.4 | BOUNDARY CONDITIONS..... | 79 |
| 4.5 | SOLUTION METHODOLOGY..... | 80 |
| 4.6 | RESULTS..... | 80 |
| 4.6.1 | EFFECT OF HEAT INPUT..... | 86 |
| 4.6.2 | EFFECT OF SLAB WIDTH..... | 87 |
| 4.6.3 | EFFECT OF MOLD PLATE THICKNESS..... | 87 |
| 4.6.4 | EFFECT OF BOLT PRE-STRESS..... | 88 |
| 4.6.5 | STRESS LEVELS..... | 89 |
| 4.7 | MODEL VERIFICATION..... | 92 |
| 4.8 | DISCUSSION..... | 92 |
| 4.9 | CONCLUSIONS..... | 97 |
| 4.10 | REFERENCES..... | 99 |
| CHAPTER 5. | SIMULATION PROCEDURE..... | 102 |
| 5.1 | PLASTICITY CONVERGENCE..... | 106 |
| 5.1.1 | EXPLICIT SCHEME..... | 106 |
| 5.1.2 | IMPLICIT SCHEME..... | 107 |
| 5.2 | INTERFACIAL GAP COUPLING..... | 107 |
| 5.3 | REFERENCES..... | 110 |
| CHAPTER 6. | MODEL VERIFICATION..... | 112 |
| 6.1 | CYLINDER UNDER INTERNAL PRESSURE..... | 112 |
| 6.2 | TENSILE TEST PROBLEM..... | 113 |
| 6.3 | CREEP TEST PROBLEM..... | 114 |
| 6.4 | 1-D SOLIDIFICATION STRESS PROBLEM..... | 115 |
| 6.5 | BREAKOUT SHELL MEASUREMENTS..... | 117 |

| | | |
|---|--|-----|
| 6.6 | REFERENCES..... | 122 |
| CHAPTER 7. APPLICATION OF THE MODEL TO WIDTH CHANGE OPERATION ... | | 124 |
| 7.1 | EFFECT OF NARROWFACE TAPER..... | 124 |
| 7.2 | EFFECT OF MOLD FLUX DISTRIBUTION..... | 126 |
| 7.3 | EFFECT OF SUPERHEAT..... | 127 |
| 7.4 | EFFECT OF NOZZLE MIS-ALIGNMENT..... | 130 |
| 7.5 | EFFECT OF CASTING SPEED..... | 133 |
| 7.6 | CONCLUSIONS | 135 |
| 7.7 | REFERENCES | 136 |
| CHAPTER 8. OPTIMIZING MOLD TAPER | | 137 |
| 8.1 | 1-D MODEL(S) | 139 |
| 8.1.1 | MESH REFINEMENT | 142 |
| 8.2 | 2-D MODEL..... | 145 |
| 8.3 | RESULTS AND DISCUSSION | 147 |
| 8.3.1 | EFFECT OF NARROWFACE TAPER | 147 |
| 8.3.2 | EFFECT OF CASTING SPEED | 151 |
| 8.3.3 | EFFECT OF MOLD DISTORTION | 152 |
| 8.3.4 | EFFECT ON MOLD WEAR | 154 |
| 8.4 | TAPER DIAGRAM..... | 154 |
| 8.5 | CONCLUSIONS | 156 |
| 8.6 | REFERENCES | 158 |
| CHAPTER 9. BULGING BELOW MOLD | | 160 |
| 9.1 | SPRAY COOLING BELOW MOLD | 161 |
| 9.2 | SIMULATION BELOW MOLD | 162 |
| 9.3 | RESULTS AND DISCUSSION | 163 |
| 9.4 | OFF-CORNER DEPRESSIONS | 169 |
| 9.5 | MECHANISM OF OFF-CORNER DEPRESSIONS..... | 171 |

| | | |
|-------------|--|-----|
| 9.6 | EFFECT OF SPRAY COOLING | 173 |
| 9.7 | CONCLUSION..... | 175 |
| 9.8 | REFERENCES..... | 176 |
| CHAPTER 10. | APPLICATION TO CRACK FORMATION | 179 |
| 10.1 | HOT TEARS | 180 |
| 10.2 | TRANSVERSE CRACKS | 182 |
| 10.3 | LONGITUDINAL CRACKS | 183 |
| 10.4 | RESULTS AND DISCUSSION | 183 |
| 10.5 | TRANSVERSE CORNER CRACKS | 189 |
| 10.6 | CONCLUSIONS | 189 |
| 10.7 | REFERENCES | 192 |
| CHAPTER 11. | SUMMARY AND FUTURE WORK..... | 195 |
| APPENDIX A. | CONSTANT TEMPERATURE GRADIENT TRIANGLES FOR HEAT FLOW MODEL | 198 |
| APPENDIX B. | LINEAR STRAIN TRIANGLES FOR STRESS MODEL | 200 |
| APPENDIX C. | EQUATIONS FOR GENERALIZED PLANE STRAIN, FORMULATION BY DIRECT METHOD..... | 204 |
| APPENDIX D | ITERATIVE METHOD OF GENERALIZED PLANE STRAIN FORMULATION | 207 |
| APPENDIX E | FINITE ELEMENT EQUATIONS FOR MOLD DISTORTION ANALYSIS | 209 |
| APPENDIX F | CALCULATION OF BOLT PRE-STRESS..... | 211 |
| APPENDIX G | CORRECTION TO SIMULATION TIME FOR DRAINAGE DURING A BREAKOUT..... | 212 |
| APPENDIX H | CALCULATIONS OF HEAT TRANSFER COEFFICIENTS FOR THE ROLLS | 214 |
| REFERENCES | | 216 |
| VITA. | | 217 |

LIST OF TABLES

| | | Page |
|-----------|---|------|
| Table 3.1 | Constants for the gap heat transfer model | 31 |
| Table 4.1 | Standard Simulation Conditions | 84 |
| Table 5.1 | List of various convergence criteria and comparison of CPU times | 109 |
| Table 6.1 | Breakout Simulation Conditions. | 121 |
| Table 9.1 | Location and size of rolls in a typical slab caster along with spray conditions . . | 163 |
| Table 9.2 | Location and size of depression for different mechanisms | 175 |

LIST OF FIGURES

| | Page |
|--|------|
| Figure 1.1: Trend in production of continuously cast steel among industrialized nations..... | 1 |
| Figure 1.2: Schematic Overview of the Continuous Casting Proces | 3 |
| Figure 1.3 Schematic representation of shell growth inside the slab casting mold..... | 4 |
| Figure 1.4 Schematic of some defects associated with continuously cast slabs..... | 5 |
| Figure 3.1 Schematic of slab caster showing transverse section simulation domain along with the finite element mesh. | 24 |
| Figure 3.2 Heat Transfer through the solidifying shell. | 27 |
| Figure 3.3 Schematic of heat transfer boundary condition.. | 28 |
| Figure 3.4 Resistor model for interfacial heat transfer. | 30 |
| Figure 3.5 Comparison of model prediction with plant measurements. | 33 |
| Figure 3.6 Velovity, temperature and heat flux in thestrand. | 35 |
| Figure 3.7 Schematic showing application of internal heat source at appropriate faces ... | 36 |
| Figure 3.8 Mechanical boundary conditions. | 45 |
| Figure 3.9 Schematic Illustration of the mold penetration algorithm. | 48 |
| Figure 3.10 Schematic of bulging of the slab below mold | 50 |
| Figure 3.11 The bulging profile between two rolls used for simulation below mold | 51 |
| Figure 3.12 Thermal conductivities of Carbon and Stainless steel as a function of temperature.. | 54 |
| Figure 3.13 Enthalpy of carbon steel and stainless steel used in the model. | 55 |
| Figure 3.14 Thermal linear expansion curves for carbon and stainless steel.. | 55 |
| Figure 3.15 Elastic Modulus Function used in the model | 56 |
| Figure.4.1 Cut away section of the slab mold. | 70 |
| Figure.4.2 Schematic top view of mold | 71 |
| Figure.4.3 2D transverse section through wide face showing detailed model domain | 71 |
| Figure.4.4 Finite element mesh and boundary conditions for 2D analysis. | 74 |
| Figure.4.5 Model mesh and boundary conditions shown in top view of mold quarter | |

| | | |
|--------------|--|-----|
| | section. | 75 |
| Figure.4.6 | Heat flux at the symmetry plane as a function of position in the mold | 76 |
| Figure.4.7 | Temperature contours with the section of the mold plate assembly (2D) | 81 |
| Figure.4.8 | Temperature distribution through mold thickness (at center of wide face) | 81 |
| Figure.4.9 | Distorted shape of the mold along with the temperature distribution on the hot face | 83 |
| Figure 4.10 | Temperature (°C) and distorted shape (exaggerated 20X) of a transverse section halfway down the mold | 85 |
| Figure. 4.11 | Distortion showing a gap formed between the copperplate and the steel backing plate. | 85 |
| Figure. 4.12 | Temperature and distortion of the narrowface copper plate as position down the mold.. . . . | 86 |
| Figure. 4.13 | Distortion of the wideface backing plate as a function of the distance across and the slab width.. . . . | 87 |
| Figure. 4.14 | Effect of mold plate thickness on the temperature and distortion.. . . . | 88 |
| Figure. 4.15 | Stress (σ_x) distribution in the domain for the 2D analysis with water slot geometry. | 89 |
| Figure. 4.16 | Comparison of z-stress for the 2D and 3D analysis | 90 |
| Figure. 4.17 | Von Mises Stress (MPa) distribution in the mold along with the distorted shape. | 91 |
| Figure. 4.18 | Distortion of the wide and narrow face along the line where they meet in the mold.. . . . | 95 |
| Figure. 4.19 | Comparison of the predicted distortion with the standard taper practices.. . . . | 95 |
| Figure 5.1 | Heat Transfer and stress analysis meshes | 103 |
| Figure 5.2 | Flow chart for the overall simulation procedure for the explicit method | 104 |
| Figure 5.3 | Flow chart for the overall simulation procedure for the implicit method | 108 |
| Figure 6.1 | (a) Finite element mesh and boundary condition for cylinder under internal pressure, (b) Comparison CONCAST solution of Stress history in the | |

| | | |
|------------|--|-----|
| | cylinder under internal pressure with that of Greenbaum & Rubinstein | 112 |
| Figure 6.2 | Tensile test curves calculated from CONCAST at different temperatures | 113 |
| Figure 6.3 | Tensile test curves at different strain rates calculated for the constitutive equation used for continuous casting simulation at 950 °C for 0.005%C steel .. | 114 |
| Figure 6.4 | Creep test curves calculated with the constitutive equation at 1300 °C | 115 |
| Figure 6.5 | Schematic of the heat transfer and mechanical boundary condition of the analytical 1-D solidification problem | 116 |
| Figure 6.6 | Comparison of Numerical and analytical solution for the 1D solidification problem | 117 |
| Figure 6.7 | Comparison of predicted shell thickness with two transverse sections through a breakout shell. | 119 |
| Figure 6.8 | Comparison of predicted shell thickness at various locations on the shell as a function of distance below meniscus with the measurements on the Breakout shell.. . . . | 120 |
| Figure 7.1 | Effect of thicker mold powder layer in the off-corner region of the narrowface on the predicted shell growth. | 128 |
| Figure 7.2 | Effect of superheat dissipation on the shell thickness (NF = Narrowface, WF = Wideface) | 129 |
| Figure 7.3 | Effect of superheat on the growth of the shell at different locations of the slab | 130 |
| Figure 7.4 | Effect of nozzle mis-alignment on the predicted shell growth.. . . . | 132 |
| Figure 7.5 | Predicted shell thickness as a function of distance below meniscus showing possible shell erosion due to nozzle misalignment. | 131 |
| Figure 7.6 | Effect of casting speed on the narrowface shell growth. | 133 |
| Figure 7.7 | Effect of casting speed on the narrowface shell shrinkage. | 134 |
| Figure 8.1 | Taper calculation on the narrowface. | 137 |
| Figure 8.2 | Schematic of the 1-D model and boundary conditions. | 139 |
| Figure 8.3 | History of various strain components of the surface node for 1-D model. . . . | 140 |
| Figure 8.4 | Stress through the shell at different times | 141 |

| | | |
|-------------|--|-----|
| Figure 8.5 | Comparison of strains for 1-D fine and coarse mesh. | 142 |
| Figure 8.6 | Comparison of stress evolution in the shell between coarse and fine mesh . . . | 143 |
| Figure 8.7 | Comparison of narrowface shrinkage predicted by Eqs. 8.3-8.5 for different meshes | 144 |
| Figure 8.8 | Comparison of shell shrinkage predicted by 1-D and 2-D models | 145 |
| Figure 8.9 | Temperature distribution along the surface of the wideface | 146 |
| Figure 8.10 | Effect of narrowface taper on the shrinkage and gap formation | 148 |
| Figure 8.11 | Effect of narrowface taper on shell growth at mold exit. | 149 |
| Figure 8.12 | Effect of Casting speed on the ideal shrinkage of the corner of the slab. | 151 |
| Figure 8.13 | Comparison of natural shrinkage of the shell with different applied taper for a casting speed of 1.02 m/min. | 153 |
| Figure 8.14 | A method of calculating the shell shrinkage for continuous slab casting to evaluate the optimum taper of the narrowface | 155 |
| Figure 9.1 | Schematic representation of interaction between the shell and the rolls | 161 |
| Figure 9.2 | Temperature history at various point on the surface and inside (16 mm below surface) of the shell as it moves down the strand with no narrowface cooling.. . . . | 164 |
| Figure 9.3 | Effective stress history at the mid-wideface (MWF) on the surface and inside (16mm below surface) of the shell as it moves down the strand with no narrowface cooling. | 166 |
| Figure 9.4 | Stress history at different locations on the surface and 16 mm inside of the shell as it moves down the strand | 166 |
| Figure 9.5 | Temperature contours and principal stresses in the shell during bulging below mold. | 168 |
| Figure 9.6 | Evolution of off-corner gutters below the mold for conditions C with high taper in Table 9.2 | 172 |
| Figure 9.7 | Transverse section of the slab at various locations below the mold, showing possible mechanism of off-corner depressions. | 178 |

| | | |
|-------------|--|-----|
| Figure 10.1 | Schematic representation of temperature zones of low hot ductility of steel . . . | 179 |
| Figure 10.2 | Comparison of transverse stress profile through the shell with and without the constitutive law for the δ -phase.at mold exit | 184 |
| Figure 10.3 | Comparison of transverse and longitudinal stresses between stainless steel and low carbon steel | 185 |
| Figure 10.4 | Variation of temperature and x-stress along the wideface surface at mold exit with a hot spot. | 186 |
| Figure 10.5 | Stress through the shell below the mold (MWF) showing high surface tensile stress in between rolls | 187 |
| Figure 10.6 | Efective inelastic strain history during bulging below mold in the off-corner region of the slab. | 188 |
| Figure 10.7 | History of transverse (σ_z) stress in the shell, a) σ_z contours at three different locations in the mold, b) Transverse stress and temperature history at three different locations on the slab surface | 190 |
| Figure B.1 | Linear strain triangular element in local and global coordinate system | 200 |
| Figure C.1 | Shape of the stiffness matrix for the generalized plane strain formulation. | 206 |

NOMENCLATURE

| <u>Symbol</u> | <u>Designation</u> | <u>SI Units</u> |
|---|--|------------------------------------|
| A | Area | m ² |
| [B] ^e | Element strain-displacement matrix | m ⁻¹ |
| [B _{3D}] | Element strain-displacement matrix in 3D | m ⁻¹ |
| [B'] | Element strain-displacement matrix for generalized plane strain | m ⁻¹ |
| C _D | Drag coefficient | |
| C _p | Heat capacity | J kg ⁻¹ K ⁻¹ |
| C _{p_{eff}} | Effective heat capacity | J kg ⁻¹ K ⁻¹ |
| [C] | Capacitance matrix | |
| [D] | 3x3 elasticity matrix for plane stress | MPa |
| [D'] | 4x4 elasticity matrix for generalized- plane strain | MPa |
| E | Elastic modulus | MPa |
| F _P | Ferrostatic pressure | MPa |
| F | Shape factor for bulging | |
| ΔF _x , ΔF _y , ΔF _z | Force in the x, y and z direction | MN |
| {F} | Total Force vector | MN |
| {ΔF _{εT} } | Incremental thermal force vector | MN |
| {ΔF _{εp} } | Incremental plastic strain force vector | MN |
| {F _{el} } | Total elastic strain force vector | MN |
| {F _{IP} } | Total ferrostatic pressure force vector | MN |
| H | Enthalpy | J kg ⁻¹ |
| [K] | Conductance matrix | |
| [K _{3D}] | Stiffness matrix for 3D element | MNm ⁻¹ |

| | | |
|-----------------|---|--------------------|
| $[K_{\sigma}]$ | Stiffness matrix for plane strain | MNm^{-1} |
| $[K'_{\sigma}]$ | Stiffness matrix for generalized plane strain | MNm^{-1} |
| $[L]$ | differential operator | |
| L | Characteristic length | m |
| L_f | Latent heat of fusion | KJ /Kg |
| L_m | Mold length | m |
| M | Moments | $MN-m$ |
| M_x, M_y | Moments in the x and y directions | $MN-m$ |
| $[N]$ | Shape function | |
| $[N_{3D}]$ | Shape function for 3D element | |
| N | Slab thickness (Narrowface) | m |
| $\{Q\}$ | Heat flow vector | W |
| R | Curvature of continuous casting machine | m |
| T | Temperature | $^{\circ}C$ |
| $\{T\}$ | Nodal temperature | |
| T_c | Coherency temperature | $^{\circ}C$ |
| T_{liq} | Liquidus temperature | $^{\circ}C$ |
| T_m | Mold surface temperature | $^{\circ}C$ |
| T_{sol} | Solidus temperature | $^{\circ}C$ |
| T_s | Surface temperature of the slab | $^{\circ}C$ |
| T_w | Spray water temperature | $^{\circ}C$ |
| T_0 | Pour temperature | $^{\circ}C$ |
| T_{∞} | Reference temperature | $^{\circ}C$ |
| \dot{T} | Time derivative of temperature | $^{\circ}C s^{-1}$ |
| TLE | Thermal linear expansion | $m ^{\circ}C^{-1}$ |
| V_x, V_y, V_z | Velocity components | $m s^{-1}$ |
| V_c | Casting speed | $m s^{-1}$ |
| V_w | Speed of narrow face movement during | |

| | | |
|--------------------|--|--------------------------------|
| | width change | m s^{-1} |
| W | Slab width (Wideface) | m |
| W_{\max} | Maximum slab bulging | m |
| ΔW | difference in mold width at top and bottom of mold | m |
| X | Distance along wideface from slab corner | m |
| Y | Distance along narrowface from slab corner | m |
| Z | Distance below meniscus down the strand | m |
| Z_b | Position of the breakout hole from the top of the shell | m |
| a | Absorption coefficient | m^{-1} |
| b | Roll pitch | mm |
| d | Simulation domain thickness | m |
| d_a | Thickness of the air gap | m |
| d_f | Thickness of the mold flux layer | m |
| d_{gap} | Total thickness of the interfacial gap | m |
| d_b | Diameter of breakout hole | m |
| d_m | Mold distortion | m |
| d_{tap} | Offset in mold wall position from taper | m |
| d_{wall} | Position of mold wall | m |
| g | Gravity | ms^{-2} |
| h | Heat transfer coefficient | $\text{W m}^{-2}\text{K}^{-1}$ |
| h_c | Shell/Flux heat transfer coefficient | $\text{W m}^{-2}\text{K}^{-1}$ |
| h_{eff} | Effective mold heat transfer coefficient | $\text{W m}^{-2}\text{K}^{-1}$ |
| h_{nconv} | Natural convection heat transfer coefficient | $\text{W m}^{-2}\text{K}^{-1}$ |
| h_{rad} | Radiation heat transfer coefficient | $\text{W m}^{-2}\text{K}^{-1}$ |
| h_{spray} | Spray zone heat transfer coefficient | $\text{W m}^{-2}\text{K}^{-1}$ |
| h_0 | Mold/Flux heat transfer coefficient | $\text{W m}^{-2}\text{K}^{-1}$ |

| | | |
|--------------------------|--|--------------------------------|
| k | Thermal conductivity of steel | $\text{W m}^{-1}\text{K}^{-1}$ |
| k_a | Thermal conductivity of air | $\text{W m}^{-1}\text{K}^{-1}$ |
| k_f | Thermal conductivity of mold flux | $\text{W m}^{-1}\text{K}^{-1}$ |
| n | No of nodes failing a convergence criteria | |
| ndf | Number of degrees of freedom | |
| n_e | No. of elements | |
| n_g | No. of gauss points | |
| q | Heat transfer rate | W |
| q'' | Heat flux | W m^{-2} |
| q''_{sh} | Superheat flux | W m^{-2} |
| s | Shell thickness | m |
| tapr_n | Nominal casting taper | $\%/m$ |
| tapr_d | Dynamic taper | $\%/m$ |
| t | Current time (since start of casting) | s |
| t_s | Time when the slice is at the meniscus | s |
| t_w | Time at the start of the width change | s |
| t_e | Time at the end of the width change | s |
| Δt | Time step | s |
| $\{u\}$ | Displacement vector | m |
| u | Total nodal displacements in x-direction | m |
| $\{\Delta u\}$ | Incremental displacement vector | m |
| $\Delta u_x, \Delta u_y$ | Incremental nodal displacements | m |
| v | Total nodal displacements in y-direction | m |
| w | Total nodal displacements in z-direction | m |
| \dot{w} | Water flux | lm^{-2} |
| x | X coordinate | m |
| y | Y coordinate | m |
| z | Z coordinate | m |

| | | |
|-------------------------------|---|-------------------|
| $\Delta x, \Delta y$ | Mesh spacing in x and y direction | m |
| α | Ferrite phase | |
| α_T | Thermal expansion coefficient | |
| β | Truncation parameter | |
| δ | Delta phase | |
| $\{\delta\}$ | Vector containing in-plane displacements and out-of-plane strain | |
| δ_m | Allowable penetration of the mold by a shell surface node | m |
| δ_{ij} | Kronecker delta function | |
| $\{\epsilon\}$ | Total strain components | |
| $\{\dot{\epsilon}\}$ | Components of total Strain rate | sec ⁻¹ |
| $\{\dot{\epsilon}_T\}$ | Components of total thermal strain rate | sec ⁻¹ |
| $\{\dot{\epsilon}_p\}$ | Components of total plastic strain rate | sec ⁻¹ |
| $\{\dot{\epsilon}_p^\Delta\}$ | Components of total plastic strain rate at an intermediate step | sec ⁻¹ |
| $\{\Delta\epsilon\}$ | Incremental total strain | |
| $\{\Delta\epsilon_p\}$ | Incremental-plastic strain | |
| $\{\Delta\epsilon_{pz}\}$ | Incremental-plastic strain in z-direction | |
| $\{\Delta\epsilon_z\}$ | Incremental total z-strain | |
| $\dot{\bar{\epsilon}}$ | Effective strain rate = $\Delta\epsilon/\Delta t$ | sec ⁻¹ |
| ϵ_m | Mold emissivity | |
| ϵ_s | Shell emissivity | |
| ϕ | Relaxation parameter for strain rate convergence | |
| γ | Gamma phase | |
| η_d | Convergence parameter for gap heat transfer | |
| η_ϵ | Convergence parameter for strain | |
| η_σ | Convergence parameter for stress | |

| | | |
|----------------------|---|--------------------------------|
| λ | Stiffness multiplier | |
| μ | Refractive index | |
| ν | Poisson's ratio | |
| ρ | Mass density | Kgm^{-3} |
| σ_{SB} | Stefan-Boltzmann constant | $\text{Wm}^{-2} \text{K}^{-4}$ |
| $\{\sigma\}$ | Total stress components | MPa |
| $\{\sigma'\}$ | Total deviatoric part of stress components $\{\sigma\}$ | MPa |
| $\{\sigma^{*'}\}$ | Total deviatoric part of stress components $\{\sigma^*\}$ | MPa |
| σ | Von Misses effective Stress for $\{\sigma\}$ | MPa |
| σ^* | Von Misses effective Stress for $\{\sigma^*\}$ | MPa |
| $\{\Delta\sigma\}$ | Incremental stress components | MPa |
| $\{\Delta\sigma_z\}$ | Incremental z-stress component | MPa |
| τ | Shear Stress | MPa |
| θ | Relaxation parameter for gap heat transfer convergence | |
| $\{ \}$ | Column vector | |
| $[]$ | Square matrix | |
| Superscripts | | |
| e | Pertaining to an element | |
| $t + \Delta t$ | Unknown time step | |
| t | Last time step | |
| $t + \Delta t$ | Previous time step to t | |
| Subscripts | | |
| copper | Mold copper plate | |
| e | Elastic | |
| pl | Plastic-creep (inelastic) | |
| steel | Steel backing plate | |
| T | Thermal | |
| x,y,z | Components | |

Abbreviations :

| | |
|------|-----------------------|
| NF | Narrowface |
| WF | Wideface |
| MNF | Mid-narrowface |
| MWF | Mid-wideface |
| OCNF | Off-corner narrowface |
| OCWF | Off-corner wideface |

CHAPTER 1

INTRODUCTION

The continuous casting process has been in operation for about three decades. The products made by this process currently account for approximately 65% of the total global steel production (Figure 1.1) [1]. In many of the industrialized nations, over 95% of the steel production is by the continuous casting process. In the U.S., roughly 70% of the 80 million metric tons of steel produced annually is manufactured by the continuous casting process and is expected to grow to 95% by the year 1995.

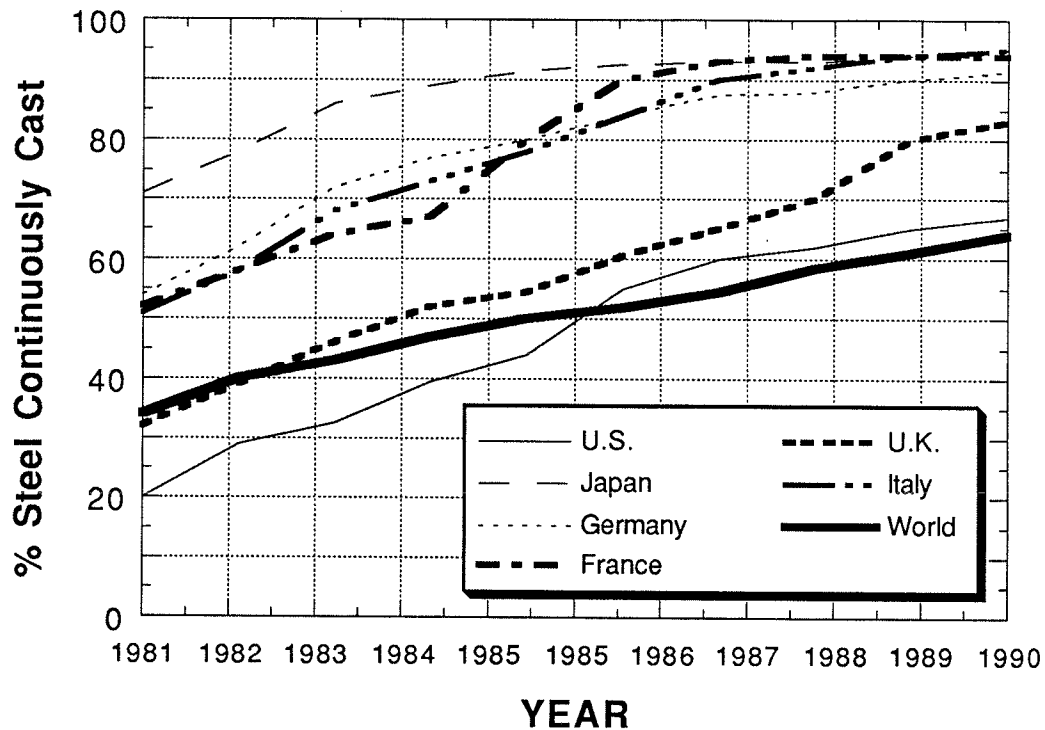


Figure 1.1: Trend in production of continuously cast steel among industrialized nations.

Although very efficient, the continuous casting process is affected by several problems, which include surface-shape distortion, surface and sub-surface cracks, and the ultimate defect, the

“breakout”¹ . Surface quality of the slab is highly dependent on casting practice and process parameters, as is the internal quality of the cast product. These problems and associated defects frequently result in tons of scrapped product annually, which is quite costly for the steel producing companies, and ultimately the consumer. In order to find the possible sources of these defects one has to fully understand and appreciate the complicated nature of the process and the various phenomena that control the behavior of the steel. A brief overview of the continuous casting process is provided in the following section.

1.1 PROCESS OVERVIEW

The schematic representation of a continuous casting machine is shown in Figure 1.2. The refined steel produced in the basic oxygen furnace is introduced into the refractory lined ladle and transferred to the caster from the melting shop. During the continuous casting process, the superheated liquid metal is poured from the ladle into a tundish. The molten steel then flows from the tundish under gravity, through the submerged entry nozzle and into the casting mold which is often curved. The liquid steel is prevented from flowing out the bottom of the mold at startup by inserting a plug, known as a dummy bar, which is withdrawn as the steel solidifies. The steel freezes against the water-cooled copper mold forming a thin solidified shell. This shell acts as a container for the remaining liquid metal, and it grows as it travels down the mold. As the solid shell is pulled down the mold it solidifies further and thickens to attain enough strength to support the liquid core at mold exit, otherwise liquid metal will break through the shell, which is commonly referred to as breakout. Mold powder spread over the liquid steel in the mold for thermal insulation, and also acts as a lubricant for the shell-mold contact. As the mold oscillates, liquid flux is pulled into the gap between the shell and mold, forming a thin lubricating film. This film prevents the shell from sticking to the mold wall, and thereby allows the slab to be withdrawn

¹ A “breakout” occurs when liquid steel flows through a punctured hole in the shell (which is caused due to localized effects such as hot spots or sticking) and falls all over the machine causing a complete shutdown. Each breakout costs about \$200,000 - \$500,000 for the steel companies in terms of machine cleanout and production loss.

without shell tearing. The oscillation is responsible for transverse ripples, called "oscillation marks" on the surface of the slab.

Upon exiting the mold, the slab enters the spray zone where it is further cooled by water jets and passes through a series of guide rollers in an arc (to reduce the height of the machine) as shown in Figure 1.2, until, upon unbending, it travels horizontally. The slab length from meniscus to the position where the liquid core vanishes is termed the "metallurgical length" which

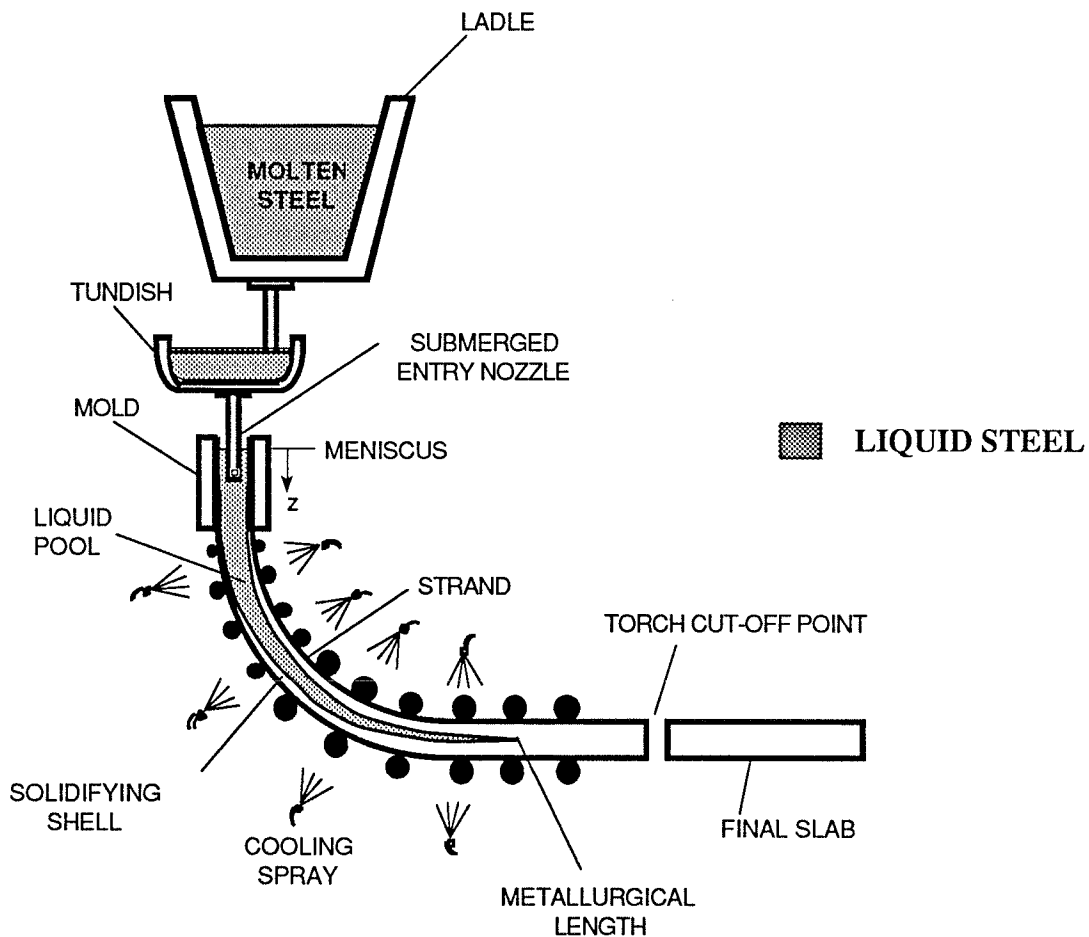


Figure 1.2: Schematic Overview of the Continuous Casting Process.

varies from 20 to 30 meters depending on the slab thickness and processing conditions. The completely solidified product is torch-cut into final slabs of desired length.

Perhaps the most critical aspects of the process occur in the relatively short region of the actual mold. Inside the mold (Figure 1.3) as the shell solidifies, it shrinks away from the mold wall possibly creating a gap, the size of which controls the heat transfer. As shown in Figure 1.3, the shell grows under the complicated action of turbulent fluid flow from the nozzle (for typical casting conditions the Reynolds Number at nozzle port is around 65,000), ferrostatic pressure, solidification shrinkage, high temperature creep plasticity, thermal distortion of the mold and intermittent contact between the rigid mold and the shell. In addition, the mold oscillates, producing significant dynamic effects of its own. The strength of the shell under the complicated action of these forces plays an important role in the formation of various defects. Interaction of these phenomena produce a complex situation which is intrinsically worthy of study.

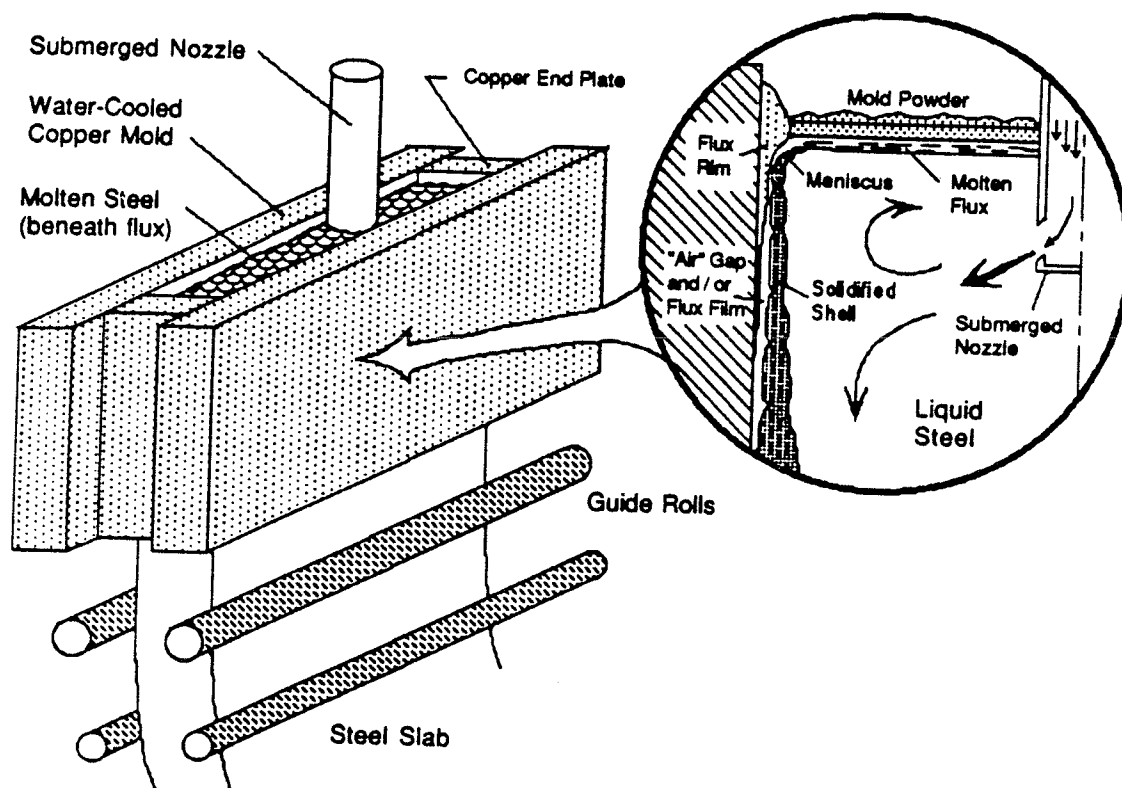


Figure 1.3 Schematic representation of shell growth inside the slab casting mold.

1.2 THE PROBLEM

Figure 1.4 illustrates some of the defects that are believed to be related to the phenomena just mentioned. Most of the surface defects are believed to have been either generated or initiated in the mold while the internal cracks form below the mold. Surface cracks are oxidised by air and therefore cannot weld during subsequent rolling unless removed by scarfing or grinding. These cracks will lead to slivers in the rolled product. Internal cracks often get welded during subsequent rolling unless they open up to the surface. Surface cracks observed in continuously cast steel slabs include longitudinal as well as transverse cracks. Longitudinal cracks form at the mid-face and

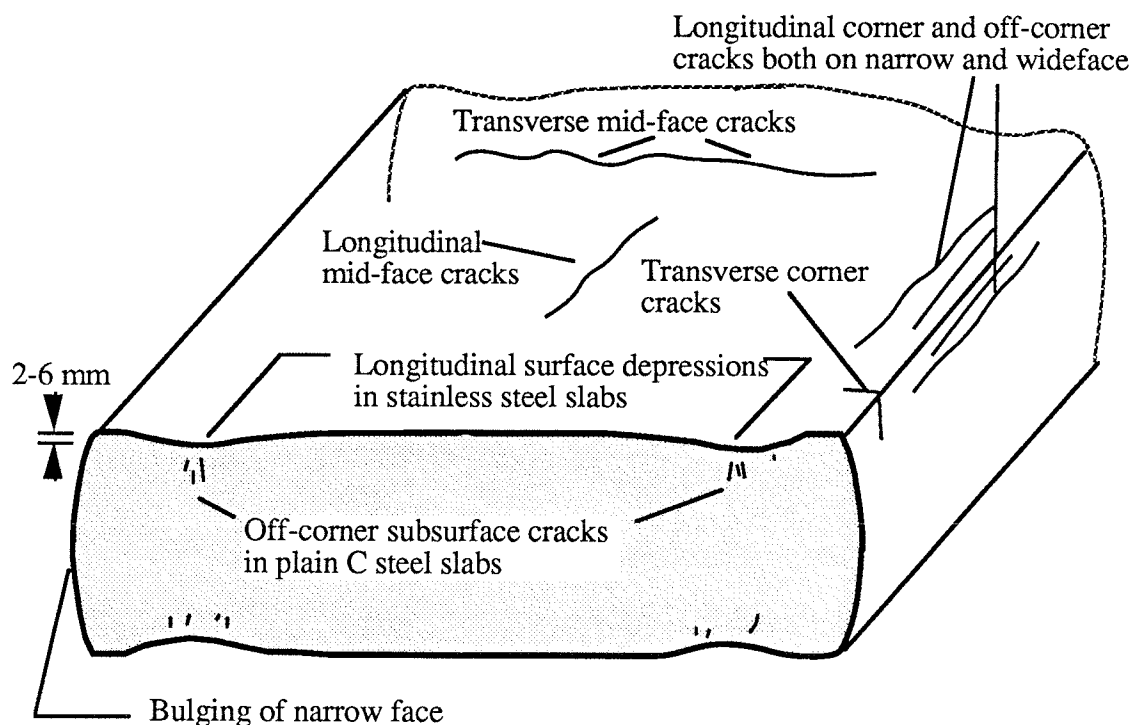


Figure 1.4 Schematic of some defects associated with continuously cast slabs.

corners of both wideface and narrowface as well as in the off-corner regions. The sub-surface cracks and corner cracks are mostly of mechanical (shell bulging, corner rotation etc.) or of thermal (shell reheating) origin and are associated with excessive stress formation at the solidification front. Stainless steel slabs often exhibit depressions or “gutters” just off the corner along the wideface of

the slab and are accompanied by bulging of the narrow face. The off-corner region of plain carbon steel slabs often exhibits subsurface cracks as well.

Thermal and mechanical loads imposed on the shell by the continuous casting process are believed to initiate these defects. The thermal loads arise from the temperature gradient over the shell thickness and by discontinuities over the width and along the strand length (e.g. surface reheating, mold flux discontinuities). Mechanical loads have several sources such as ferrostatic pressure, withdrawal forces, friction with the mold, bending and straightening and by permanently deformed or mis-aligned rollers. Mold taper is one of the controllable process variables that may affect these problems. Prevention of these defects requires good machine design and careful control of the processing variables.

During solidification, the shell dissipates the superheat contained in the liquid, solidifies, cools and shrinks away from the mold due to thermal contraction. Over most of the wideface, ferrostatic pressure maintains good contact between the shell and the mold. However, a gap may form at the interface near the corners and narrow face, where the heat flow is greatly reduced. The extent of the gap depends on the strength of the shell to withstand the ferrostatic pressure pushing it outward, the casting speed, the heat transfer characteristics of the interface between the mold and shell, and the position of the mold wall, which is determined by the amount of mold taper and the thermal distortion of the mold. Thus, a comprehensive model should incorporate the diverse phenomena of fluid flow, and heat transfer in the liquid pool, heat conduction, shrinkage and stress development within the solidifying steel shell, temperature and thermal distortion of the mold. Of paramount importance is a realistic treatment of heat flow across the interface, which is coupled with the shrinkage.

1.3 MOTIVATION

Many of the problems mentioned above are initiated in the mold by complex interactions between thermal and mechanical stresses and microstructural phenomena. The causes of these and

other problems are still not fully understood and are the subject of ongoing research. Mathematical modeling, in combination with physical models, experiments and measurements on the operating caster can aid in generating this understanding. The thermo-mechanical behavior of the solidifying shell during the early stages of solidification plays an important role in the formation of some of these defects, which inspired the development of the comprehensive model presented in this research.

There are several important reasons and uses for the thermo-mechanical modeling of the continuous casting process. Understanding the history of the slab shape and the stress is important for the process development and improvement. Thermal stresses imposed on the shell by the continuous casting process are believed to initiate the defects mentioned above. The thermal strain which is induced in the shell by the cooling history, can be affected by the heat transfer in the mold (which is affected by the distribution and properties of mold flux) or by the spray cooling below the mold. Ferrostatic pressure which is important only in slabs and large blooms also affects the stresses through contact forces in the mold and bulging below in between rolls. Mechanical forces introduced during unbending or by roll mis-alignment also affects the stresses in the shell. Stress models can also assist in the design of mold shape (taper) to match shrinkage and in production of cracks (in conjunction of a fracture criteria) and residual distortion.

Thus the overall objective of this research is to develop a comprehensive mathematical model of coupled heat transfer and stress analysis and apply the model to understand the formation of some of the defects mentioned above and to optimize the mold taper to match the shrinkage of the shell to prevent taper related problems. In justification for the need of a comprehensive model, the next chapter will discuss the previous mathematical models and some of the important phenomena that have often been neglected. Then a detailed description of the model will be provided. The verification of the model will be done using analytical solutions of well established test problems as well as comparing model predictions with the experimental measurements in a slab caster. Having described the model and verified it, the model will then be applied to simulate breakout formation during an automatic width change operation, taper optimization, bulging below

the mold followed by a discussion on crack formation using the results of the model. Finally, some useful conclusions based on the findings of the model simulations and a recommendation of future enhancement of the present work will be provided.

1.4 REFERENCES

1. International Iron and Steel Institute: "Percentage of Crude Steel Continuously Cast", *Iron and Steelmaker*, 1991, vol. 18 (12), pp. 1-16.

CHAPTER 2

PREVIOUS MATHEMATICAL MODELS

The solidification of the steel shell during continuous casting in the mold takes place under various interacting phenomena such as turbulent flow from the nozzle and its effect on shell growth, interaction of the shrinkage of the shell and ferrostatic pressure leading to intermittent contact with the mold, interaction of the interfacial heat transfer with air gap formation, high temperature creep plasticity and many more. The complicated nature of the continuous casting process makes it very difficult to conduct any experiment inside the mold to understand the behavior of the solidifying shell. Mathematical modeling has helped researchers to understand the underlying principles of various materials processing operations for over a decade. The continuous casting process has been subjected to more mathematical models than any other process. Recent reviews of these models can be found in^[1] on slab casting and in^[2] on billet casting. Earlier works focused on predicting the progress of solidification, as this information is essential to correctly account for the relationship between casting speed, the position of straightening rollers and the metallurgical length to decide the location of the cutting torch. To predict and prevent formation of cracks, requires a much more detailed analysis and complex models incorporating fluid flow, heat transfer, solidification and viscoplastic stress analysis. The following historical survey will give the progress of mathematical modeling as well as the state of this complex subject at the present time.

2.1 SOLIDIFICATION HEAT TRANSFER MODELS

By far the most common and widely used models are simple solidification models, based on transient heat conduction with latent heat evolution, that can predict temperature evolution and thickness of the solidifying shell as it moves down the caster^[3-5]. The models range from 1-D analytical solutions to 3-D models. Hills^[4] used a simple 1-D analytical solidification model for

billet casting with constant material properties. Mizikar^[3] using a finite difference method, extended Hill's model by using temperature dependent material properties as well as experimentally derived heat transfer coefficients. Validated models are commonly used by steel companies as a tool for design or various trouble shooting purposes^[6, 7]. These solidification models are useful for monitoring several difficult to measure parameters such as, shell thickness, metallurgical length, and strand surface temperature.

Heat transfer models have been used for designing continuous casting machines. The rate at which the heat is extracted from the steel is critical to the smooth operation of the process, excessive cooling can lead to the formation of cracks at the bending or straightening rolls. Laitinen and Neittaanmaki^[8] used a steady state finite element heat transfer model of the entire continuous caster for testing of new designs of continuous casting machines. They also solved the inverse problem by specifying the shell surface temperature to obtain the heat transfer conditions in terms of water flux in the spray zone. Lally et al.^[9, 10] used a 2-D transient finite difference heat transfer model for optimizing the processing conditions for both billet and slabs.

Most of the solidification heat transfer models mentioned above include the convection in the liquid by enhancing the conductivity of the liquid by a factor of 6-8^[3, 8]. However coupled heat transfer and fluid flow analysis of the mold region^[11, 12] have suggested that super-heat dissipation is non-uniform in the slab casting, more heat being convected by the turbulent flow to the narrowfaces than to the widefaces and such effects cannot be incorporated into a heat transfer solidification model by simply enhancing the conductivity of the liquid. Not much effort has been given in the literature to incorporate this effect in a heat transfer model or a coupled heat transfer stress model. In this work an attempt has been made to resolve this issue and will be discussed in chapter 3.

2.2 THERMAL STRESS MODELS OF THE SHELL

Comparatively fewer thermo-mechanical models of slab casting have been reported in the literature. The poor attention to stress modeling can be attributed to the complex nature of the governing phenomena as well as a large number of computational difficulties. The numerical difficulties encountered in this type of model arise from several sources, all of which require iteration : these include the non-linear mechanical behavior of steel, intermittent contact between the shell and mold, and the coupling between the thermal and stress analysis through the air gap. The strand movement relative to the mold and the rolls calls for a moving boundary condition. The inherent 3D nature of the problem when simplifying to 2D needs generalized plane strain which requires a special formulation. Also special precautions are necessary for the co-existing solid/liquid phases in the domain to prevent any stresses in the liquid. In addition to all these, strains from elastic-plastic-creep and phase transformations are also very important to the process. The inseparable creep-plasticity at high temperatures calls for unified constitutive models, which constitute an important field of research.

2.2.1 2-D SLICE MODELS

For continuous casting of steel, the Peclet number which characterizes the importance of convection over conduction, is of the order of 500. Due to the large Peclet number for the continuous casting process of steel, it has been possible to use 2-D slice models of the strand as it moves down the caster, by neglecting the heat flow in the axial direction. Using a 2-D mechanical model requires an assumption of the stress state in the third (out-of-plane) direction. The two most commonly used simplification for two dimensional stress analysis is to assume a state of plane stress $\sigma_z = 0$ or plain strain i.e. $\epsilon_z = 0$. Neither of these assumptions correctly describe the stress state of the 2-D slice as it moves down the strand, because of considerable thermal gradient in the z-direction. The most appropriate stress state for the slice is generalized plane strain i.e. $\tau_{xz} = \tau_{yz} = 0$ and $\epsilon_z = \text{constant}$. Most of the work in published literature either assumes plane stress or plane

strain. Previous thermo-mechanical models have simulated both billet casting^[13-17] and slab casting^[18-28].

2.2.1.1 BILLET CASTING

Several thermal stress models of billet casting have been used to investigate defects, including those forming or initiating in the mold. Grill et al.^[13] initiated the thermo-mechanical modeling of the billet strand by applying an elastic - plastic model to explain internal crack formation. By coupling heat flow to air gap computed from stress analysis they calculated the heat transfer coefficients in the corner region and were able to predict corner cracks in the billet while in the mold. The model was improved later by Sorimachi and Brimacombe^[14] incorporating improved material property data. Kristiansson^[15, 16] further improved the traveling slice method of analysis by developing a step-wise coupled 2-D thermal and mechanical model including the effect of changing gap size on heat transfer and creep deformation of a slice through the solidifying shell. It was used to understand the formation of longitudinal and sub-surface cracks in the mold region of continuously cast billets. The results were analyzed for crack susceptibility using a 0.2% strain based fracture criterion. By incorporating the thermal distortion of the mold Kristiansson was able to predict excessive mold wear. Calculated results were in reasonable agreement with observations reported in the literature.

Kelly et al.^[17] developed a coupled 2-D axisymmetric thermo-mechanical model for the steel shell behavior in round billet casting molds. Their results suggested that thermal shrinkage associated with the phase change from delta-ferrite to austenite in 0.1%C steel accounts for the decreased heat transfer observed in the alloy as well as its crack susceptibility. Tszeng and Kobayashi^[29] used the temperature recovery method of latent heat evolution to get the temperature solution for their un-coupled thermo-mechanical model of billet casting. They used their plane-strain deformation and stress analysis of the billet to get a qualitative basis of possible defect

occurrence without any fracture criteria. Models such as these have been used to obtain an understanding of the thermo-mechanical of the billets.

2.2.1.2 SLAB CASTING

Most stress models of slab casting have been concerned with bulging below the mold.^[30-36] However, finite element thermal stress models have played an important role in understanding behavior in the slab mold as well^[19-25, 27, 28, 30-33, 35-38]. These models have been applied to various aspects of mold design, such as mold taper^[27, 28, 39] and to understand various defects, such as off-corner depressions^[25, 27, 28, 37] and cracks^[15, 16, 19, 21, 24, 37, 39]. Such models are capable of predicting stress distributions in the solidifying shell and by adopting a “critical stress” (e.g. 20 MPa for steels above 1340 °C)^[13] or a critical “strain to fracture” (e.g. 0.2% for steels above 1340 °C)^[14], it is possible to identify casting conditions that are prone to crack formation.

Grill et al.^[18] developed an elasto-plastic finite element model to analyze stress distribution and applied it to understand how to avoid corner crack formation by avoiding the tensile stresses associated with surface reheating just below the mold. They studied the effects gap formation and its interaction with heat flow and the effects of operating conditions such as casting speed, slab size and mold taper on the shell deformation and corner rotation just below mold for predicting breakouts and mold wear. Kinoshita et al.^[19, 21] used a coupled 2-D heat conduction and elasto-plastic stress model to investigate the temperature and stress fields in a transverse slice through the solidifying shell in a continuous slab casting mold. The calculated heat flux and shell thickness profiles closely resembled the experimental ones. They studied the effects of operating variables such as slab size, withdrawal rate, mold taper, and mold flux to understand how to avoid various crack defects in slabs.

Rammerstorfer et al.^[20] used a one dimensional elastic-visco-plastic thermal stress model to simulate the mid-width cross-section through a slab. Their results suggested that reheating of the slab below mold should be avoided to reduce the probability of occurrence of internal cracks. Their conclusions were based on a maximum strain level of 2-6 % at the solidification front (mushy zone) suggested by Puringer^[30].

Thermal-mechanical models of slab casting have also been used to improve mold design. Williams et al.^[40] and Lewis et al.^[41] had developed an uncoupled visco-plastic model using the 'initial strain approach' of Zienkiewicz and Corneau^[42] under plane stress conditions. They have shown that accelerated cooling using concave mold surfaces reduce the stress levels by 15% compared to straight molds, thereby reducing the thermal cracking. Ohnaka and Yashima^[24] studied the effects of mold taper and mold corner design on stress generation in the off-corner region of the mold using a thermal elasto-plastic finite element model. The stress model included ferrostatic pressure and shell/mold interaction. It was shown that shell deformation due to thermal stress and ferrostatic pressure changes the shell-mold thermal resistance resulting in tensile stresses that might cause longitudinal cracks down the corner. Rounded corners and taper less than 1% were predicted to reduce the extent of off-corner hot spots and subsequent thermal stresses.

Takemoto et al.^[39] developed a coupled solidification-deformation model to obtain the optimum design of the mold shape in order to prevent the formation of transverse corner cracks in medium carbon steels. In the experimental castings, the occurrence of cracks were found to increase with the narrowface taper. Model results suggested that high contact pressure and hence large frictional force, are developed in the corner region at tapers exceeding the solidification shrinkage. Thus the tapers should be selected to avoid occurrence of high contact pressure when the shell is relative thin, hot and weak.

Recently Okamura and Yamamoto^[37] have developed a 2-D slice model of the shell to understand the formation of corner cracks. Their model included a steady state analysis of the

mold heat conduction while tracking the slice in the time domain. They were able to show that by increasing the applied taper, the off-corner stress peaks are reduced to a great extent, thereby reducing chances of crack formation in these locations. This is obviously in contrary to the findings of Takemoto et al.^[39].

2.2.2 SLAB BULGING BELOW MOLD

Solidification stress analysis has been used to design casting machine (location of unbending rolls etc.) in order to minimize the internal strain introduced by unbending and bulging^[34]. The effect of bulging due to ferrostatic pressure, reheating of slab surface due to inappropriate cooling and unbending during straightening on internal crack formation has been extensively studied^[30-36]. Models have predicted internal strains close to the solidification front in excess of critical strains of 0.25-0.3% as a result of unbending.

2.3 STEADY STATE MODELS

Steady state heat transfer models of the longitudinal section of the strand has been used for design of the caster^[8]. Steady state thermo-viscoplastic model for the 2D longitudinal section of the strand was modeled by Inoue and Wang^[43] to simulate temperature fields and deformation as well as stress in the strand. Manesh^[44] used a thermo-elastic 3D steady state model for process optimization. Using the ratio of the maximum applied stress to yield stress as a basis location of bending rollers and their diameters were predicted. The stress ratios provides the design engineers with a tool for predicting effective parameters on a continuous casting machine for a new installation design.

Models have been used with great success to understand qualitative behavior - e.g. reheating below mold generates stress, but have had problems making quantitative predictions.

Although successful, the models described above are not general since they ignore some of the complex phenomena known to be present. In addition to solidification shrinkage, thermal stresses, creep-plasticity, ferrostatic pressure and intermittent contact between the shell and mold, the effects of non-uniform superheat dissipation via turbulent fluid flow and distortion of the mold may play a role in defect formation. The lack of knowledge regarding the relative importance of these other phenomena provided the motivation for the present work, in which a model has been developed to incorporate all of these effects.

2.4 REFERENCES

1. B.G. Thomas: "Mathematical Modeling of the Continuous Slab Casting MOld : A State of the Art Review", *74th Steelmaking Conference*, ISS, Washington, D.C, 1991, Vol. 74.
2. I.V. Samarasekera and J.K. Brimacombe: "Application of Mathematical Models for the Improvement of Billet Quality", *74th Steelmaking Conference*, ISS-AIME, Warrendale, PA, Washington, D.C, 1991, Vol. 74.
3. E.A. Mizikar: "Mathematical Heat Transfer Model for Solidification of Continuously Cast Steel Slabs", *Trans. TMS-AIME*, 1967, vol. 239, pp. 1747-1753.
4. A.W.D. Hills: "A Generalized Integral-Profile Method for the Analysis of Unidirectional Heat Flow During Solidification", *Transactions TMS-AIME*, 1969, vol. 245, pp. 1471-1479.
5. J. Lait, J.K. Brimacombe and F. Weinberg: "Mathematical Modeling of Heat Flow in the Continuous Casting of Steel", *Ironmaking and Steelmaking*, 1974, vol. 2, pp. 90-98.
6. R. Davies, N. Blake and P. Campbell: "Solidification Modelling - an Aid to Continuous Casting", *Proceedings of the 4th International Conference on Continuous Casting*, Brussels, 1988, Vol. 2, pp. 645-654.
7. E.A. Upton, T.R.S. Rao, P.H. Dauby and R.C. Knechtges: "Physical Metallurgy and Mathematical Modelling as Tools for Continuous Casting Optimization at LTV Steel", *Iron and Steelmaker*, 1988, vol. 15 (5), pp. 51-57.
8. E. Laitinen and P. Neittaanmaki: "On Numerical Simulation of the Continuous Casting Process", *Journal of Engineering Mathematics*, 1988, vol. 22 (4), pp. 335-354.
9. B. Lally, L. Biegler and H. Henein: "Finite Difference Heat Transfer MOdeling for Continuous Casting", *Metallurgical Transactions*, 1990, vol. 21B (August), pp. 761-770.
10. B. Lally, L. Biegler and H. Henein: "Optimization and Continuous Casting, Part 1: Problem Formulation and Solution Strategy and Part 11: Application to Industrial Casters", 1991, ,

11. X. Huang, B.G. Thomas and F.M. Najjar: "The Removal of Superheat from Continuous Casting Molds", *Metallurgical Transactions B*, 1992, vol. 23 B (June), pp. 339-356.
12. P.J. Flint, Q.L. He, R.B. Mahapatra and J. Herbertson: "Heat Transfer, Fluid flow and Solidification Modelling of the Continuous Casting Mould", *Process Technology Conference Proceedings*, ISS-AIME, Warrendale, PA, Toronto, Canada, 1992, Vol. 10, pp. 279-291.
13. A. Grill, J.K. Brimacombe and F. Weinberg: "Mathematical analysis of stresses in continuous casting of steel", *Ironmaking and Steelmaking*, 1976, vol. 3 (1), pp. 38-47.
14. K. Sorimachi and J.K. Brimacombe: "Improvements in Mathematical Modelling of Stresses in Continuous Casting of Steel", *Ironmaking and Steelmaking*, 1977, vol. 4, pp. 240-245.
15. J.O. Kristiansson: "Thermal Stresses in Early Stages of Solidification of Steel", *Journal of Thermal Stresses*, 1982, vol. 5, pp. 315-330.
16. J.O. Kristiansson: "Thermo Mechanical Behavior of the Solidifying Shell within Continuous Casting Billet Moulds - A Numerical Approach", *Journal of Thermal Stresses*, 1984, vol. 7, pp. 209-226.
17. J.E. Kelly, K.P. Michalek, T.G. O'Connor, B.G. Thomas and J.A. Dantzig: "Initial Development of Thermal and Stress Fields in Continuously Cast Steel Billets", *Metallurgical Transactions A*, 1988, vol. 19A (10), pp. 2589-2602.
18. A. Grill, K. Sorimachi and J.K. Brimacombe: "Heat Flow, Gap Formation and Break-Outs in the Continuous Casting of Steel Slabs", *Metallurgical Transactions*, 1976, vol. 7B, pp. 177-189.
19. K. Kinoshita, T. Emi and M. Kasai: "Thermal Elasto-plastic Stress Analysis of Solidifying Shell in Continuous Casting Mold", *Tetsu-to-Hagane*, 1979, vol. 65 (14), pp. 2022-2031.
20. F.G. Rammerstorfer, C. Jaquemar, D.F. Fischer and H. Wiesinger. *Temperature Fields, Solidification Process and Stress Development in the Strand During a Continuous Casting Process of Steel*. International Conference on Numerical Methods in Thermal Problems. 712-722, 1979.

21. K. Kinoshita and T. Emi: *Numerical Analysis of Heat Transfer and Stress in Solidifying Shell within the Mold of Continuous Casting*, Kawasaki Steel Corp., Japan, Report No. 822278, 1980, (translated from Kawasaki Seitetsu Giho Vol. 12 No. 3, 1980).
22. K. Kinoshita, H. Kitaoka and T. Emi: "Influence of Casting Conditions on the Solidification of Steel Melt in Continuous Casting Mold", *Tetsu-to-Hagane*, 1981, vol. 67 (1), pp. 93-102.
23. K. Sorimachi, H. Shiraishi and K. Kinoshita: "Continuous Casting of High Carbon Steel Slabs at Chiba Works", *2nd Process Technology Division Conference*, ISS, Chicago, IL, 1981, pp. 188-193.
24. I. Ohnaka and Y. Yashima: "Stress Analysis of Steel Shell Solidifying in Continuous Casting Mold", *Modelling of Casting and Welding Processes IV*, A.F. Giamei and G.J. Abbaschian, eds., TMS, Warrendale, PA, Palm Coast, FL, 1988, Vol. 4.
25. W.R. Storkman and B.G. Thomas: "Heat Flow and Stress Models of Continuous Casting to Predict Slab Shape", *Modeling of Casting and Welding Processes*, TMS/AIME, April, 14-17, Palm Coast, FL, 1988.
26. B.G. Thomas: "Application of Mathematical Models to the Continuous Slab Casting Mold.", *ISS Transactions*, 1989, vol. 16 (12), pp. 53-66.
27. W.R. Storkman: *Optimization of Mold Taper Design Using Mathematical Models of Continuous Steel Slab Casting*, Masters Thesis, University of Illinois, 1990.
28. B.G. Thomas, W.R. Storkman and A. Moitra: "Optimizing Taper in Continuous Slab Casting Molds Using Mathematical Models", *The Sixth International Iron and Steel Congress*, ISIJ, Nagoya, Japan, 1990, Vol. 2, pp. 348-355.
29. T.C. Tszeng, Y.T. Im and S. Kobayachi: "Thermal Analysis of Solidification by the Temperature Recovery Method", *International Journal of Machine Tools Manufacture*, 1989, vol. 29 (1), pp. 107-120.
30. O.M. Puhringer: "Strand Mechanics for Continuous Slab Casting Plants", *Stahl und Eisen*, 1976, vol. 96 (6), pp. 279-284.

31. A. Grill and K. Schwerdtfeger: "Finite-element analysis of Bulging Produced by Creep in Continuously Cast Steel Slabs", *Ironmaking and Steelmaking*, 1979, vol. 6 (3), pp. 131-135.
32. B. Barber, B.A. Lewis and B.M. Leckenby: "Finite-element Analysis of Strand Deformation and Strain Distribution in Solidifying Shell During Continuous Slab Casting", *Ironmaking and Steelmaking*, 1985, vol. 12 (4), pp. 171-175.
33. J.B. Dalin, Y. Germain and F.L. Chenot: "Finite element computation of bulging in continuously cast steel with a viscoplastic model", *2nd Int. Conf. on Numerical Methods in Industrial Forming Processes*, K. Mattiasson, A. Samuelsson, R.D. Wood and O.C. Zienkiewicz, eds., A.A. Balkema, Rotterdam, Netherlands, Gothenburg, Sweden, 1986, pp. 355-60.
34. M. Uehara, I.V. Samarasekera and J.K. Brimacombe: "Mathematical Modeling of Unbending of Continuously cast Steel Slabs", *Ironmaking and Steelmaking*, 1986, vol. 13 (3), pp. 138-153.
35. J.B. Dalin and J.L. Chenot: "Finite element computation of bulging in continuously cast steel with a viscoplastic model", *International Journal for Numerical Methods in Engineering*, 1988, vol. 25, pp. 147-163.
36. B. Barber and A. Perkins: "Strand Deformation in Continuous Casting", *Ironmaking and Steelmaking*, 1989, vol. 16 (6), pp. 406-411.
37. K. Okamura and K. Yamamoto: "Coupled Analysis Between Thermal Deformation and Heat Transfer of Solidifying Shell in Continuous Casting Mold", *Modeling of Casting, Welding and Advanced Solidification Processes VI*, T.S. Piwonka, V. Voller and L. Katgerman, eds., TMS-AIME, Warrendale, PA, Palm Beach, FL, 1993, pp. 535-541.
38. B.G. Thomas and W.R. Storkman: "Mathematical Models of Continuous Slab Casting to Optimize Mold Taper", *Modeling and Control of Casting and Welding Processes - IV*, A.F. Giamei and G.J. Abbaschian, eds., The Metallurgical Society, Warrendale, PA, Palm Coast, FL, 1988, pp. 287 - 297.

39. K. Takemoto, M. Tateno, S. Nakayama and K. Ebina: "Optimum Design of Mold Shape by Solidification-Deformation Coupled Analysis", *9th Process Technology Conference Proceedings*, ISS-AIME, Detroit, MI, 1990, Vol. 9.
40. J.R. Williams, R.W. Lewis and K. Morgan: "An Elasto-Viscoplastic Thermal Stress Model with Applications to Continuous Casting of Metals", *International Journal of Numerical Methods in Engineering*, 1979, vol. 14, pp. 1-9.
41. R.W. Lewis, K. Morgan and P.M. Roberts. *Determination of Thermal Stresses in Solidification Problems*. Numerical Analysis of Forming Processes. 405-431, 1984.
42. O.C. Zienkiewicz and I.C. Corneau: "Visco-Plasticity -Plasticity and the Creep in Elastic Solids - A Unified Numerical Solution Approach", *International Journal of Numerical Methods in Engineering*., 1974, vol. 8, pp. 821-845.
43. T. Inoue and Z.G. Wang: "Thermal and mechanical Fields in Continuous Casting Slab - A Steady State Analysis Incorporating Solidification", *Ingenieur-Archiv*, 1988, vol. 58, pp. 265-275.
44. A.A.I. Manesh: "Thermo-elastic Stress Analysis to Predict Design Parameters of Continuous Casting", *Journal of Materials Science*, 1992, vol. 27, pp. 4097-4106.

CHAPTER 3

MODEL DESCRIPTION

A two-dimensional (2-D) transient, step-wise coupled thermo-elasto-viscoplastic finite element model, CONCAST, has been developed to understand the behavior of the solidifying shell within the mold region of a continuous slab casting machine. As shown in Figure 3.1, this model tracks the thermal and mechanical behavior of a transverse slice through the continuously cast strand as it moves down through the caster at the casting speed, so is similar to the coupled models of previous workers such as Kristiansson^[1, 2], Grill^[3], Kinoshita^[4-6] and Okamura^[7]. By moving the slice through time in the z-dimension at the same rate as casting speed, it is possible to incorporate the full 3-D phenomena. Incorporating the appropriate 2-D stress state of generalized plane strain, this model attempts to account for those phenomena important to the formation of both longitudinal and transverse defects. The present model includes separate finite element models of heat transfer and stress generation that are coupled through the size and properties of the interfacial gap. The effects of superheat convection in the liquid and mold distortion are incorporated, via links with results from separate model calculations.

3.1 ASSUMPTIONS

The following major assumptions were made in developing the model :

- (i) The input metal temperature, liquid level and casting speed are assumed to be constant.
- (ii) Two-fold symmetry of the slab is assumed, which allows to model only a quarter of a transverse section of the slab.
- (iii) The mold powder layer thickness is constant along the slab perimeter, but varies with the distance down the mold.
- (iv) Axial conduction in the casting direction is neglected.

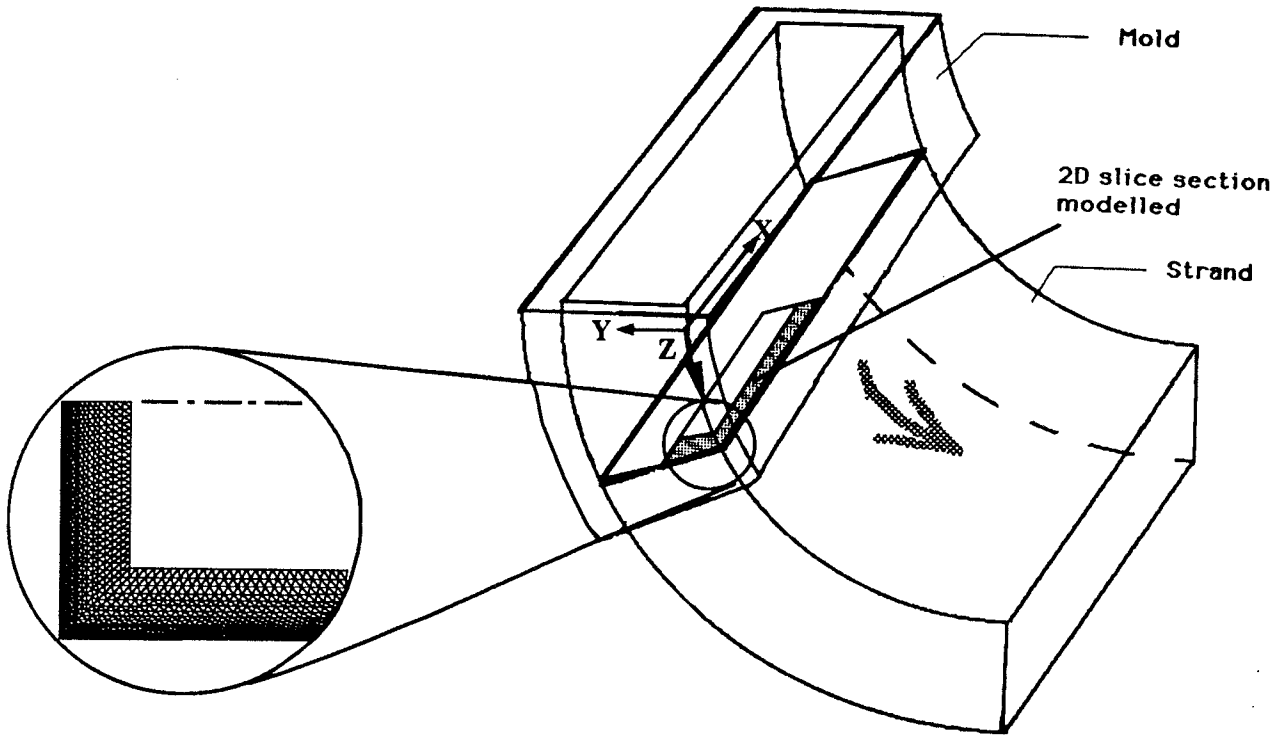


Figure 3.1 Schematic of slab caster showing transverse section simulation domain along with the finite element mesh

- (v) Mold oscillation and friction between the shell and the mold are neglected.
- (vi) Temperature dependent thermo-physical properties are used in the analysis.
- (vii) The stress state is assumed to be generalized plane strain.
- (viii) The visco-plastic behavior of the shell is governed by a temperature, strain and stress-state and compositions dependent unified constitutive law and von Misses yield criterion and Prandtl-Reuss flow rule.

3.2 HEAT TRANSFER MODEL FORMULATION

The partial differential equation governing heat transfer in the continuously-cast strand is given by the 3-D energy equation:

$$\frac{\partial}{\partial x} (k_x \frac{\partial T}{\partial x}) + \frac{\partial}{\partial y} (k_y \frac{\partial T}{\partial y}) + \frac{\partial}{\partial z} (k_z \frac{\partial T}{\partial z}) = \rho C_p \left(\frac{\partial T}{\partial t} + V_x \frac{\partial T}{\partial x} + V_y \frac{\partial T}{\partial y} + V_z \frac{\partial T}{\partial z} \right) \quad (3.1)$$

The symbols are defined in the nomenclature section at the end of the thesis. For the solid portion of the domain the V_x and V_y terms automatically drop out as they are zero, and for the liquid portion of the domain their effects are taken into account through enhanced conductivity of the liquid or through boundary conditions (to be discussed later) and thus can be neglected. The superheat transport in the liquid due to velocity in the x and y directions is accounted for from a separate model of the fluid through superheat boundary conditions as explained later.^[8] The importance of heat conduction in the casting direction (z dimension) is negligible relative to the heat carried by the strand movement, since the Peclet Number (Pe), $\frac{\rho C_p V_z L}{k}$, is about 500 for the typical values (for example $\rho = 7400 \text{ Kg/m}^3$, $C_p = 670 \text{ J/Kg/K}$, $V_z = 0.0166 \text{ m/min}$ and $L = 0.2 \text{ m}$) used in the model. Hence the term for conduction in the vertical direction (z) can be neglected with respect to convection in that direction. In addition, this work adopts a Lagrangian frame of reference fixed on the strand moving at constant velocity (same as casting speed) in the z-direction. Eq. (3.1) then simplifies to:

$$\frac{\partial}{\partial x} (k_x \frac{\partial T}{\partial x}) + \frac{\partial}{\partial y} (k_y \frac{\partial T}{\partial y}) = \rho C_p \frac{\partial T}{\partial t} \quad (3.2)$$

where $t = \frac{Z}{V_z}$.

Applying the standard Galerkin finite element formulation^[9] to the governing two-dimensional transient heat conduction Eq. (3.3) yields the following matrix equations:

$$[K]\{T\} + [C]\{\dot{T}\} = \{Q\} \quad (3.3)$$

where $[K]$ is the conductance matrix, $[C]$ is the capacitance matrix including the effects of solidification, and $\{Q\}$ is the heat flow vector. Terms in these matrices were evaluated exactly using the standard consistent formulation^[10] as detailed in Appendix A.

The latent heat of solidification is incorporated into Eq. (3.4) through an effective specific heat in $[C]$, which is evaluated using the spatial averaging technique suggested by Lemmon^[11].

$$C_{p_{\text{eff}}} = \sqrt{\left(\frac{\partial H}{\partial x}\right)^2 + \left(\frac{\partial H}{\partial y}\right)^2} / \left(\frac{\partial T}{\partial x}\right)^2 + \left(\frac{\partial T}{\partial y}\right)^2 \quad (3.4)$$

Here, $H(T)$ is the temperature-dependent enthalpy function for the steel alloy which includes the latent heat of solidification and is defined in terms of nodal values and element shape functions in the same manner as temperature.

This model employs the Dupont ^[12] three level time-stepping technique, which utilizes results of two previous time steps to approximate the temperature $\{T\}$ and the time derivative of temperature $\{\dot{T}\}$ as,

$$\{\dot{T}\} = \left\{ \frac{T^{t+\Delta t} - T^t}{\Delta t} \right\} \quad (3.5a)$$

$$\{T\} = \frac{1}{4} \{3T^{t+\Delta t} + T^{t-\Delta t}\} \quad (3.5b)$$

where $\{T^{t+\Delta t}\}$ are the unknown temperatures, for which the current equations are being solved, $\{T^t\}$ are the temperatures at the last time step, and $\{T^{t-\Delta t}\}$ are the temperatures at the time step before $\{T^t\}$.

Eqs. (3.5a) and (3.5b) are substituted into Eq. (3.3) and rearranged to obtain the finite element form of Eq. (3.2) as

$$\left[\frac{3}{4} [K] + \frac{[C]}{\Delta t} \right] \{T^{t+\Delta t}\} = \{Q\} - \frac{1}{4} [K] \{T^{t-\Delta t}\} + \frac{[C]}{\Delta t} \{T^t\} \quad (3.6)$$

The material properties such as $[K]$ and $[C]$ are evaluated based on the temperature at time t . Eq. (3.6) is solved at each time step for the unknown temperatures $\{T^{t+\Delta t}\}$ using the standard Choleski decomposition solution routine.^[13]

The finite element domain where Eq. (3.7) is solved in this study is shown in Figure 3.1, along with the mesh of 3-node, constant temperature-gradient triangular elements that was employed. Since the superheat effects are incorporated through a boundary condition, it is not required to include the entire liquid region of the domain (as shown in Figure 3.1), thereby saving computational cost.

3.2.1 HEAT FLOW BOUNDARY CONDITIONS

This model considers the shell to grow under the action of two distinct heat fluxes. Superheated liquid delivers heat to the inside surface of the shell while heat is extracted through the water cooled mold from the outside of the shell as shown in Figure 3.2. Notice the locations of the peaks of these heat fluxes which causes the shell to grow non-uniformly. These phenomena are

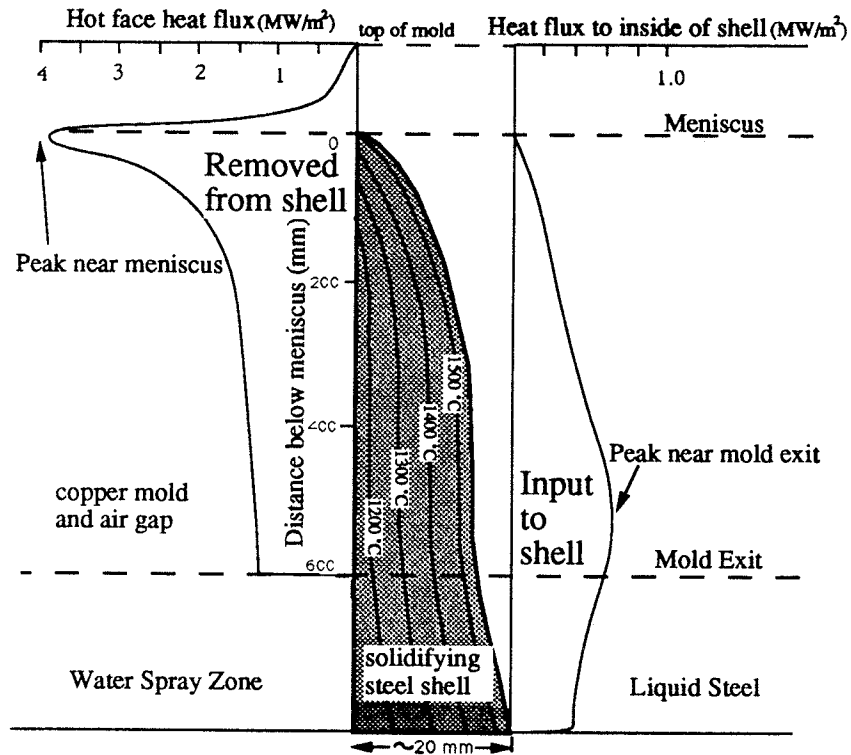


Figure 3.2 Heat Transfer through the solidifying shell

incorporated using separate boundary conditions and are described below. The boundaries on the heat transfer model domain, as shown in Figure 3.3 are all insulated except for the surface facing the mold, where heat is extracted from the shell through the interfacial flux layer, air gap and the mold. In addition, internal boundaries were created to incorporate heat input to the inside of the shell from the turbulent convective heat transfer from the superheated liquid steel flowing from the

nozzle. These two heat transfer boundary conditions for the slab section are shown schematically in Figure 3.3 and are next discussed in greater depth.

3.2.1.1 INTERFACE HEAT TRANSFER MODEL

In the mold region of a continuous caster, heat extraction from the shell surface is primarily controlled by heat conduction across the interface between the mold and the solidifying steel shell. Heat transfer across the interface is controlled by the thickness and thermal properties

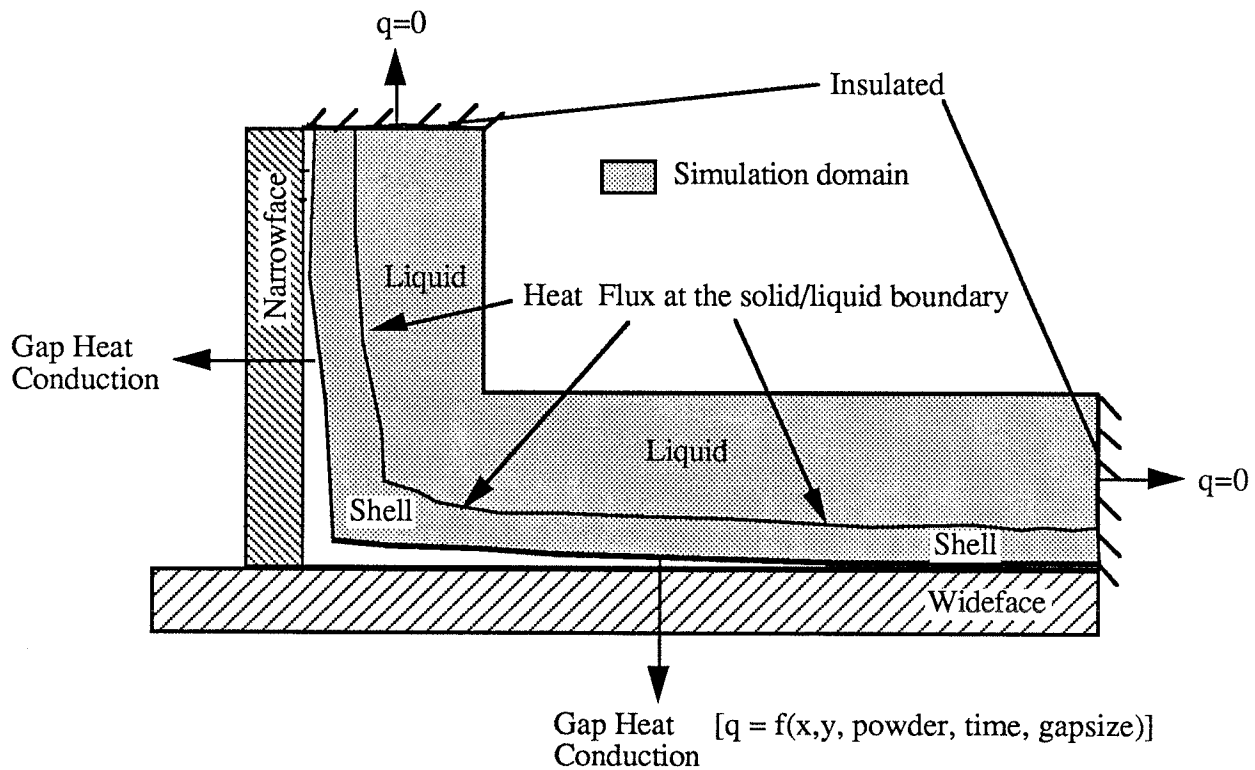


Figure 3.3 Schematic of heat transfer boundary condition.

of the materials filling the gap. Researchers such as Riboud^[14], Branion^[15], Yoshida et. al.^[16] and others^[17-19] have attempted to quantify this heat transfer. They have found that over most of the wideface, the interface consists of thin layers of solid and liquid mold powder of varying thickness and that heat transfer is affected by powder viscosity, feeding rate at the meniscus (consumption), casting speed, uniformity of the shell (which depends on grade) and the thermal

conduction properties of the powder layers. In presence of an air gap (as in the corners) the mode of heat transfer is dominated by radiation. In addition to the mold flux properties, the size of the gap is influenced by factors such as steel shrinkage, taper and thermal distortion of the mold, which are all included in the present model calculations.

Heat transfer across the gap between the shell and the mold is represented by a convection boundary condition as:

$$q'' = h_{eff} (T_s - T_m) \quad (3.7)$$

where T_s is the shell temperature calculated at the previous time step (t) and T_m is the mold wall temperature, calculated by a separate model.^[20] The overall heat transfer coefficient, h_{eff} depends on the size and composition of the interfacial gap and is calculated by the resistor model as:

$$h_{eff} = \left(\frac{1}{\frac{1}{h_0} + \frac{d_f}{k_f} + \frac{d_a}{k_a} + \frac{1}{h_c}} + h_{rad} \right) \quad (3.8)$$

The terms of the Eq. (3.8) are defined in Table 3.1 along with standard values used in the model. The values of the contact resistances were obtained by trial and error, through comparison of thermocouple measurements at an operating caster and the prediction of the 1-D model^[20] as discussed later in this section. This model includes a series of four resistances to heat conduction across the gap in parallel with radiation, as illustrated in Figure 3.4 and described in the following paragraph.

Contact resistances between the mold and solid flux film and those between the flux and the shell are given by the first and last terms, respectively of the denominator. The resistance for conduction through the solid and liquid flux film layers, (which is based on average thermal conductivity of the mold flux and a thickness that is assumed to increase from a minimum at the meniscus to a maximum (see Table 3.1) depending on the flux viscosity, flux consumption rate and casting speed) is represented by the second term in the denominator. Air gaps are assumed to form when the calculated displacements of the shell surface from the mechanical model exceed the

combined thickness of the solid and liquid flux films. The resistance for conduction through the air (or gas vapor) gap, d_a , is represented by the third term in the denominator. Finally, the resistance due to radiative heat flow through the transparent portion of the powder is linearized with the temperature difference between the two radiating surfaces

$$h_{\text{rad}} = \sigma_{\text{SB}} \epsilon (T_s + T_m) (T_s^2 + T_m^2) \quad (3.9)$$

where σ_{SB} is the Stefan-Boltzman constant and ϵ is the effective emissivity for radiation between the two parallel flat plates given by^[21, 22]

$$\epsilon = \frac{\mu^2}{\frac{1}{\epsilon_m} + \frac{1}{\epsilon_s} - 1 + \frac{3}{4} a d_f} \quad (3.10)$$

Note that absorption, a , in this equation gives rise to the heat transfer mode referred to as radiation conduction.^[23]

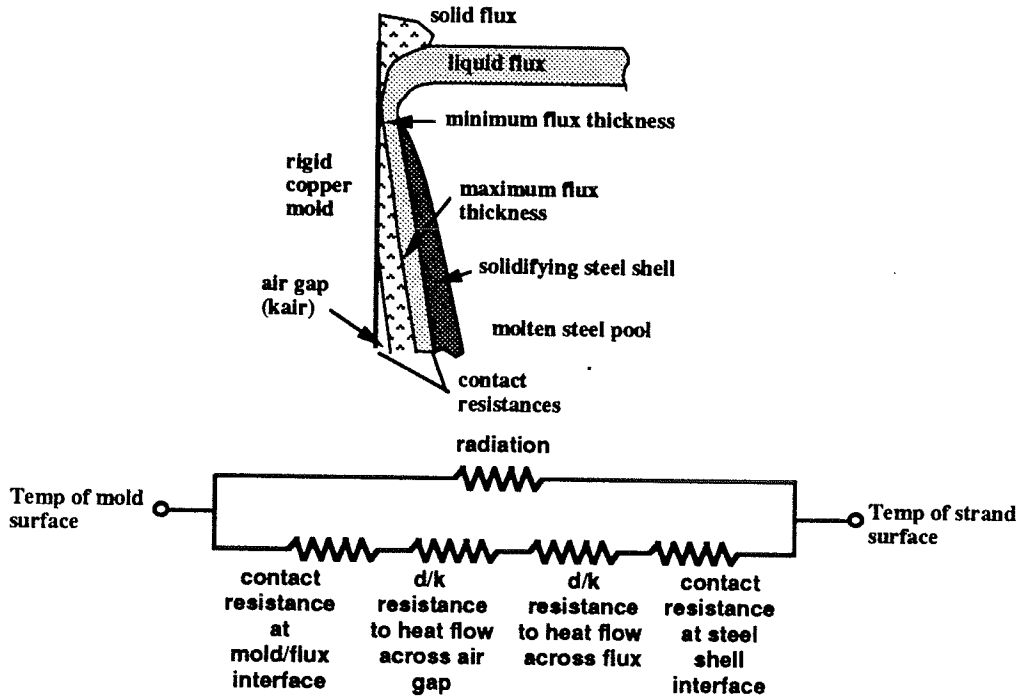


Figure 3.4 Resistor model for interfacial heat transfer

TABLE 3.1 Constants for the Gap heat transfer model

| | | | |
|--|---------------|--------------------|--|
| Convection Coefficient at mold surface | h_0 | $\frac{W}{m^2K}$ | 3000 |
| Conductivity of molten and solid flux | k_f | $\frac{W}{mK}$ | 0.70 |
| Conductivity of air | k_a | $\frac{W}{mK}$ | 0.06 |
| Contact convection coefficient at T_{crys} | h_c | $\frac{W}{m^2K}$ | 1000 |
| Contact convection coefficient at T_{soft} | h_c | $\frac{W}{m^2K}$ | 2000 |
| Contact convection coefficient at T_{sol} | h_c | $\frac{W}{m^2K}$ | 6000 |
| Contact convection coefficient at T_{liq} | h_c | $\frac{W}{m^2K}$ | 20000 |
| Emissivity for mold (Copper) | e_m | | 0.5 |
| Emissivity for shell (Steel) | e_s | | 0.8 |
| Refractive index | μ | | 1.5 |
| Absorption coefficient | a | m^{-1} | 250 |
| Powder Solidus Temperature | | $^{\circ}C$ | 1050 |
| Powder Conductivity | k_f | $\frac{W}{mK}$ | 0.8 |
| Air Conductivity | k_a | $\frac{W}{mK}$ | 0.06 |
| Stefan Boltzman constant | σ_{SB} | $\frac{W}{m^2K^4}$ | 5.67×10^{-8} |
| Total thickness of the interfacial gap | d_{gap} | m | Implicit Calculations |
| Total powder layer thickness | d_f | m | 0.4 mm at meniscus 0.7 mm at mold exit |
| Thickness of the air gap | d_a | m | $d_{gap} - d_f$ for $d_{gap} > d_f$ 0.0 for $d_{gap} < d_f$ |

A separate model, CON1D^[24], has been developed to predict the formation of the mold powder layers in the interfacial gap based on the measured powder consumption and performing heat, mass and momentum balances on the flux layers. CON1D calculates the solid and liquid flux layer thicknesses at the center of the wide face, where ferrostatic pressure holds the shell against

the mold and the air gap is a minimum. Since ferrostatic pressure prevents shrinkage of the shell away from the mold over most of the wide face, heat transfer is dominated by the powder properties over most of the mold. Small air gaps may still be present, however, in the form of a contact resistance, due to the roughness of the copper plate surface, non-uniformities in the shell surface, and incomplete wetting of the mold flux.

Experimental data is crucial in developing a reasonable model of the interface. The CON1D model was calibrated by comparing mold thermocouple measurements with that of model predictions. The heat transfer conditions at the mold/shell interface required to produce a previously measured set of mold temperatures are found using CON1D. Model parameters in the present work are chosen so that model predictions match thermocouple measurements in the mold wide face, for the same casting conditions.^[24] Figure 3.5 compares the temperatures measured on an instrumented mold at LTV Steel with the temperature distribution down the mold predicted by the CON1D model. This profile is controlled by the calculated variations of the mold-powder solid and liquid layers, conduction through the shell and mold, properties of the powder and steel, mold geometry and input conditions. The predicted solid and liquid powder thickness of CON1D along with the model parameters were used in CONCAST, to represent the interfacial heat conduction. The values used for the model parameters in the calibration of the model as well as the present simulation are shown in Table 3.1. It is hoped that the extrapolation of the interface model which is valid at the center of the wideface, to regions of the mold (near the corner) where a larger air gap exists is reasonable.

In the off-corner regions of the wide face and along the narrow face, shell shrinkage, mold taper, and mold distortion can significantly affect heat transfer by changing the local gap thickness. Thus, the model calculates the thickness of the gap at each location and time, knowing the position of the strand surface (from the stress model), and the position of the mold wall (from the mold taper and distortion) at that location and time. The model then calculates heat flow at every location and time step using the same interface model, assuming that the powder layer

thickness remains same all along the slab surface and that air fills the remaining gap. The total size of the gap, d_{gap} , is the sum of the powder layer thickness, d_f , and the air gap, d_a :

$$d_{\text{gap}} = d_f + d_a \quad (3.11)$$

The size of the gap d_{gap} is calculated from the stress model from the nodal displacements and the position of the distorted mold as

$$d_{\text{gap}} = u(x,y,t) - d_{\text{wall}}(x,y,t) \quad (3.12)$$

Equations 3.11 and 3.12 couples the heat transfer and the stress model at each time step and the procedure is discussed in the simulation procedure section in chapter 5.

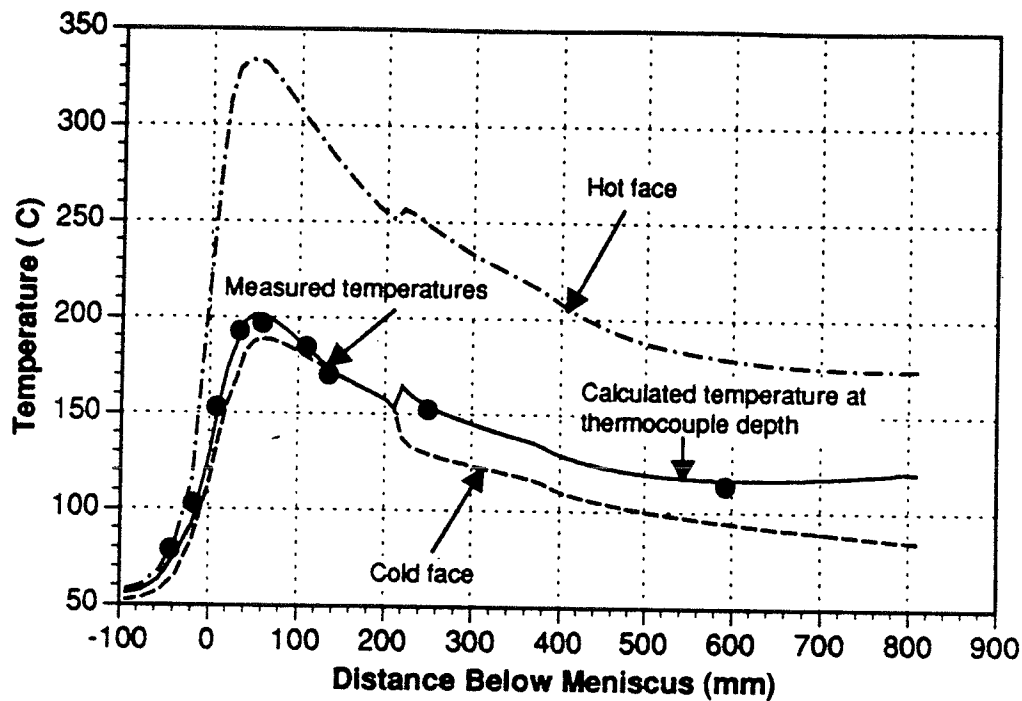


Figure 3.5 Comparison of model prediction with plant measurements^[25].

3.2.1.2 SUPERHEAT FLUX

Liquid steel is poured into the mold at a temperature above the liquidus. The sensible heat contained in the liquid steel represented by this temperature difference is known as superheat.

Superheat is proportional to the difference between the pour temperature and the liquidus temperature and must be dissipated before the steel can solidify. Since more than half of this heat is removed in the mold and its distribution is uneven, superheat dissipation represents a significant fraction of the total heat removed by the mold in some places [8, 26, 27]. The relative importance of the dissipation of this superheat to the growth of the shell is not clear. It is thus necessary to account for this uneven dissipation of superheat in the mathematical model.

Traditionally, the convection of superheat is accounted for in a thermal stress model by simply enhancing the liquid conductivity by a factor of 7-10 [28, 29]. This “enhanced conductivity method” requires enmeshment of the entire liquid pool (i.e. the finite element mesh should contain the entire liquid region), so is inefficient. Furthermore, this isotropic enhancement does not reproduce the phenomena related to non-uniform distribution of superheat.

To overcome these deficiencies, a new method is used in the model^[30], which characterizes the superheat from the flowing liquid to the solidifying shell as an internal boundary condition which applies a heat flux source at the solid/liquid interface, using data sets at several positions across the solid/liquid shell boundary. The heat flux data was generated with a three-dimensional, finite volume model of turbulent fluid flow and heat transfer by Huang and Thomas^[8]. This sophisticated 3D fluid flow and heat transfer model calculates velocities and temperature of liquid steel inside the solidifying shell by solving 3D steady state Navier Stokes equations with the standard K- ϵ turbulence model and an empirical wall law. The model domain is up to but not including the mushy zone and the boundaries which correspond to dendrite tips are treated as very rough solid walls. A fixed temperature, T_{liq} , is imposed along these boundaries. The heat flux exiting the entire boundary of this domain generated the 'Superheat flux' data sets (as a function of position both across and down the mold faces) used in this work.

Figure 3.5 presents typical 3-D model results for velocity, temperature and heat flux. ^[8] The flow of superheated liquid steel leaves the nozzle as a strong hot jet and impinges on the narrowface carrying heat across the mold. These results show that the heat flux which represents the rate of superheat dissipation to the inside of the shell, reaches a maximum at the impingement

point on the narrowface wall. It is important to note that the narrowface receives the most superheat, exceeding that of wideface by several times. This non-uniform dissipation of superheat is partly responsible for unequal shell thickness around the shell perimeter. Casting speed and superheat temperature both directly increase the superheat extraction rate at the narrowface and off-corner wideface.

As shown in Figure 3.6 for 3 example elements, the superheat heat flux is applied to all elements in the domain which contain exactly two solid nodes and one liquid node. A coherency temperature T_c , is defined to distinguish between solid and liquid nodes as

$$T_c = \theta T_{sol} + (1-\theta) T_{liq} \quad (3.13)$$

where the solid fraction, θ is taken as 0.8. The heat flux to apply to these two solid nodes is extracted via 3-D linear interpolation of the database values both down and across the mold face.

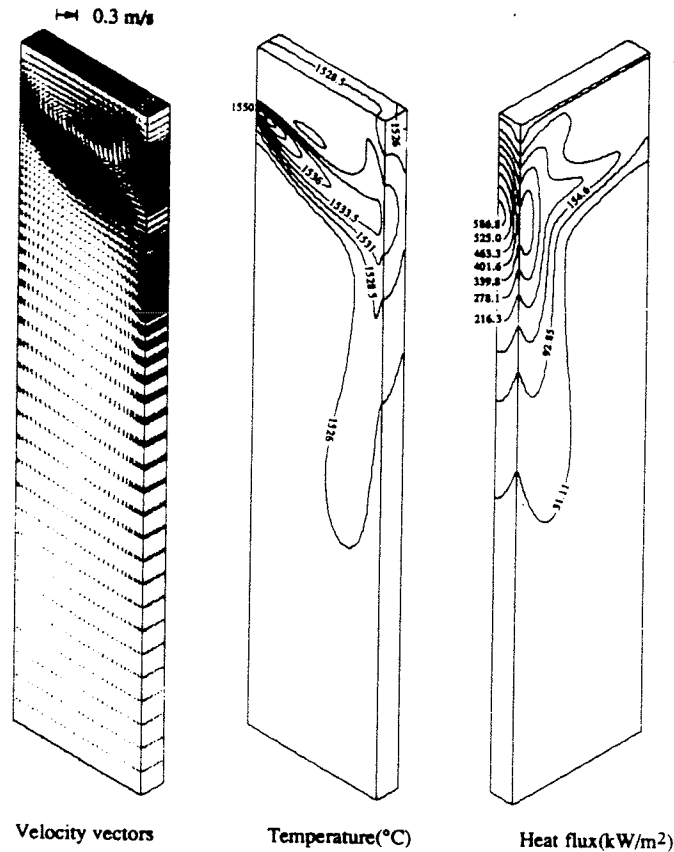


Figure 3.6 Velocity, temperature and heat flux in the strand. [8]

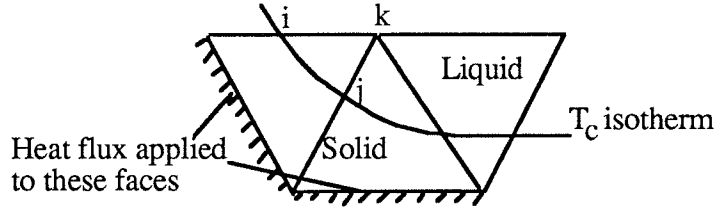


Figure 3.7 Schematic showing application of internal heat source at appropriate faces.

Heat is calculated from this heat flux value according to the time step size, the casting speed, and the distance joining these two solid nodes, which define the solidification front and added to the thermal load vector as an internal heat source term as per Eq. 3.14

$$\{Q\} = \int N^T q''_{sh} dA = \frac{L_{ij} q''_{sh}}{2} \quad (3.14)$$

where L_{ij} is the length of the internal boundary over which the superheat flux is applied as shown in Figure 3.6.

This "superheat flux" approach reasonably incorporates the effect of convection due to turbulent fluid flow on superheat removal. The heat flux distribution can be calculated as a function of process variables such as, casting speed, superheat temperature difference, submergence depth, nozzle angle, steel grade etc. A database is being developed to extend versions of the model over a range of operating conditions.

3.2.1.3 SPRAY ZONE BOUNDARY CONDITION

Below the mold, the heat flux to the steel slab surface, q'' in Eq. 3.7, is replaced by water spray zone boundary condition:

$$q'' = (h_{\text{spray}} + h_{\text{rad}} + h_{\text{nconv}}) (T_s - T_w) \quad (3.15)$$

The heat transfer coefficient for the spray is taken from Nozaki^[31] as a function of the water spray flux, \dot{w} , and water temperature T_w ,

$$h_{\text{spray}} = 392.5 (\dot{w})^{0.55} (1 - 0.0075T_w) \quad (3.16)$$

The linearized heat transfer coefficient due to radiation given by Eq. 3.17

$$h_{\text{rad}} = \sigma_{\text{SB}} \epsilon (T_s + T_\infty) (T_s^2 + T_\infty^2) \quad (3.17)$$

where T_∞ is the ambient temperature taken as 35 °C. The heat transfer condition for natural convection is taken as 8.7 W/m²K from Haegle^[32]. This heat transfer condition was applied over all of the wideface. Over the narrowface where the cooling is not as strong as the wideface, only natural convection and radiation were applied.

3.3 MECHANICAL MODEL FORMULATION

Stresses arising during solidification are highly dependent on the temperature differences in the shell, the loading history and time-dependent creep. Therefore, the mechanical model tracks displacements, strains, stresses, and forces as they evolve incrementally through time. For the 2-D analysis, as in the present case assumptions are needed to represent the stress state in the out-of-plane direction. Many previous 2-D models of continuous casting have assumed plane stress^[3, 30, 33-35] or plane strain^[36, 37] except the models of Kristiansson^[1, 2, 38] who assumed generalized plane strain for the billet section. However, both plane stress and plane strain are inappropriate, because non uniform thermal strains in the out-of-plane are usually very significant. Neither of these assumptions accurately describe the stress state of the 2-D slice. When modeling a 2D slice through a typical casting, the best approximation is usually generalized plane strain, which allows both translation and rotation of the 2D plane section. For, the slab section in consideration the rotations of the plane can be easily be neglected because of the rigid construction of the mold and the applied constraints as well as the symmetry assumption.

The basic governing differential equations for the 2D generalized plane strain model are the mechanical equilibrium equations:

$$\frac{\partial \Delta \sigma_x}{\partial x} + \frac{\partial \Delta \tau_{xy}}{\partial y} = \Delta F_x \quad (3.18a)$$

$$\frac{\partial \Delta \tau_{xy}}{\partial x} + \frac{\partial \Delta \sigma_y}{\partial y} = \Delta F_y \quad (3.18b)$$

$$\int \Delta \sigma_z dA = \Delta F_z \quad (3.18c)$$

$$\int x \Delta \sigma_z dA = \Delta M_x \quad (3.18d)$$

$$\int y \Delta \sigma_z dA = \Delta M_y \quad (3.18e)$$

which relate the incremental stresses to external force increments, and the compatibility equations which relate increments of total strain to displacement increments :

$$\Delta \epsilon_x = \frac{\partial \Delta u_x}{\partial x} \quad (3.19)$$

$$\Delta \epsilon_y = \frac{\partial \Delta u_y}{\partial y} \quad (3.20)$$

$$\Delta \epsilon_{xy} = \frac{1}{2} \left(\frac{\partial \Delta u_y}{\partial x} + \frac{\partial \Delta u_x}{\partial y} \right) \quad (3.21)$$

$$\Delta \epsilon_z = a + bx + cy \quad (3.22)$$

For the present simulation of continuous casting, the two-fold symmetry assumptions makes the terms $b=c=0$ which prevents any rotation of the plane and makes the Eqs. 3.18d and 3.18e vanish. This produces a constant value for the z strain increment, $\Delta \epsilon_z$ over the entire domain, to be solved during each time step. The small strain assumption invoked in these equations is quite reasonable for stress analysis of the continuous casting processes. The stresses and strains are related through the Hooke's Law:

$$\{\Delta \sigma\} = [D'] \{\Delta \epsilon_e\} + [\Delta D'] \{\epsilon_e\} \quad (3.23)$$

where $[D']$ contains the elastic constants, which depend only upon the material properties of elastic modulus, $E(T)$ and Poisson's ratio, ν , for an isotropic material:

$$[D'] = \frac{E(T)}{(1+\nu)(1-2\nu)} \begin{bmatrix} 1-\nu & \nu & 0 & \nu \\ \nu & 1-\nu & 0 & \nu \\ 0 & 0 & \frac{(1-2\nu)}{2} & 0 \\ \nu & \nu & 0 & 1-\nu \end{bmatrix} \quad (3.24)$$

and $[\Delta D']$ is based on the change in $E(T)$ due to temperature changes over the time step. The finite element formulation for the 2-D generalized plane strain are given in detail in Appendix C.

One way to find $\Delta \epsilon_z$ is to improve on initial guesses through iteration using Eq. 3.18c^[39] with $\Delta F_z = 0$ as shown in APPENDIX D. Unfortunately, this extra effort can double the execution time, despite the efficient iteration for incremental z-strain, $\Delta \epsilon_z$ possible because the stiffness matrix need not be retriangularized^[40]. In the present work the direct method which solves for $\Delta \epsilon_z$ at once, by adding one extra node to the finite element mesh is used, because it was found to be more efficient than iterating for the z-strain. The extra node upsets the banded nature of the stiffness matrix $[K_\sigma]$, giving the non-zero terms an “arrowhead” shape^[41] (see details in Appendix C). However, utilizing the efficient matrix storing scheme of the variable bandwidth Cholesky Solver it was possible to use the same code with minimal modifications. The Cholesky solver used in the present model stores the banded symmetric stiffness matrix in an one dimensional array and keeps a counter for the number of terms in each row of the stiffness matrix within the bandwidth including the diagonal. Since the number of equations solved in this case is $(ndf+1)$ (APPENDIX C), the counter for the last row will have $(ndf+1)$ terms.

Applying the Galerkin finite element formulation to the mechanical problem defined by the equilibrium equations (Eq. 3.18), along with the strain-displacement (Eq. 3.19 - 3.22) and stress-strain (Eqs. 3.23) relations results in a set of simultaneous equations

$$[K'_\sigma] \{ \delta \} = \{ \Delta F_{ET} \} + \{ \Delta F_{EP} \} + \{ F_{FP} \} - \{ F_{el} \} \quad (3.25)$$

to be solved at each time step. Here the vector $\{\delta\}$ contains the incremental in-plane displacements and the incremental out-of-plane strain. Loads arise from the thermal strains, $\{\Delta F_{\epsilon T}\}$, the inelastic strains, $\{\Delta F_{\epsilon p}\}$, ferrostatic pressure and interaction with the mold, $\{F_{fp}\}$, and a correction term from the elastic strain accumulated up to the previous time step. Terms in this equation are defined in Appendix B. Notice that a mixed formulation is adopted in which the thermal and plastic loads are based on incremental strains whereas the ferrostatic pressure and residual loads are based on total formulation.

Stresses, strains and displacements are calculated within the same domain as the heat transfer model shown in Figure 3.1. The heat transfer model uses the 3-node triangular elements while stress model uses same nodes connected into 6-node triangles as shown in Figure B.1. The incremental total strain vector, $\{\Delta \epsilon\}$, is composed of elastic, thermal and inelastic strain components:

$$\{\Delta \epsilon\} = \{\Delta \epsilon_e\} + \{\Delta \epsilon_T\} + \{\Delta \epsilon_p\} \quad (3.26)$$

where $\{\Delta \epsilon_e\}$ is the elastic strain increment, $\{\Delta \epsilon_T\}$ is the thermal strain increment, (incorporating volume changes from both temperature changes and phase transformations) and $\{\Delta \epsilon_p\}$ is the inelastic strain increment, (incorporating both plastic and creep strain). These terms are explained below.

3.3.1 THERMAL STRAIN

Thermal strains arise from volume changes caused by both temperature differences and phase changes (including both solidification and solid state transformations). This creates a “thermal load”, $\{\Delta F_{\epsilon T}\}$ that is incorporated into the stress model through the incremental thermal strains $\{\Delta \epsilon_T\}$ as given by Eq. B15. $\{\Delta \epsilon_T\}$ is calculated in each element based on the temperatures determined in the heat transfer analysis and the thermal linear expansion of the material, TLE:

$$\{\Delta\epsilon_T\} = (TLE(T_{t+\Delta t}) - TLE(T_t)) \{1,1,0,1\}^T \quad (3.27)$$

By storing the contraction information directly into the state function TLE, incorporates thermal strains due to both phase changes and temperature changes.

3.3.2 INELASTIC STRAIN

In most previous continuous casting models, ^[42, 43] unverified models of structure-independent plasticity or a simple creep constitutive model have been used. In many commercial packages (e.g. ABAQUS ^[44]) the inelastic strains are decomposed into (i) a rate-independent *plastic* part and (ii) a rate-dependent *creep* part. This unnatural separation makes it difficult to accurately predict the combined effect of the two. At higher temperatures, important to stress development during solidification, creep is significant even during a tensile test and cannot be distinguished from plastic strain. The mechanical behavior is very sensitive to strain rate. Thus, “unified” constitutive models have been developed to treat inelastic strain as a single function, whose instantaneous rate of change, $\dot{\epsilon}_p$, depends on the current stress, temperature, structure, and rate of phase transformation,

$$\Delta\epsilon_p = \int_t^{t+\Delta t} \dot{\epsilon}_p(T, \sigma, \text{structure}) dt \quad (3.28)$$

Several different methods are available to treat inelastic strain, $\{\Delta\epsilon_p\}$, numerically over the time step. The inelastic strain rate function can be integrated by explicit and implicit methods. The explicit forward Euler time-integration procedure is often restricted by the time step size for stability^[45]. As such a more stable implicit scheme was developed ^[46] to allow larger time steps for integrating the constitutive equation. These two methods are described next.

3.3.2.1 EXPLICIT METHOD

In this model, the simple, explicit time-integration procedure based on the visco-plastic model of Zienkiewicz and Corneau^[47] is used to integrate Eq (3.25) over the time step for the incremental inelastic strain is characterized by

$$\Delta \epsilon_p = \Delta t \dot{\epsilon}_p(\sigma, T, \epsilon_p, t) \quad (3.29)$$

where $\dot{\epsilon}_p$ is the scalar function given in Eq.(3.28) dependent on the current temperature, T , the total plastic strain accumulated to that time, ϵ_p , and the current effective stress, σ . The Von Mises effective stress for an isotropic constitutive model is found from the spatial components of stress, σ as:

$$\sigma = \frac{1}{\sqrt{2}} \sqrt{(\sigma_x - \sigma_y)^2 + (\sigma_y - \sigma_z)^2 + (\sigma_z - \sigma_x)^2 + 6(\tau_{xy}^2)} \quad (3.30)$$

Next, the constitutive model, $\dot{\epsilon}_p$ in Eq. 3.29, is integrated using an appropriate numerical algorithm to find a scalar value of the incremental inelastic strain, $\Delta \epsilon_p$, which is then decomposed into spatial components, $\{\Delta \epsilon_p\}$, using a flow rule. Usually, inelastic strain is assumed to be incompressible and proportional to the deviatoric stresses, which leads to the Prandtl-Reuss equations (Eq. B.20) or “associated flow rule”^[48].

3.3.2.2 IMPLICIT METHOD

As mentioned before, the time step size restriction of the explicit integration schemes led to the development^[46] of the two-level implicit scheme similar to the one proposed by Lush et al. ^[49] for internal variable constitutive equations. In the implicit algorithm the evolution of elastic strain, and hence stress, is written in the rate form,

$$\{\dot{\epsilon}_e\} = \{\dot{\epsilon}\} - \{\dot{\epsilon}_T\} - \{\dot{\epsilon}_p\} \quad (3.31)$$

where the plastic strain rate vector $\{\dot{\epsilon}_p\}$ is expressed by the Prandtl-Reuss equation (Eq. A30)

$$\{\dot{\epsilon}_p\} = \frac{3}{2} \dot{\bar{\epsilon}}_p \frac{\{\sigma'\}}{\bar{\sigma}} \quad (3.32)$$

where $\dot{\bar{\epsilon}}_p$ is the unified constitutive law given by Eq. 3.29, $\{\sigma'\}$ are the deviatoric stresses, and $\bar{\sigma}$ is the effective stress.

It is assumed that the stress state (σ^n, ϵ^n) at time t^n is known and the purpose is to find the stress state $(\sigma^{n+1}, \epsilon^{n+1})$ at time t^{n+1} . The integration of the evolution equation Eq. 3.31 was adopted from the viscoplastic algorithm proposed by Glowinski and Talle^[50], which is based on the ADI scheme of Douglas and Rachford^[51]. The integration is carried out in two steps. Step a) involves finding an intermediate value for the incremental plastic strain increment by implicitly solving the necessary equations locally at the Gauss points, and in step b) the intermediate strains are used to solve the global finite element equations.

Step a)

$$\{\hat{\sigma}\}^{n+1} = \{\sigma\}^n + [D] \left(\{\dot{\epsilon}\}^n - \{\dot{\epsilon}_T\}^{n+1} - \{\hat{\epsilon}_p\}^{n+1} \right) \Delta t \quad (3.33)$$

Step b):

$$\{\sigma\}^{n+1} = \{\sigma\}^n + [D] \left(\{\dot{\epsilon}\}^{n+1} - \{\dot{\epsilon}_T\}^{n+1} - \{\hat{\epsilon}_p\}^{n+1} \right) \Delta t \quad (3.34)$$

Here the terms with \wedge represents intermediate values. For isotropic materials, using the deviatoric part of Eq. 3.33, the two tensor equations above (with 14 unknowns) can be reduced to two-unknown scalar equations, which are:

$$\hat{\bar{\epsilon}}_p^{n+1} = \bar{\epsilon}_p^n + f(\hat{\bar{\sigma}}^{n+1}, \hat{\bar{\epsilon}}_p^{n+1}) \Delta t \quad (3.35)$$

$$\text{and} \quad \hat{\bar{\sigma}}^{n+1} = \sigma^{*n+1} - \frac{3E(T)}{2(1+\nu)} f(\hat{\bar{\sigma}}^{n+1}, \hat{\bar{\epsilon}}_p^{n+1}) \Delta t \quad (3.36)$$

$$\text{where:} \quad \{\sigma^*\}^{n+1} = \{\sigma\}^n + [D] \left(\{\dot{\epsilon}\}^n - \{\dot{\epsilon}_T\}^{n+1} \right) \Delta t \quad (3.37)$$

Here f represents the unified constitutive law given by the $\dot{\bar{\epsilon}}_p$ function in Eq. 3.29. Finally, the non-linear equations Eq. 3.35 and 3.36 are solved iteratively for $\hat{\bar{\epsilon}}_p^{n+1}$ and $\hat{\bar{\sigma}}^{n+1}$ using the two-level iteration scheme proposed by Lush^[49]. After solving these equations the incremental plastic strains $\Delta \hat{\bar{\epsilon}}_p^{n+1}$ are updated as:

$$\{\Delta \hat{\epsilon}_p\}^{n+1} = \frac{3}{2} \frac{\hat{\epsilon}_p^{n+1}}{\hat{\sigma}^{n+1}} \{\hat{\sigma}'\}^{n+1} \quad (3.38)$$

The term $\{\hat{\sigma}'\}^{n+1}$ is written as:

$$\{\hat{\sigma}'\}^{n+1} = \frac{\hat{\sigma}^{n+1}}{\bar{\sigma}^{*n+1}} \{\sigma^{*'}\}^{n+1} \quad (3.39)$$

where $\{\sigma^{*'}\}^{n+1}$ is the deviatoric part of $\{\sigma^*\}^{n+1}$ and $\bar{\sigma}^{*n+1}$ is the Von Mises effective stress. The incremental plastic strain components of Eq. 3.38 are used to generate the plastic load vector as per the Eq. B.16. Thus in the above scheme the equations 3.35 and 3.36 are implicitly solved locally at each Gauss point and then the global finite element equations are solved explicitly using the intermediate effective plastic strain $\Delta \hat{\epsilon}_p$. Using this scheme a considerable saving in computational time for integrating the constitutive equation is achieved compared to other implicit schemes proposed by researchers such as Argyris et al.^[52], Snyder and Bathe^[53], Fjaer and Mo^[54], Tanaka and Miller^[55], in which the global system of equations are solved iteratively several times during each time step.

For step b, using the finite element procedure based on "initial strain method", the equilibrium equation $B^T \sigma = 0$, along with the Eq. 3.34 produces the following global finite element system of equations :

$$\left(\int B^T D B \, dV \right) \{\Delta u\}^{n+1} = - \int B^T \{\sigma\}^n \, dV + \int B^T [D] \left(\{\dot{\epsilon}_T\}^{n+1} + \{\hat{\epsilon}_p\}^{n+1} \right) \Delta t \, dV \quad (3.40)$$

After solving the global linear equation, the stress is updated as

$$\{\sigma\}^{n+1} = \{\sigma\}^n + [D] \left(\{\dot{\epsilon}\}^{n+1} - \{\dot{\epsilon}_T\}^{n+1} - \{\hat{\epsilon}_p\}^{n+1} \right) \Delta t \quad (3.41)$$

3.3.3 MECHANICAL BOUNDARY CONDITIONS

The equations described above are subject to the boundary conditions illustrated schematically in Figure 3.7 for a slab. The dimensions of the slab used in the simulation is given

Chapter 5. The two-fold symmetry assumed in the geometry is imposed by fixing normal displacements on the symmetry planes :

$$\begin{aligned} t > 0 \quad x = W \quad 0 < y < d, \quad u_x = 0 \\ t > 0 \quad y = N \quad 0 < x < d, \quad u_y = 0 \end{aligned} \quad (3.42)$$

These conditions also prevent rigid body motion of the slab.

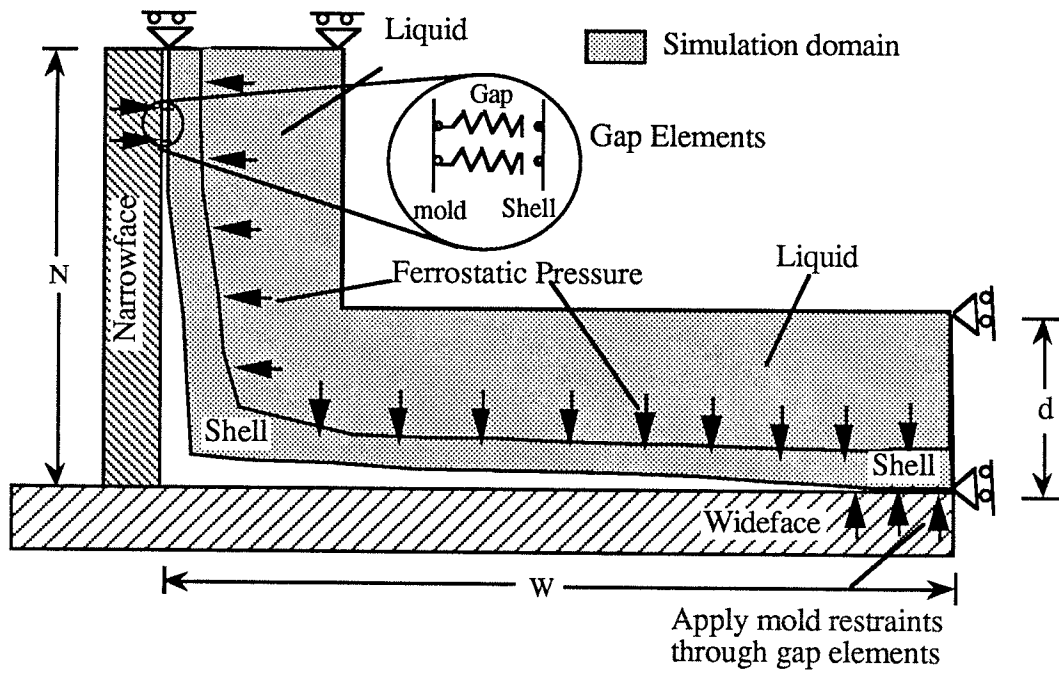


Figure 3.8 Mechanical boundary conditions.

3.3.3.1 FERROSTATIC PRESSURE

Ferrosstatic pressure from the liquid generates forces which, though small cannot be ignored in slab casting. They constitute an important source of bulging enhanced by creep both in and below the mold. This pressure, F_p , acts on the inside surface of the solidifying shell and increases due to gravity, g , in proportion to distance, Z , below the liquid surface:

$$\begin{array}{ll}
\text{For straight mold} & : \quad F_P = \rho g Z \\
\text{For curved mold} & : \quad F_P = \rho g \sin (Z/R)
\end{array} \tag{3.43}$$

where Z is calculated as

$$Z = V_c \cdot t \tag{3.44}$$

This pressure is applied mathematically as an internal boundary condition to appropriate nodes (see Figure 3.6) at the solid/liquid interface^[30]. Ferrostatic pressure is applied as an internal load in the same manner as the superheat flux boundary condition described earlier. This interface is defined by the 80% solid isotherm in the domain. The isotherm that defines "coherency", is defined through Eq. (3.13) with θ taken as 0.8.

3.3.3.2 SHELL/MOLD CONTACT

Further boundary conditions are applied when the shell contacts the mold to ensure that no portion of the shell surface penetrates into the mold, as described in a later section. One of the most difficult tasks is to properly account for the restraining effect of the mold on the thin shell which is bulging due to creep deformation driven by the ferrostatic pressure. The interaction between the shell and the mold not only affects the loading on the exterior position of the shell, but also influences the heat transfer significantly. Ohnaka^[56] employed a technique accounting for contact loading, which estimates the load required to avoid penetration of mold by the shell and applies the load on the shell at the first iteration. The procedure iterates until the penetration is negligible. A more stable method for contact loading, used in commercial packages such as ABAQUS^[57], is to fix the displacements of penetrating shell surface nodes to the mold wall one at a time. This method would be prohibitively expensive for the present problem, however, since many iterations of the mechanical model would be required within each time step.

In the present model, penetration of mold wall by nodes on the slab surface is prevented by creating "spring elements" at each surface node along the narrow face and wide face where the shell tends to penetrate the mold. This is done by first finding the position of the mold

wall, d_{wall} , at the next time step, $t+\Delta t$, based on the known mold taper, d_{tap} , and the mold distortion, d_m , which is known from prior calculations using a separate model^[58] discussed in Chapter 4 and stored in a data base:

$$d_{\text{wall}}^{t+\Delta t} = d_{\text{tap}}(x,y,t+\Delta t) + d_m(x,y,t+\Delta t) \quad (3.45)$$

where t is the time since the slice was at meniscus and is usually equal to $\frac{Z}{V_c}$. The mold distortion is not sensitive to local variations in gap and can be approximated reasonably from a priori knowledge of the heat flux for the given casting conditions. The size of the gap, d_{gap} , is then calculated for each shell surface node, based on the best available estimate of the surface node displacements perpendicular to the mold wall (i.e. u_x for the narrow face and u_y for the wide face) at current iteration i .

$$d_{\text{gap}} = u^i(x,y,t) - d_{\text{wall}}(x,y,t) \quad (3.46)$$

The size of this gap, d_{gap} , is also very important to the heat transfer calculations. Nodes with a negative gap exceeding the allowable limit of δ are considered to have penetrated the mold. Normal displacements of those nodes are fixed to a new position, u_{fix} that corresponds to the position that the wall will have moved to by the next time step:

$$u_{\text{fix}} = d_{\text{wall}}^t - u^t + 2 * |d_{\text{wall}}^{t+\Delta t} - d_{\text{wall}}^t| \quad \text{for } d_{\text{gap}} < 0 \text{ and } |d_{\text{gap}}| > \delta \quad (3.47)$$

Fixing each nodal displacement is accomplished approximately by adding a "spring element" to pull that node towards its intended destination. This involves multiplying the appropriate diagonal entry in the stiffness matrix by a large stiffness multiplier λ , and setting the corresponding force vector term to the new stiffness multiplied by u_{fix} given by Eq. 3.47.

$$[K_{\sigma}]_{\text{diag}} = \lambda * [K_{\sigma}]_{\text{diag}} \quad (3.48)$$

$$\{F\} = \lambda * [K_{\sigma}]_{\text{diag}} * u_{\text{fix}} \quad (3.49)$$

Spring elements are used so that checks of tension or compression of the spring can easily be made to indicate whether the node is trying to shrink or not.

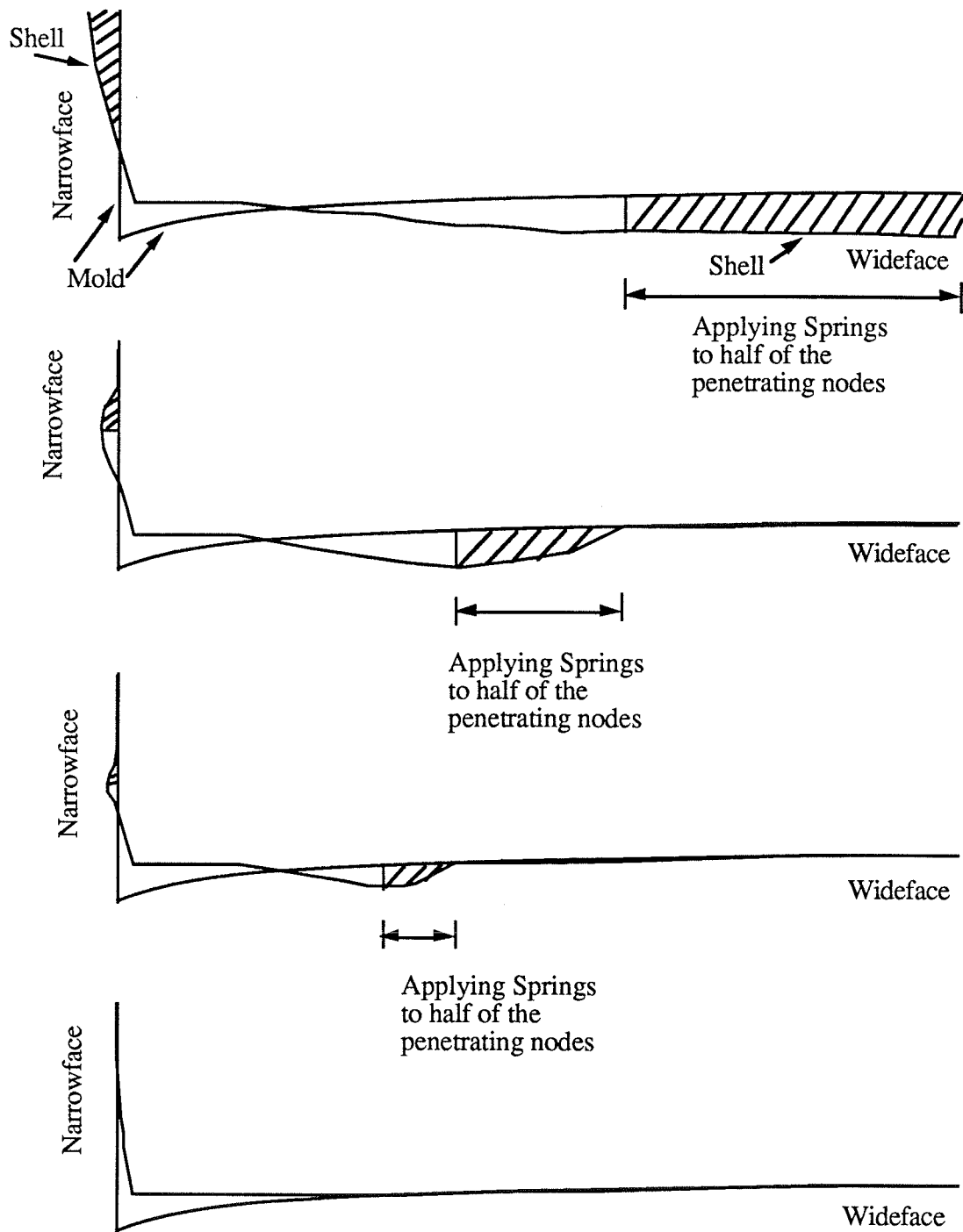


Figure 3.9 Schematic illustration of the mold penetration algorithm.

This procedure of pushing the node farther away from the mold than necessary prevents the phenomenon of nodes improperly "sticking" to the mold wall when the taper exceeds the natural shrinkage during that time step. The inaccuracy is small and occurs only at the time step when shell / mold contact is lost at a given node. Since the model takes advantage of the knowledge that ferrostatic pressure applied at the inner surface of the solidifying shell induces a maximum mold penetration at the center of the wideface or narrowface and that the rest of the shell behaves in a continuous manner, the convergence of this algorithm is greatly improved. Based on the relative position of the maximum bulge, only 50% of the penetrating nodes are selected for applying spring forces as illustrated in Figure 3.8. The coupling procedure for the gap heat transfer is discussed in the simulation procedure section in Chapter 5.

3.3.3.3 CONSTRAINT FOR BULGING BELOW MOLD

Below mold the shell is only supported by rollers as shown in Figure 3.9 and practically unconstrained to bulge under ferrostatic pressure and creep deformation. For a 2-D slice model, as in the present case, the ferrostatic pressure force needs to be counter balanced by some bulging moments acting on the plane, or by constraining the slab surface to conform to the bulge shape between rollers as the slice moves down. If one can accurately calculate the bulging moments acting on the plane, it is possible to apply the moments as a force vector using the generalized plane strain formulation described in Appendix B. However, calculation of bulging moments needs involved calculations and verification of the code and the model would need the entire slab section instead of the quarter section used in this analysis.

Therefore, a different approach was adopted in this work, where the shell surface position was constrained by a fictitious mold representing the bulge shape of the slab, at the center of the wideface and the mold contact constraint of section 3.3.1 was applied. The bulge shape of the slab has been predicted by several researchers^[7, 42, 43, 59-62] and compared to experimental

measurements. Recently Wang and Thomas [63] developed a relationship for the maximum bulging as a function of shell thickness, casting speed, shell surface temperature as given by Eq. 3.50.

$$W_{\max} = F \times 5.844 \times 10^{-20} \exp(1.955 \times 10^{-3} T_s) \frac{b^{6.001} \times F_p^{1.936}}{V_c^{0.416} \times s^{4.875}} \quad (3.50)$$

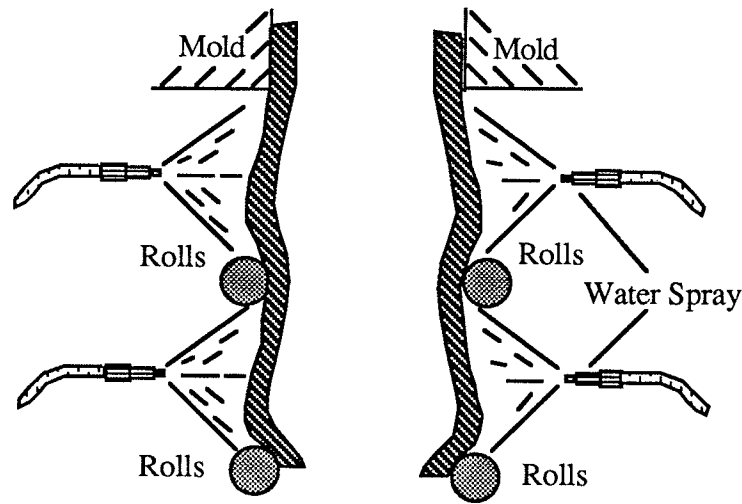


Figure 3.10 Schematic of bulging of the slab below mold.

Symbols are defined in the nomenclature section. The experimental measurements as well as mathematical simulation indicate some negative bulging near rollers. Most of the work on slab bulging consider the slab far below in the strand where the shell is thick (30-50 mm) and the surface temperature is low (800 °C). The data on slab bulging just below the mold is not available. So the empirical relationship of Wang [63] was used to get the maximum bulging of the slab at the center of the wideface. As reported in most literature [7, 42, 43, 59-62] the location of the maximum bulging was taken at a roll pitch of 0.65 as shown in Figure 3.10. Inconsistence with the experimental measurements as well as simulations, the ratio of the maximum bulging to the maximum negative bulging was fixed at 5:1 similar to that reported in the literature [64]. At the location of rollers the shell is forced to touch the rollers. These four points were then fitted to a

cubic relationship to obtain the shape of the fictitious mold used in the model to represent the bulge shape.

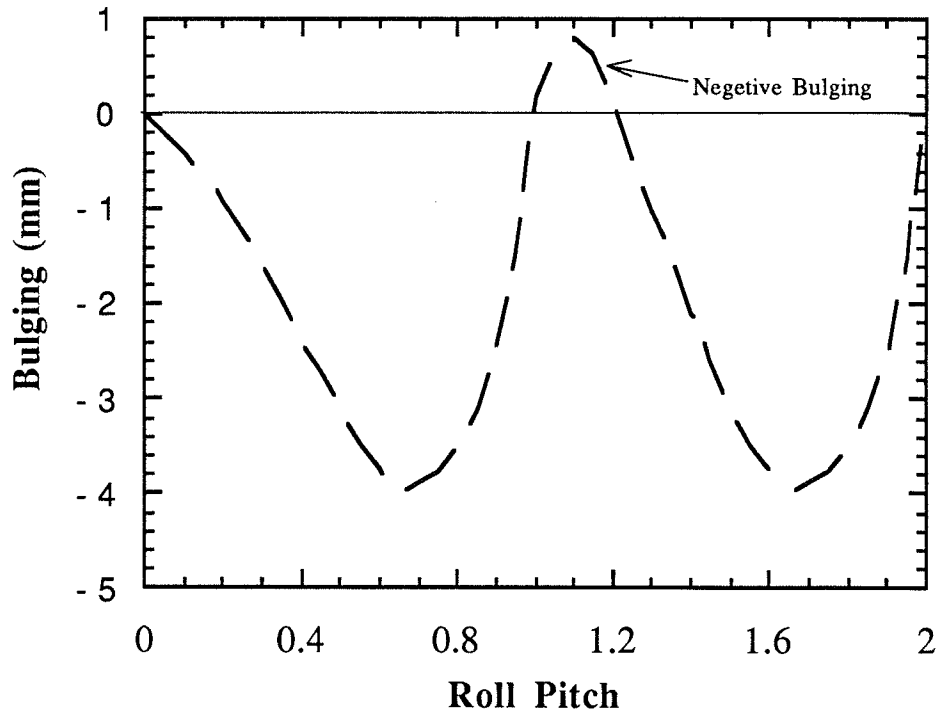


Figure 3.11 The bulging profile between two rolls used for simulation below mold.

3.4 INITIAL CONDITIONS

The model simulation starts at the meniscus and the initial shape of the domain is same as the distorted shape of the mold cavity at the meniscus. The starting temperature of the domain is set to the liquidus temperature for the super heat flux method

$$T(x,y,0) = T_{liq} \quad (3.51)$$

or to the pour temperature for the enhanced conductivity method. The gaps between the shell and the mold at the meniscus are filled with liquid mold flux and the thickness of the mold powder

layer was obtained from the CON1D model as a function of position down the mold. The initial stress strain in the domain is zero :

$$\sigma_x = \sigma_y = \sigma_z = \tau_{xy} = 0$$

and

$$\epsilon_x = \epsilon_y = \epsilon_z = \epsilon_{xy} = 0 \text{ for } t = 0 \quad (3.52)$$

3.5 TREATMENT OF LIQUID

Since the model domain contains both the liquid and the solid, special care should be taken to handle the liquid region. To avoid generating unnecessary stresses in the liquid, Kristiansson^[1, 2] assigned zero stiffness to those integrating points whose temperature is above the coherence temperature and prescribed zero displacements to the corresponding nodal points. This method have the potential to introduce singularity in the stiffness matrix and may not properly take in to account the effect of ferrostatic pressure at the solid/liquid boundary. Tszeng and Kobayashi^[34] artificially in creased the Poisson's ratio of the liquid close to 0.5 to provide a hydrostatic stress state in the liquid region. However, this is not necessary when using the ferrostatic pressure as an internal boundary condition as in the present case.

In continuous casting, where the liquid is exposed to ambient pressure all times, the liquid elements should contribute no stresses to the shell other than through Eq. (3.40). This is accomplished in the model simply through careful choice of temperature dependent functions of elastic modulus $E(T)$ and thermal linear expansion (TLE) especially above the solidus temperature. The elastic modulus is gradually reduced from its value at solidus temperature to 10 MPa at the liquidus temperature. To avoid generating troublesome stresses in the liquid, TLE of the liquid above the solidus temperature is made same as the value at solidus temperature. This is reasonable because any shrinkage of the liquid will be compensated by liquid level fluctuation in the mold at the free surface.

3.6 THERMO-MECHANICAL PROPERTY DATA

Accurate material property is a key to the successful prediction of any model. Therefore a careful choice was made in selecting the property data used in the simulation. Most of the thermo-mechanical properties used in the model were temperature dependent. They are discussed in detail below.

3.6.1 THERMAL CONDUCTIVITY

The temperature dependent thermal conductivity function used in the model is shown in Figure 3.11, which also shows the effect of carbon content on the thermal conductivity function.

3.6.2 ENTHALPY

The enthalpy, which represents the total heat content, is shown as function of temperature and carbon in Figure 3. 12. The curve for stainless steel is also plotted in the same figure.

3.6.3 THERMAL LINEAR EXPANSION

TLE is calculated from other measured quantities: thermal expansion coefficient and density. Firstly, TLE can be found from temperature dependent thermal linear expansion coefficient data, and its corresponding reference temperature, T_0 :

$$TLE(T) = \int_{T_0}^T \alpha_T(T) dT \quad (3.53)$$

where α_T is the temperature-dependent coefficient of thermal expansion. Alternatively, TLE can be defined as a function of the mass density, ρ :

$$TLE(T) = \sqrt[3]{\frac{\rho(T_0)}{\rho(T)}} - 1 \quad (3.54)$$

Currently, the TLE function used in the model for plain carbon steel is based on the data obtained by Harste^[65] using Eq. 3.54. The volume change due to phase transformations is accounted for by taking a weighted average of TLE based on the fraction of phases present. During the solidification of steel, liquid (l), ferrite (α or δ) and austenite (γ) is present:

$$\text{TLE} = (\%l) \text{TLE}_l + (\%\delta) \text{TLE}_\delta + (\%\gamma) \text{TLE}_\gamma + (\%\alpha) \text{TLE}_\alpha \quad (3.55)$$

where a separate TLE curve is found for each phase from measurements. Whenever phase transformation kinetics data are absent, the equilibrium conditions based on phase diagram are used to calculate the phase fractions.

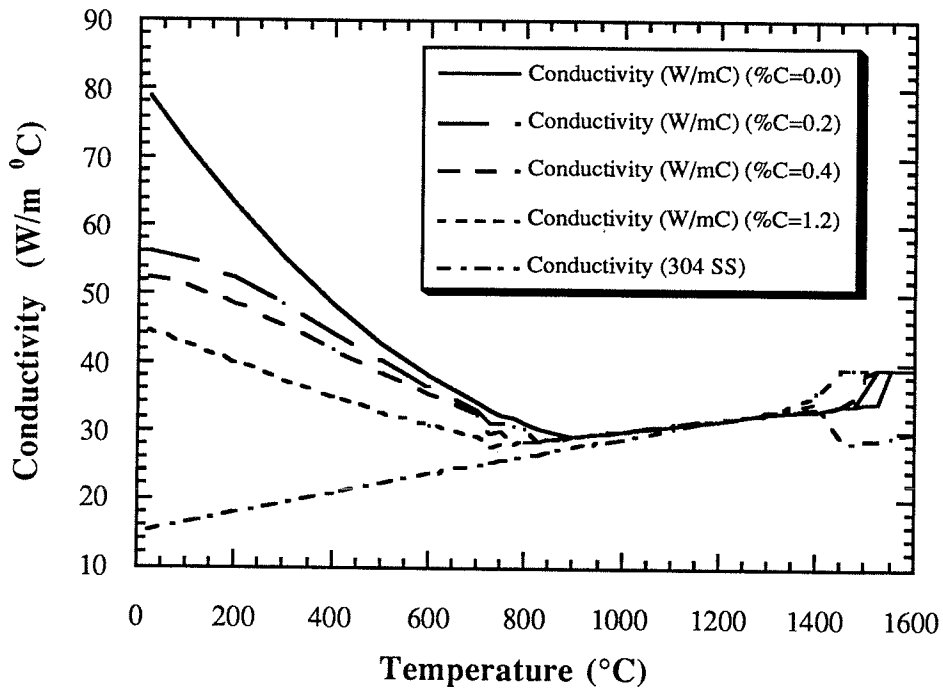


Figure 3.12 Thermal conductivities of Carbon^[65] and Stainless steel^[66] as a function of temperature

The thermal linear expansion function (Eq. 3.54) used in the model is shown in Figure 3.13 as a function of both temperature and carbon percentage for plane carbon steels. The TLE function for autenitic stainless steel used in the model is mainly based on the expansion of austenite

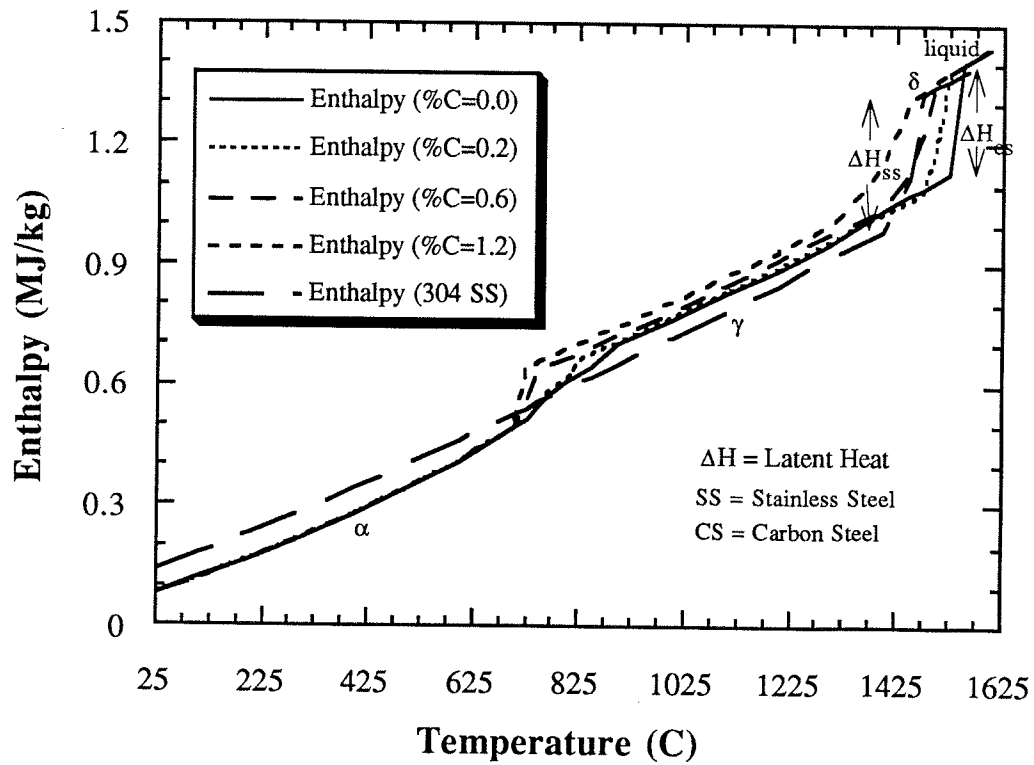


Figure 3.13 Enthalpy of carbon steel^[65] and stainless steel^[66] used in the model

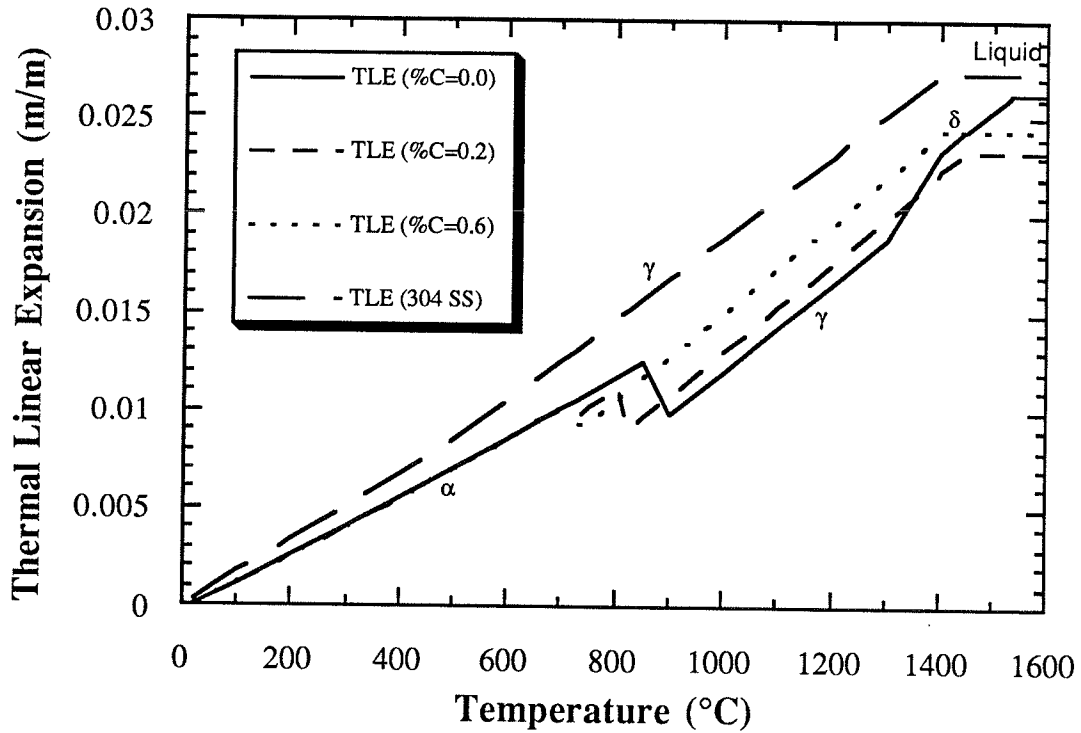


Figure 3.14 Thermal linear expansion curves for carbon^[65] and stainless steel.

using Eq. 3.53 as shown in Figure 3.13. For carbon steel, the function which is taken from Harste^[65] shows a sharp transition representing the δ - γ transformation. As seen from these curves the TLE remains constant (same as the value at solidus temperature) above the solidus temperature to avoid generating stresses in the liquid as discussed in section 3.5.

3.6.4 ELASTIC MODULUS

The elastic modulus of steel varies significantly with increasing temperature in addition to its effect on strain rate. A wide range of elastic modulus data are available in the literature. They depend on both the steel grade and the testing technique. Uncertainty exists concerning the true value of E at high temperatures. This is due to the fact that some experimental methods allow time for some creep to occur during the test, resulting in a smaller estimate of E modlus. On the other hand unrelaxed test data tend to produce relative larger estimates of elastic modulus. Two extreme of such data reported by Mizukami^[67] and Hub^[68] were used in the model is shown in Figure 3.14. The modulus is assumed to be the same for both plane-C and stainless steel grade and the

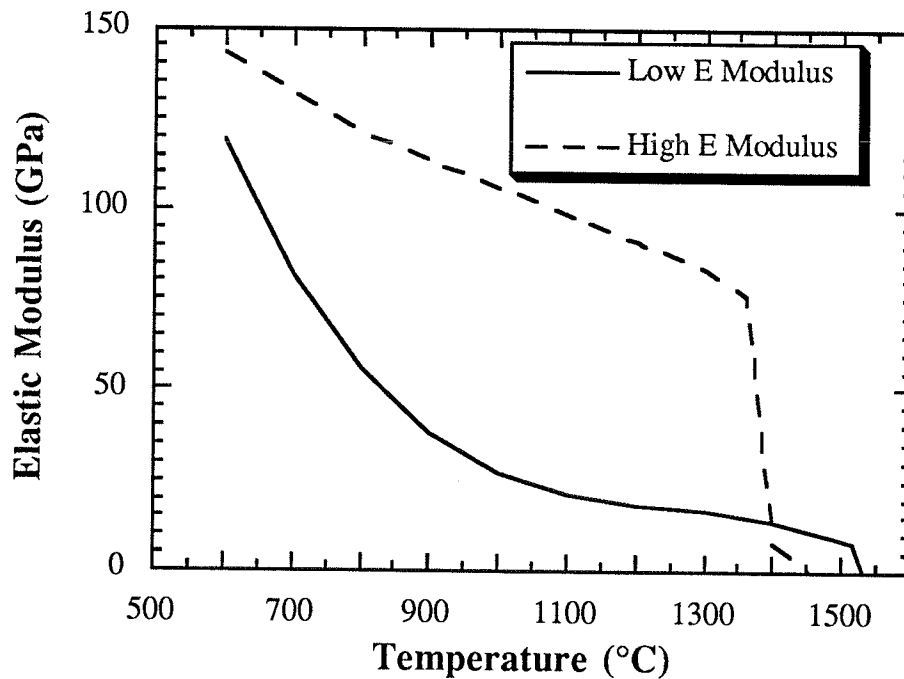


Figure 3.15 Elastic Modulus Function used in the model

results reported in this work is based on the low E modulus as the constitutive equation used in the model is based on this E modulus.

3.6.5 CONSTITUTIVE BEHAVIOR

The accuracy of stress model predictions has been limited in the past by the lack of general constitutive and appropriate experimental data with which to quantify the visco-plastic behavior described in Eq. 3.28. In recent years the visco-plastic constitutive behavior has been expressed through unified equations based on the experimental measurements.^[69-72] Among the various unified approaches, internal state variables which evolve with time are often used to characterize the structure^[70-72] and can even accommodate microstructural changes due to phenomena such as recovery and recrystallization. For the present model of continuous casting, the latter models were judged to be overly complex, since the strains are very small, loading is almost monotonic and convergence difficulties from other more important sources must be dealt with. Kozlowski et al.^[73] have recently developed simplified constitutive equations for inelastic strain in plain-carbon steel under continuous casting conditions. Tensile and creep test simulations with these equations match experimental tensile test data measured by Wray^[74] and creep test data measured by Suzuki et al.^[75] over a wide range of strain rates (10^{-3} - 10^{-6} sec.⁻¹) and high temperatures (950 - 1400 °C) and varying carbon contents (0.005 - 1.54 Wt.-%C). One of these equations have been incorporated into the CONCAST model and is provided below.

$$\dot{\epsilon}_p = f_c * \exp\left(-\frac{Q}{T}\right) * (\sigma - f_1 \epsilon_p^{f_2})^{f_3-1} \quad (3.56)$$

where

$$Q = 44650$$

$$f_c = 4.655 \times 10^4 + 7.14 \times 10^4 (\%C) + 1.2 \times 10^5 (\%C)^2$$

$$f_1 = 130.5 - 5.128 \times 10^{-3} T$$

$$f_2 = -0.6289 + 1.114 \times 10^{-3} T$$

$$f_3 = 8.132 - 1.54 \times 10^{-3} T$$

The inelastic strain in the above equation is used to characterize the structure parameter often referred in internal state variable constitutive equations. Comparison with the experimental data suggest that the model can reasonably describe the plastic-creep behavior for steels under continuous casting conditions.^[73]

3.6.6 CONSTANT PROPERTIES

Thus far only temperature dependent properties are mentioned. Other properties that were kept constant during the model simulation include density, Poisson's ratio, solidus and the liquidus temperature. For the present case the liquidus and solidus temperatures are expressed as

$T_{liq} = 1454$ and $T_{sol} = 1399$ °C for the stainless steel and for the carbon steel they are expressed as

$$T_{liq} = 1536.0 - 78.846 * (\% C) \quad (3.57)$$

$$T_{sol} = 1536.0 - 455.55 * (\% C) \quad (3.58)$$

The effect of other compositions on these temperatures are being neglected as this would not affect the temperature or stress calculations. The density and Poisson's ratio of the steel are assumed to be temperature independent. This is done to maintain a constant mass. The density of stainless steel is taken to be 7800 Kg/m³ while that of carbon steel is taken as 7400 Kg/m³ and the Poisson's ratio is taken as 0.3 for both the material.

3.7 REFERENCES

1. J.O. Kristiansson: "Thermal Stresses in Early Stages of Solidification of Steel", *Journal of Thermal Stresses*, 1982, vol. 5, pp. 315-330.
2. J.O. Kristiansson: "Thermo Mechanical Behavior of the Solidifying Shell within Continuous Casting Billet Moulds - A Numerical Approach", *Journal of Thermal Stresses*, 1984, vol. 7, pp. 209-226.
3. A. Grill, K. Sorimachi and J.K. Brimacombe: "Heat Flow, Gap Formation and Break-Outs in the Continuous Casting of Steel Slabs", *Metallurgical Transactions*, 1976, vol. 7B, pp. 177-189.
4. K. Kinoshita, T. Emi and M. Kasai: "Thermal Elasto-plastic Stress Analysis of Solidifying Shell in Continuous Casting Mold", *Tetsu-to-Hagane*, 1979, vol. 65 (14), pp. 2022-2031.
5. K. Kinoshita and T. Emi: *Numerical Analysis of Heat Transfer and Stress in Solidifying Shell within the Mold of Continuous Casting*, Kawasaki Steel Corp., Japan, Report No. 822278, 1980, (translated from Kawasaki Seitetsu Giho Vol. 12 No. 3, 1980).
6. K. Kinoshita, H. Kitaoka and T. Emi: "Influence of Casting Conditions on the Solidification of Steel Melt in Continuous Casting Mold", *Tetsu-to-Hagane*, 1981, vol. 67 (1), pp. 93-102.
7. K. Okamura and K. Yamamoto: "Coupled Analysis Between Thermal Deformation and Heat Transfer of Solidifying Shell in Continuous Casting Mold", *Modeling of Casting, Welding and Advanced Solidification Processes VI*, T.S. Piwonka, V. Voller and L. Katgerman, eds., TMS-AIME, Warrendale, PA, Palm Beach, FL, 1993, pp. 535-541.
8. X. Huang, B.G. Thomas and F.M. Najjar: "The Removal of Superheat from Continuous Casting Molds", *Metallurgical Transactions B*, 1992, vol. 23 B (June), pp. 339-356.
9. O.C. Zienkiewicz: *The Finite Element Method*, third ed., McGraw Hill, New York, NY, 1977.

10. B.G. Thomas, I.V. Samarasekara and J.K. Brimacombe: "Comparison of Numerical Modeling Techniques for Complex, Two-Dimensional, Transient Heat-Conduction Problems", *Metallurgical Transactions*, 1984, vol. 15B (June), pp. 307-318.
11. E. Lemmon. *Multi-dimensional Integral Phase Change Approximations for Finite-Element Conduction Codes*. Numerical Methods in Heat Transfer. 201-213, 1981.
12. T. DuPont, G. Fairweather and J. Johnson: "Three-level Galerkin Methods for parabolic Equations", *Siam Journal of Numerical Analysis*, 1974, vol. 11, pp. 392-410.
13. G. Forsythe and C. Moler: *Computer Solution of Linear Algebraic Systems*, Prentice Hall, Englewood Cliffs, NJ, 1967.
14. P.V. Riboud and M. Larrecq: "Lubrification et transferts de chaleur dans la lingotiere de coulee continue", *Revue de Metallurgie - CIT, Jan*, 1981, , pp. 41-50.
15. R.V. Branion: "Mold Fluxes for Continuous Casting", *Iron and Steelmaker*, 1986, , pp. 41-50.
16. K. Yoshida: "Controlling Technology for Solidification of Continuously Cast Steel Slabs", *9th Process Technology Conference Proceedings*, ISS-AIME, Warrendale, PA, Detroit, MI, 1990, Vol. 9, pp. 183-191.
17. T. Inouye, K. Noro, Y. Akita and I. Katano: *Heat Transfer in the Continuous Casting Mold*, Kawasaki Steel, Report No. 12, 1978.
18. H. Fredriksson and K. Thegerstrom: "On the Formation of an Air Gap Between the Mould and the Strand in Continuous Casting", *Scand. J. Metallurgy*, 1983, vol. 8, pp. 232-240.
19. S. Ohmiya, K.H. Tacke and K. Schwerdtfeger: "Heat Transfer Through Layers of Casting Fluxes", *Ironmaking and Steelmaking*, 1983, vol. 10 (1), pp. 24-30.
20. B.G. Thomas, A. Moitra, D.J. Habing and J.A. Azzi: "A Finite Element Model of Thermal Distortion of Continuous Slab Casting Molds", *1st European Conference on Continuous Casting*, Florence, Italy, 1991.

21. F.P. Incropera and D.P. DeWitt: *Fundamentals of Heat Transfer*, John Wiley and Sons, New York, 1981.
22. R. Siegel and J.R. Howell: *Thermal Radiation Heat Transfer*, Vol. SP 167, NASA Special Publication, SP 167, 1971.
23. K.C. Mills, A. Olusanya, R. Brooks, R. Morell and S. Bagha: "Physical Properties of Casting Powders : Part 4 Physical Properties Relevant to FLuid and Thermal Flow", *Ironmaking and Steelmaking*, 1988, vol. 15 (5), pp. 257-263.
24. D. Lorento: "Observations of Mold Wear Patterns from Continuous Casting", *AIME Electric Furnace Conference*, New York, N.Y., 1981, Vol. 39, pp. 44-47.
25. B. Ho: *Characterization of Interfacial Heat Transfer in the Continuous Slab Casting Process*, Masters Thesis Thesis, University of Illinois, 1991.
26. P. Flint: "A Three-dimensional Finite Difference Model of Heat Transfer Fluid Flow and Solidification in the Continuous Slab Caster", *73rd Steel Making Conference*, ISS/AIME, Detroit, 1990.
27. P.J. Flint, Q.L. He, R.B. Mahapatra and J. Herbertson: "Heat Transfer, Fluid flow and Solidification Modelling of the Continuous Casting Mould", *Process Technology Conference Proceedings*, ISS-AIME, Warrendale, PA, Toronto, Canada, 1992, Vol. 10, pp. 279-291.
28. G.A. Fischer: *Proceedings of ASTM*, 1970, , pp. 1137.
29. A.A.I. Manesh: "Thermo-elastic Stress Analysis to Predict Design Parameters of Continous Casting", *Journal of Materials Science*, 1992, vol. 27, pp. 4097-4106.
30. A. Moitra, B.G. Thomas and W.R. Storkman: "Thermo-Mechanical Model of Steel Shell Behavior in the Continuous Casting Mold", *EPD Congress 1992*, TMS/AIME, Warrendale, PA., TMS Annual Meeting, San Diego, CA, March 1-5, 1992.
31. T. Nozaki, J. Matsuno, K. Murata, H. Ooi and M. Kodama: "A Secondary Cooling Pattern for Prevention of Surface Cracks of Continuous Casting Slab", *Transactions of Iron and Steel Institute of Japan*, 1978, vol. 18, pp. 330-338.

32. G. Haeghele: *Application of Mathematical Models to Investigate Defect Formation During Hot Charging of Continuously Cast Steel Slabs*, Masters Thesis, University of Illinois at Urbana, Champaign, 1988.
33. A. Grill, J.K. Brimacombe and F. Weinberg: "Mathematical analysis of stresses in continuous casting of steel", *Ironmaking and Steelmaking*, 1976, vol. 3 (1), pp. 38-47.
34. T.C. Tszeng and S. Kobayashi: "Stress Analysis in Solidification Processes: Application to Continuous Casting", *International Journal of Machine Tools Manufacturing*, 1989, vol. 29 (1), pp. 121-140.
35. W.R. Storkman: *Optimization of Mold Taper Design Using Mathematical Models of Continuous Steel Slab Casting*, Masters Thesis, University of Illinois, 1990.
36. J.R. Williams, R.W. Lewis and K. Morgan: "An Elasto-Viscoplastic Thermal Stress Model with Applications to Continuous Casting of Metals", *International Journal of Numerical Methods in Engineering*, 1979, vol. 14, pp. 1-9.
37. F.G. Wimer, T. Fastner, H.P. Narzt and E.T. Till: "Theoretical Analysis of Strand Shell Behavior in the Mold", *CCC'90*, Linz/Austria, June 1990, 1990.
38. E.H. Zetterlund and J.O. Kristiansson: "Continuous Casting - Numerical Study of the Influence of Mold Waer on Crack Formation", *Scandinavian Jopurnal of Metallurgy*, 1983, vol. 12, pp. 211-216.
39. J. Donea and S. Giuliani: "Creep Analysis of Transversely Isotropic Bodies Subjected to Time-Dependent Loading", *Nuclear Engineering and Design*, 1973, vol. 24, pp. 410-419.
40. A. Moitra, H. Zhu and B.G. Thomas: *unpublished research*, University of Illinois, Report, 1992.
41. M. Bourdouxhe, R. Charlier and S. Cescotto: "A finite element for thermo-mechanical problems", *2nd Int. Conf. on Numerical Methods in Industrial Forming Processes*, K. Mattiasson, A. Samuelsson, R.D. Wood and O.C. Zienkiewicz, eds., A.A. Balkema, Rotterdam, Netherlands, Gothenburg, Sweden, 1986, pp. 97-102.

42. A. Grill and K. Schwerdtfeger: "Finite-element analysis of Bulging Produced by Creep in Continuously Cast Steel Slabs", *Ironmaking and Steelmaking*, 1979, vol. 6 (3), pp. 131-135.
43. B. Barber, B.A. Lewis and B.M. Leckenby: "Finite-element Analysis of Strand Deformation and Strain Distribution in Solidifying Shell During Continuous Slab Casting", *Ironmaking and Steelmaking*, 1985, vol. 12 (4), pp. 171-175.
44. Hibbitt, Karlsson and Sorensen: *ABAQUS Theoretical Manual*, Hibbitt, Karlsson, & Sorensen, Inc., Providence, Rhode Island, 1990.
45. I. Cormeau: "Numerical Stability in Quasi-Static Elasto-Viscoplasticity", *International Journal of Numerical Methods in Engineering*, 1975, vol. 9, pp. 109-130.
46. H. Zhu, A. Moitra and B.G. Thomas: *Un-published research*, University of Illinois, Report, 1993.
47. PATRAN : User Manual - ver. 2.5, P.D.A. Engineering, Costa Mesa, CA, 1991.
48. A. Mendelson: *Plasticity - Theory and Applications*, R.E. Krieger Publishing, Malabar, FL, 1983, pp. 213-215.
49. A.M. Lush, G. Weber and L. Anand: "An Implicit Time-integration Procedure for A Set of Internal Variable Constitutive Equations for Isotropic Elasto-Viscoplasticity", *International Journal of Plasticity*, 1989, vol. 5, pp. 521-549.
50. R. Glowinski and P.L. Tallec: *Augmented Lagrangian and Operator-Splitting Methods in Non-linear Mechanics*, Vol. 9, Studies in Applied Mathematics, SIAM, Philadelphia, PA, 1989.
51. J. Douglas and H.H. Rachford: "On the numerical solution of the Heat Conduction Problem in second or third space variables.", *Transactions of American Mathematical Society*, 1956, vol. 82, pp. 421-439.
52. J.H. Argyris, L.E. Vaz and K.J. Willam: "Improved Solution Methods for Inelastic Rate Problems", *Computer Methods in Applied Mechanics and Engineering*, 1978, vol. 16, pp. 231-277.

53. M.D. Snyder and K.J. Bathe: "A solution Procedure for Thermo-Elastic-Plastic and Creep Problems", *Nuclear Engineering and Design*, 1981, vol. 64, pp. 49-80.
54. H.G. Fjaer and A. Mo: "ALSPEN - A mathematical model for thermal stresses in DC-cast Al billets", *Metallurgical Transactions B*, 1990, vol. 21B (6), pp. 1049-1061.
55. T.G. Tanaka and A.K. Miller: "Development of a Method for Integrating Time Dependent Constitutive Equations with Large or Negative Strain Rate Sensitivity", *International Journal for Numerical Methods in Engineering*, 1988, vol. 26, pp. 2457-2485.
56. I. Ohnaka and Y. Yashima: "Stress Analysis of Steel Shell Solidifying in Continuous Casting Mold", *Modelling of Casting and Welding Processes IV*, A.F. Giamei and G.J. Abbaschian, eds., TMS, Warrendale, PA, Palm Coast, FL, 1988, Vol. 4.
57. ABAQUS: *User's Manual*, Hibbitt, Karlsson & Sorensen, Inc., Providence, RI, 1990.
58. B.G. Thomas, A. Moitra, D.J. Habing and J. Azzi A.: "A Finite Element Model for Thermal Distortion of Continuous Casting Slab Molds", *1st European Conference on Continuous Casting*, Associazione Italiana di Metallurgia, Florence, Italy, 1991, Vol. 2, pp. 2.417-2.426.
59. O.M. Puhlinger: "Strand Mechanics for Continuous Slab Casting Plants", *Stahl und Eisen*, 1976, vol. 96 (6), pp. 279-284.
60. J.B. Dalin, Y. Germain and F.L. Chenot: "Finite element computation of bulging in continuously cast steel with a viscoplastic model", *2nd Int. Conf. on Numerical Methods in Industrial Forming Processes*, K. Mattiasson, A. Samuelsson, R.D. Wood and O.C. Zienkiewicz, eds., A.A. Balkema, Rotterdam, Netherlands, Gothenburg, Sweden, 1986, pp. 355-60.
61. J.B. Dalin and J.L. Chenot: "Finite element computation of bulging in continuously cast steel with a viscoplastic model", *International Journal for Numerical Methods in Engineering*, 1988, vol. 25, pp. 147-163.
62. B. Barber and A. Perkins: "Strand Deformation in Continuous Casting", *Ironmaking and Steelmaking*, 1989, vol. 16 (6), pp. 406-411.

63. H. Wang and B.G. Thomas: *Unpublished research*, University of Illinois at Urbana-Champaign, Report, 1992.
64. Y. Sugitani, N. Nakamura, T. Kanazawa and Y.J. Lamont: *Transactions of the Iron and Steel Institute of Japan*, 1985, vol. 25,
65. K. Harste: *Investigation of the shrinkage and the origin of mechanical tension during the solidification and successive cooling of cylindrical bars of Fe-C alloys.*, Dissertation (German) Thesis, Technical University of Clausthal, 1989.
66. R.D. Pehlke, A. Jeyarajan and H. Wada: *Summary of Thermal Properties for Casting Alloys and Mold Materials*, Vol. NTIS-PB83-211003, University of Michigan, Ann Arbor, MI, 1981.
67. H. Mizukami, K. Murakami and Y. Miyashita: "Mechanical Properties of Continuously Cast Steels at High Temperatures", *Nihon Kokan Corporation, Tetsu-to-Hagane (Iron and Steel)*, 1977, vol. 63 (146), pp. S 652.
68. P.J. Wray: "Mechanical, Physical and Thermal Data for Modeling the Solidification Processing of Steels", *Modelling of Casting and Welding Processes*, Ringe, Hew Hampshire, 1980, pp. 245-257.
69. A.K. Miller: "An inelastic constitutive model for monotonic, cyclic, and creep deformation: part 1 equations development and analytical procedures", *J. of Engineering Materials & Technology*, 1976, vol. April, pp. 97-105.
70. L. Anand: "Constitutive Equations for Rate Dependent Deformation of Metals at Elevated Temperatures", *Transactions of ASME, Journal of Engineering Materials and Technology*, 1982, vol. 104 (January), pp. 12-17.
71. A. Miller: *Unified Constitutive Equations for Creep and Plasticity*, Elsevier Applied Science Publishers Ltd, Essex, United Kingdom, 1987, pp. 1-341.
72. S. Brown, K. Kim and L. Anand: "An Internal Variable Constitutive Model for Hot Working of Metals", *International Journal of Plasticity*, 1989, vol. 5 (2), pp. 95-130.

73. P. Kozlowski, B.G. Thomas, J. Azzi and H. Wang: "Simple Constitutive Equations for Steel at High Temperature", *Metallurgical Transactions A*, 1992, vol. 23A (March), pp. 903-918.
74. P. Wray and M.F. Holmes: "Plastic Deformation of Austenitic Iron at Intermediate Strain Rates", *Met. Trans.*, 1975, vol. 6A (6), pp. 1189-1196.
75. T. Suzuki, K.H. Tacke, K. Wunnenberg and K. Schwerdtfeger: "Creep Properties of Steel at Continuous Casting Temperatures", *Ironmaking and Steelmaking*, 1988, vol. 15 (2), pp. 90-100.

CHAPTER 4

MOLD DISTORTION

4.1 INTRODUCTION

Thermal distortion of the mold tube has been found to be very important to heat transfer, dimensional accuracy, strand quality, and life of billet molds, and has been the subject of several studies, e.g.^[1-4]. Relatively less effort has been invested to understand the distortion of continuous slab casting molds^[5-9]. Perhaps this is because little residual distortion has been observed in slab molds. However, recent models have provided some insight into the mechanical behavior of the continuous slab casting mold during operation^[5-9]. Significant elastic distortion can occur during operation at elevated temperatures without any measurable residual distortion of the mold, when it returns to ambient temperature. Residual distortion is found only when significant plastic deformation at operating temperature is allowed by the constraint system.

The air gaps that form due to shrinkage in the corner regions of the slab are very small, (only a few tenths of a millimeter), but have a great effect on heat transfer from the shell to the mold^[5, 10]. Mold taper to compensate for the shrinkage is on the order of a few millimeters over the length. Thus, even a small mold distortion could have a significant effect on heat transfer. Mold distortion could also accelerate wear between the mold parts and the strand, leading to reduced mold life. Mold distortion coupled with wear is an important factor in the formation of break-outs and has also been linked with longitudinal corner cracking and rhomboidity in billets^[1-4]. The mechanical interaction with the weak, solidifying steel shell could induce undesirable shape distortion, crack formation or other quality problems. The distortion of the mold arises mainly due to the non-uniform heating of the mold walls during operation which in turn causes high thermal gradients resulting in differential thermal expansion. The accompanying thermal stresses may cause permanent creep deformation in parts of the mold, especially near the meniscus region where the temperature gradients are large. It is thus desirable to understand the thermal and

mechanical behavior of continuous casting slab molds. The work reported here is based on the paper^[11] presented at the 1st European conference on continuous casting, at Florence Italy.

4.2 PREVIOUS WORK

Several significant studies have applied mathematical models to understand the thermal and mechanical behavior of billet molds ^[1-4]. Samarasekera et al. ^[1, 3], developed an alternating direction implicit finite difference heat conduction model, combined with a finite element stress model to predict the temperature, distortion, and stress fields in a billet mold wall under different operating conditions. During operation, molds were seen to assume a characteristic shape in the longitudinal direction, which corresponded to the mold temperature. An outward bulge was found at the meniscus region, with a maximum distortion of 0.1 to 0.3 mm at 90 mm below the meniscus. Above the meniscus bulge, the mold wall assumed a negative taper of 1-2 %/m, while a positive taper of .4%/m was produced below ^[3]. Strains were greatest near the meniscus and were significantly affected by the meniscus level and the type of mold constraint. Negative taper of the mold due to distortion was found responsible for transverse depressions and cracks. Other problems including billet rhomboidity and corner cracks were attributed to asymmetric mold distortion, which was caused by asymmetric boiling heat transfer and made worse by insufficient mold constraint ^[1].

This predicted behavior was confirmed by monitoring mold movement in an operating billet machine ^[3]. Predicted values of distortion compared favorably with values measured by linear displacement transducers, except in the meniscus region. Industrial observations also showed that permanent plastic deformation was reduced by increasing the degree of constraint holding the top of the mold tube (from two to four sided clamping), and by lowering the meniscus level. Furthermore, increasing mold wall thickness increased both peak wall temperature and local distortion, causing higher stress levels. Increasing water velocity reduced both wall temperature and distortion. In conclusion, thermal distortion of the mold, as influenced by mold geometry,

temperature, and constraint, is a critical concern in avoiding quality problems in billet casting. Similar quality problems also arise from the thermal distortion of the slab mold^[12], but the behavior of slab molds during operation is not yet fully understood.

Hashimoto et al. ^[6] have conducted one of the few studies of temperature, thermal stress and mold plate deformation in slab casting molds using a finite element model. They included the effects of creep and predicted a permanent 0.1 to 0.2 mm contraction of the wide face after repeated thermal cycling, depending on the copper properties. Thinning of the mold plate was found to reduce the temperature and thermal stress resulting in less distortion of mold plates. They also observed that the presence of horizontal water slots had little effect on mold plate deformation and as such should be omitted from the design. The roots of the vertical water slots were found to act as sites for stress concentration and potential cracking ^[6]. This occurrence was predicted to be greatly reduced if the roots are rounded. Constraints (through clamping forces), mold temperature and creep deformation were all found to be important to slab quality and mold life.

Tada et al. ^[7] studied the factors affecting the performance and service life of continuous casting slab molds. Care in choosing mold clamping forces and plating the mold with Ni-Fe or Ni-W-Fe was reported to triple the mold life. They also emphasized the importance of designing and maintaining the cooling water delivery system to ensure high, uniform velocity in each cooling channel. This reduces creep-deformation of the mold and improves uniformity of heat transfer, with resulting quality improvements.

The present study aims to accurately predict slab mold distortion during operation as a function of design and operating variables, using realistic assumptions for both the thermal boundary conditions and mechanical constraints.

4.3 MOLD CONSTRUCTION

To understand the model and the distortion calculations, it is important to know how a slab mold is constructed and constrained. Figures 4.1-4.3 show different sections through the mold,

which consists of several connected parts, including the two wide face copper plates and two narrow faces. This construction allows movement of the narrow faces to form a mold cavity of the desired width. The narrow faces can usually slide between the wide faces during operation and are held in position accurately through inclinometers, to control mold taper.

Each mold plate is bolted to a welded steel enclosure or "water box", which controls circulation of the cooling water needed to dissipate the heat absorbed by the mold during operation. The water boxes also contain internal reinforcing plates to provide extra stiffness to restrict their movement. Cooling water channels are machined vertically in the back of the copper plates, as shown in Figure 4.3. The water enters the channels from the bottom and leaves at the top. The plates are connected to the water boxes with evenly-spaced bolts placed every 4 - 6 slots, depending upon the design.

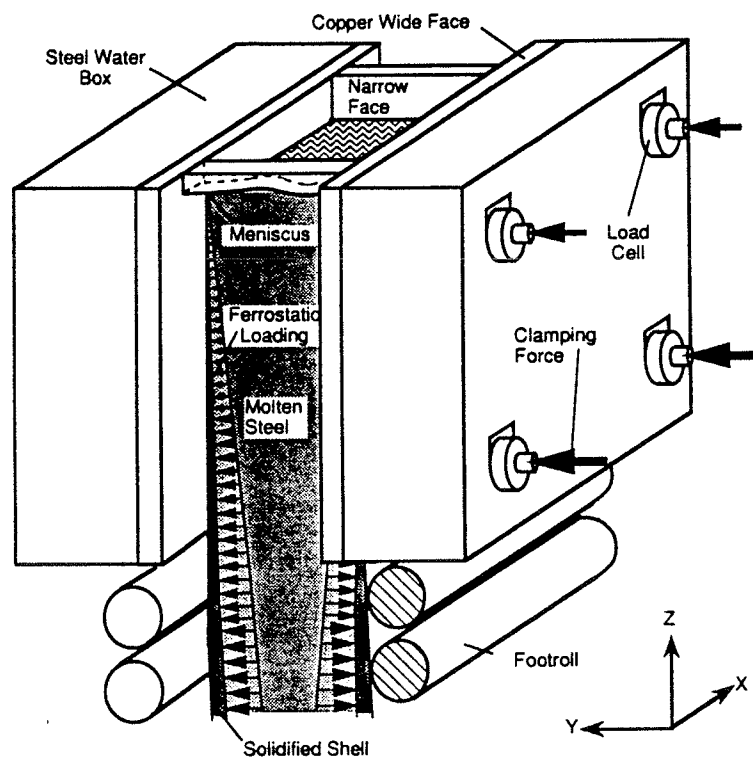


Figure. 4.1 Cut away section of the slab mold.

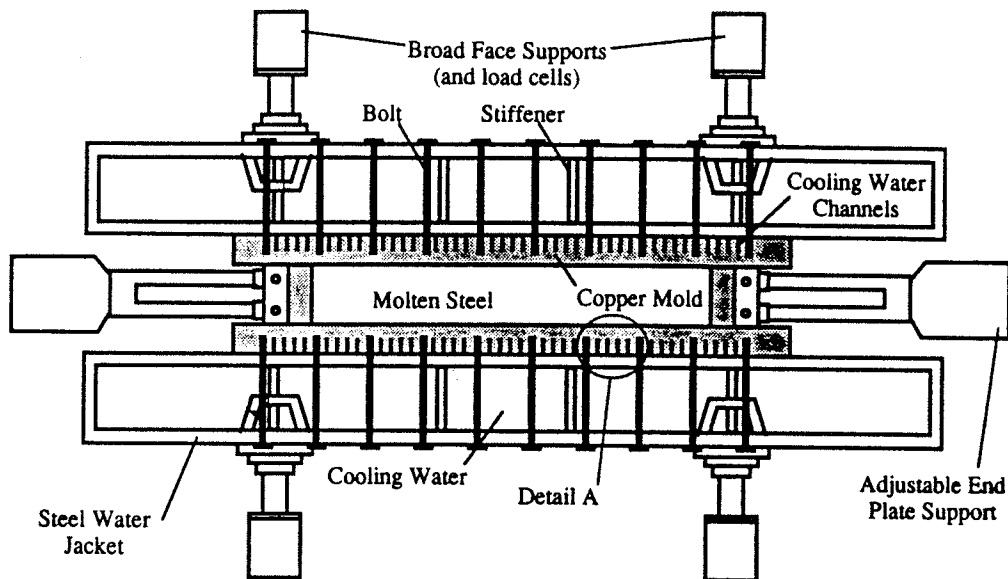


Figure. 4.2 Schematic top view of mold

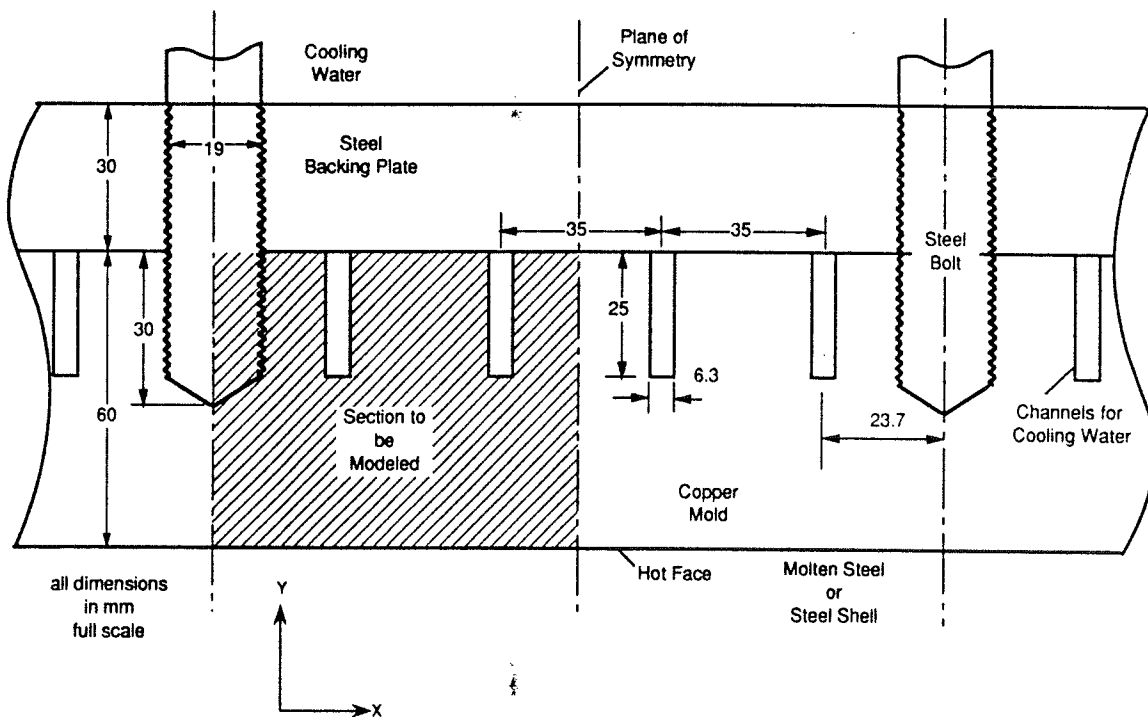


Figure. 4.3 2D transverse section through wide face showing detailed model domain

Finally the mold assembly is clamped together at four positions on the back of each water box, as shown in Figures 4.1 and 4.2. The clamping forces are provided with the support of a huge, steel frame that surrounds the entire mold. The narrow faces can usually slide between the wide faces during operation and are held in position through adjustable spring loading devices with inclinometers that also control mold taper. In contrast, a billet mold consists of a single piece thin walled tube held with in an outer box. Water flows through the space between the tube and box. A bloom mold is machined from a solid copper block, so likely behaves in a similar manner to the billet mold.

4.4 MODEL FORMULATION

To investigate the mechanical behavior of the continuous slab casting mold during operation, a 2D and a 3D finite-element thermal-stress model of a typical slab mold have been developed. The 3D model calculates temperature, displacement, and elastic stress distributions in one quarter of a typical slab casting mold (assuming two-fold symmetry and ignoring curvature), under steady-state operating conditions. A similar two-dimensional finite element model of the shaded region in Figure 4.3 was used to study the steady state temperature and stress distribution in transverse sections through the mold.

4.4.1. HEAT TRANSFER MODEL

The heat transfer model is based on the Fourier law of heat conduction and for steady state conditions is given by

$$\nabla \cdot (K \nabla T) = 0 \quad (4.1)$$

where K is the thermal conductivity of the material. The finite element form of the steady-state heat conduction equation along with appropriate boundary conditions is solved to yield the temperature distribution in the mold under operating conditions. Two separate models were developed to study thermal and mechanical behavior. A 2D model of a representative piece of the

mold was developed to examine the local effects of the water channels on the heat transfer as well as stress distribution. A 3D model was developed to study the overall behavior of the entire mold. Each model is described separately below.

4.4.1.1 2D MODEL

The 2D model was developed out of a slice at the center of the wideface near the meniscus region as shown by the shaded region in Figure 4.3. The actual geometry of the water slots and the position of the bolts were incorporated into the model. The computational domain was discretized with 4-noded quadrilateral elements as shown in Figure 4.4. Both a fine mesh with slot geometry and a coarse mesh without a slot were used. For the coarse mesh, the water slot was approximated by a convecting surface at the common boundary of two elements as shown in Figure 4.4, extracting approximately similar amounts of heat as the water slots. The validity of this approximation is the basis of the 3D model.

4.4.1.2 BOUNDARY CONDITIONS

The heat transfer boundary conditions for both the fine and coarse mesh are shown in Figure 4.4. Mathematically it can be represented as :

At $x = 725 \text{ mm}$ for $0 \leq y \leq 60 \text{ mm}$ $q = 0$ (insulated)

At $x = 801 \text{ mm}$ for $0 \leq y \leq 60 \text{ mm}$ $q = 0$ (insulated)

At $y = 60 \text{ mm}$ for $725 \text{ mm} \leq x \leq 801 \text{ mm}$ $q = 0$ (insulated)

At $y=0$ for $725 \text{ mm} \leq x \leq 801 \text{ mm}$ $q = 2.68 \text{ MW m}^{-2}$.

Inside water slots for all element surfaces we have convective boundary condition as

$q = h (T - T_{\infty})$ where $h = 35000 \text{ W m}^{-2} \text{ K}^{-1}$ and $T_{\infty} = 15 \text{ }^{\circ}\text{C}$.

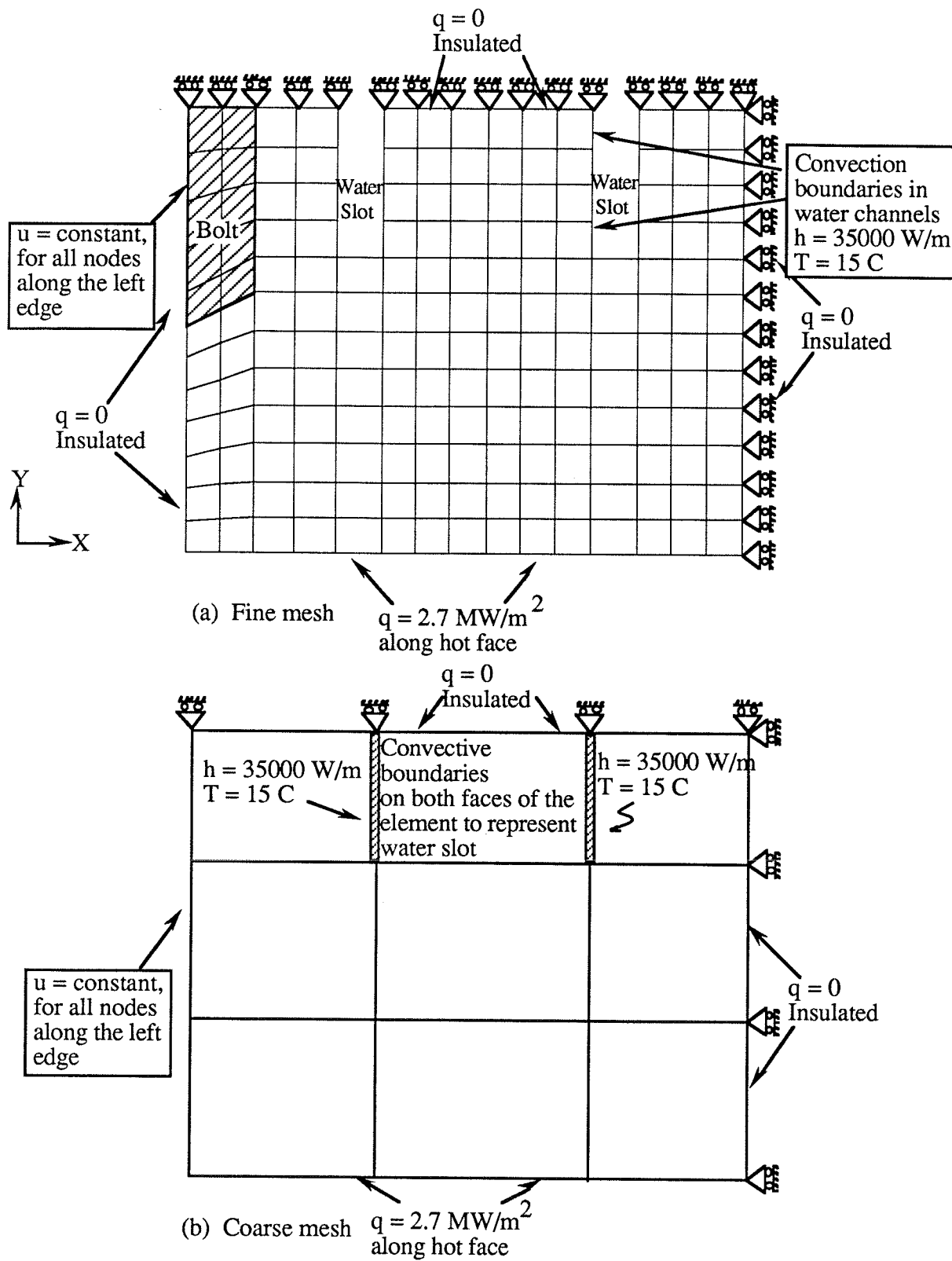


Figure 4.4 Finite Element meshes and boundary conditions for 2D analysis.

4.4.1.3 3D MODEL

The 3D model was developed using a quarter section of the slab mold utilizing the two-fold symmetry of the geometry neglecting curvature and taper. The computational domain was discretized with 8-noded brick elements for 3D analysis. Heat was input to the exposed surfaces of interior mold elements as a function of distance both down and across the mold. Each cooling water channel was represented simply as a boundary between two appropriate elements within the mold which was treated as a convective heat transfer surface similar to that shown in Figure 4.4(b). This allowed a relatively coarse, but carefully-designed mesh to extract the correct total amount of heat from approximately the right places in the mold, as shown in Figure 4.5.

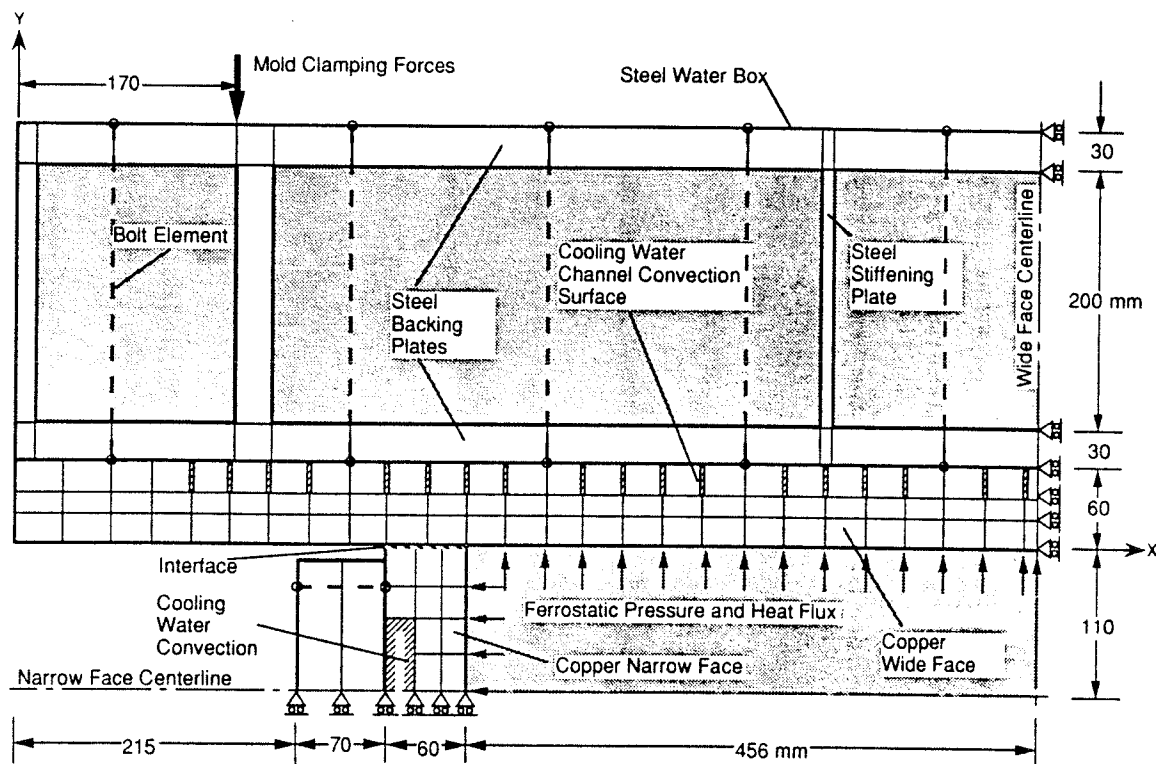


Figure. 4.5 Model mesh and boundary conditions shown in top view of mold quarter section

4.4.1.4 BOUNDARY CONDITIONS

The boundary conditions used in the simulation are illustrated in Figure 4.5. Heat flux into the hot face was varied as a function of position both across and down the mold, to account for the known drops in heat flux near the bottom, narrow face and corners of the mold. The functions for heat flux down the mold for were derived from available measurements^[13-15] and are shown in Figure 4.6. Figure 4.6 shows the variation of heat flux with position down the mold at various locations on the hotface. Standard conditions, based on Savage and Pritchard^[13] included a peak heat flux of 2.7 MW/m^2 at the meniscus, located 84 mm below the mold top at the center of the wideface. A "high heat flux" condition, based on data from Samarasekera and Brimacombe^[14]

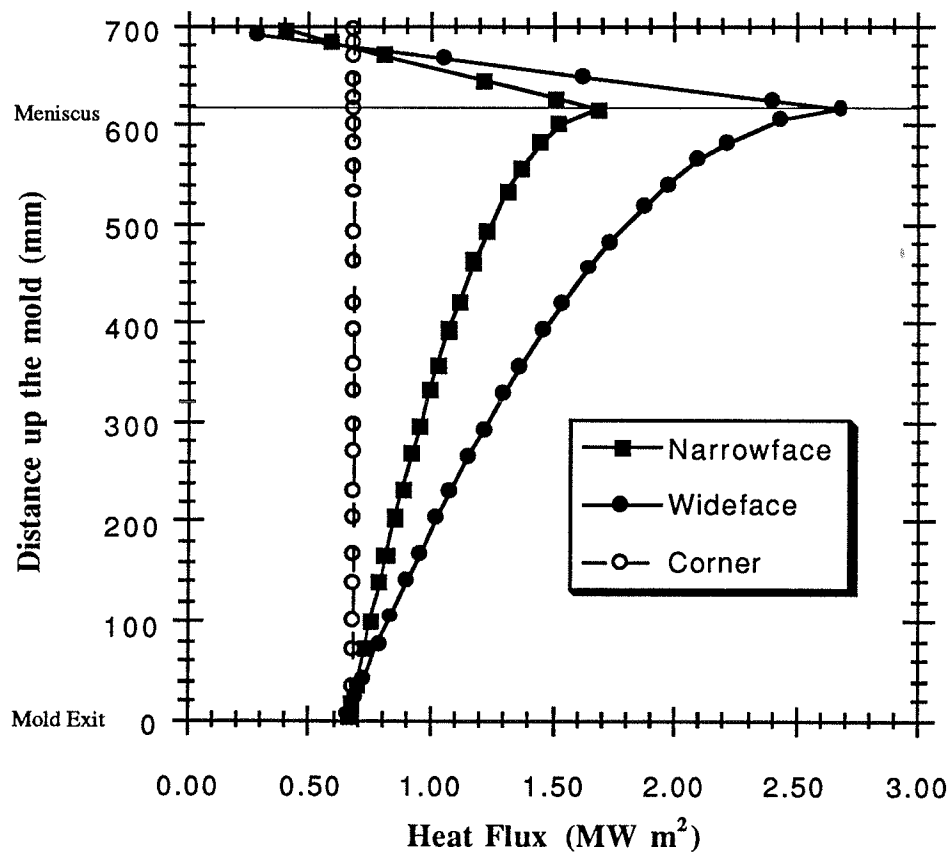


Figure 4.6 Hotface heat flux at the symmetry plane as a function of position in mold.

reached 3.8 MW/m^2 . Heat flux at the narrow face and corners was reduced to 62% and 25% respectively, of the nominal wide face values. To simulate the air gaps formed at the corners

during casting, the heat flux across the wideface was increased from 25%(of the nominal wideface values) at the corner to 62% at 31 mm from the corner and to full 100% at 93 mm from the corner and beyond. Along the narrowface the heat flux was varied from 25%(of the nominal wideface values) at the corner to 62% at 31 mm from the corner and beyond. These values are based on the data from Grill et al. [10]. The heat transfer coefficient on the water side was taken to be 0.035 MW/m²K for standard conditions and 0.02 MW/m²K for the high heat flux practice. The standard conditions are based on the experimental calculation of Sliecher and Rouss [16] assuming a water velocity of 8 m/s and neglecting boiling. At the interface where the narrowface touches the wideface (see Figure 4.5), heat transfer is properly accounted for through a convective boundary with a heat transfer coefficient of 0.000015 MWm⁻²K. The ambient and water temperatures were assumed to be 35 and 15 °C respectively.

4.4.2. STRESS MODEL

The basic governing differential equations for the stress model are given in the Appendix F. The present results are done mostly for elastic analysis only, the effects of creep and plasticity are neglected since in most cases the stresses in the copper plates were found to be below yield stresses of most mold materials. However, it is expected that at high temperature the material will creep a considerable amount resulting in a change of the behavior. One simulation was carried out to include the effects of creep and plasticity and will be discussed in a last section.

4.4.2.1 2D MODEL

The stress calculations were carried out using the same mesh as the heat transfer model. Four-noded quadrilateral elements were also used for the stress analysis. A more realistic stress state, namely the generalized plane strain condition (constant strain in the out-of-plane z-direction and zero rotation of the plane with respect to the in-plane directions x,y) was used for the 2D stress analysis. This stress state has been found to be the most accurate stress state for 2D thermal stress

problems [17, 18]. Special elements (GPE4) with three additional degrees of freedom (one translation and two rotation) were chosen to do this. Moreover, the elements in the plane are prevented from rotation about the in plane axes x and y. This can be expressed as

$$\begin{aligned}\epsilon_z &= \text{constant for } 725 \text{ mm} \leq x \leq 801 \text{ mm and } 0 \leq y \leq 60 \text{ mm and} \\ M_x &= \int_A y \sigma_z dA = 0 \\ M_y &= \int_A x \sigma_z dA = 0\end{aligned}$$

In ABAQUS the latter two conditions are achieved by explicitly setting the rotational degrees of freedom of each element to zero.

4.4.2.2 BOUNDARY CONDITIONS

The boundary conditions for the 2D models are shown schematically in Figure 4.4. Mathematically these can be represented as

$$\begin{aligned}\text{At } x &= 801 \text{ mm for } 0 \leq y \leq 60 \text{ mm, } u = 0 \\ \text{At } y &= 60 \text{ mm for } 725 \text{ mm} \leq x \leq 801 \text{ mm, } v = 0 \\ \text{At } x &= 725 \text{ mm for } 0 \leq y \leq 60 \text{ mm, } u = \text{constant.}\end{aligned}$$

4.4.2.3 3D MODEL

To perform the stress calculations, the 3D domain is divided into four separate meshes, for the mold coppers and steel backing plates. They are coupled mathematically only at those points where they connect mechanically in the caster during operation. The same mesh of eight-noded brick elements with 2x2x2 Gaussian quadrature is used in the heat flow and stress models, which neglects any potential effect of the cooling water channel spaces on distortion and stress. Different slab widths are achieved simply by changing the location of the contact points of the narrow and wide faces.

4.4.2.4 BOUNDARY CONDITIONS

Boundary conditions for the 3D stress analysis are shown in Figure 4.5. Symmetry planes at the narrow and wideface centers are mechanically constrained to prevent normal displacements. The wide face copper plate is bolted to the back of the water box at 30 locations, while the narrow face is bolted to its backing plate at 6 locations. Two-noded bar elements were used to connect the back of the copper plate with the far back of the water jacket, in order to properly account for the 19mm diameter restraining bolts. Since there are no threads in the water jacket itself, the bolt elements are constrained only to move vertically and horizontally with the water jacket front face. However, they are free to be pulled outward by the expansion of the copper. Mathematically this can be represented as the displacement constraint at the copper plate & water box interface in the location of bolts, for example on wideface,

$$\begin{aligned}u_{\text{copper}} &= u_{\text{steel}} \\w_{\text{copper}} &= w_{\text{steel}}\end{aligned}$$

Some molds include slots for bolts, instead of holes. For these molds the relative displacements of the bolts normal to its axis will not be fixed as the bolts are free to move in the slots. Loads representing one side of the mold clamping forces are applied at the two appropriate locations on the exterior of the backing plate, as shown in Figure 4.2. The values of these loads are 8.9 kN and 22.2 kN at 0.658 m and 0.154 m from the bottom of the mold respectively. Ferrostatic pressure loads were applied over all of the inside surfaces. Finally, the top and bottom of the copper wide faces had to be constrained from moving into the water box under deformation. Thermal expansion loads are then applied to each node in the domain, based on the previously calculated temperature increases from the ambient temperature of 35 °C.

4.5 SOLUTION METHODOLOGY

The commercial package, ABAQUS ^[19] was used for the finite element computations of heat transfer and stress analysis. The generation of the finite element mesh and post-processing of results employed PATRAN ^[20] on a Silicon Graphics Personal Iris workstation. The finite element equations of stress analysis are solved uncoupled with the heat transfer calculations, by a wavefront solver in ABAQUS ^[19]. Based on the solution of the heat transfer equations, thermal loads are applied at each node to get the displacements, strains and the resulting thermal stresses. The average CPU time for the full 3D heat transfer analysis is about 89 sec. while that for the elastic stress analysis is about 267 sec. on a SGI 4D35 workstation.

4.6 RESULTS

Typical results from the 2-D model are shown in Figures 4.7 and 4.8. Figure 4.7 shows temperature contours in a section of the wide face taken near the meniscus region. Figure 4.8 shows the temperature profile calculated through the mold thickness at the location of highest temperature, about 20 mm below the meniscus. Results such as these are useful in designing cooling water slot geometry ^[6, 21]. These figures show that a linear temperature gradient is established within most of the copper plate except at locations in-between the slots where the heat transfer is two dimensional. As seen from Figure 4.7 the hot face position across from each bolt is about 15°C hotter than the adjacent surface, since a missing cooling water slot is replaced by low-conductivity steel.

Figure 4.8 also compares the results of 2D and 3D analysis. The 3D results here, are based on a constant heat flux of 2.68 MW/m² all through out the hot face. It can be seen from Figure 8 that the temperature distribution for the 3D analysis is much closer to that of the 2D analysis in the region in between water slots, for most parts of the copper. These results also validate the assumption made about simplifying water channel geometry in the 3D model.

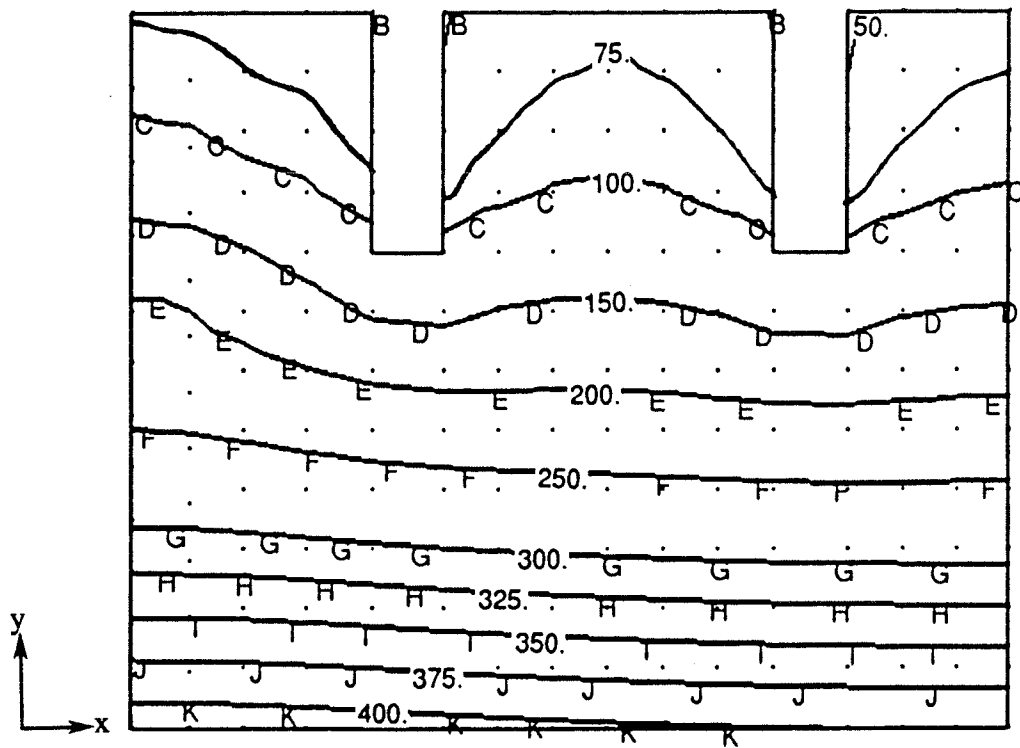


Figure 4.7 Temperature contours with section of the mold plate assembly (2D)

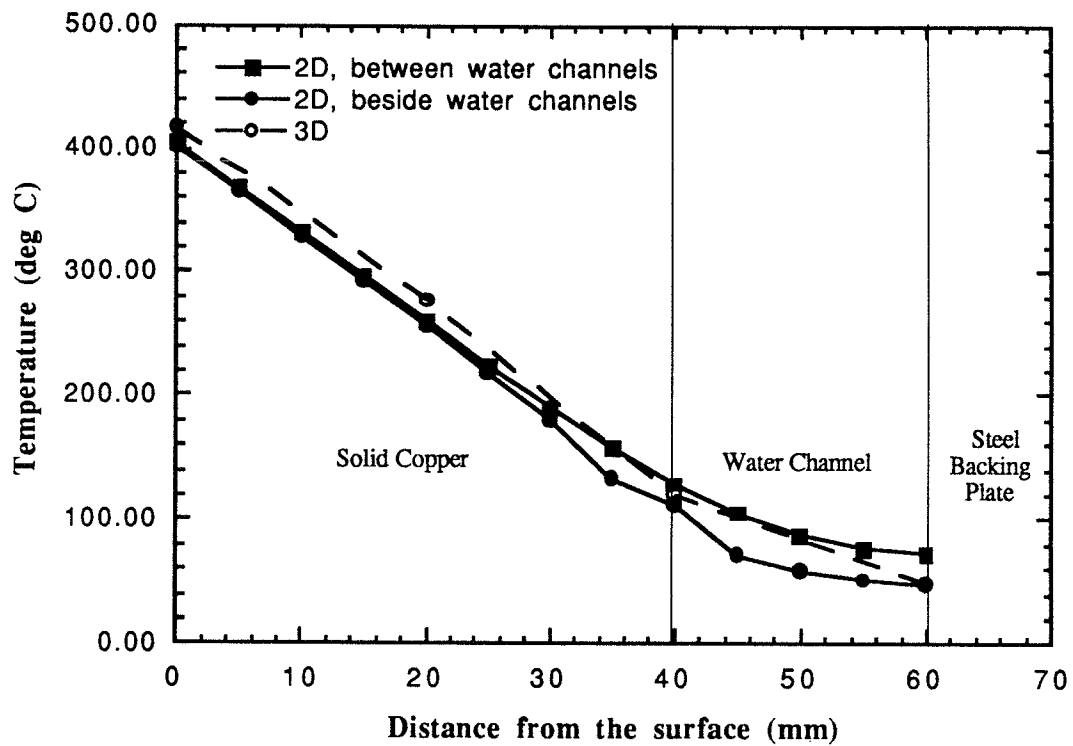


Figure 4.8 Temperature distribution through the mold thickness (at center of wideface)

The 3-D model just described was used to calculate temperature, displacement, and stress in a typical mold, under conditions given in Table 4.1. Figure 4.9 shows the complete 3-D mesh, temperature contours, and distorted shape of the mold, magnified 10 times. The hot face against the solidifying shell heats to over 300 °C, while the cooling water channels keep the cold face and the entire steel backing plate below 100 °C approximately. This is typical of the values measured in practice and predicted with previous models [6, 14, 21]. In the absence of a proper interfacial boundary condition (where the narrow and the wide copper plates meet, see Figure 4.5), the hottest spot in the mold tends to form along the corner of the narrowface. The missing water slot on the narrowface copper plate at the location of bolts and the presence of an adiabatic boundary at the interface, tend to increase the temperature at the corner of the narrowface. Incorporation of proper convective boundary condition as mentioned in the model formulation section, shifts the hottest spot on the wideface center opposite to the bolt as seen in Figure 4.9. Similar observations by Lonsbury et al. [22] have led to improved mold design. Also shown in the figure are the three slices of the distorted mold taken at the meniscus, middle and bottom locations of the mold. This distorted shape is used in the finite element model CONCAST as a boundary condition for checking mold penetration as discussed in section 3.3.3.1. The initial shape of the domain in this model is taken as the distorted shape of the mold cavity at the meniscus as shown in Figure 4.9.

A transverse section at the middle is shown in Figure 4.10 and compared with the original outline. Figure 4.11 shows a longitudinal section at the wide-face symmetry plane. These results provide insight into the behavior of the mold during operation. The hot face side of each copper plate attempts to expand more than its cold, water-cooled side. In addition, the copper plate is constrained by bolts to the outside of the cold, stiff steel water box. These effects force the entire wide face to bend inward toward the liquid steel, acting like a bimetallic strip in both the vertical and horizontal directions. A maximum distortion of 0.7 mm is predicted to occur near the very center of the wide face hot face for standard conditions. In addition, compressive stresses are produced in the copper hot face, offset by tension in the colder copper and steel interior.

Figures 10 and 11 show that the bending copper plate pulls on the initially unstressed bolts and stretches them. The tension on the outside of the water box is sufficient to distort it inward

TABLE 4.1 **STANDARD SIMULATION CONDITIONS**

| | | |
|--------------------------------|-------------------------------|---|
| Mold geometry | Cu plate thickness | 60 mm |
| | Water slot depth | 20 mm |
| | slab width | 914 mm (36") |
| | mold height | 700 mm |
| | other dimensions | See Figs. 3 and 5 |
| Copper properties | Elastic Modulus | 117 GPa |
| | Density | 8940 kg/m ³ |
| | Thermal expansion coefficient | 17.7 x 10 ⁻⁶ °C ⁻¹ |
| | Thermal conductivity | 374 W(m°C) ⁻¹ |
| Steel Properties | Elastic Modulus | 200 GPa |
| | Density | 7860 kg/m ³ |
| | Thermal expansion coefficient | 11.7 x 10 ⁻⁶ °C ⁻¹ |
| | Thermal conductivity | 49 W/(m°C) |
| Heat Flux (MW/m ²) | | See Figure 5 |
| Water inlet temperature | | 15 °C |
| Ambient temperature | | 35 °C |
| Water Convection co-efficient | | 35 KWm ⁻² K ⁻¹ |
| Clamping force | | 8.9 KN at z = 0.658 m 22.2 KN at z = 0.154 m |
| Ferrostatic pressure | | ρg (0.7 - z) |

also. A thin gap that opens between the copper and water box as the bolts stretch, was found to close if the bolts are pre-stressed. Since the narrow face is connected to the wide face only through clamping pressure, the wide face is free to rotate around the expanded narrow face, touching the narrowface at only one point. This causes the far edge of the wide face to rotate outward relative to its original position.

The predicted distortion is due almost entirely to thermal strain in the copper. A parametric study was next undertaken to determine the effect of various casting variables on mold distortion.

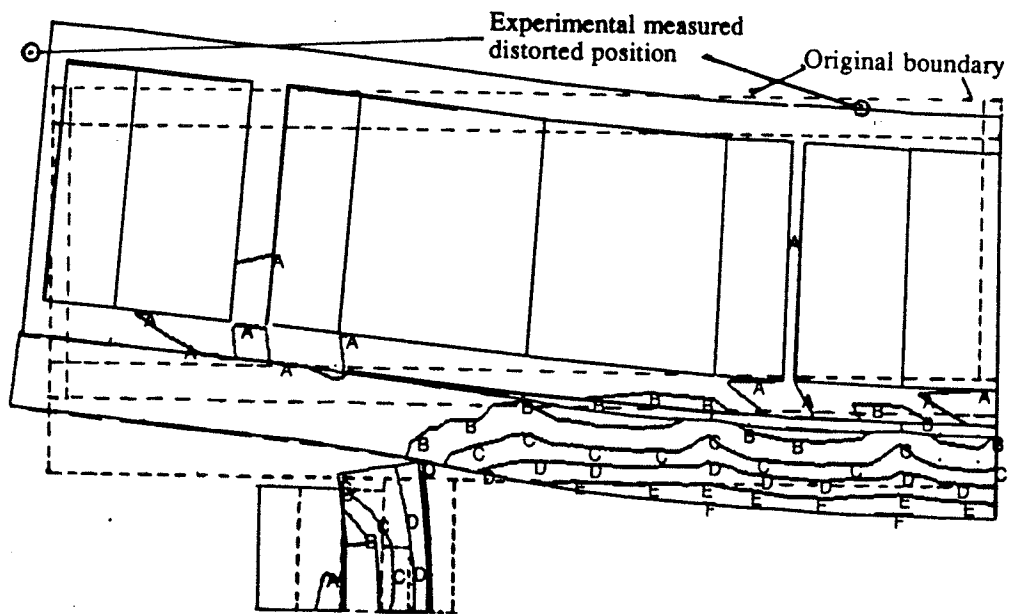


Figure. 4.10 Temperature ($^{\circ}\text{C}$) and distorted shape (exaggerated 20X) of a transverse section halfway down the mold; A=15, B=50, C=100, D=150, E=200, F=250, G=300, H=325 $^{\circ}\text{C}$?

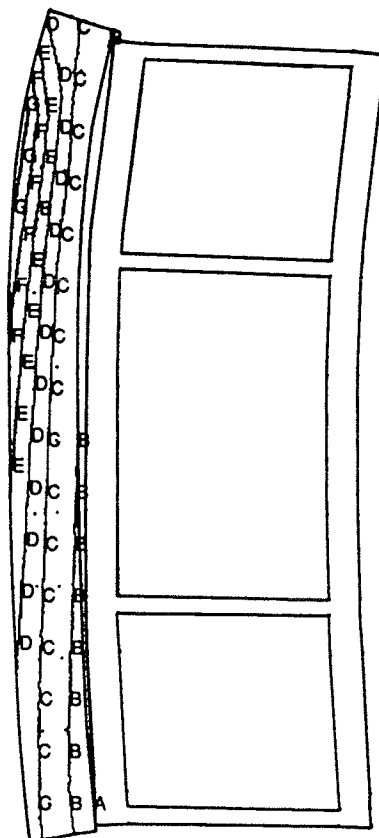


Figure. 4.11 Distortion showing a gap formed between the copperplate and the steel backing plate

4.6.1 EFFECT OF HEAT INPUT

Heat flux input to the mold changes according to the casting speed, steel grade, mold powder, and other factors. To investigate the combined effects of all of these variables on mold distortion, model simulations were conducted at two different levels of heat input, as mentioned earlier. Figure 4.12 shows that a higher heat flux practice produces higher temperatures and corresponding higher distortion of the wide face plate, as one might expect. Casting speed, powder type, oscillation frequency, stroke length and taper have all been reported to affect mold distortion [8]. The present model results are consistent with the explanation that all of these variables influence distortion solely by changing the heat input to the mold. For example, Carlsson et. al [8] reported a strong correlation between increased oscillation frequency, increased total mold heat transfer, and increased mold distortion. It should be noted that factors that increase heat flux are likely to increase interfacial friction in addition to mold distortion.

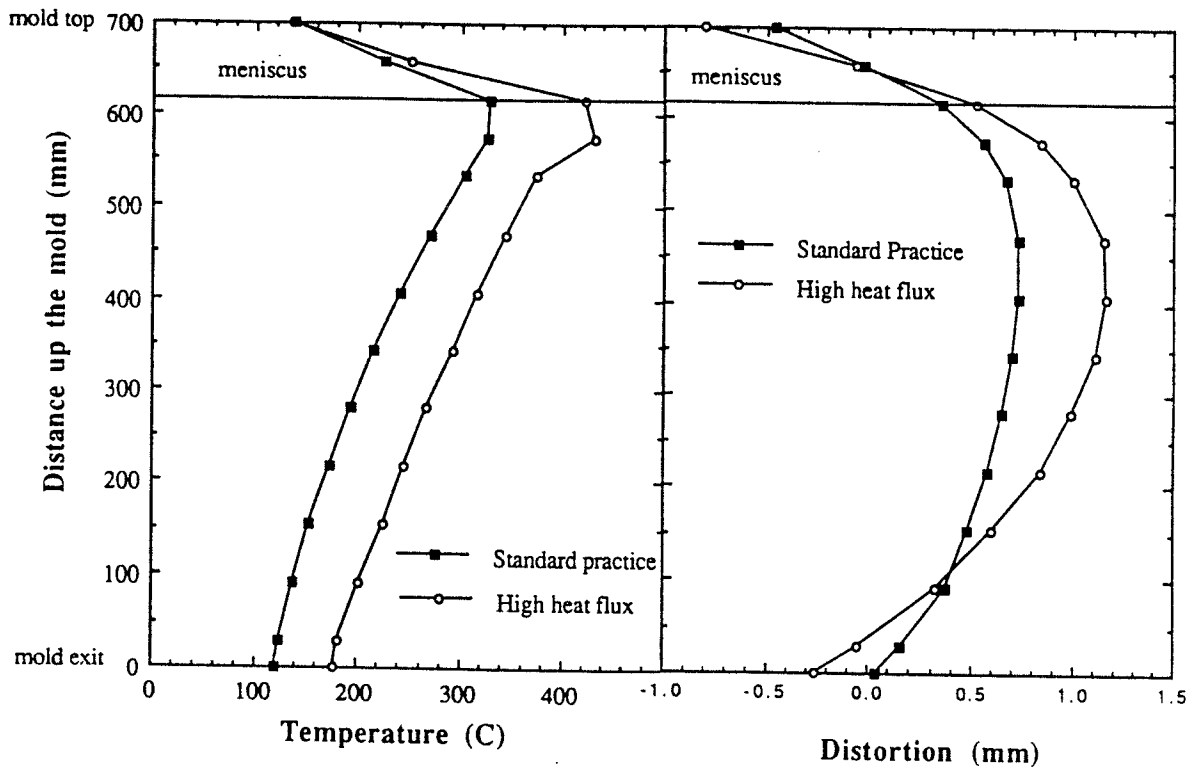


Figure 4.12 Temperature and distortion of the wideface copper plate at symmetry plane

4.6.2 EFFECT OF SLAB WIDTH

Moving the narrow face to cast a wider slab produces a significant increase in mold distortion. This can be seen in Figure 4.13, which compares the calculated distortions of the outside backing plate for 914 mm (36") and 1320 mm (52") wide slabs. Wider slabs experience more distortion since the larger surface area for heat input produces more total bending strain in the wide face. The shape is less affected, as the same pattern of maximum distortion just above half-way down the mold can be observed.

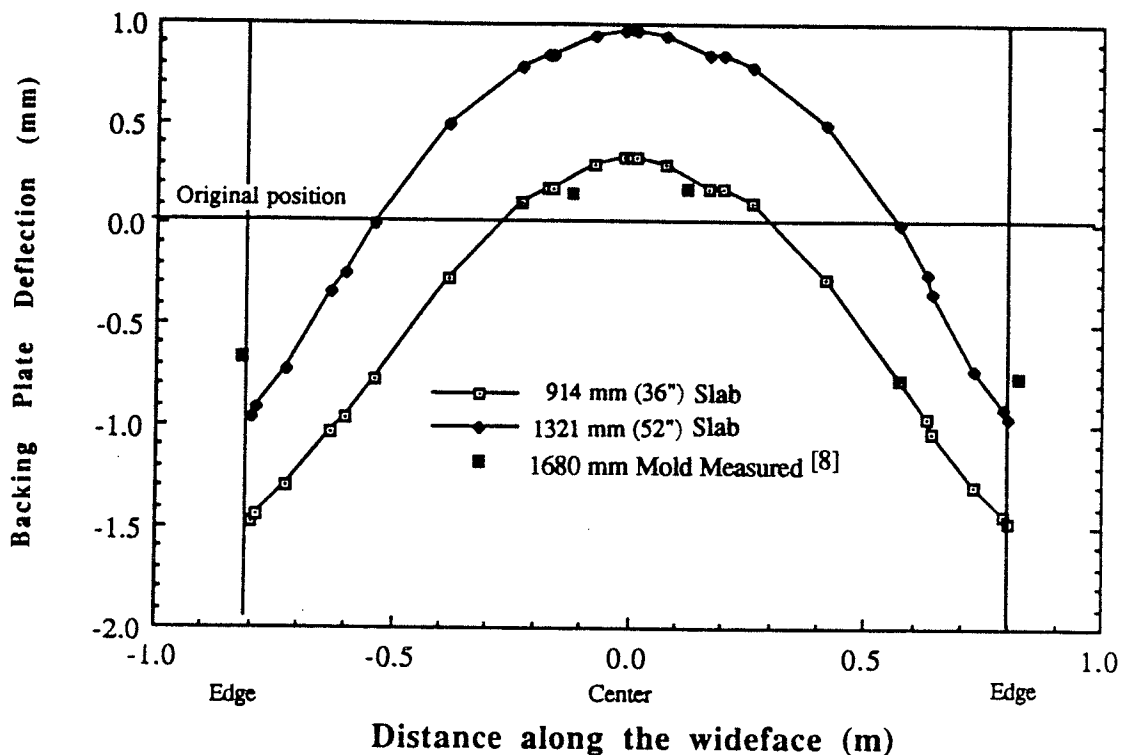


Figure 4.13 Distortion of the wideface backing plate as a function of the distance across and the slab width.

4.6.3 EFFECT OF MOLD PLATE THICKNESS

The effect of copper plate thickness on the distortion was studied by decreasing the standard copper plate thickness from 60 mm to 40 mm, while keeping the dimensions of the water

channels the same. Hot face temperature is directly proportional to mold thickness. Figure 4.14 compares the predicted temperature and distortion in a 1320 mm mold with 40 mm and 60 mm thick plates. The smaller resistance to heat flow through the thinner plate decreases its hot face temperature, which produces a corresponding decrease in distortion and thermal stress. This agrees with results reported by Samarasekera et al. [3] in billet molds and Hashimoto et al. [6] in slab molds. Other results showed that a thinner mold produces more temperature variation across the hot face because heat transfer is more influenced by the missing water slot at each bolt. Bolt pre-stress also has a greater effect on the peak stress generated in thinner molds.

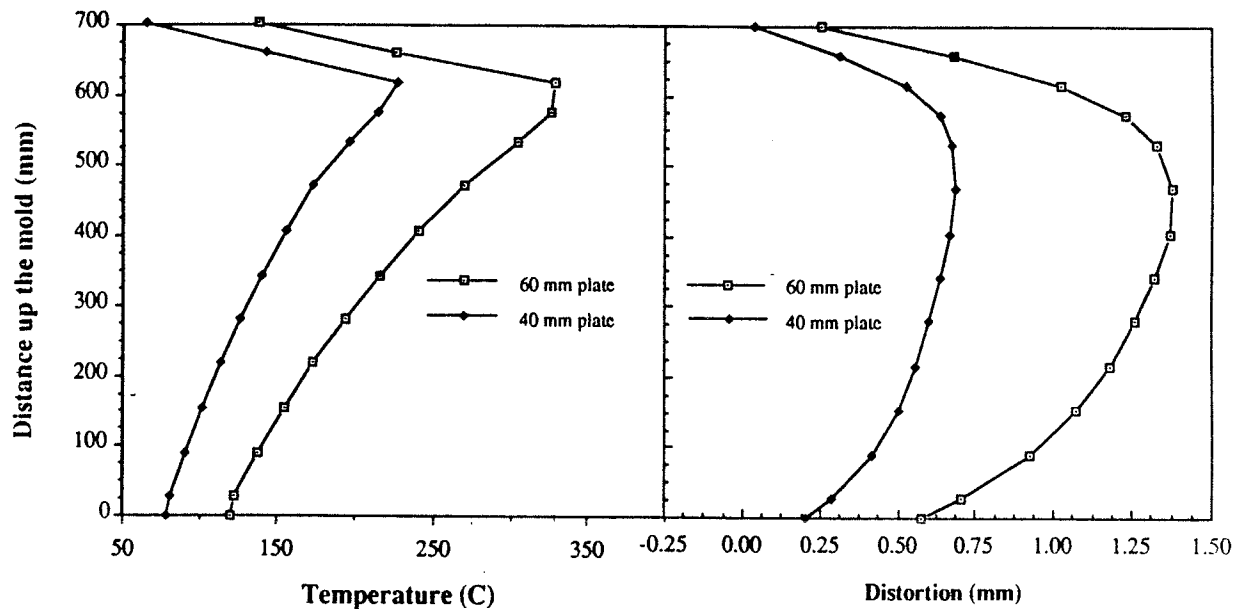


Figure 4.14 Effect of mold plate thickness on the temperature and distortion

4.6.4 EFFECT OF BOLT PRE-STRESS

Pre-stress in the bolts increases the peak stress on the hot face by 2% for a 40 mm thick mold plate and less than 1% for a 60 mm thick plate. However, it has a larger effect on the stress in the vicinity of the bolts on the cold back of the copper plate. Here, the stress increases by about 50% for 60 mm plate or 25% for 40 mm plate. The effect on hot face distortion is very small, as

the back of the water jacket simply moves closer to the copper reducing the gaps that are formed between the copper plate and the backing plate (see Figure 4.10 and 4.11) when the bolts are not pre-stressed.

4.6.5 STRESS LEVELS

The results of 2D stress analysis is shown in Figure 4.15 and 4.16. Figure 4.15 shows the x-stress contours in the domain, which suggest that the hotface copper is always in a state of compressive stress while the cold backside is under tension. Higher stress concentration near the water slots are mainly due to notch effects. During thermal cycling, fatigue cracks may initiate at the root of water channels. In some mold designs rounding off the sharp corners have prevented the cracking problem at the root of water channels [6]. Figure 4.16 compares the out-of-plane z stress for the 2D results to that of the 3D analysis. These results suggest that although the 3D

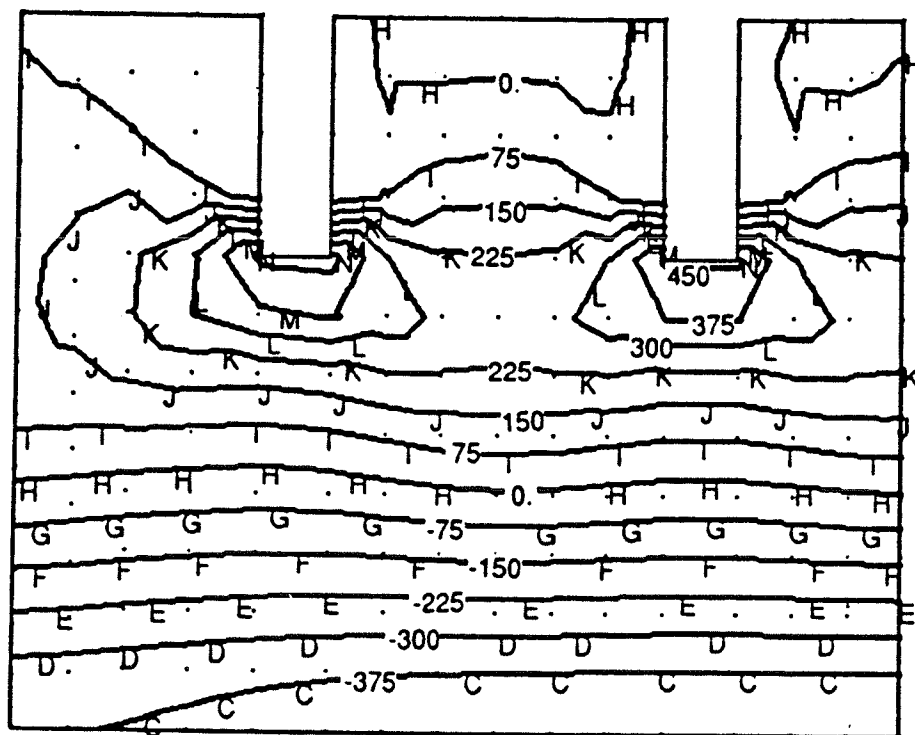


Figure 4.15 Stress (σ_x) distribution in the domain for 2D analysis with water slot geometry

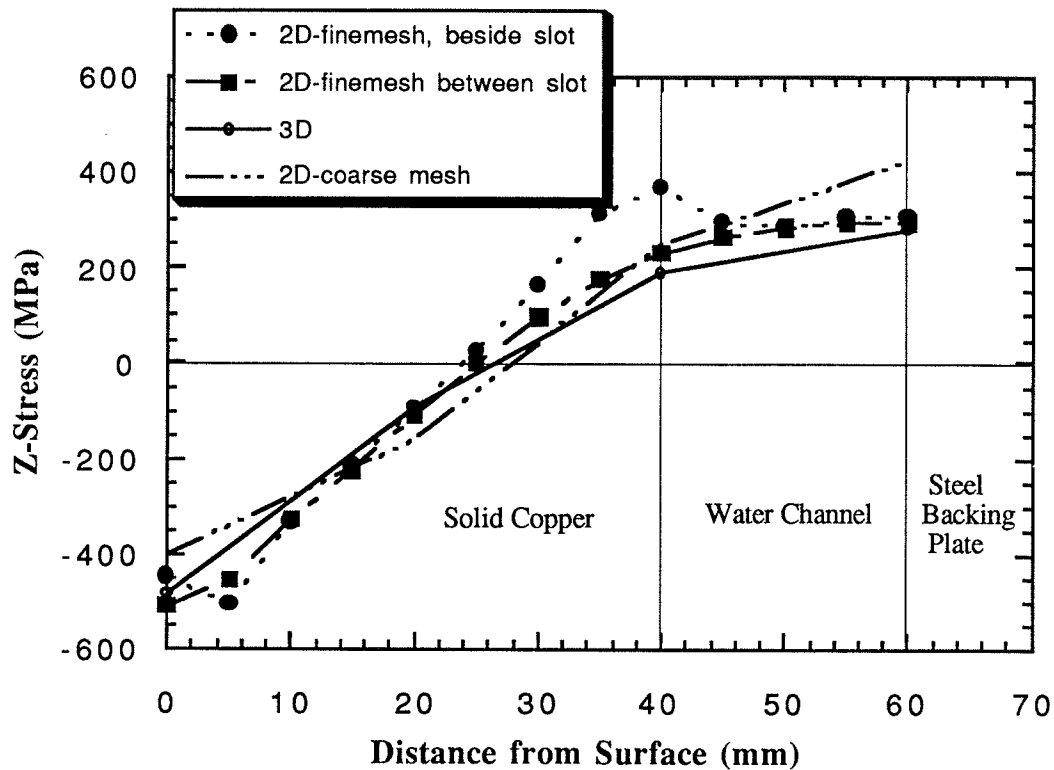


Figure 4.16 Comparison of z-stress for the 2D and 3D analysis

model is relatively coarse, it can still predict reasonably accurate stresses and distortion for the mold copper plates.

Figure 4.17 shows the Von Mises effective stress distribution superimposed on the distorted shape of the mold. These calculated stresses are always less than about 400 MPa. This indicates that the mold will return to its original shape after casting with negligible permanent distortion if the yield strength of the copper is higher than this. However, copper strength varies greatly with temperature and composition. These predicted stresses exceed the yield strength of unalloyed copper, which is around 200 MPa at the peak temperature. Thermal cycling over several hundred heats of operation, as is common practice, can allow creep to build and even induce metallurgical changes in the copper. Residual creep distortion is most likely at the points of highest temperature and stress, which occur along the hot face surface of the wide face just below the meniscus region. The high compressive stresses produced here during operation then become

tensile residual stresses after cooling. The 'spring back' found at the edges when detaching the copper mold plates from the water boxes is an indication of this residual stress.

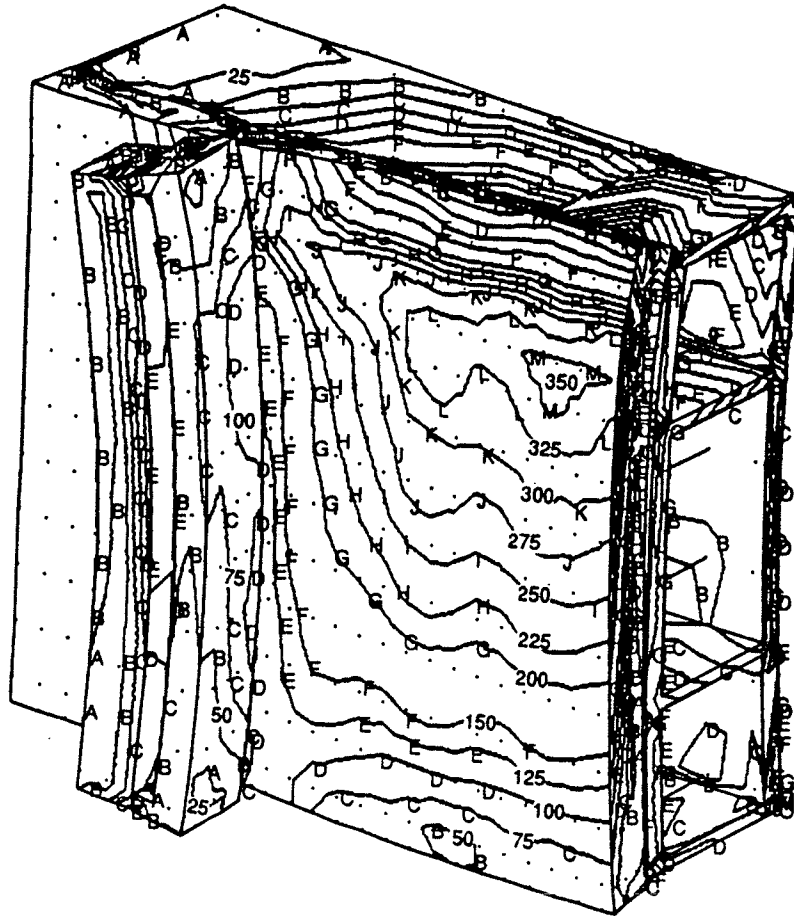


Figure 4.17 Von Mises Stress (MPa) distribution in the mold along with the distorted shape.

A good deal can be learned from these elastic distortion calculations. If the mold copper is sufficiently strong and creep resistant to withstand maximum elastic stresses, then a plastic calculation is not necessary. Permanent plastic deformation would not be found as the elastic stresses would completely relax upon cooling to ambient temperature. High strength copper alloys often have yield strengths greater than 400 MPa at the highest operating temperatures [23]. Thus a copper alloy with higher creep resistance should perform better than regular copper, as long as it does not have low thermal conductivity which would produce higher temperature and resulting distortion.

4.7 MODEL VERIFICATION

To verify these model predictions, comparisons with experimental measurements were sought. The predicted mold temperature profiles are typical of many temperature measurements that have been reported [6, 14, 21]. Unfortunately, very few slab mold distortion measurements have been reported in the literature. Work by Carlsson et. al. [8] was compared with predictions from the present model. Distortions measured using displacement transducers located at four different locations on the back of the fixed broad face [8] are included in Figures 4.10 and 4.13. These measurements were carried out on a 1680 x 220 x 785 mm mold for 8-30 minutes of casting, but distortions were found to stabilize to their steady-state values about 5 minutes after the start of casting. The qualitative nature of the measured distortions is seen to agree with the calculations: the mold shape becomes convex as it distorts inward towards the liquid at the center of the wide face and outward at its extremities. Significant distortions were also reported in the vertical plane [8]. The measured convex shape again appeared similar to the model predicted shape shown in Figure 4.11 and quantified in Figure 4.12. The magnitudes of the predicted distortions appear to be somewhat large, but important experimental conditions, such as the slab size and heat transfer factors (eg. casting speed) were not reported.

4.8 DISCUSSION

The 2D analysis of the section of the hotface copper plate has shown the heat transfer is mostly one-dimensional, except in between the water channels. The presence of water channel geometry in the model does not affect the hotface temperature very much. As shown in Figure 4.8, there is almost no variation in the hotface temperature in front of water channels and at positions away from water channels. The local variation is only near water channels and needs careful thermocouple analysis. This substantiates our assumption of not including the water slot geometry in the 3-D model. Far below meniscus and near surface on the hotface, simple 1-D

analysis of thermo-couples can be used to reasonably predict the heat flux. Near the channels, as seen in Figure 4.8, the 1-D assumption is no longer reliable and 2-D or even 3-D analysis is needed. Near the meniscus a 2D vertical slice and near water slots a 2-D horizontal slice (as in the present case) will be useful.

But for stress calculations, the water channel geometry has some effect on the stress distribution in the domain. The geometry of the water slots (sharp corners) contributes mostly to the large stress concentrations around the neck of the water slots. The tensile nature of these stresses are the cause of cracks observed at the root of the water slots. Rounding off the corners has prevented this problem in many mold designs. But the overall stress distribution in the solid copper is not affected by the presence of water slot geometry as shown in Figure 4.12. The 2D results for this analysis are very much similar to the 3D results. These facts suggest that much insight can be gained from simpler models of complicated materials processing operations, such as continuous casting.

The 3D thermal stress model of the slab casting mold has predicted distortions during operation on the order of a millimeter. These hot-face distortions are greater than those calculated by Hashimoto et al [6], who predicted distortions on the order of only 0.1 mm. However, their calculations assumed the back of copper was held rigidly, and did not take into account deformation of the water box and extension of the bolts.

It is interesting to note that the maximum distortion, which occurs half way down the mold, does *not* correspond to the maximum temperature, which appears near the top of the mold, just below the meniscus (Figure 4.15). Since the separate plates of the slab mold distort due to bending, the maximum deflection is always found closer to the center of the plate. This is contrary to experience with the smaller, thinner billet molds, where the maximum distortion always coincides with the peak temperature [3]. The difference arises because the copper billet mold is a single unit and is not constrained by backing plates. When heated, it expands as a tube outward in all directions in proportion to its temperature, so the peak distortion is found near the meniscus.

This illustrates the importance of mold construction and constraint design to mold distortion behavior.

The mold distortion predictions also have implications regarding mold wear, stress generation in the shell and heat transfer. The thin line of contact between narrow and wide face is a source of accelerated wear, particularly during width changes. As shown in Figure 4.18, the gaps that open up in the corner along the junction between the narrow and wide faces are high near the meniscus, and low near the mold exit. The gap of more than 0.1 mm at the meniscus is likely the most serious, since mold powder could penetrate, freeze, and exacerbate mold wear. In addition, steel can leak through this gap producing fins at the meniscus as observed by Lonsbury et al. [22].

Combined with taper and shrinkage of the solidifying steel shell, mold distortion affects formation of the air gap between shell and mold. Even a small distortion could have a significant effect on heat transfer across the interface. The most important measurement in this regard is the *difference* between the distorted mold position at the meniscus, where the shell first forms, and the distorted positions down the rest of the mold. Figure 4.19 shows that this difference increases from zero at the meniscus to a maximum of almost 0.5 mm half way down, to roughly -.3mm at mold exit on the wide face. This creates a slight *negative taper* over the bottom half of the mold which exceeds the typical 0.1% taper employed on the wide face and may contribute to the reduced heat transfer always observed in the lower portion of the mold.

This calculated shape of the mold surface is remarkably close to the natural shape of the shrinking strand down the narrow face of the mold. As discussed in the previous chapter, separate mathematical model of the solidifying, cooling and shrinking shell has been used to predict more shrinkage of the shell at the top of the mold than near the bottom [5]. Figure 4.19 compares this calculated shape of the shell down the narrow face with the sum of the predicted mold distortion and a typical linear taper (0.72%) used there. Mold distortion exceeds the shrinkage of the shell on the wide face, so the shell is generally forced by ferrostatic pressure to navigate around the convex mold surface. This distortion may also contribute to generating tensile stresses in the shell, important to crack sensitive grades. In the center regions of the mold, the thin shell must bend first

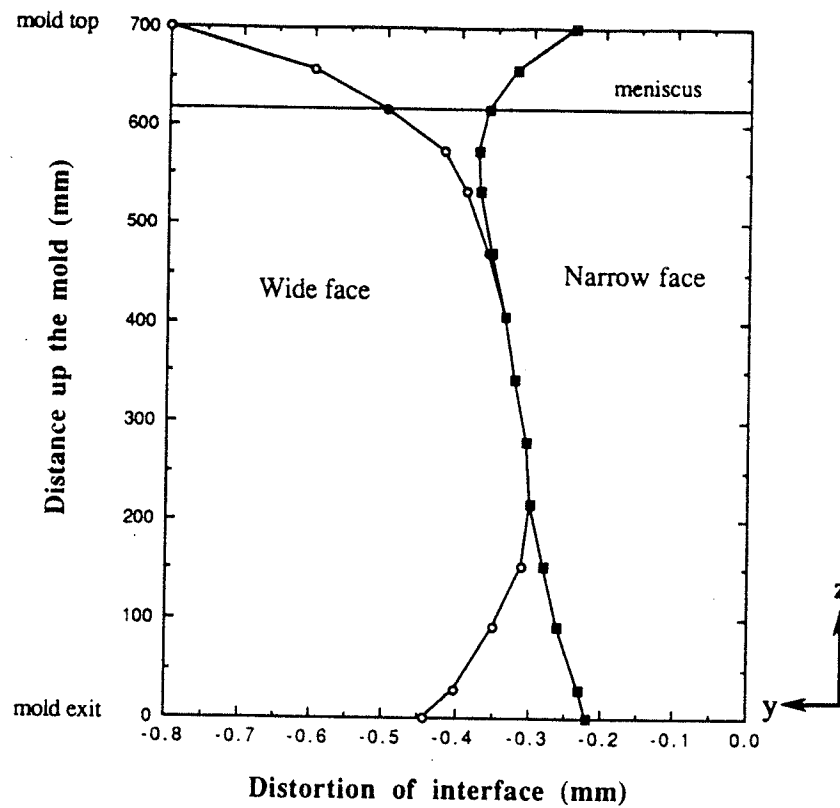


Figure 4.18 Distortion of the wide and narrowface along the line where they meet in the mold.

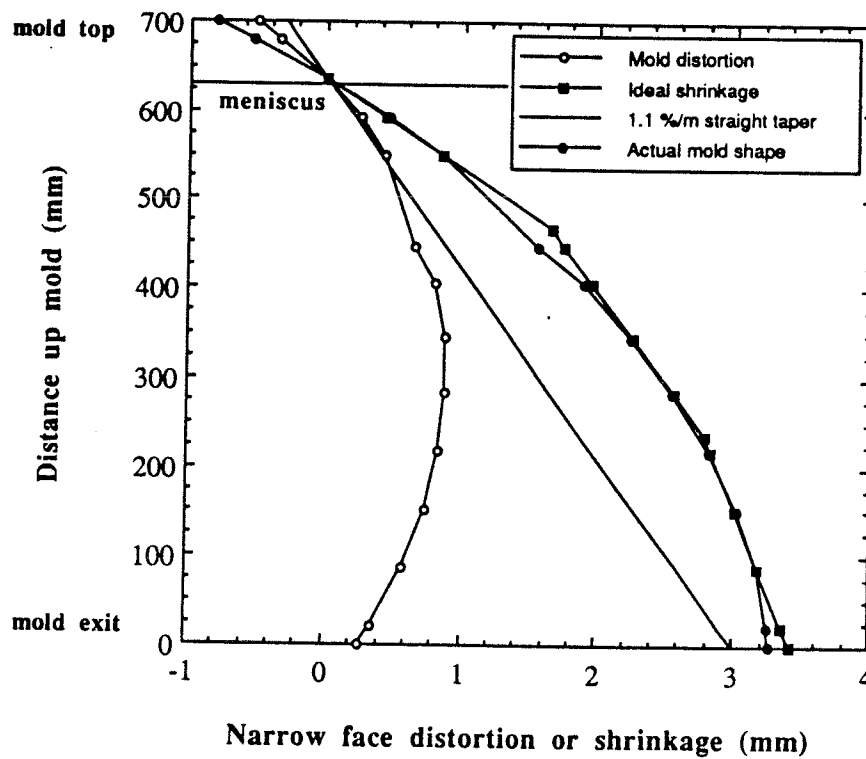


Figure 4.19 Comparison of predicted distortion with the standard taper practices.

inwards, and then outwards, to navigate around the bulge in the center of the mold. In the corners, however, shrinkage of the shell combines with the mold distortion to create a larger air gap, relative to an undistorted mold. These results suggest that mold distortion could have significant impact on heat transfer and likely helps to create the hot spots on the off-corner regions of the slab and associated defects [5, 10].

Finally, the results shown in this chapter were based on the elastic distortion of the mold. Although the stresses in the mold plate are below the yield stress of various high strength copper alloys used for mold material, it is believed that the mold material will undergo some creep deformation at the high temperature operating for several hours. As such an elasto-visco-plastic stress analysis was carried out on the mold using the yield strength and creep properties of regular copper-zirconium alloy [24, 25]. For accurate prediction of the mold deformation during operation experimentally verified creep and high temperature strength of the mold material are needed. At present such data are scarce in literature. In this analysis the mold was loaded elastic-plastically from room temperature to the steady operating temperature and was held at that temperature for about 8 hrs and then cooled to room temperature. The deformation of the wideface at the symmetry plane at various stages is shown in Figure 4.20. During the initial heating the mold undergoes some amount of plastic deformation. The smaller yield stress values for pure copper used in this case is responsible for the plastic deformation. It is expected that these deformations will be almost negligible for high yield material. After 8 hours of creep holding at the operating temperature the material undergoes small amounts of creep. Creep is higher near the meniscus region where the mold is very hot. However, the distorted shape of the model does not change much as compared to the elastic solution. As the mold cools to room temperature very little residual distortion is observed in the mold plates. The elastic deformation values used in the present model (CONCAST) can be viewed as an extreme case of mold distortion such as during a high heat flux practice or during high casting speed operations.

In the casting of thin sections, which has been the focus of much recent research on net shape casting processes, mold distortion will have an additional important effect on the final

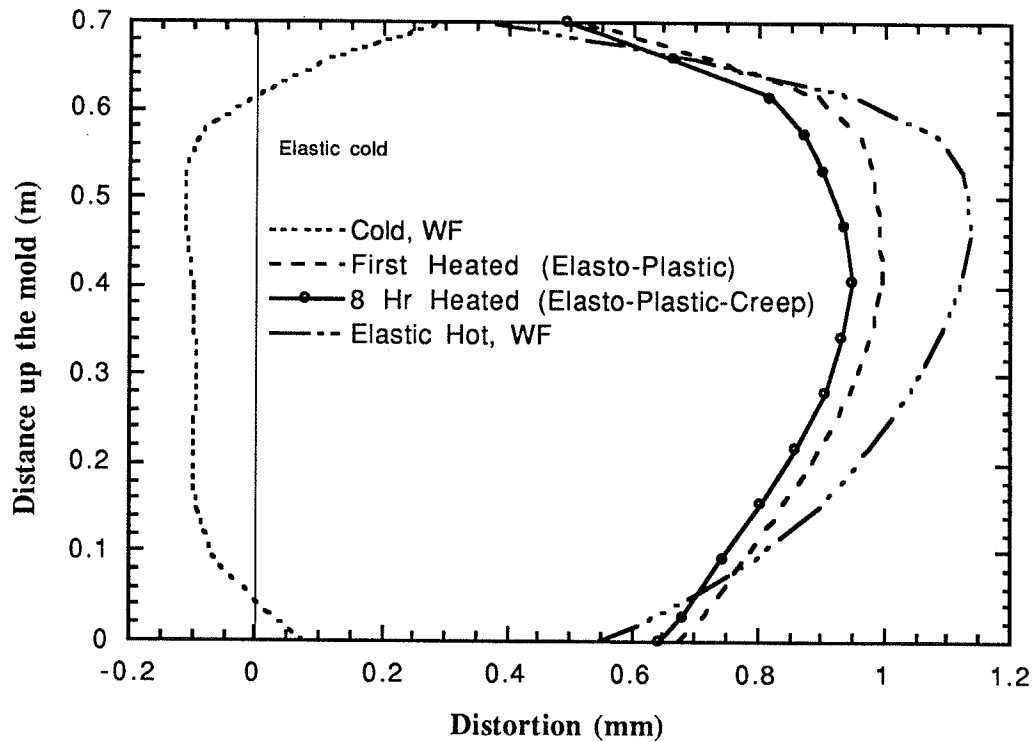


Figure 4.20 Progression of wideface distortion at the symmetry plane during a casting sequence.

dimensions of the cast product itself. Without a great deal of rolling to control the final product gage, these processes must rely on the accurate prediction and control of the temperature and shape of the casting and mold surfaces. If these processes are ultimately to succeed, mathematical models, such as the ones discussed here, will likely play an important role in their development.

4.9 CONCLUSIONS

A 3D thermal-elastic finite-element model has been developed of a continuous slab casting mold and support structure using ABAQUS. The multi-piece construction of the mold makes it behave very differently from the tube construction of billet molds. The mold plates distort inward with maximum distortion found near center of wide face. Mold distortions on the order of a millimeter have been predicted. This is sufficient to alter the effective taper of the narrow face, and may partially compensate for non-linear shrinkage of shell. It could have a significant effect on

heat transfer and growth of the shell also, particularly in the corners where the largest gaps form. The junction between narrow and wide faces does not match exactly during operation as gaps open up near top and bottom of corner edges, where solidified mold powder may get entrapped. Mold wear is predicted to be worse on the corner of the narrow copper plate hot face, since this thin edge must withstand the entire mold clamping force, plus endure wear during width changes and creep deformation. Distortion increases for wider slabs and thicker mold plates. Increasing heat input (from higher casting speed, more taper, changing mold flux, etc.) increases mold temperatures and distortion. During operation at high temperature for several hours, creep deformations can reduce the distortion of the slab mold, but in absence of better mechanical properties further conclusions cannot be made. Stress calculations on the hotface suggest that residual distortion may be possible in some low strength copper alloys and can be prevented through proper material selection and design.

4.10 REFERENCES

1. I.V. Samarasekera and J.K. Brimacombe: "Thermal and Mechanical Behavior of Continuous Casting Billet Molds", *Ironmaking and Steelmaking*, 1982, vol. 1, pp. 1-15.
2. I.V. Samarasekera and J.K. Brimacombe: "The Continuous Casting Mould", *International Metals Review*, 1978, vol. 23 (6), pp. 286-300.
3. I.V. Samarasekera, D.L. Anderson and J.K. Brimacombe: "The Thermal Distortion of Continuous Casting Billet Molds", *Metallurgical Transactions*, 1982, vol. 13B (March), pp. 91-104.
4. J.K. Brimacombe, E.B. Hawbolt and F. Weinberg. *Metallurgical Investigation of Continuous Casting Billet Molds, Part I, Distortion, Fouling and Wear*. Continuous Casting. 2: 73-84, 1984.
5. B.G. Thomas: "Application of Mathematical Models to the Continuous Slab Casting Mold.", *Transactions of Iron and Steel Society*, 1989, vol. 16 (12), pp. 53-66.
6. T. Hashimoto, K. Ohnishi, M. Yamaguchi, M. Kinugawa and M. Ueda: "An Analysis of the Thermal Load of Mold Plates in a Continuous Casting Plant", *The Hitachi Zosen Technical Review*, 1982, vol. 43 (3),
7. K. Tada, Kasai. S., A. Ichihara and Onishi: *Improvements in Service life of Continuous Casting Mold*, Kawasaki Steel, Report No. 17, 1987.
8. G. Carlsson, B. Brolund and R. Nystrom: "Measurements of Mould Distortion and Mold Heat Flux in Industrial Casters", *Journées Siderurgiques ATS*, Paris, Dec. 6-7, 1989.
9. J. Azzi: *Preliminary Steps in the Development of a 3-D Thermal-Stress Model of Continuous Casting*, Masters Thesis, University of Illinois at Urbana-Champaign, 1986.
10. A. Grill, K. Sorimachi and J.K. Brimacombe: "Heat Flow, Gap Formation and Break-Outs in the Continuous Casting of Steel Slabs", *Metallurgical Transactions*, 1976, vol. 7B, pp. 177-189.

11. B.G. Thomas, A. Moitra, D.J. Habing and J. Azzi A.: "A Finite Element Model for Thermal Distortion of Continuous Casting Slab Molds", *1st European Conference on Continuous Casting*, Associazione Italiana di Metallurgia, Florence, Italy, 1991, Vol. 2, pp. 2.417-2.426.
12. D. Lorento: "Observations of Mold Wear Patterns from Continuous Casting", *AIME Electric Furnace Conference*, New York, N.Y., 1981, Vol. 39, pp. 44-47.
13. J. Savage and W.H. Pritchard: "The Problem of Rupture of the Billet in the Continuous Casting of Steel", *Journal of the Iron and Steel Institute*, 1954, vol. 178, pp. 268-277.
14. I.V. Samarasekera and B.J. K.: "The Thermal Field in Continuous Casting Molds", *Canadian Metallurgical Quarterly*, 1979, vol. 18, pp. 251-266.
15. R.B. Mahapatra, B.T. Sellers and J.D. Young: "Influence of Slab Casting Practices on Mould Heat Transfer", *Steelmaking Conference Proceedings*, Iron and Steel Society of AIME, Toronto, Ontario, Canada, 1988, Vol. 71, pp. 423-432.
16. C.A. Sliecher and M.W. Rouse: "A Convection Correlation for heat Transfer to Constant and variable Property Fluids in Turbulent Pipe Flows", *International Journal of Heat & Mass Transfer*, 1975, vol. 18, pp. 677-683.
17. M. Bourdouxhe, R. Charlier and S. Cescotto: "A Finite Element for Thermo-mechanical Problems", *2nd Int. Conf. on Numerical Methods in Industrial Forming Processes*, K. Mattiasson, A. Samuelsson, R.D. Wood and O.C. Zienkiewicz, eds., A.A. Balkema, Rotterdam, Netherlands, Gothenburg, Sweden, 1986, pp. 97-102.
18. M. Abouaf, J.L. Chenot and J.L. Marcelin: "A Two Dimensional Finite Element Idealization for Thermo-Elastic Deflection in Beams", *International Journal for Numerical Methods in Engineering*, 1983, vol. 19, pp. 1453-1465.
19. ABAQUS: *User's Manual*, Hibbitt, Karlsson & Sorensen, Inc., Providence, RI, 1990.
20. PATRAN : User Manual - ver. 2.5, P.D.A. Engineering, Costa Mesa, CA, 1991.
21. H.L. Gilles: *9th Process Technology Conference*, Iron and Steel Society of AIME, Detroit, MI, 1990, Vol. 9.

22. T.J. Lonsbury, R.E. Fash and T.J. Russo: "Mold Copper Design Improvements Enhance Productivity and Quality", *75th Steelmaking Conference*, Iron and Steel Society of AIME, Toronto, Ontario, Canada, 1992, Vol. 75, pp. 497-505.
23. D. Salkiewicz: Brush Wellman, private communication, 1992.
24. H. Gravemann: "Materials for Mold Liners for Continuous Casting of Steel - Present Positions and Latest Trends", *Presented at the Duisburger StranggieBstage*, London, England, 1984.
25. Z.D. Jastrzebski: *The Nature and Properties of Engineering Materials*, John Wiley and Sons, New York, NY, 1977.

CHAPTER 5

SIMULATION PROCEDURE

As mentioned in chapter 3 the present model links various other models such as coupled heat transfer and fluid flow^[1], thermal distortion of the mold^[2] and the interfacial gap heat transfer model^[3] through its boundary condition. Thus before using the present model several other models were run to set up the boundary condition. First of all, the coupled fluid flow heat transfer model^[1] generates the superheat flux which is used as an internal heat source boundary condition at the solid/liquid interface. For the heat transfer conditions at the outside surface of the shell, the CON1D model^[3] (discussed in section 3.2.1.1) generates the thickness of the mold flux based on the mold powder consumption and similar casting conditions. Finally, the 3-D thermal distortion model^[2] of the mold described in chapter 4, generates the surface temperature and the distorted shape of the mold, which is again used as a boundary condition for checking and prevention of mold penetration by the shell. This completes the generation initial data necessary to run the 2-D slice model developed in this work.

The simulation in the mold starts with the slice at the meniscus. The initial temperature of the domain is kept at the pouring or the liquidus temperature depending on the method used for the treatment of superheat flux as discussed in section 3.2.1.2. Figure 3.1 also shows the simulation domain and a typical mesh. For spatial discretization for the heat transfer model, the nodes are connected into a mesh of three-noded triangular elements while the stress model employs the same nodes connected into six-noded triangles as shown in Figure 5.1. A flow chart of the overall solution procedure is shown in Figure 5.2.

Knowing the temperature, stress and the gap sizes (initially all filled with liquid flux) from the previous step (time t), the conductivity, the capacitance matrices and the thermal load vectors are formed. The finite element form of the heat transfer equation (Eq. 3.7) is solved first for the temperature distribution in the domain.

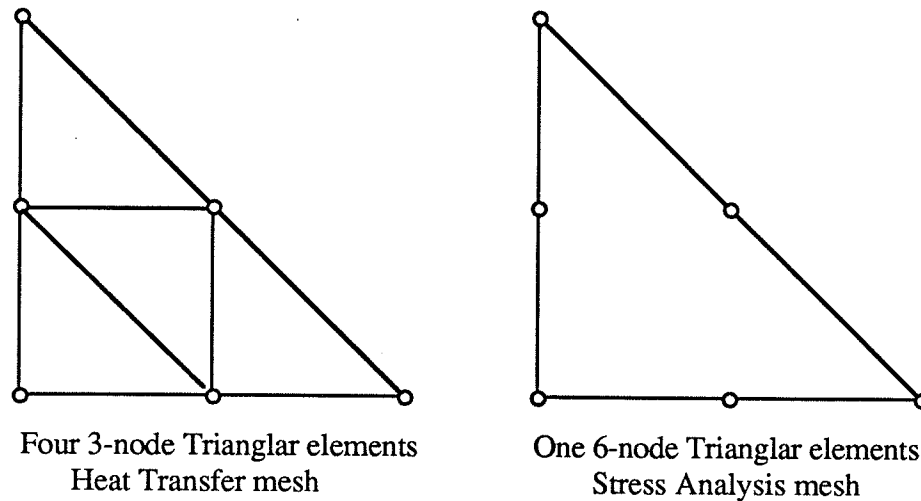


Figure 5.1 Heat Transfer and stress analysis meshes

The nodal temperature obtained from the heat transfer solution is then used to calculate the stiffness matrix (Eq. A.23) and the thermal load vector (Eq. A.25). The force vector due to incremental plastic strain (Eq. A.26), total ferrostatic pressure (Eq. A.27) and the total elastic strain up to the previous time step (Eq. A.28) are evaluated and assembled. The forward Euler type incremental plasticity algorithm used in this model is a combination of the “successive elastic solution” technique of Mendelson^[4] and the “initial strain” method of Zienkiewicz and Corneau^[5]. The implicit scheme is adopted from the visco-plastic scheme proposed by Glowinski and Talle^[6] which uses the ADI method of Douglas and Rachford^[7] for the integration of constitutive equations and uses the two level integration procedure of Lush^[8] for solving the non-linear system of equations locally at the material integration points. The stress model is stepwise coupled with the heat flow model. The solution alternates between the thermal and stress calculations as the slice travels down through the strand in successive time steps. Numerical difficulties arise from the many nested iterations required for convergence. First, iterative checks are required to prevent mold penetration of any node on the shell. Next, iterations are needed for solving the non-linear constitutive equations for the scalar incremental plastic strain, especially for the implicit scheme. Finally iterations are required to ensure that the heat transfer through the shell/mold interface based

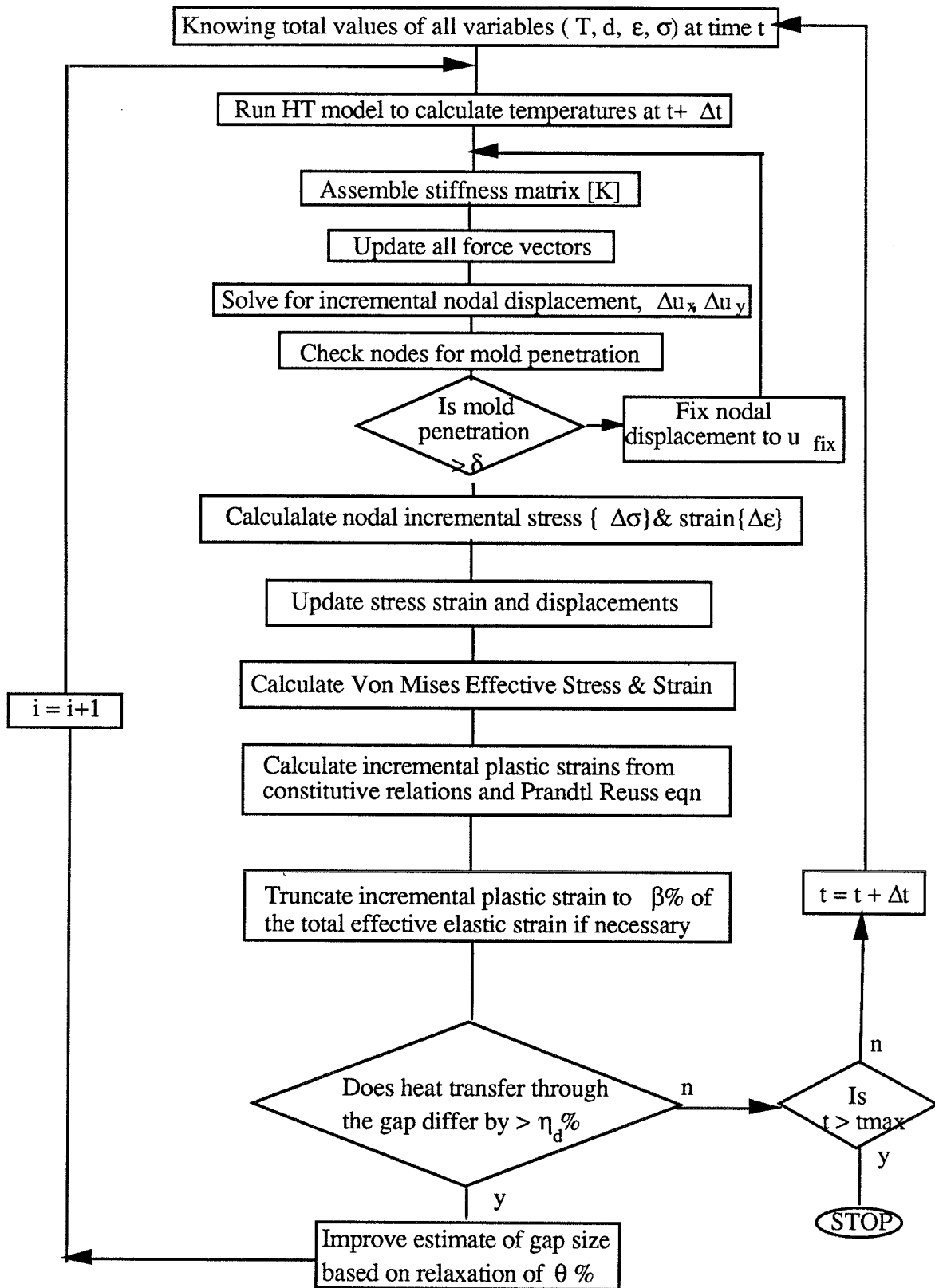


Figure 5.2 Flow chart of the overall simulation procedure for Explicit method

on the gap calculated by the stress model at the end of each step are consistent with that based on the assumed gap in the heat transfer calculations.

The finite element form of the equilibrium equation (Eq. 3.21) is then solved for incremental in-plane nodal displacements and out-of-plane strain using the Choleski solution routine^[9]. Before calculating the incremental strains or stresses, a check is made to see if any node has penetrated the mold. Spring elements are added to those nodes that tend to penetrate the mold and the procedure is repeated until no node violates the penetration criteria explained in section 3.3.3.1. During each iteration spring elements are added to the selected nodes using the procedure explained through Eq. 5.4 and 5.5. A tolerance of 0.01 mm is set for the node penetration. Although this method does not completely prevent mold penetration, it allows only a little interference without greatly influencing the shell displacement. Using this method, avoidance of mold penetration required about three to five iterations each time step.

After convergence has been achieved within the time step, incremental strains (Eq. B.1) and stresses (Eq. B.4) are calculated. Finally, the total vectors are updated to begin the next time step, $t+\Delta t$, as in:

$$\{u_{t+\Delta t}\} = \{u_t\} + \{\Delta u\} \quad \{\sigma_{t+\Delta t}\} = \{\sigma_t\} + \{\Delta \sigma\} \quad \{\epsilon_{t+\Delta t}\} = \{\epsilon_t\} + \{\Delta \epsilon\} \quad (5.1)$$

To derive the finite element equations, a quadratic displacement element, which offers better accuracy than constant strain triangles for solidification stress problems,^[10] is used. Further details regarding the derivation of the finite element equations and expressions for calculating the various terms are given in Appendix A and B.

The time step size used in the calculations is based on the following criterion for the optimum time step size, Δt , which was found by comparing model predictions with an analytical solution to a test problem^[11].

$$\Delta t \approx \frac{0.3 \rho C_p (\Delta x)^2}{k} \quad (5.2)$$

Here, Δx is the size of the smallest element in the direction of heat flow and the material properties are evaluated just below the liquidus temperature.

The procedure for the plasticity convergence and interfacial gap heat transfer convergence is discussed below.

5.1 PLASTICITY CONVERGENCE

5.1.1 EXPLICIT SCHEME

In the explicit scheme, incremental plastic strain for the next step is evaluated after updating the stresses in the element. The constitutive relation in Eq. 3.25 is used to find the scalar increment of inelastic strain, $\Delta \epsilon_p$. For explicit time-integration schemes, both accuracy and stability deteriorate with increasing time step size [Zienkiewicz, 1974 #73]. Zienkiewicz and Corneau [Zienkiewicz, 1974 #73], suggest that stability requirements can be met by limiting the maximum increment of inelastic strain at each node to a small fraction of the total accumulated strain :

$$\Delta \epsilon_p \leq \beta \ \bar{\epsilon} \quad (5.3)$$

where $\bar{\epsilon}$, the effective strain is given by

$$\bar{\epsilon} = \frac{1}{\sqrt{2}(1+\nu)} \sqrt{(\epsilon_x - \epsilon_y)^2 + (\epsilon_y - \epsilon_z)^2 + (\epsilon_z - \epsilon_x)^2 + 6 \epsilon_{xy}^2} \quad (5.4)$$

and β is in the range of 1 - 15%. In the present simulation the optimum value of β was found to be 5%. This criterion was checked at each iteration and, if necessary, satisfied by limiting the inelastic strain as per Eq. 5.3. To limit the maximum size of $\Delta \epsilon_p$, a truncation routine in the program forces the value of $\Delta \epsilon_p$ at every node to satisfy Eq. 5.3, and issues an warning that inelastic strains of those nodes are not as large as they should be. This truncation procedure has been found to be useful and does not affect the solution in the solid part of the domain.

5.1.2 IMPLICIT SCHEME

For the implicit scheme, the non-linear equations Eq. 3.36 - 3.37 are solved iteratively. A two-level scheme proposed by Lush^[8] was used in the formulation. The overall flow chart of the implicit scheme is shown in Figure 5.3. The main difference between the two schemes is in the integration of the visco-plastic strain rate to obtain the incremental plastic strain which is applied as a force vector as in the "initial-strain" method proposed by Zienkiewicz^[5, 12] for visco-plasticity. A converged solution plastic strain increment at every Gauss point is obtained before updating the global force vector. Since only two unknowns were solved for, the convergence is usually faster and there is no need for any iteration for the global finite element system. The convergence criteria used for the simulation is based on Eq. 3.36 and 3.37 and can be written as

$$\eta_{\sigma} = \left| \frac{\hat{\sigma}^{n+1} - \sigma^{*n+1} + \frac{3E(T)}{2(1+\nu)} f(\hat{\sigma}^{n+1}, \hat{\epsilon}_p^{n+1}) \Delta t}{\sigma^{*n+1}} \right| \leq 10^{-5} \quad (5.7)$$

$$\text{and} \quad \eta_{\epsilon} = \left| \frac{\hat{\epsilon}_p^{n+1} - \bar{\epsilon}_p^n - f(\hat{\sigma}^{n+1}, \hat{\epsilon}_p^{n+1}) \Delta t}{\bar{\epsilon}_p^n} \right| \leq 10^{-5} \quad (5.8)$$

5.2 INTERFACIAL GAP COUPLING

In the mold region, coupling allows the heat flow model to determine the heat flux across the mold/shell interface based on the gap thickness calculated by the stress model. Within each time step, iterations are performed to ensure that the heat transfer is consistent with both assumed and calculated gap size. In this way, coupling between the thermal and the mechanical models is achieved by ensuring that the size of the interfacial gap and the heat flux through it are consistent between the models. The heat flow model starts with the previous gap size, d_{gap}^t . A new gap size is then calculated after the stress model has solved for the new displacements. At the end of the stress analysis at each time step, the heat flux($q''(d^i)$) leaving every node on the slab surface, based on the assumed (d^i), is compared with the value($q''(d^i)$) based on the new gap size(d^i) :

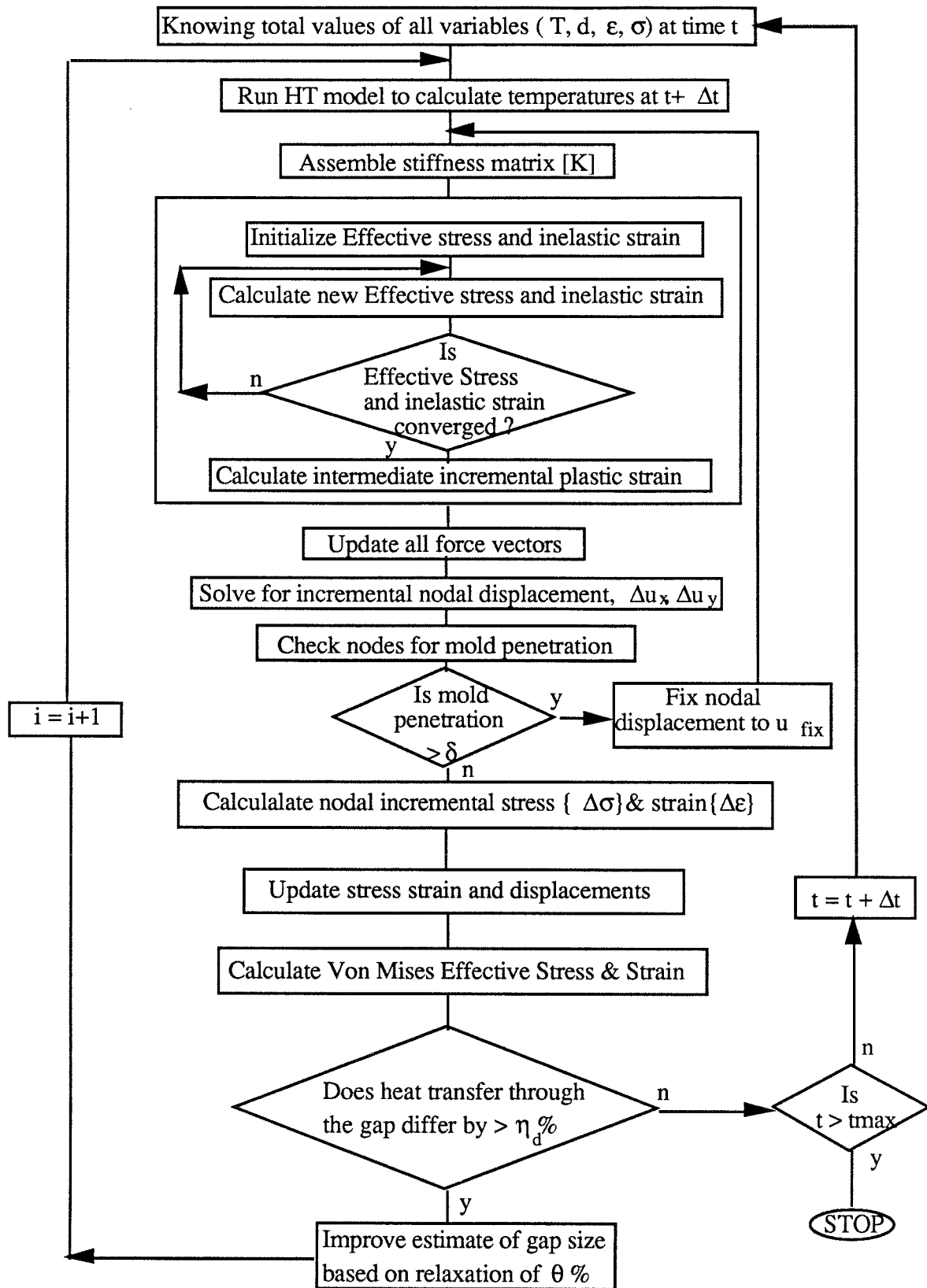


Figure 5.3 Flow chart of the overall simulation procedure for the Implicit method

$$\left| \frac{\sum q''(d^i) - \sum q''(d^t)}{\sum q''(d^i)} \right| \leq \eta_d \quad (5.7)$$

where the summations are carried out on the slab surface nodes along the interface. If this convergence criterion is satisfied, the program continues to the next step. If not the time step is repeated starting with a better guess on the gap size as per Eq. 5.8 :

$$d^{i+1} = \theta d^i + (1-\theta) d^t \quad (5.8)$$

with $\theta = 0.6$ was used for the present calculations.

The thermal calculations were found to be only a small part of the computing time with a coupled run. Table 5.1 lists the number of iterations the program takes during a time step as well as compares the CPU time for the complete simulation through the mold. A complete coupled simulation through the mold takes about 10 hours of CPU time on a Silicon Graphics Personal Iris workstation or about two hours on a CRAY-2 super computer for the explicit method. The computation time for the implicit scheme is almost 5 times smaller than the explicit one.

Table 5.1 List of various convergence criteria and comparison of CPU times.

| Algorithm | Iteration | Convergence/Tolerance |
|-------------------------------|-----------------|---|
| 1. Shell/Mold Contact | 3-5 | $\delta_m = 0.01\text{mm}$ |
| 2. Plasticity | 5-10 | $\eta_\sigma = \eta_\epsilon = 10^{-5}$ |
| 3. Gap Heat Transfer Coupling | 1-2 | $\eta_d = 0.05$ |
| Complete in mold Simulation | Time Step | CPU Time |
| 1. Explicit | 0.025 - 0.1 sec | 20 - 24 hrs |
| 2. Implicit | 0.1 - 0.2 sec | 4.1 - 4.3 hrs |

5.3 REFERENCES

1. X. Huang, B.G. Thomas and F.M. Najjar: "The Removal of Superheat from Continuous Casting Molds", *Metallurgical Transactions B*, 1992, vol. 23 B (June), pp. 339-356.
2. B.G. Thomas, A. Moitra, D.J. Habing and J.A. Azzi: "A Finite Element Model of Thermal Distortion of Continuous Slab Casting Molds", *1St European Conference on Continuous Casting*, Florence, Italy, 1991.
3. B. Ho: *Characterization of Interfacial Heat Transfer in the Continuous Slab Casting Process*, Masters Thesis Thesis, University of Illinois, 1991.
4. A. Mendelson: *Plasticity - Theory and Applications*, R.E. Krieger Publishing, Malabar, FL, 1983, pp. 213-215.
5. O.C. Zienkiewicz and I.C. Corneau: "Visco-Plasticity -Plasticity and the Creep in Elastic Solids - A Unified Numerical Solution Approach", *International Journal of Numerical Methods in Engineering.*, 1974, vol. 8, pp. 821-845.
6. R. Glowinski and P.L. Talle: *Augmented Lagrangian and Operator-Splitting Methods in Non-linear Mechanics*, Vol. 9, Studies in Applied Mathematics, SIAM, Philadelphia, PA, 1989.
7. J. Douglas and H.H. Rachford: "On the numerical solution of the Heat Conduction Problem in second or third space variables.", *Transactions of American Mathematical Society*, 1956, vol. 82, pp. 421-439.

8. A.M. Lush, G. Weber and L. Anand: "An Implicit Time-integration Procedure for A Set of Internal Variable Constitutive Equations for Isotropic Elasto-Viscoplasticity", *International Journal of Plasticity*, 1989, vol. 5, pp. 521-549.
9. G. Forsythe and C. Moler: *Computer Solution of Linear Algebraic Systems*, Prentice Hall, Englewood Cliffs, NJ, 1967.
10. A. Moitra, H. Zhu and B.G. Thomas: *unpublished research*, University of Illinois, Report, 1992.
11. W.R. Storkman: *Optimization of Mold Taper Design Using Mathematical Models of Continuous Steel Slab Casting*, Masters Thesis, University of Illinois, 1990.
12. O.C. Zienkiewicz: *The Finite Element Method*, third ed., McGraw Hill, New York, NY, 1977.

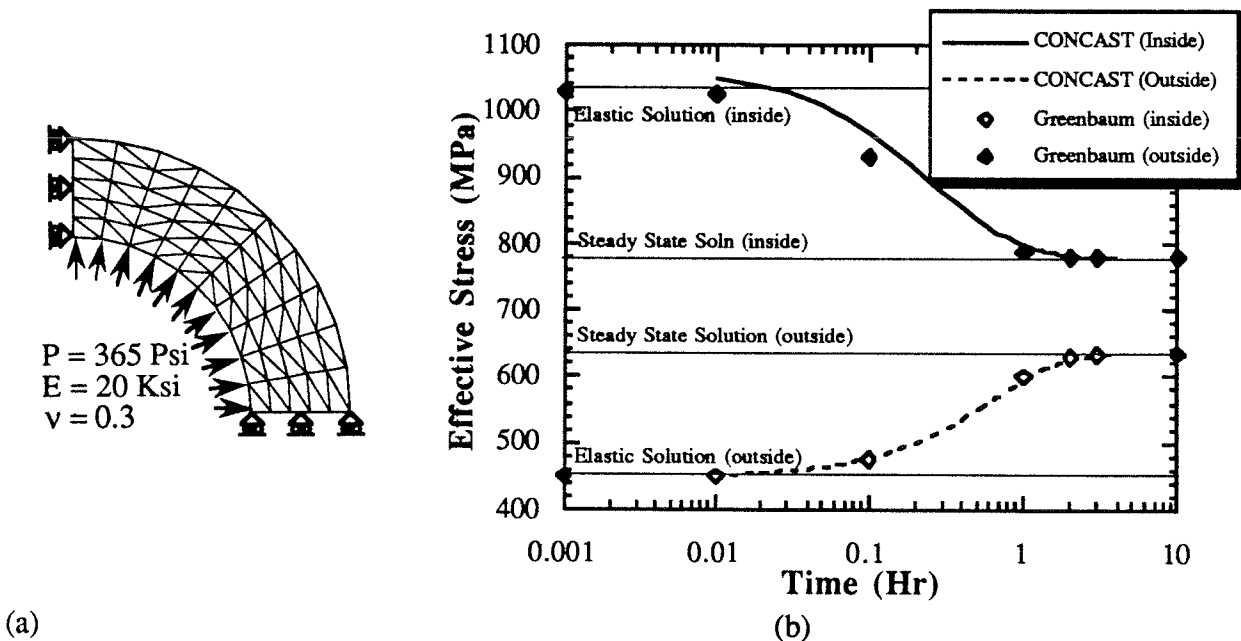
CHAPTER 6

MODEL VERIFICATION

Rigorous verification in several ways is a crucial part of the development of a complex model. The predictions can only be trusted to the extent that the model has been validated. The internal consistency of the stress model has been validated using analytical solutions of several test problems as well as experimental measurements reported in the literature. Four relevant ones are presented here.

6.1 CYLINDER UNDER INTERNAL PRESSURE

The first test problem is a steady-state creep analysis of a thick-walled cylinder under internal pressure used to validate the 2-D elasto-viscoplastic and pressure procedures. Utilizing only two-fold symmetry, a quarter of a 2-D slice through the cylinder was modeled. The finite element mesh of the domain along with the boundary conditions is shown in Figure 6.1a. The domain was discretized with 100 linear strain triangular elements. The stress analysis simulated



(a) Figure 6.1 (a) Finite element mesh and boundary condition for cylinder under internal pressure, (b) Comparison of CONCAST solution of Stress history in the cylinder under internal pressure with that of Greenbaum and Rubinstein [1].

100 hours of creep using the conditions and steady state creep law investigated by Greenbaum & Rubinstein^[1]. The steady state creep law was integrated using the explicit (forward Euler) time integration scheme discussed in chapter 3. The Von Misses effective stress on the inside and outside of the cylinder is plotted as function of time and compared with the Greenbaum & Rubinstein^[1] solution and the steady state analytical solution in Figure 6.1b. It can be seen that the model predictions are in reasonable agreement with the analytical solutions. The 3 % error in the initial elastic solution is likely due to the relatively coarse mesh used, however, the steady state solution had less than 0.1% error.

6.2 TENSILE TEST PROBLEM

The second test problem involved a tensile test under constant strain rate as shown in Figure 6.2. The simulation was carried out using a two 6-node element mesh with a time dependent fixed displacement boundary condition to verify the plasticity algorithm of CONCAST

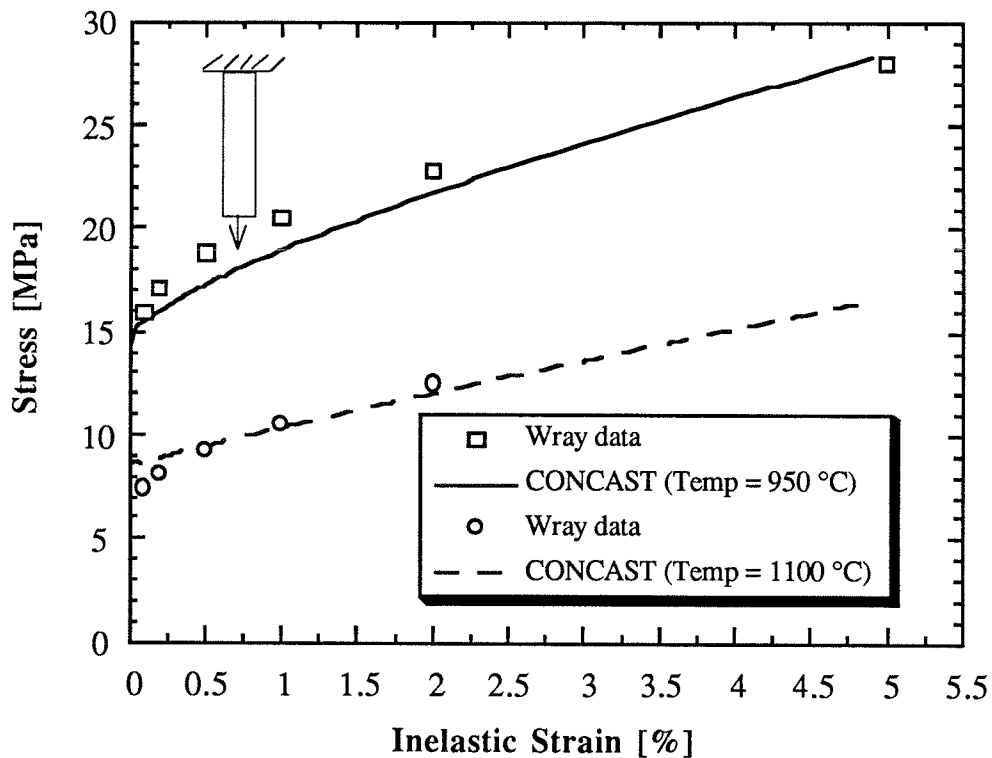


Figure 6.2 Tensile test curves calculated from CONCAST at different temperatures (compared with Wray data ^[2]).

on the constitutive equation of Kozlowski^[3]. Figure 6.3 shows the tensile curves generated at two different strain rates. As compared to the measurements by Wray^[2], the model is able to characterize the mechanical behavior of austenite including strain rate variations. The inaccuracy at strains less than 2% is within 5% and is due to fit of the constitutive equation. The curves match those generated by Kozlowski^[3] through numerical integration. So the part of the algorithm is acceptable. These strains and strain rates are most important to continuous casting.

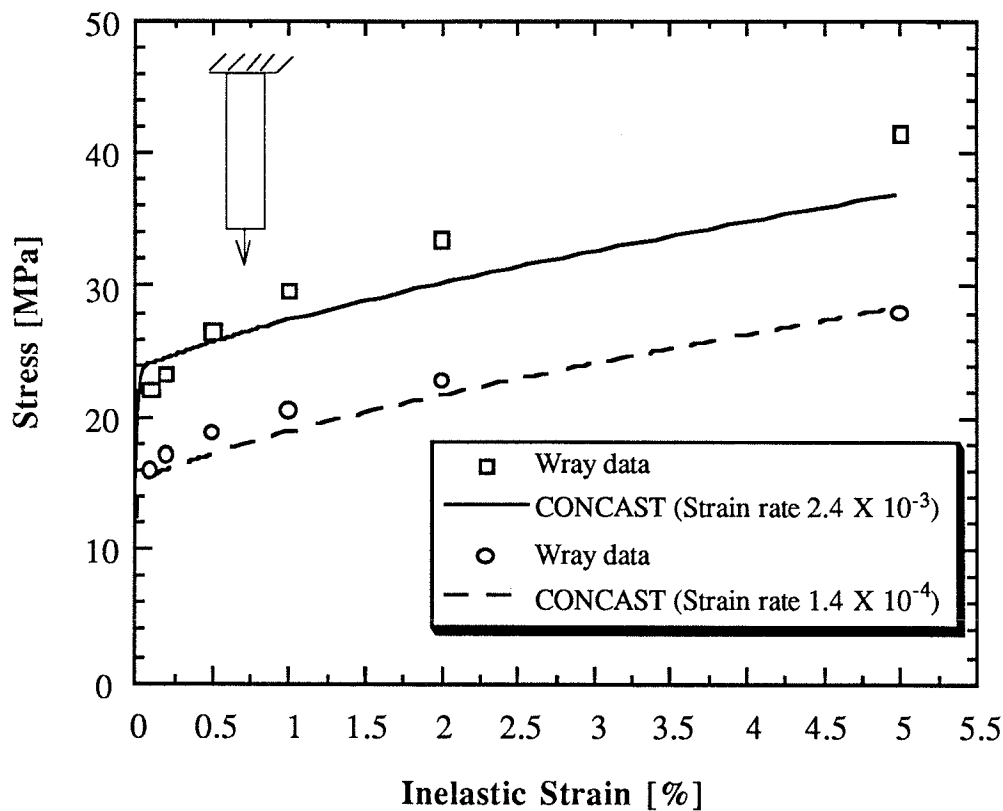


Figure 6.3 Tensile test curves at different strain rates calculated for the constitutive equation used for continuous casting simulation at 950 °C for 0.005%C steel (compared with Wray^[2] tensile data).

6.3 CREEP TEST PROBLEM

The third test problem involved creep deformation of a tensile specimen under constant load. The same two six-node element mesh as in the tensile test was used with a constant surface load boundary condition. The tensile creep test was carried out at 1300 °C with a constant axial

stress of 5.5 MPa and 7.1 MPa. The model calculated total strain increases with time and are shown in Figure 6.4 along with the experimental creep curves measured by Suzuki et al. [4]. The model is seen to produce acceptable behavior at small strains and short times which are of interest to this work. Moreover, the CONCAST simulated tensile and creep curves using fairly large time steps (about 0.1-0.5 sec for tensile and 1.0 sec for creep) are also in good agreement with the solution obtained by Kozlowski et al. [3] using a backward Euler type numerical integration scheme with small time steps (0.001-0.01s). This proves the robustness of the new implicit scheme currently used in the model.

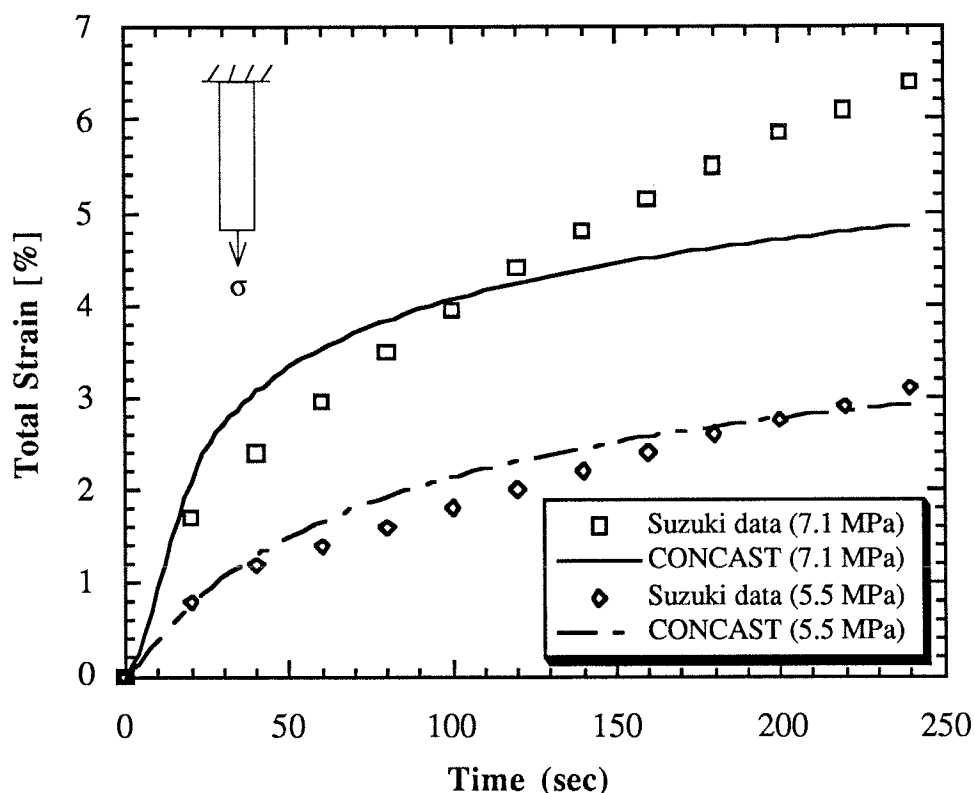
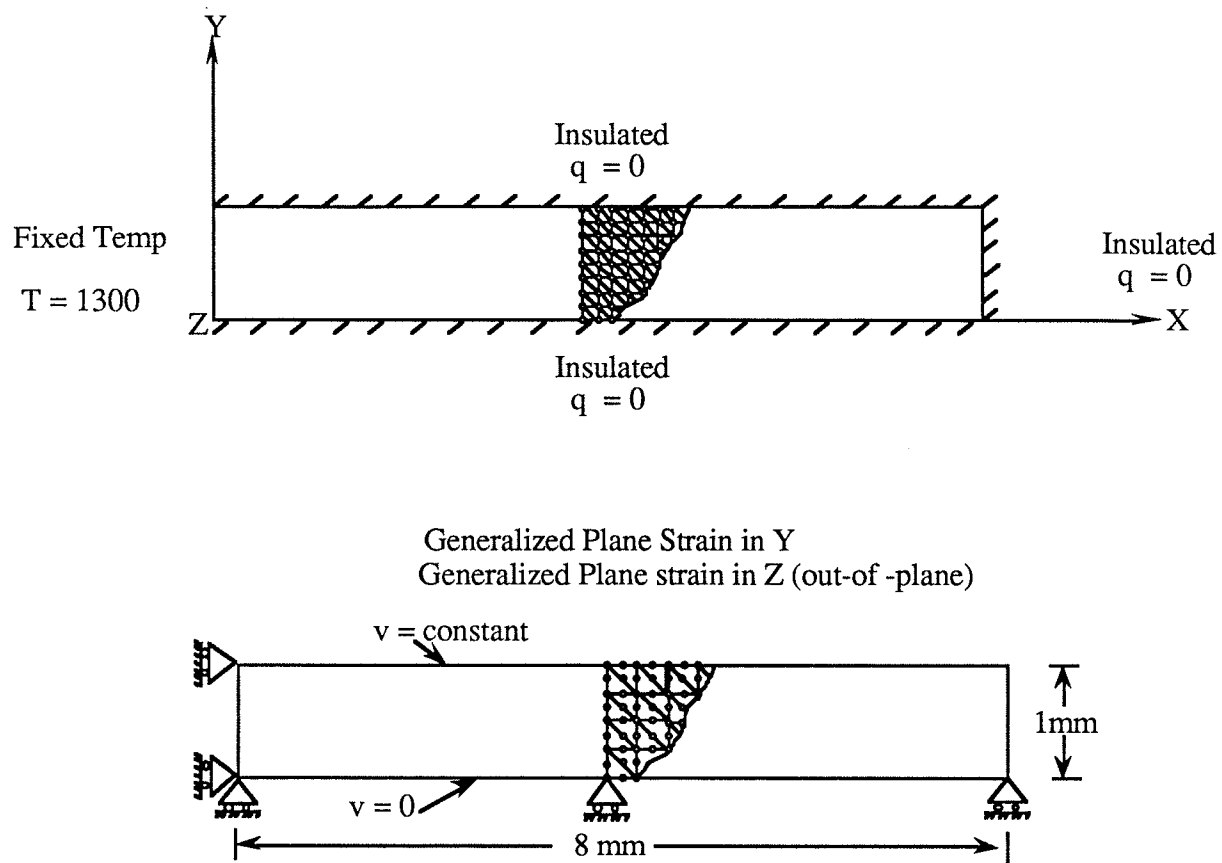


Figure 6.4 Creep test curves calculated with the constitutive equation at 1300 °C and compared with Suzuki et al. [4] data.

6.4 1-D SOLIDIFICATION STRESS PROBLEM

The next test problem models solidification of a 1-D slab. The problem and the associated boundary conditions are given in Figure 6.5 along with its finite element representation. Weiner

and Boley^[5] derived one of the few exact analytical solutions of thermal stresses during the solidification. It assumes a condition of constant generalized plane strain in a semi-infinite elastic



Material Properties used :

| | | |
|------------------------------|---|--|
| $\rho = 7400 \text{ Kg/m}^3$ | $\alpha_T = 20 \times 10^{-6}$ | $T_0 = T_{\text{liq}} = 1525 \text{ }^\circ\text{C}$ |
| $C_p = 700 \text{ J/KgK}$ | $E = 40 \text{ GPa}$ | $T_{\text{sol}} = 1468 \text{ }^\circ\text{C}$ |
| $k = 33 \text{ W/mK}$ | $\nu = 0.35$ | $T_{\text{surf}} = 1300 \text{ }^\circ\text{C}$ |
| $L_f = 272 \text{ KJ/Kg}$ | $\sigma_y = 20 \text{ MPa at } T_{\text{surf}}$ | |
| | $= 0 \text{ MPa at } T_s$ | |

The plastic strain rate $\dot{\epsilon}_p = A \times \left(\frac{\sigma - \sigma_y}{\sigma_y} \right)^n$ $A = 2.86 \times 10^{-3}$, $n = 1.0$

Figure 6.5 Schematic of the heat transfer and mechanical boundary condition of the analytical 1-D solidification problem solved by Weiner and Boley^[5] along the material properties used by Kristiansson^[6] for the same problem.

perfectly-plastic body subjected to a sudden decrease in surface temperature. Figure 6.6 compares the results of this solution with two numerical calculations. The analytical solution of Weiner and Boley^[5] is reproduced using the elasto-viscoplastic algorithm of CONCAST^[7]. The elasto-viscoplastic calculation methods of CONCAST can model a time-independent constitutive law (such as elasto-plastic case), by using a strain rate function (shown in Figure 6.5) that will force the stresses to come back to yield stress level whenever the stresses exceeds the yield stress. This is a particularly rigorous test of CONCAST, due to the numerical challenge required to model a time-independent constitutive equation with an elasto-viscoplastic calculation method. The plane-strain elasto-plastic solutions of Tszeng & Kobayashi^[8] are also compared in this figure. This result is believed to indicate the accuracy expected of the continuous casting

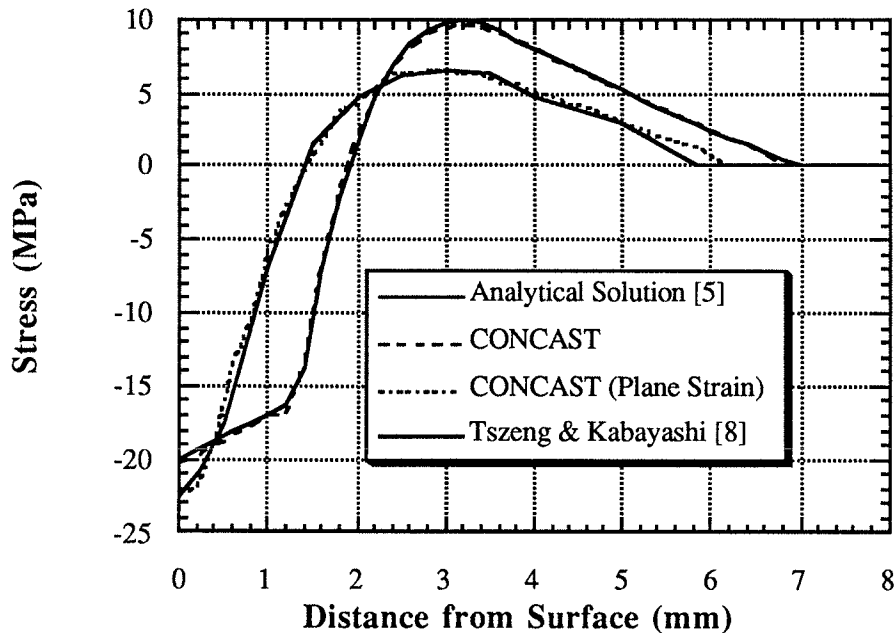


Figure 6.6 Comparison of Numerical and analytical solution for the 1D solidification problem. simulations, which use a similar mesh density in the solid elements, similar convergence parameters and time step sizes.

6.5 BREAKOUT SHELL MEASUREMENTS

Finally, the entire system of models was verified by comparing the model predictions of

shell thickness with measurements from a breakout shell. The first step is verification of the models providing input data to CONCAST, which is explained in Chapter 3 and reported elsewhere^[9-11]. Casting conditions for the simulation are given in Table 6.1. These were chosen to match the actual conditions experienced by several slices through the strand as closely as possible. A 203 mm (8") thick and 914.4 mm (36") wide slab was simulated instead of the 229 x 1016 mm (9" x 40") breakout slab. This should not affect the model predictions because the same percent taper was used as that experienced by the breakout slab and the corner region is about the same importance. Note that the effective taper on the narrow face is much lower than typically employed. This is because the breakout occurred during a widening width change operation, which lowers the taper actually experienced by the slice. Where actual conditions were not recorded, the model parameters are best estimates derived from other operations or trials.

The CON1D program was previously calibrated with this particular mold by matching model predictions of mold temperatures^[9] with thermocouple measurements. Cooling water temperature increase for the current breakout slab conditions was 5.85 and 8.1 °C for the broadface and the narrowface respectively. This compares with 5.1 °C predicted by CON1D, showing that calibration with previous temperatures is still reasonable. The gap heat transfer model parameters in Table 6.1 were chosen by calculated variations in order to match the thermocouple measurements. This produced a prediction of profile of solid and liquid mold powder layers down the center of the wide face. To adapt these results horizontally around the mold perimeter, the CONCAST model simply assumes that any additional interfacial gap calculated due to the shrinkage of the shell away from the mold walls is filled with air, to the extent that the shrinkage gaps exceed the combined powder layer thickness. This assumes that the powder consumption at the meniscus is uniform around the mold perimeter.

To properly compare the model predictions with the breakout slab, the "drainage time" of the liquid metal during the breakout should be taken into account. The sections of the breakout slab should be compared with the simulation slice at a later time, to account for the additional time available for solidification during drainage of the liquid metal through the breakout hole, as

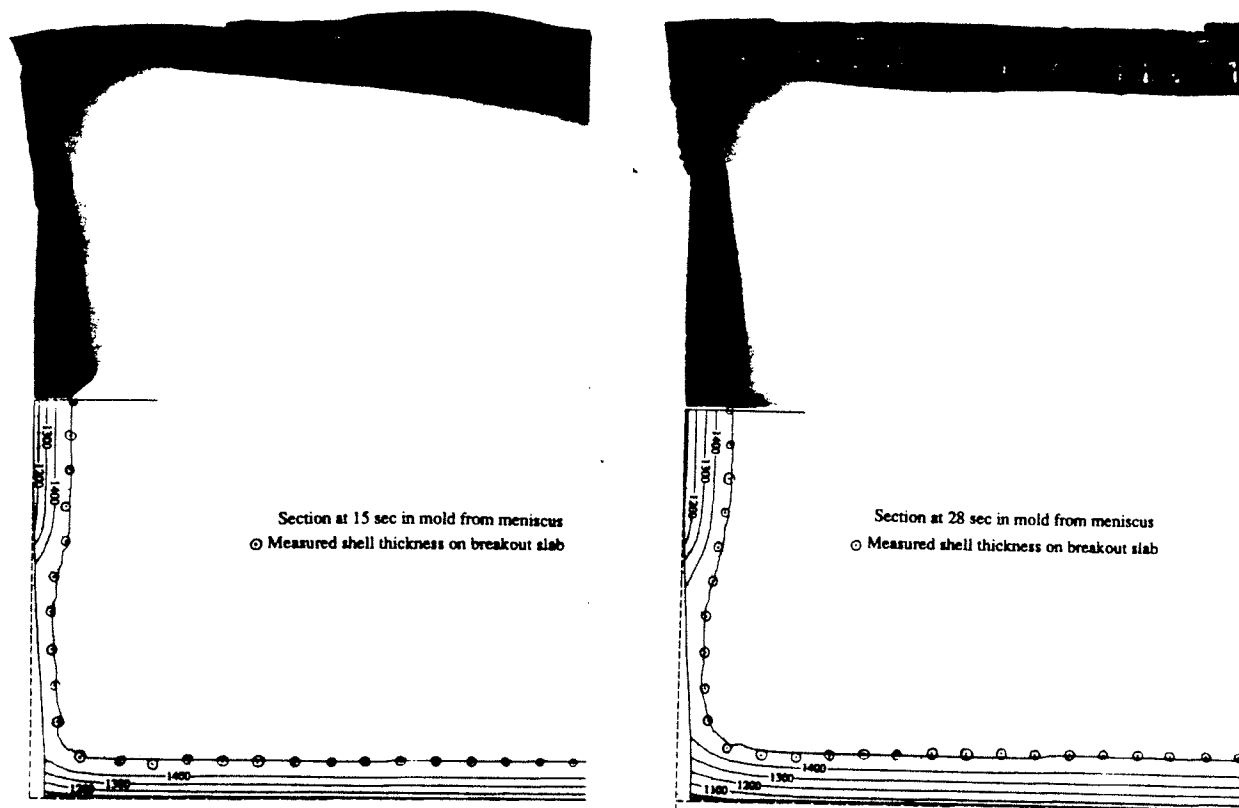


Figure 6.7 Comparison of predicted shell thickness with two transverse sections through a breakout shell.

explained in Appendix G. Simulations were conducted under conditions for two separate slices. The slices were taken at distances below the top of the breakout shell of 225 mm and 431 mm, which corresponds to simulation times of 15 s and 28 s respectively and includes drainage times of 1.5 s and 2.5 s respectively.

Figures 6.7a and 6.7b compare transverse sections through the two breakout shell with the corresponding model predictions for these two slices. The deformed shape (1.0 X magnification) of the strand is superimposed with temperature contours in the same figure. The general shapes of the predicted and observed breakout shells do not match closely, owing to the significant deformation and rolling experienced by the breakout shell during its removal from the casting machine.

Shell thickness was defined in the model as the isotherm corresponding to the coherency

temperature, assumed to be 80% solid (for $\theta=0.8$ as defined by Eq. 3.13). As seen from Figures 6.7a and 6.7b, the predicted shell thicknesses match the thicknesses around the perimeter of the breakout slab section very well. This agreement appears to validate the remaining features of this model, including the non-uniform dissipation of superheat via the superheat flux method and the treatment of the flux layers and air gap in the corner region.

The shell thickness as a function of distance down the mold was plotted in Figure 6.8. Also plotted in the figure are the experimental measurements done on the breakout shell. To compare the model predictions with the breakout shell, the measured distances on the shell were corrected to compensate for the drainage of the liquid steel during break out as per the calculations shown in Appendix F. As seen in Figure 6.8 the model predictions are in fairly good agreement with the measurements near the lower half of the mold, while near the upper region there is considerable disagreement. The relative magnitude of the differences in the measured shell

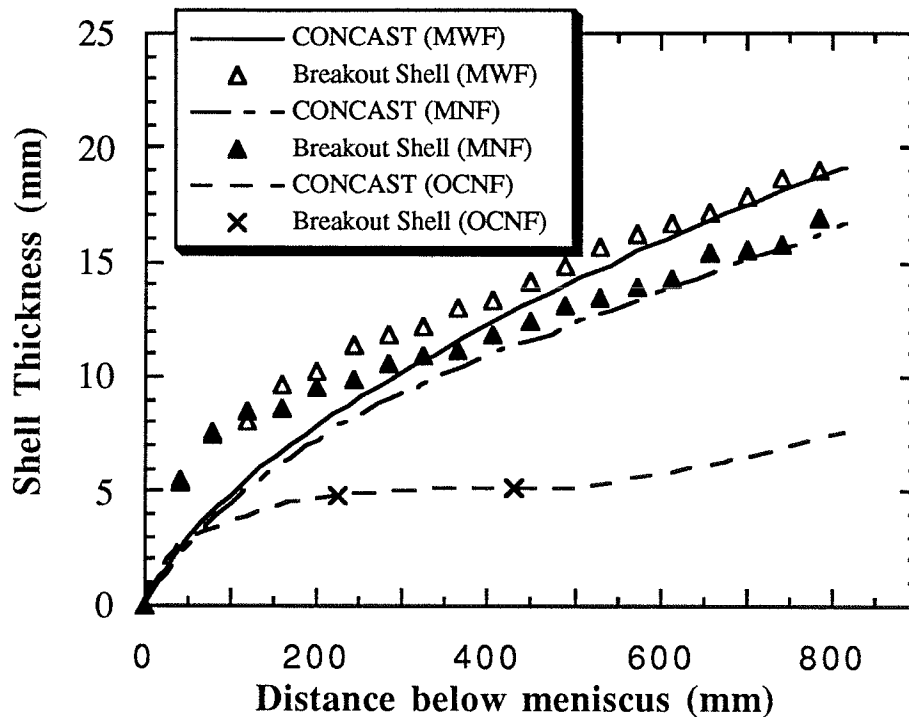


Figure 6.8 Comparison of predicted shell thickness at various locations on the shell as a function of distance below meniscus with the measurements on the Breakout shell.

thickness between the mid-wideface and the mid-narrowface is of the same order as that predicted by the model. The higher shell thickness in the upper part of the shell can be attributed to momentary stoppage of casting at the initial detection of the breakout, and the other errors could be contributed by the assumptions on the size of the breakout hole in drainage time calculations. The exact size of the breakout hole could not be determined as the shell was badly damaged in that location. An estimated holesize of 50 mm was used in these calculations. These results suggest that the model can accurately predict the shell growth inside the mold including the non-uniformities which are believed to be due to non-uniform superheat delivery, as discussed in Chapter 3.

TABLE 6.1 Breakout Simulation Conditions

| | |
|----------------------------------|--|
| Mold Dimensions: | |
| Strand width, W | 914 mm (36") |
| Strand thickness, N | 203 mm (8") |
| Mold Length, L_m | 900 mm |
| Mold Taper | 0.675 %/m (narrow face) 0.122 %/m (wide face) |
| Casting Conditions: | |
| Superheat | 25 °C |
| Casting speed | 16.9 mm/s (40 in/min) |
| Meniscus level | 85 mm below mold top |
| Powder Consumption | 0.4 Kg/m ² |
| Powder Solidus Temp | 1050 °C |
| Powder Conductivity | 0.8 W/m/K |
| Total powder layer thickness | 0.4 mm at meniscus 0.7 mm at mold exit |
| Nozzle Angle | 15 ° down |
| Nozzle Submergence | |
| top surface to top of port | 235 mm (9.25") |
| top surface to top of jet | 272 mm (10.7") |
| Material Properties: | |
| Grade | Low Carbon steel (0.044 %C) |
| Liquidus temperature | 1532 °C |
| Solidus temperature | 1518 °C |
| Solid fraction for T_c, θ | 0.8 |

6.6 REFERENCES

1. G.A. Greenbaum and M.F. Rubinstein: "Creep Analysis of Axisymmetric Bodies Using Finite Elements", *Nuclear Engineering and Design*, 1968, vol. 7 (4), pp. 378-397.
2. P.J. Wray: "Effect of Carbon Content on the Plastic Flow of Plain Carbon Steels at Elevated Temperatures", *Metallurgical Transactions A*, 1982, vol. 13A (1), pp. 125-134.
3. P. Kozlowski, B.G. Thomas, J. Azzi and H. Wang: "Simple Constitutive Equations for Steel at High Temperature", *Metallurgical Transactions A*, 1992, vol. 23A (March), pp. 903-918.
4. T. Suzuki, K.H. Tacke, K. Wunnenberg and K. Schwerdtfeger: "Creep Properties of Steel at Continuous Casting Temperatures", *Ironmaking and Steelmaking*, 1988, vol. 15 (2), pp. 90-100.
5. J.H. Weiner and B.A. Boley: "Elasto-plastic thermal stresses in a solidifying body", *J. Mech. Phys. Solids*, 1963, vol. 11, pp. 145-154.
6. J.O. Kristiansson: "Thermal Stresses in Early Stages of Solidification of Steel", *Journal of Thermal Stresses*, 1982, vol. 5, pp. 315-330.
7. A. Moitra, B.G. Thomas and W.R. Storkman: "Thermo-Mechanical Model of Steel Shell Behavior in the Continuous Casting Mold", *EPD Congress 1992*, TMS/AIME, Warrendale, PA., TMS Annual Meeting, San Diego, CA, March 1-5, 1992.
8. T.C. Tszeng and S. Kobayashi: "Stress Analysis in Solidification Processes: Application to Continuous Casting", *International Journal of Machine Tools Manufacturing*, 1989, vol. 29 (1), pp. 121-140.
9. B. Ho: *Characterization of Interfacial Heat Transfer in the Continuous Slab Casting Process*, Masters Thesis Thesis, University of Illinois, 1991.
10. X. Huang, B.G. Thomas and F.M. Najjar: "The Removal of Superheat from Continuous Casting Molds", *Metallurgical Transactions B*, 1992, vol. 23 B (June), pp. 339-356.

11. D.E. Hershey, B.G. Thomas and F.M. Najjar: "Turbulent Flow through Bifurcated Nozzles", *International Journal for Numerical Methods in Fluids*, 1993, vol. 17, no. 1, pp. 23-48.

CHAPTER 7

APPLICATION OF THE MODEL TO WIDTH CHANGE OPERATION

A major application of the model is to simulate and understand the various casting conditions that can lead to problems and defects. One of the most costly problems is a breakout. Breakouts, particularly for low carbon (%C < 0.08) and high carbon (%C > 0.15) steels (ie. non-peritectic grades) are often associated with sticking of the shell to the mold due to inadequate lubrication or oscillation practice.^[1] However, breakouts may also be caused by inadequate or non-uniform shell growth due to insufficient narrowface taper, poor mold flux distribution, high superheat, a misaligned or blocked nozzle, and high casting speed. The following sections explore the relative effects of these factors contributing to this and other breakouts.

7.1 EFFECT OF NARROWFACE TAPER

Breakouts in slab casting operations are often associated with inadequate heat transfer, such as caused by inadequate mold taper, particularly of the narrowface. When the narrowface taper is small, the strand continues to shrink forming air gaps. This will cause reduced heat transfer to the narrowface, where the shell can become thin, reheat and bulge. One such breakout was used to validate the mathematical model in the previous section.

The gap at the narrowface is determined primarily by the difference between the shrinkage of the wide face shell and the position of the narrowface wall, which depends primarily on the narrowface taper. During steady operation, this “nominal mold taper”, tapr_n , is defined by:

$$\text{tapr}_n = \frac{\Delta W}{W L_m} * 100 \% / \text{m} \quad (7.1)$$

where:

W = mold width

ΔW = difference in mold width at top and bottom of mold

L_m = mold length

One of the practices which greatly affects the narrow face taper experienced by the moving strand, is the automatic width change operation. During a width change operation, the narrow faces are moved inward or outward for casting narrower or wider slabs respectively without stopping operation. Operating practice varies from caster to caster. Although, the width adjustments during the casting process produce a 30-50% increase in productivity and 40-50% savings in energy [2], the practice can lead to breakouts, often near the narrow face [3]. During a widening width change, the narrow faces move outwards, and tend to reduce the contact between the strand and the narrow face mold wall. The actual narrow face taper experienced by an individual slice passing through the mold decreases. This taper may vary for different individual sections through the strand. Moreover, the taper on the narrow face actually experienced by a strand section can change with time, especially if a width change starts or ends while the strand section is moving through the mold. For strand sections cast during the middle of a width change, this “dynamic taper”, tapr_d , can be expressed as:

$$\text{for } t_w < t_s < t_e - \frac{Z}{V_c}$$
$$\text{tapr}_d = \text{tapr}_n - \frac{V_w}{V_c W(t)} * 100 \% / m \quad (7.2)$$

where:

$$W(t) = \text{the current mold width,} = W + V_w(t - t_w)$$

and the other symbols are defined in the nomenclature section. These equations should be expressed in differential form and integrated to account for any gradual changes in V_w , ΔW , W that occur during the width change.

Note that during a widening width change, this equation indicates that the outward movement of the narrow faces will decrease the taper experienced by the slab section unless the nominal taper, tapr_n is increased by increasing ΔW . For example, changing width at a speed of 0.08 mm/s (0.19"/min) will effectively decrease mold taper from 1.6 %/m to 0.675 %/m for a 1016 mm (40") wide slab cast at 16.9 mm/s (40"/min). If the narrow face position is adjusted simultaneously with the width change, large width change speeds (up to 3.3 mm/s) can be

achieved [2]. If allowed by the mold construction, the following relation should be satisfied to achieve this:

$$\Delta W = \text{tapr}_n W L + \frac{V_w W L}{V_c W(t)} \quad (7.3)$$

Narrowing width changes simply imply negative values of V_w in these relations.

The low taper simulation considered in Figures 6.9a & 6.9b could represent either a steady casting condition with low nominal taper or a widening width change with a regular nominal taper. As seen from the Figures 6.9a and 6.9b, the gaps and corresponding thinner shell on the off-corner narrow face indicates that the taper does not match the shrinkage. The shrinkage is governed mainly by the behavior of the wide face shell. Since the shell is in good contact over most of the wide face, it shrinks to form a large gap on the narrow face (3.8 mm at mold exit for conditions in Table 6.1). The thinnest shell arises in the off-corner region, which can become the location for a breakout hole in extreme circumstances, as happened in this case. To avoid this, the narrow face taper should be chosen to match the shrinkage of the wide face shell, in order to prevent formation of gaps in the off-corner region and associated danger of breakouts.

7.2 EFFECT OF MOLD FLUX DISTRIBUTION

The characteristics of the mold flux in the interfacial gap are known to greatly influence the shell growth^[4, 5]. The distribution of mold flux around the perimeter of the shell is one of these characteristics. The simulation conditions discussed above assumed a constant mold powder layer thickness. The flux layer thicknesses are calculated as a function of position down the mold based on the measured mold flux consumption rate and thermal properties using CON1D^[6]. As seen in Figures 6.7a and 6.7b, gaps of the order of 3.8 mm are produced, which are only about 10-15% filled with mold flux (0.4-0.7 mm). This reduces heat transfer across the gap and is mainly responsible for the thinner shell observed in the off-corner region.

If more fluid flux fills the gap instead of air, however, improved heat transfer across the gap should result. To investigate this phenomenon, the mold flux thickness around the corner

region was doubled over the values used in Table 6.1 conditions. The results of this simulation are shown in Figure 7.1 at three locations down the mold. It can be seen from the figure that feeding additional mold powder into the gap improves the heat transfer and increases the minimum shell thickness in the off corner region from 6.6 to 7.6 mm. This compares with 17.6 mm thick shell at the mid narrow face, where there is no gap. This confirms expectations that the influence of powder feeding on heat transfer is an important factor for breakouts, beyond its influence on lubrication. However additional powder feeding cannot overcome the severe gaps produced from insufficient taper.

7.3 EFFECT OF SUPERHEAT

As discussed earlier, the distribution of superheat has an important influence on the growth of the solidified shell. The importance of superheat dissipation is shown in Figure 7.2, through a comparison of the shell growth found with the two different methods for accounting for the superheat flux. In the enhanced conductivity method, the conductivity of the liquid is enhanced isotropically by a factor decreasing from 10 to 1.5 over the mold length and the superheat flux method boundary condition is not applied. This makes the shell grow equally on the wide and narrow faces. On the contrary, when the more accurate superheat flux method is used, the shell grows differently on the two faces. Initially, the enhanced conductivity method predicts a slower growth rate because of the large superheat temperature difference present. Later, when most of the superheat is directed towards the narrow face, the superheat flux method shows that the shell here grows more slowly. This difference in shell thickness on the narrow face and wide face has been reported by other researchers^[7, 8] using coupled finite difference fluid flow and heat transfer models.

The effect of superheat dissipation on the shell growth is shown in Figure 7.3, where the shell thickness at three different locations on the slab is compared for the two different superheats. As can be seen from the figure that with increasing superheat the shell thickness decreases. The

effect is not as pronounced on the wideface as on the narrowface. The wideface is less sensitive to the superheat variation because most of the superheat is directed towards the narrowface. The off-

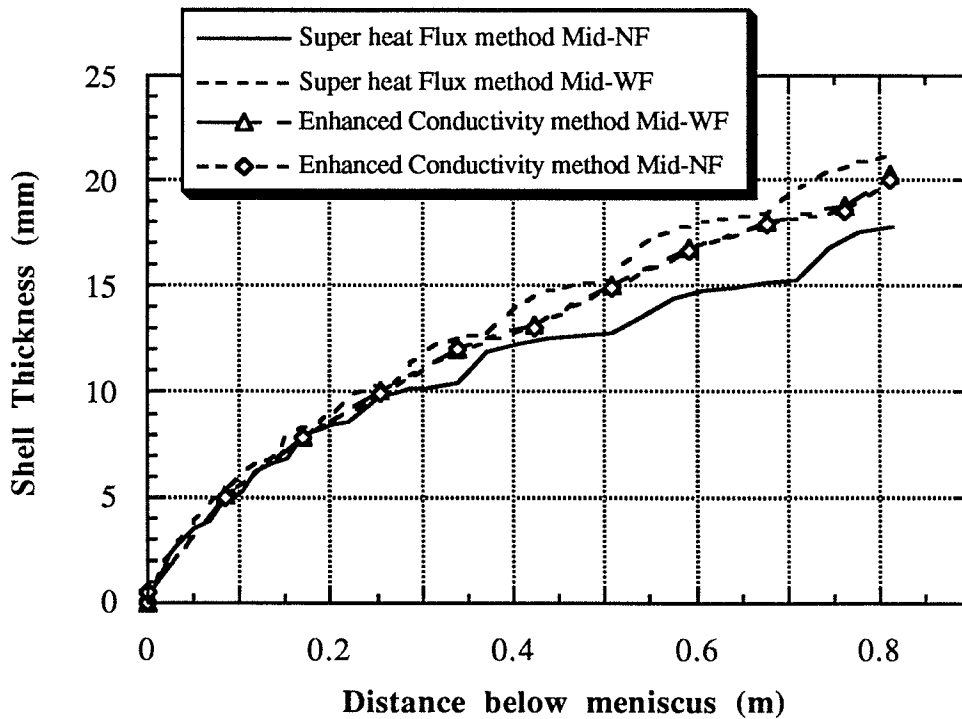


Figure 7.2 Comparison of the shell thickness predicted by two different methods of calculating superheat dissipation (NF = Narrowface, WF = Wideface)

corner region of the narrowface is more sensitive to the variation in superheat than the mid-face. In fact, at high superheat (40°) the off-corner region grows much slower because of an already existing airgap due to low taper ($0.65\%/m$). There is a clear evidence of shell remelting (minimum shell thickness of about 2.2 mm near the impingement point of the incoming jet from the nozzle). It can be pointed out that superheat does not influence the shell growth when there is a good contact between the shell and the mold (e.g. mid-wideface) indicating that the superheat flux alone is not a critical factor causing breakouts. However, if the nozzle is blocked, or if the nozzle is not centered properly between the narrow faces (often observed in multi-strand casters), a preferential flow pattern could develop resulting in higher superheat delivered to one side than the other, making a breakout more likely.

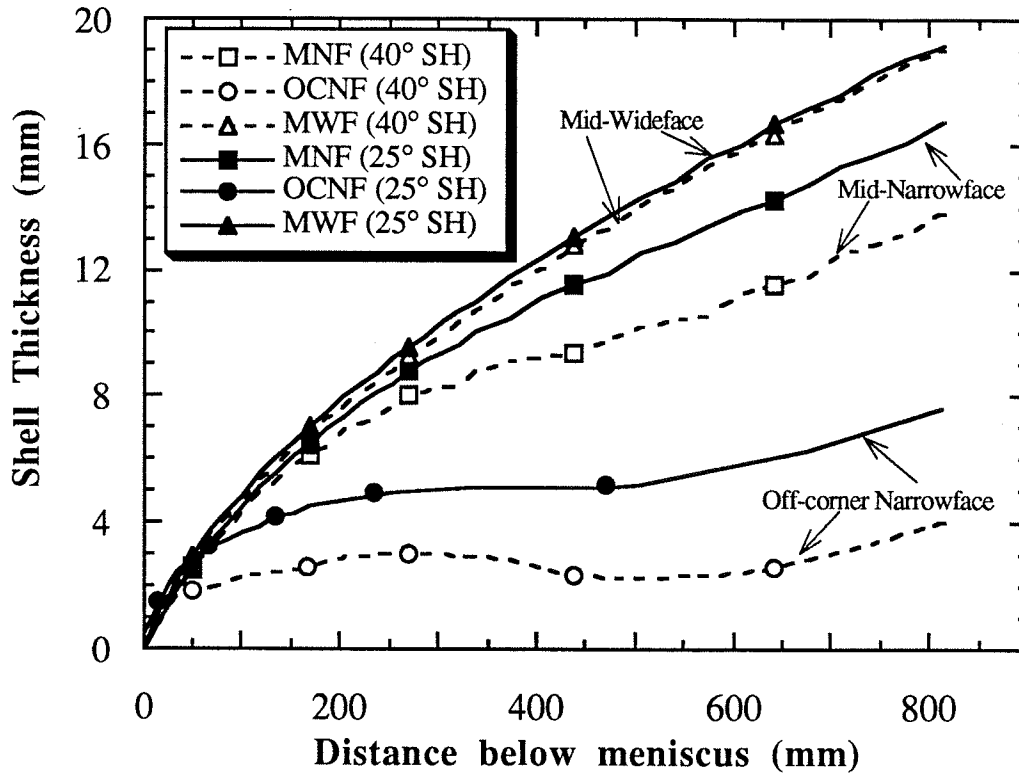


Figure 7.3 Effect of superheat on the growth of the shell at different locations of the slab.

7.4 EFFECT OF NOZZLE MIS-ALIGNMENT

The nozzle is usually aligned to deliver its maximum jet to the center of the narrow face. Although nozzle misalignment is a rare event, an 8° rotation would direct the flow of the liquid metal toward the off-corner region instead of the center of the narrow face. This would deliver more superheat to this naturally thin region, making the danger of a breakout due to shell erosion even higher. The effect of nozzle mis-alignment was investigated to determine if shell growth in this naturally thin region is more sensitive to superheat flux from the impinging jet than at the mid narrow face. To investigate this phenomena, the model was run with the conditions of Table 6.1 but with the superheat fluxes shifted 8° anti-clockwise around the mold perimeter to approximate the boundary conditions expected.

Slices at three different locations down the mold are shown in Figure 7.4. The thinning of the shell is aggravated when the superheat flux in the off corner region is increased due to a misaligned nozzle. Furthermore, these results suggest that a possible remelting of the shell could occur, when the effects of higher heat flux are combined with reduced heat transfer already present in this region due to the interfacial gap. The shell thinning is most severe at around 30 s below the meniscus, which coincides with the location of the peak superheat flux at the impingement point.

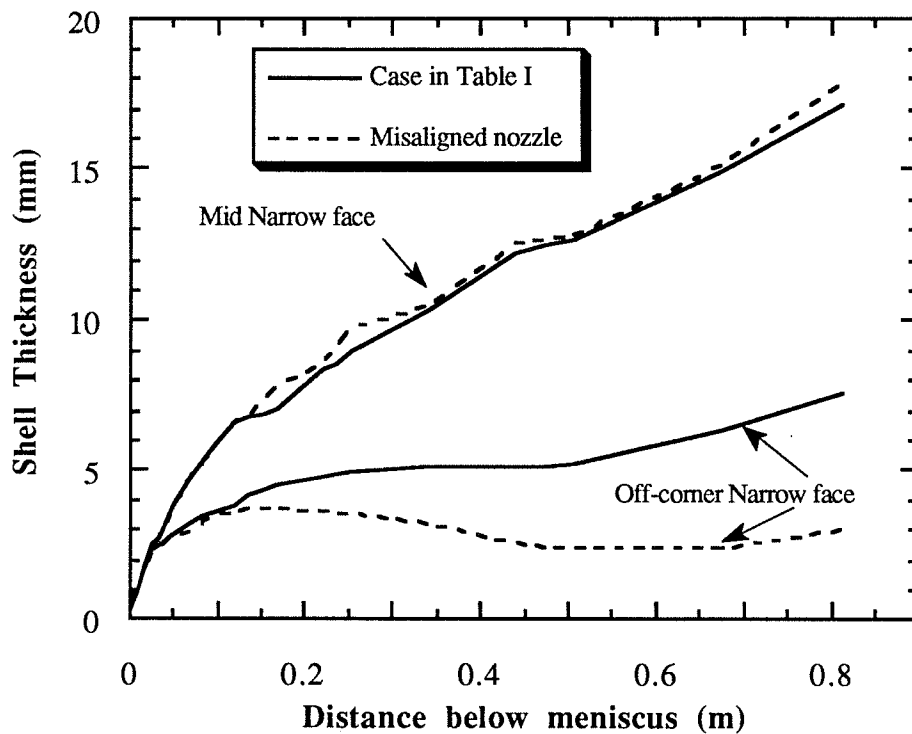


Figure 7.5 Predicted shell thickness as a function of distance below meniscus showing possible shell erosion due to nozzle misalignment.

Figure 7.5 compares the shell profiles down the narrow face at the mid-face and off-corner locations, for the conditions with a centered and a 8° misaligned nozzle jet. The off-corner location is clearly more sensitive to the change in superheat input owing to its smaller rate of heat extraction to the mold. Thus the model results suggest that the combined effects of reduced narrow face taper with higher superheat delivery to the inside of the shell and insufficient flux distribution in the gap could be responsible for off-corner narrow face breakouts such as observed during a widening width change operation.

7.5 EFFECT OF CASTING SPEED

The effect of casting speed on shell growth is shown in Figure 7.6. These results were obtained using the conditions of Table 6.1, with only a change in casting speed. It should be noted that all other parameters including the powder consumption and taper were left the same, even though during actual operation, these might change with casting speed. However, the superheat flux was increased in proportion to the casting speed. Superheat is found to increase linearly with casting speed.[Huang, 1992 #15] As expected, the results show that increasing the casting speed decreases the shell thickness at the center of both the narrowface and wideface. This is because much less heat is extracted from the strand in the mold due to the shorter residence time at higher casting speed.

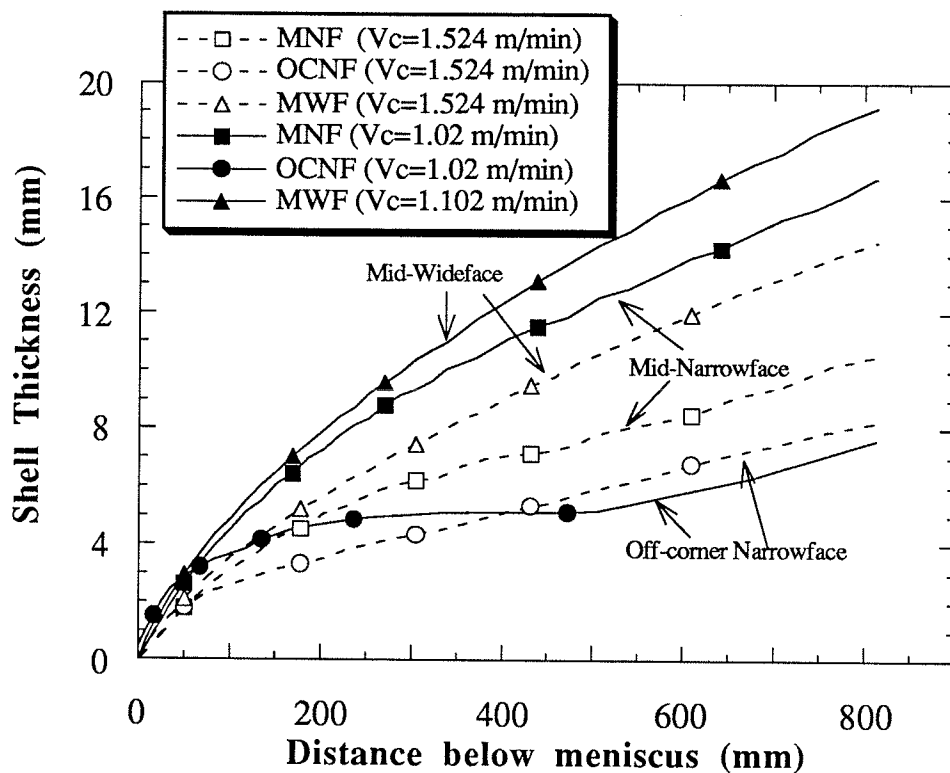


Figure 7.6 Effect of casting speed on the narrowface shell growth.

Figure 7.6 also shows that shell growth at the off-corner region is affected differently by the casting speed, and may even increase slightly at higher casting speed. Initially the shell grows faster at low speed than that high speed because of low residence time. But at the lower region of the mold as the shell sinks less creating smaller gaps, increasing the heat transfer and the shell growth. This result can be understood by examination of Figure 7.7, which shows the calculated shrinkage of the shell away from the narrow face wall at the corner, corresponding to these conditions. At higher casting speed, there is less shrinkage of the shell, so the gap on the narrow face off corner region, including the corner, are smaller. The smaller gap at the off-corner region tends to increase the heat transfer rate in this region. This tends to compensate for the shorter residence time in the mold. The net result is that shell thickness in the critical thin off-corner region is almost the same, as shown in Figure 7.6. This result implies that decreasing casting speed might not help prevent a breakout associated with low narrow face taper. However, increasing casting speed is dangerous also, because it could aggravate other factors, such as the superheat flux.

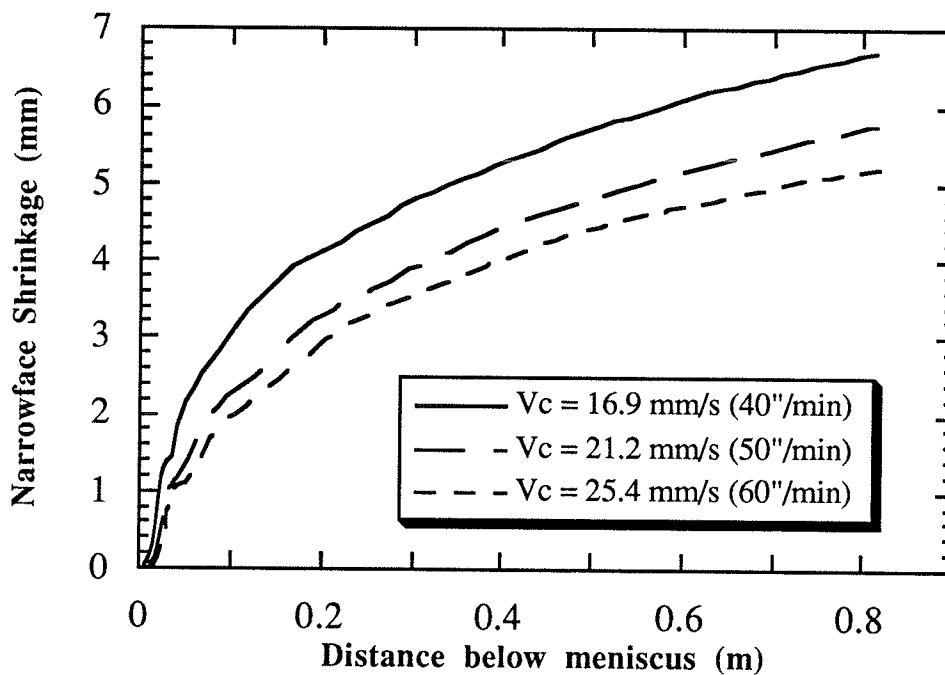


Figure 7.7 Effect of casting speed on the narrowface shell shrinkage.

7.6 CONCLUSIONS

It can be concluded from the above discussions that the combined effect of superheat dissipation, narrowface taper, flux distribution around the shell and the casting speed influence the growth of the shell on the narrowface specially in the off-corner region where large gaps can exist due to insufficient taper. Breakouts during widening width change are mostly caused by the loss of support of the narrow face shell combined with the effects of higher superheat from the impinging jet and insufficient mold flux distribution. These should be preventable by dynamically changing the taper to compensate for the loss due to width change.

7.7 REFERENCES

1. M.M. Wolf: "Mold Oscillation Guidelines", *Mold Operation for Quality and Productivity*, ISS-AIME, Warrendale, PA, 1992, pp. 15-25.
2. H.F. Schrewe: *Continuous Casting of Steel - Fundamental Principles and Practice*, Stahl-Eisem, 1990.
3. W. Emling and G. Lawson: LTV Steel, private communication, 1993.
4. M.M. Wolf: "Investigation into the Relationship between Heat Flux and Shell Growth in Continuous Casting Molds", *Proceedings of the 97th ISIJ Meeting*, ISIJ, Japan, 1979.
5. K.C. Mills: "The Performance of Casting Powders and their Effect on Surface Quality", *Mold Operation for Quality and Productivity*, ISS-AIME, Warrendale, PA, 1992.
6. B. Ho: *Characterization of Interfacial Heat Transfer in the Continuous Slab Casting Process*, Masters Thesis, University of Illinois, 1991.
7. X. Huang, B.G. Thomas and F.M. Najjar: "The Removal of Superheat from Continuous Casting Molds", *Metallurgical Transactions B*, 1992, vol. 23 B (June), pp. 339-356.
8. P.J. Flint, Q.L. He, R.B. Mahapatra and J. Herbertson: "Heat Transfer, Fluid flow and Solidification Modelling of the Continuous Casting Mould", *Process Technology Conference Proceedings*, ISS-AIME, Warrendale, PA, Toronto, Canada, 1992, Vol. 10, pp. 279-291.

CHAPTER 8

OPTIMIZING MOLD TAPER

It has been shown in previous chapters that the heat transfer through the interfacial gap is dependent on the size and constituent of the gap. The extent of this gap depends among other things, on the position of the mold walls and is determined by the mold distortion and mold taper. Mold taper is one of the few important casting variables that is readily controllable and adjustable. It has an important influence on the early stages of solidification in the mold, and the ultimate quality of the continuously cast steel. The long, weak, unsupported shell solidifying against the wide face is generally held against the copper mold by ferrostatic pressure, so is not very affected by the taper. To compensate for shrinkage of the wide face, the mold walls on the narrow face are usually given a linear taper. Figure 8.1 shows that major source of shrinkage is thermal strain due to contraction of the wide face from the initial solidification temperature of about 1500 °C to a mold exit surface temperature of about 1000 °C. For a typical low carbon steel, this requires an average linear taper down the mold of:

$$\% \text{ taper} = \frac{\Delta W}{W} = \alpha \Delta T = (0.002 \text{ \%}/^{\circ}\text{C}) * (1500 - 1000 \text{ }^{\circ}\text{C}) = \underline{1\%} \quad (8.1)$$

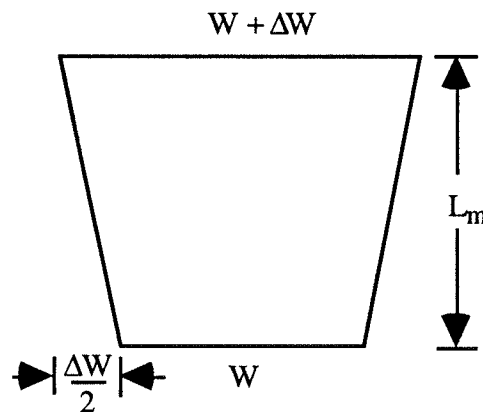


Figure 8.1 Taper calculation on the narrowface.

It should be noted that taper is also commonly reported on the basis of "per unit length down the mold":

$$\% \text{ taper / m} = \frac{\Delta W}{L_m W} \quad (8.2)$$

In this example, this produces a taper of 1.25%/m for a typical effective mold length (distance from meniscus to mold exit) of 0.8m, so it is important to distinguish between these two different methods for measuring mold taper. Tapers here are reported on a "per unit length" basis using Eq. (8.2).

The calculation of Eq. 8.1 assumed a continuous, linear shrinkage of the shell. However, previous work has determined that more shrinkage occurs near the top of the mold.^[1-4] Thus, billet casting machines often employ a multiple taper.^[3] Most slab molds usually use a simple linear taper. Some recent work in slab molds suggests that more taper near the top would be beneficial for slab mold narrow faces also. [5, 6]

Inadequate taper can give rise to many different quality problems. These arise from two causes: excessive gap formation, where the shell shrinks away from the mold due to insufficient taper, and mechanical forces compressing the shell, where the taper exceeds the shrinkage. Both of these conditions may lead to quality problems. The problem of too little taper leads to decreased heat flow, high surface temperatures, and consequently a thin shell. This in turn can lead to bulging both in and below the mold, with the generation of longitudinal cracks in fragile steel grades and surface shape problems such as longitudinal depressions, or "gutters" down the off-corner region of the wide face surface. Too much taper also produces many problems such as: 1) excessive mold wear, which may also cause star cracks by rubbing copper from the mold into the surface of the steel shell, 2) deformation and distortion of the shell, and 3) high friction and binding of the shell in the mold, which can produce transverse cracks or even breakouts.

In this chapter the mathematical model described in chapter 3 will be applied to explore the influence of mold taper on temperature and shrinkage. The goal is to find taper designs for the narrow face that more closely match the natural shrinkage of the shell, in order to improve heat transfer, reduce mold wear, and avoid defects caused by deformation and stress of the shell.

The shrinkage of the slab in the corner region is mainly governed by contraction of the wideface. The heat transfer of the wideface is mostly one dimensional where the slab is in good contact with the mold and the slab surface temperature is uniform over most of the wideface except near the corner, where the heat transfer is two-dimensional. It is, therefore, expected that shrinkage of the corner region will be closely governed by the drop in the slab surface temperature along the mid-wideface which can be modeled using a simpler 1-D calculation using a generalized version of Eq. 8.1. To verify this hypothesis comparisons of slab shrinkage based on 1-D thermal analysis are necessary with the shrinkage calculated from a full 2-D analysis of the slab.

8.1 1-D MODEL(S)

A simple 1-D model representing the slab section at the center of the wideface was developed as shown in Figure 8.2. The boundary conditions used are also shown in the figure. The heat transfer boundary is similar to the continuous casting simulation with gap heat transfer conditions on the wideface with the rest of the boundary being insulated. For the stress boundary symmetry conditions were applied at the symmetry plane and generalized plane strain conditions were applied in the x and z direction as shown in Figure 8.2. The heat transfer simulation is

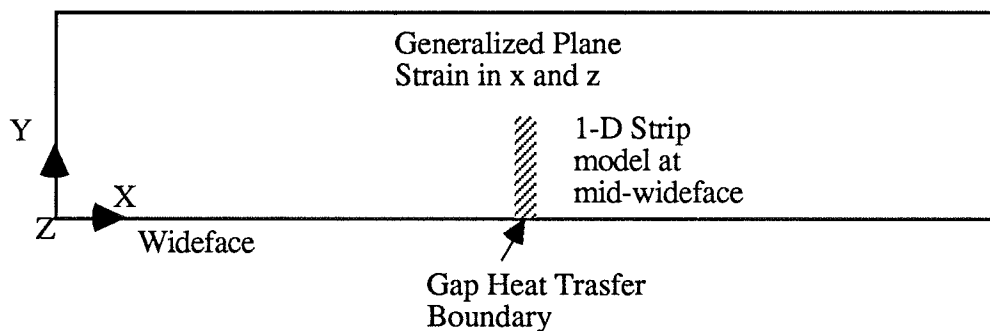


Figure 8.2 Schematic of the 1-D model and boundary conditions.

equivalent to running the CON1D model and can produce identical temperature results.

Figure 8.3 compares the various strain components of the surface node for the 1-D analysis. As seen in the figure, the thermal strains are the major part of the total strain. The plastic strains are very small compared to the thermal strain as seen in Figure 8.3. The plastic strains are higher during the initial stages of solidification. The first layer of steel solidifies in tension producing unreasonably large plastic strains at high temperature as evident from Figure 8.4. As the solidification proceeds in the subsequent layer of elements, the surface stress relaxes and the surface goes into compression while the interior goes into tension. The source of the tensile peaks and their implications will be discussed in chapter 10.

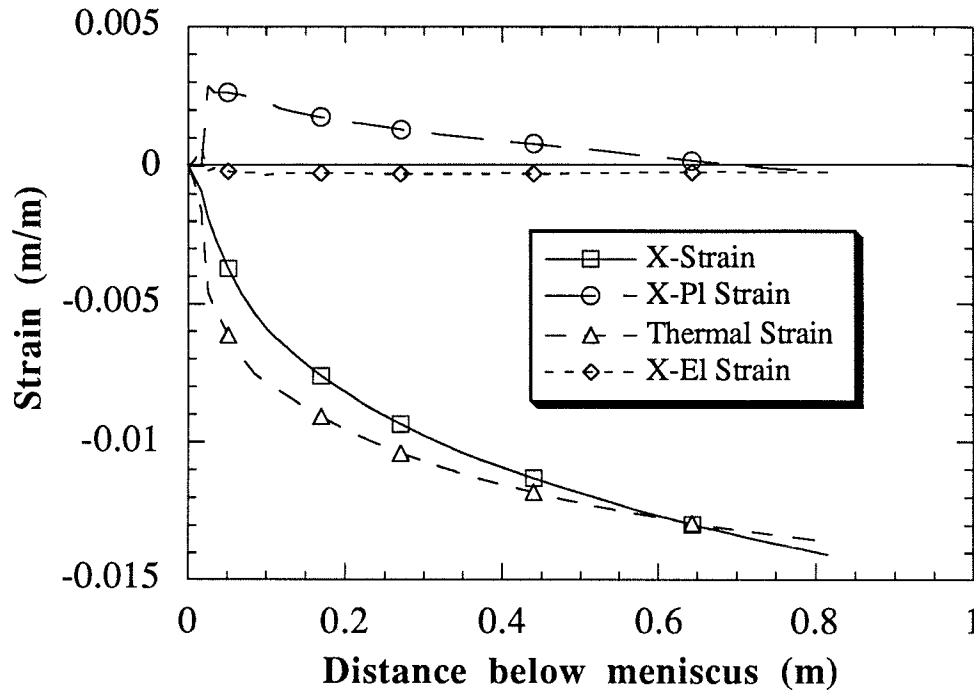


Figure 8.3 History of various strain components of the surface node for 1-D model.

The shrinkage at the corner can be predicted using the temperature of the surface node based on the Eq.8.3 using the 1-D heat transfer model, CON1D :

$$\Delta W = [TLE(T_{sol}) - TLE(T_s)] W \quad (8.3)$$

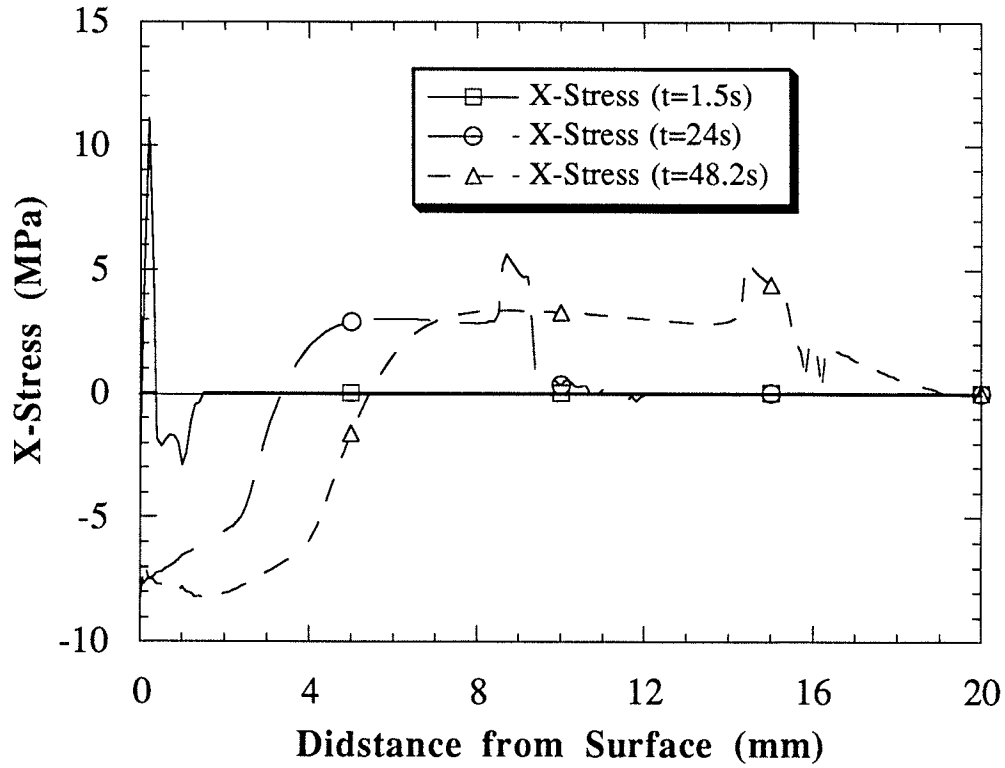


Figure 8.4 Stress through the shell at different times

The displacements at the corners can be approximated by converting the total x-strain of the surface node of the 1-D finite element model shown in Figure 8.2 as

$$\Delta W = \epsilon_x \cdot W \quad (8.4)$$

The thermal strains from the 1-D finite element model can also be converted similar to Eq. 8.4 to get the shrinkage of the corner of the slab, i.e.

$$\Delta W = \epsilon_T \cdot W \quad (8.5)$$

Eqs. 8.4 and 8.5 are true when the shell is in good contact with the wideface mold and the surface temperatures are uniform over the entire wideface and the inelastic strains are negligible. It will be interesting to see which of the above equations could be used to represent the ideal shrinkage of the shell, by comparing the shrinkage results of the 2-D model with that obtained by Eqs. 8.3-8.5. This is done in section 8.2.

8.1.1 MESH REFINEMENT

It was observed that the stress results are very sensitive to the mesh size in the solid portion of the domain. To obtain an acceptable mesh the 1-D model with different mesh densities was studied. Three different meshes were used for the entire 30mm of the simulation domain.

Mesh A : 903 nodes, 300 6-node elements (element length 0.2 mm uniform)

Mesh B : 93 nodes, 30 6-node elements (element length 2.0 mm uniform)

Mesh C : 75 nodes, 24 6-node elements (element length varied from 1.4 to 2.4 mm)

It was found that the results with mesh C were better than that with mesh B, so the comparisons were made between mesh A (fine) and mesh C (coarse) only. Mesh C was chosen because it has exactly the same number of nodes through the shell thickness as the 2-D mesh with the same element length.

Figure 8.7 compares the total strain history predicted by the fine and the coarse mesh. As

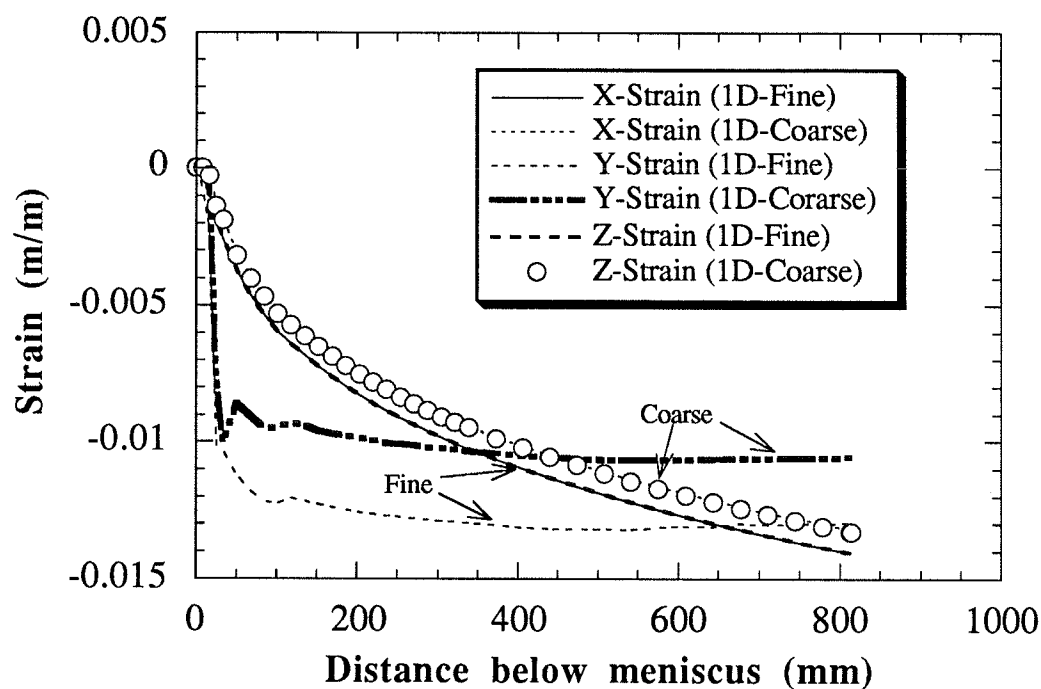


Figure 8.5 Comparison of strains for 1-D fine and coarse mesh.

expected the coarse mesh underpredicts the strains compared to the finer mesh by about 7.0 %. Therefore, one would expect that using a similar mesh in 2-D as that of the coarse mesh in 1-D, would introduce error of the order of 7% in the displacement calculation. This is again acceptable in lieu of the tremendous computational cost associated with further mesh refinement in 2-D. The evolution of stress distribution through the shell for the two meshes are shown in Figure 8.6. It can be seen that the fine mesh produces a smoother stress distribution than the coarse mesh. Moreover, the stress peaks associated with the δ - γ phase transformation are captured only with the fine mesh. The region of this phase transformation varied from about 0.7 mm in the beginning to about 1.6 mm near the end. This suggests that to capture the effects of the phase transformation the length of the element should be between 0.35 mm to 0.8 mm. Note that the coarse mesh has element sizes varying from 1.4 mm to 2.4 mm. It should also be noted that heat transfer analysis does not need any further mesh refinement, as the coarse and fine meshes produce temperatures that differ by only 2.5 % at the beginning to about 0.1% at the end of simulation.

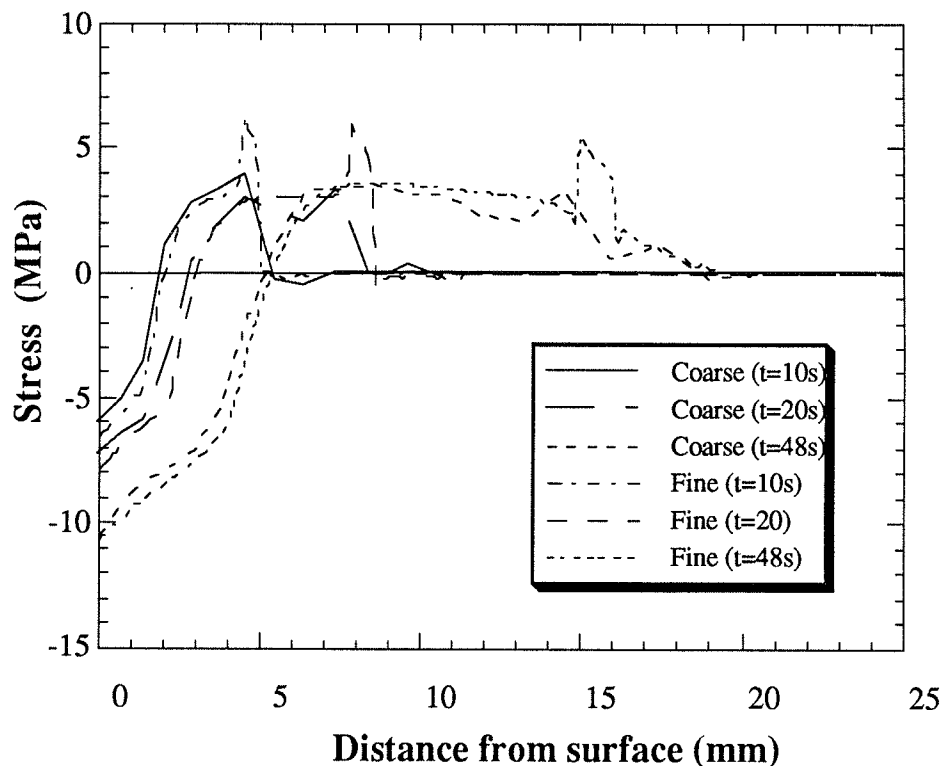


Figure 8.6 Comparison of stress evolution in the shell between coarse and fine mesh.

Finally the shrinkage predicted by Eqs. 8.3-8.5 are plotted in Figure 8.7. As seen in the figure, using Eq. 8.4 both coarse mesh and the fine mesh underpredicts the thermal shrinkage based on Eq. 8.3. For the coarse mesh, there is an initial delay in generating any shrinkage because the solidification time for the first layer of element of the coarse mesh is longer than the fine mesh. Shrinkage calculation based on Eq. 8.5 also reflects similar differences. However, when using Eq. 8.3 to calculate the narrowface shrinkage the difference between the coarse mesh and the fine mesh results are at minimal and the results are close to the finemesh results using Eq. 8.5. These results suggest the need for a very fine mesh for accurate calculation of shrinkage. However 2D coarse meshes such as the one presented in this work, are expected to produce results with in 5-10 % accuracy which are acceptable for these calculations. Comparison of the best shrinkage predictions by Eq. 8.3-8.5 with shrinkage based on 2-D simulation will be done in the next section.

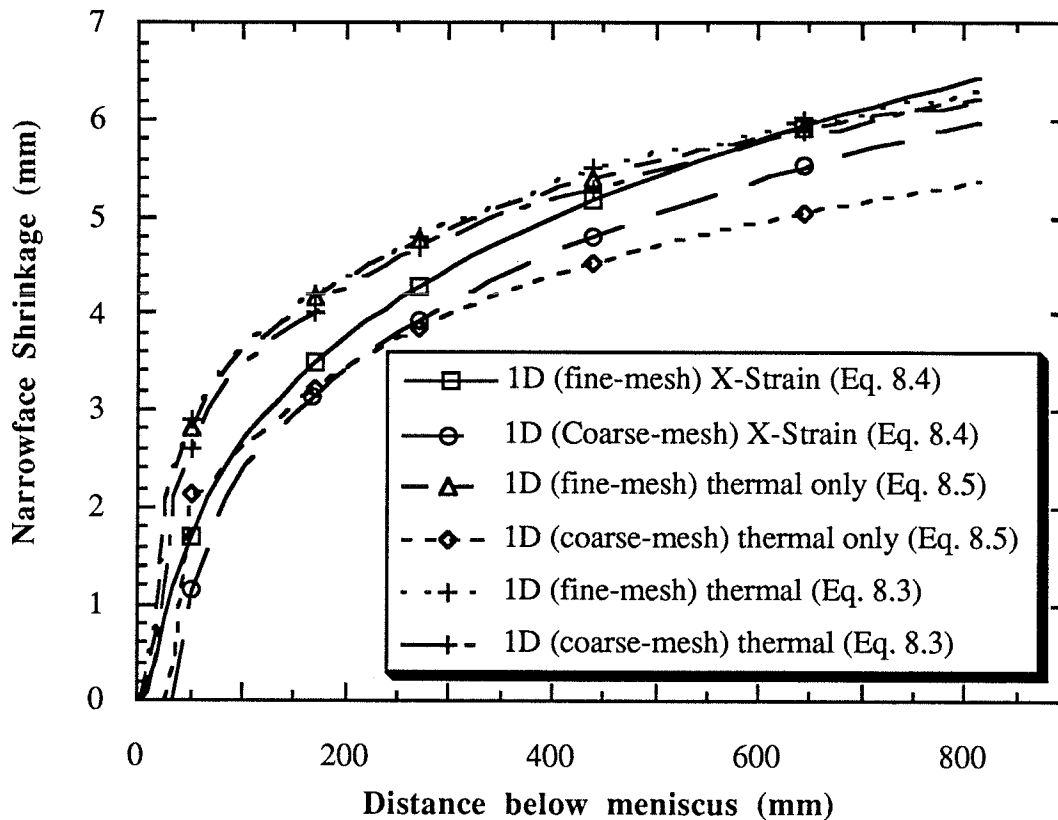


Figure 8.7 Comparison of narrowface shrinkage predicted by Eqs. 8.3-8.5 for different meshes.

8.2 2-D MODEL

The shrinkage based on the thermal strain of the surface node("thermal only") can be compared to the actual displacement of the corner obtained from the 2-D elasto-viscoplastic model, which takes ferrostatic pressure and creep-plasticity into account (CONCAST 2D-Corner). Based on the surface temperature history, Eq. 8.3 can predict the shrinkage profile as a function of position in the mold. Figure 8.8 compares the shrinkage based on Eq. 8.3 with the natural shrinkage of the slab corner predicted by the 2-D model. It is surprising to see that the simple 1-D calculations can produce such accurate results . The figure shows that the shrinkage calculated using Eq. 8.3 slightly over-predicts the natural shrinkage of the shell (freely shrinking without

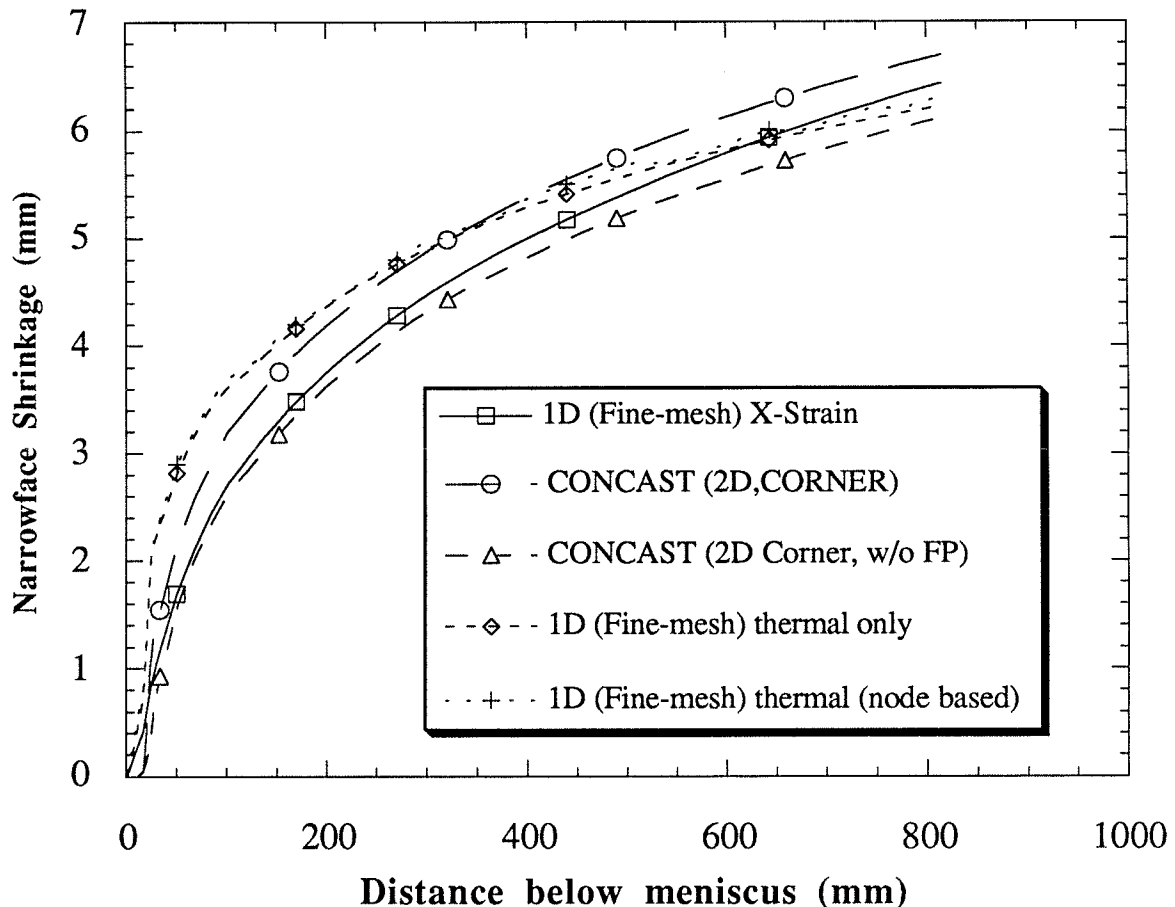


Figure 8.8 Comparison of shell shrinkage predicted by 1-D and 2-D models.

any imposed taper) in the upper part of the mold and under-predicts in the lower part. Eq. 8.4 also underpredicts the shrinkage of the corner region as seen from Figure 8.8. This is due to relatively larger plastic strains generated in the upper part of the mold compared to the lower part as shown in Figure 8.3.

Figure 8.8 also shows the effect of ferrostatic pressure on the shrinkage. As the shell is held in good contact over the most part of the wideface mold by the ferrostatic pressure, gaps are minimal and very good heat transfer persists. As a result the wideface shell shrinks about 0.65 mm more compared to the case without ferrostatic pressure. The 1-D model cannot reproduce this effect. The 1-D calculations also assume a uniform surface temperature along the wideface. Because of the two-dimensional heat transfer in the corner region the temperature along the wideface is not uniform as shown in Figure 8.9. The corner is the coldest region while the off-corner is the hotter compared to the center of the wideface because of little gaps formed in the off-corner region. The differences in the 1-D and 2-D shrinkage calculations (which is about 10-15%) can be attributed to this surface temperature variation for the 2-D analysis.

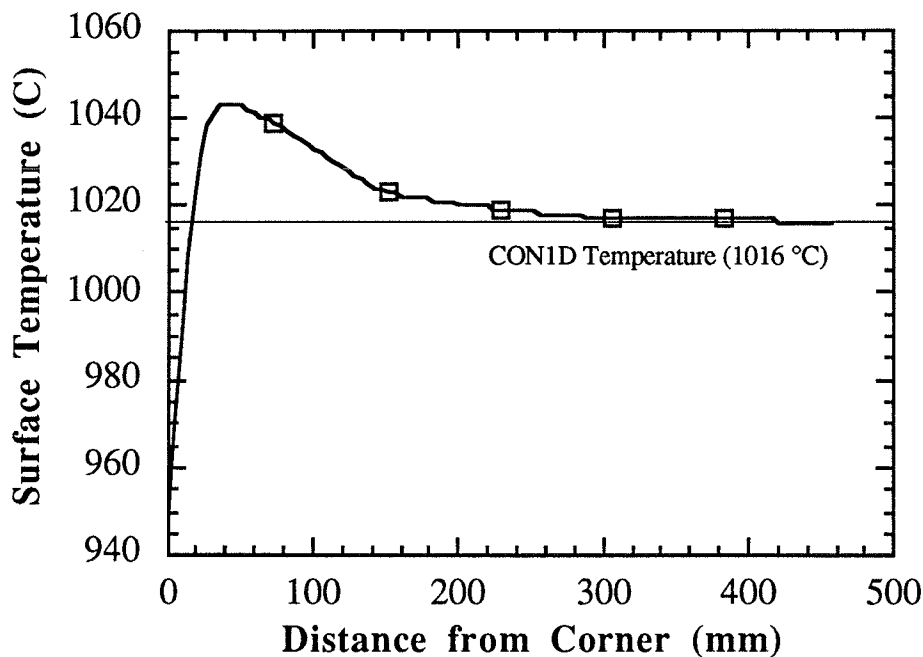


Figure 8.9 Temperature distribution along the surface of the wideface

It should however, be noted that the shrinkage calculation based on surface nodal temperature (Eq. 8.3) almost matches the shrinkage based on thermal strains from the 1-D finite element model. The small differences are due to the fact that for the finite element model, thermal strains are generated as the elements solidify, and as such there is an initial delay for the first layer of elements to solidify and generate thermal strains. These differences tend to increase when the mesh becomes coarse. To match the predictions of the 1-D calculations, considerable mesh refinement is necessary; and for 2-D analysis, such refinements can tremendously increase the computational cost. The 1-D model results presented in Figure 8.3 used a very fine mesh (element length of 0.1 mm), while the 2-D model used a relatively coarse mesh (mesh length varied from 0.7mm to 1.2 mm). A mesh refinement study was carried out to justify the use of the mesh density for most of the 2-D simulations carried out in this study.

8.3 RESULTS AND DISCUSSION

Several full 2-D model simulations were performed on a 203 x 914 mm slab with a working mold length of 815 mm. Standard operating conditions assumed a casting speed of 1.016 m/min (40.0 inches/min) and a superheat of 25 °C. Material properties for a plain carbon (0.044 %C)^[7] and stainless steel were assumed.

8.3.1 EFFECT OF NARROWFACE TAPER

Figure 8.10 compares the shrinkage of the corner region of the slab for different narrowface taper. As seen in the figure, the shrinkage of the shell in the corner does not depend on the imposed taper on the narrowface side. This is due to the fact that the shrinkage in the corner is mainly governed by the overall shrinkage of the wideface which is in good contact with the mold and should not be affected by the imposed taper on the narrowface. Shrinkage, however, depends on casting variables such as casting speed and slab size and should be taken into account while setting the taper for the mold.

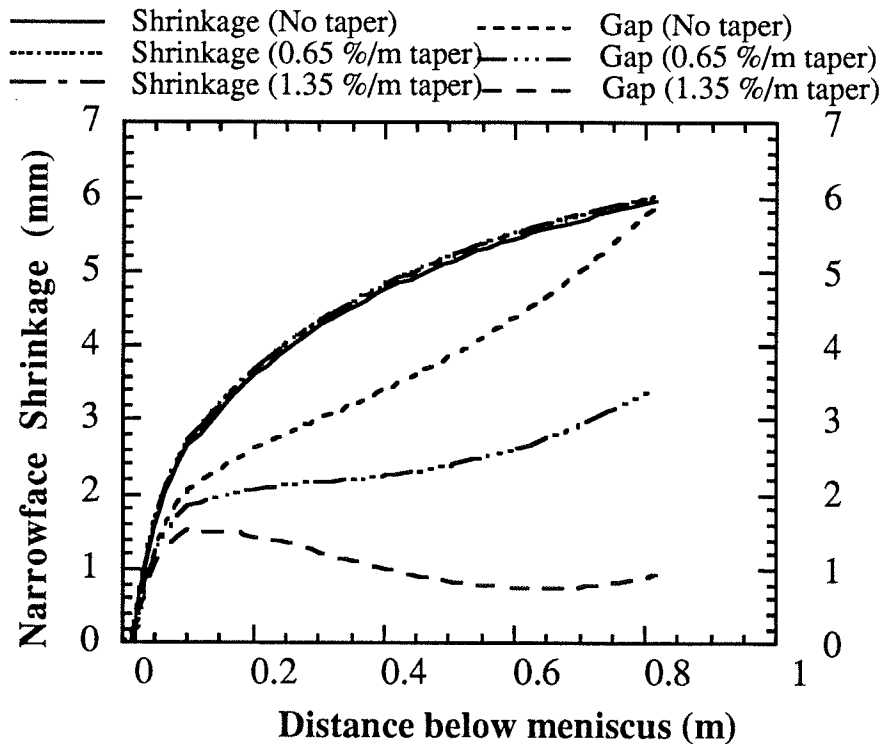


Figure 8.10 Effect of narrowface taper on the shrinkage and gap formation.

The figure also shows the behavior of the gaps formed in the corner region of the narrowface as a function of distance below meniscus for various imposed narrowface tapers. The rate of gap formation is initially very high, due to large shrinkage during the initial solidification. Near the lower region, the mold tends to bow out due to thermal distortion, creating an increase in gap size towards the bottom of the mold. As the taper increases, the gaps tend to decrease, which improves the heat transfer in this region. The effect is shown in Figure 8.11, where the deformed shape of the slab is superimposed with temperature contours at mold exit for the three different tapers.

Just below the meniscus, steel solidifies against the mold to form a continuous shell and starts to shrink away from the mold walls. This first occurs near the corner, where an air gap forms. Two dimensional heat flow keeps the corner cold, thick, and rigid. However, the gap reduces heat flow in the off-corner region of narrowface, resulting in a hotter, thinner shell there.

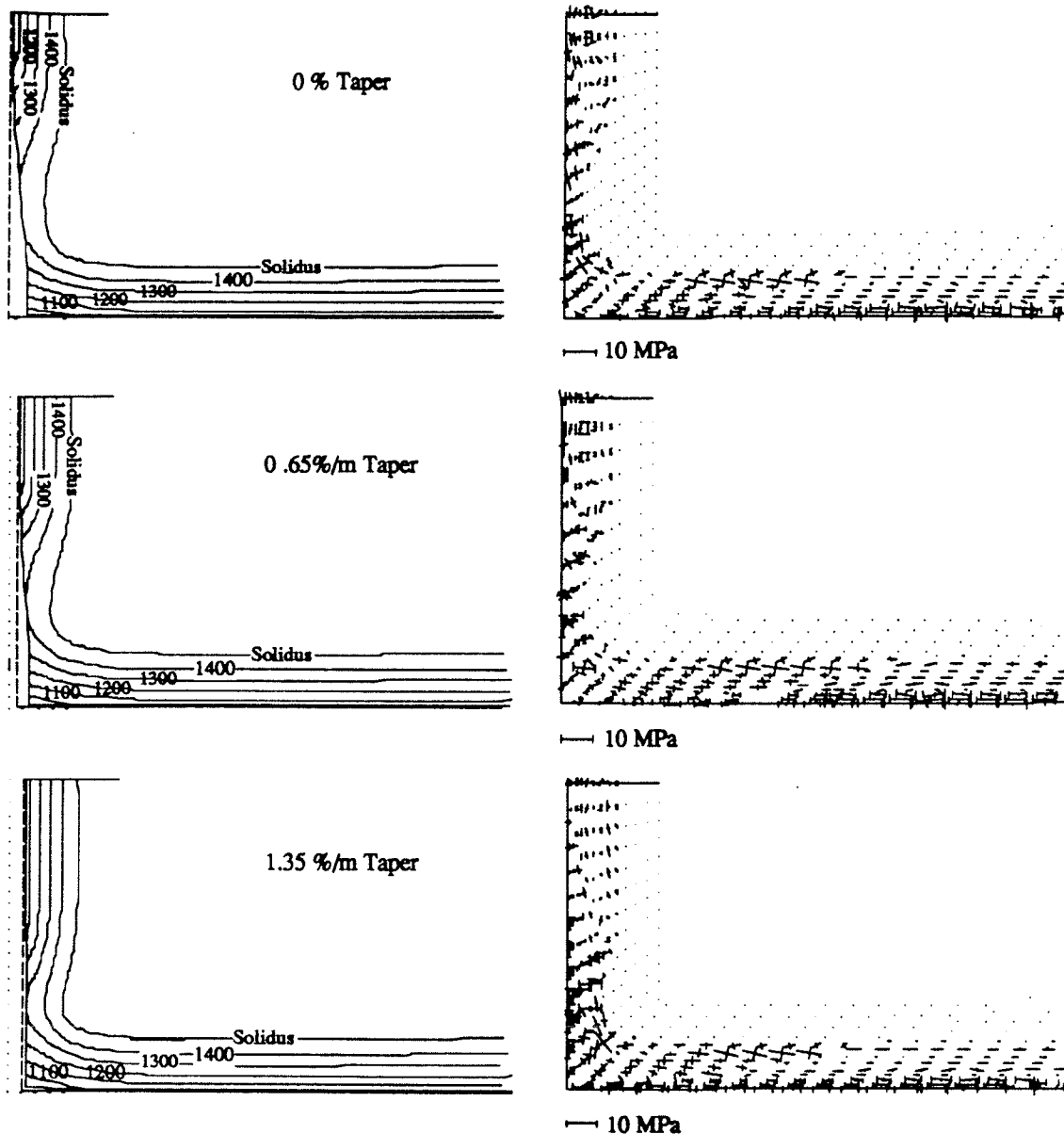


Figure 8.11 Effect of Narrowface taper on Shell growth at mold exit.

With very little narrow-face taper, shrinkage of the wide face produces a large gap on the narrow face, as shown in Figure 8.10. The entire narrow face remains hot and thin, particularly in the off-corner region (see Figure 8.11). Ferrostatic pressure makes the narrow face shell bulge outward toward the mold wall. As the wide face cools and shrinks, the gap near the corner along the narrow face increases, maintaining high temperatures in the region. This hot spot is only observed when taper is relatively small. It is apparent from Figure 8.10 that almost from the beginning, the

large taper(1.35 %/m) on the narrowface of the mold compensates for the shrinkage of the wideface and maintains the narrowface of the slab in good contact with the mold. Due to the disappearance of the air gap at high taper, the heat flow to the mold is uniform resulting in a more uniform shell at exit than with lower taper as seen from Figure 8.11. An increase in the taper beyond this would cause the ΔW in Eq. 8.1 exceed the shrinkage of the shell and the shell will be squeezed by the end plates.

The importance of superheat, mold flux and casting speed on the formation of breakouts have already been discussed in the previous chapter. Results presented here further strengthen the implications of narrowface taper on the formation of breakouts. It has been observed that the surface temperature of the slab near the hot spot reaches as high as 1350 °C or above. The low strength of the thin shell, can give rise to the collapse of the air gap as the ferrostatic pressure pushes the shell against the wideface. As proposed by Grill et al.^[8], this possible collapse of the gap can generate enough tensile strain to rupture the shell near the hot spot. If the rupture occurs in the upper part of the mold, it can give rise to "bleeding" of small amount of liquid which can freeze between the shell and the mold producing a surface defect. However, if the rupture occurs in the lower part of the mold it causes a breakout.

Because of the complex nature of the gap formation and the shrinkage of the shell and their dependence on the casting variables such as casting speed, slab width, super heat etc., it is difficult to postulate an optimum taper condition for a wide range of casting practices. As such each case must be considered separately. However, the model can be used to get the optimized taper conditions that will prevent breakout for a given casting conditions.

These results show evidence for a potential mechanism of defect initiation in the off-corner region. Consistent with the findings of previous chapter, increasing the taper improves heat transfer in the off-corner region making a more uniform shell, thereby decreasing the chances of off-corner breakouts. However, increasing the taper beyond a critical value (8mm/m), sometimes increases the occurrence of transverse corner cracks (below deep oscillation marks), in slabs due to

effects of excessive contact pressure and friction on the weak shell as reported by Takemoto et al.^[9] In contrast, Okamura and Yamamoto^[10] suggested that by increasing the taper up to 2.2%/m for a thin slab (120 mm) caster, the tensile stress peaks were reduced, implying the prevention of possible corner cracks. It has already been shown (Chapter 7) that too little taper, such as during widening width change can produce breakouts. Therefore, it is necessary to operate the caster with an optimized taper that is consistent with the casting condition.

8.3.2. EFFECT OF CASTING SPEED

Before implementing an optimized taper design into service, it is important to consider the range of operating conditions the mold taper must accommodate. Thus, the effect of increasing casting speed on the natural shrinkage of the shell was investigated. Figure 8.10 shows the narrowface mold wall profile needed to exactly match the shrinkage of the wideface for various

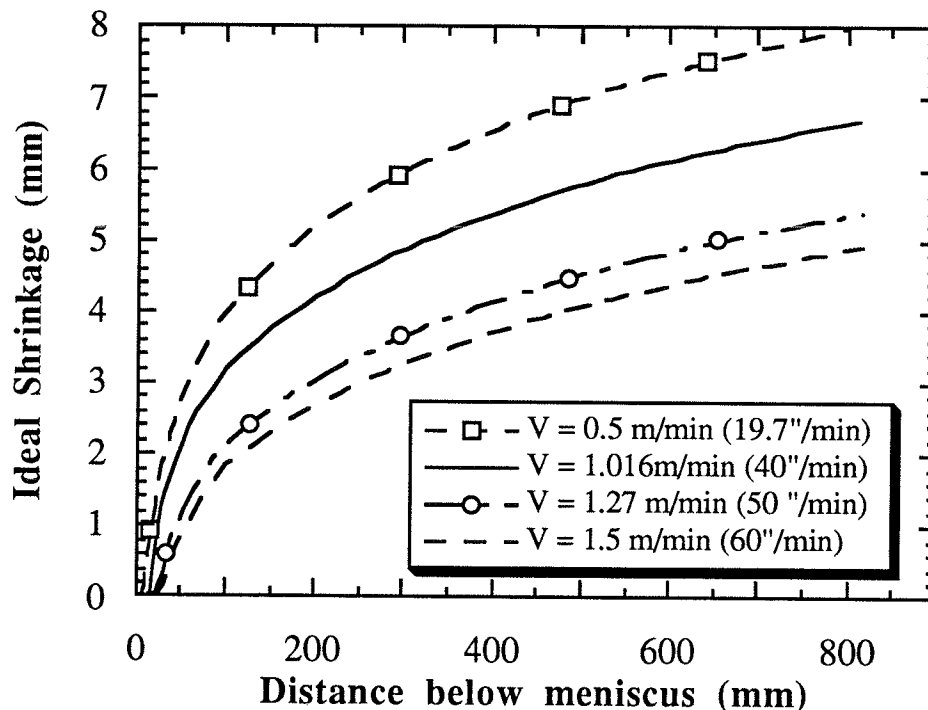


Figure 8.12 Effect of Casting Speed on the ideal shrinkage of the corner of the slab.

casting speeds. These results were obtained using the full 2-D model, by matching the mold wall position to the center of the narrowface. This allowed the narrowface to shrink as it pleased (after first solidifying against the resisting wall) with heat transfer behaving as if a fortuitous continuously-varying taper had been employed along the narrowface. This figure shows that less shrinkage is found at higher casting speeds. This is expected because, increasing the casting speed increases shell surface temperature on the wideface since the shell has less time to cool. The higher temperature results in less shrinkage of the wideface, implying a closer distance between the shell and the narrowface mold wall for a given taper. In addition, it shows that the shrinkage is more uniform down the mold, so a linear taper should produce less problems at higher speeds. Shrinkage is most non-linear at low casting speed, such as encountered during a ladle change. Thus, a single taper design cannot match shrinkage under all casting conditions.

8.3.3. EFFECT OF MOLD DISTORTION

In Chapter 4 we have seen that the thermal distortion of the mold could be significant and must be considered. During operation, the narrowface bends inward toward the steel a significant distance, due to the expanding copper surface constrained by a cold copper layer and water box beneath it. The largest distortion of the mold near the middle region can partially compensate for the large shrinkage in the upper part of the mold. Thus, thermal distortion of mold may actually be beneficial in many cases and should be taken into account when designing taper. From the previous section it is seen that a linear taper is not sufficient to compensate for the non-linear shrinkage in the mold. Other factors such as the build-up of solidified mold flux against the mold walls, can also contribute to altering the effective taper.

Figure 8.12 compares the natural shrinkage of low carbon and stainless steel for the standard conditions. Also plotted in the figure is the thermal distortion of the narrowface mold. The distortion of the mold superimposed with various imposed linear tapers is compared with the shrinkage of the two different steels. As seen from Figure 8.12, the shrinkage of the low carbon

steel is much more than the stainless steel, due to the δ - γ phase transformation in the former. The shrinkage of stainless steel is less non-linear and a simple linear taper of 1.0 %/m should be sufficient to compensate for the shrinkage when combined with mold distortion. For low carbon steel, however, a linear taper even up to 1.9 %/m does not exactly prevent gap formation for that steel. Moreover, this taper becomes excessive near the lower part of the mold. Thus, for low carbon steel it is difficult to compensate for the shrinkage through a simple linear taper. Most plants operate with a 1.3 %/m - 1.7 %/m^[11] which appears to be insufficient. Thus mold distortion could be beneficial for some grades of steel while it is not as much useful for other grades. Nevertheless, the taper calculations should always be carried out taking into account the mold distortion.

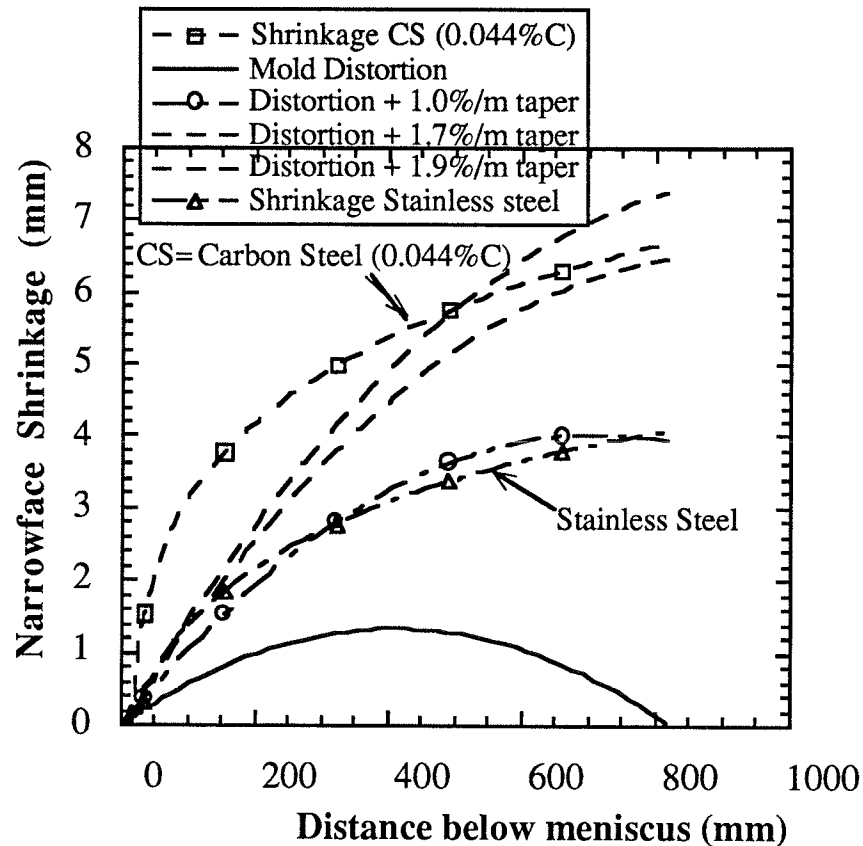


Figure 8.13 Comparison of natural shrinkage of the shell with different applied taper for a casting speed of 1.02 m/min.

8.3.4 EFFECT ON MOLD WEAR

Wear of the slab mold arises as a result of the physical abrasion of the mold wall by the solid shell and is dependent on the normal force which presses the shell against the mold wall. Intuitively, wear should therefore occur wherever the gap between the mold and the shell closes to zero. The variation of the gap at various location in the mold (similar to Figure 8.8) for various taper conditions can give further insight into the possible locations of mold wear. However, the present mechanical model ignores the effects of the frictional forces acting on the slab, and as such the model can be used for making qualitative predictions about mold wear. Among the cases presented in Figure 8.9, closure of the narrowface gaps is predicted in the lower part of the mold at high taper (greater than 1.35 %/m).

8.4 TAPER DIAGRAM

It has been established that simple 1-D heat transfer calculations can generate reasonable results that can be used by the caster operator as a first guess for the new mold taper design. It has been seen that the shrinkage of the shell is very non-linear, especially during the initial stages of solidification and depends on various factors such as casting speed, width, superheat etc.. It is therefore a difficult task to optimize the taper for a wide range of casting conditions. However, the results of the 1-D analysis can be carefully evaluated to get a reasonable estimate of the taper necessary for the particular casting conditions. Since the majority (more than 90%) of the shrinkage of the corner is contributed by thermal strain only, an accurate 1-D heat transfer calculation should be able to provide necessary guide lines for selecting taper for the narrow faces. To do so, a taper diagram similar to the one used by Alberny^[12] was developed using the results of the 1-D calculations. Surface temperature calculations and a graphical version of Eq. 8.3 is shown in Figure 8.14. This diagram does not take into account the mold distortion, and necessary corrections will be needed to compensate for the distortion. The diagram includes the temperature history of the surface node of the slab and the thermal linear expansion function of

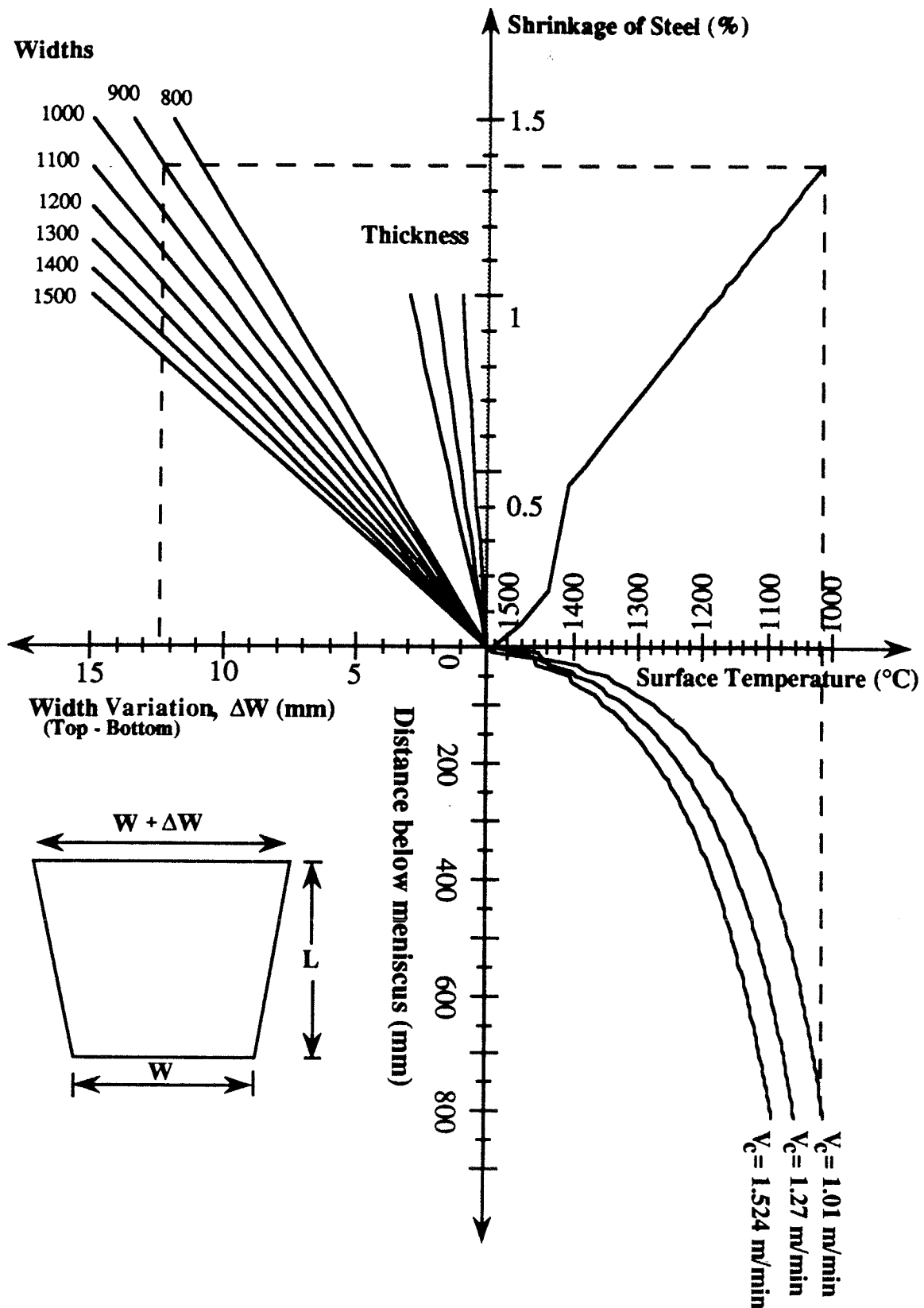


Figure 8.14 A method of calculating the shell shrinkage for continuous slab casting to evaluate the optimum taper of the narrowface.

low carbon steel for standard conditions of 25 degree superheat. Similar diagrams can be made for various superheat practices. It is assumed that the surface temperature of the center of the slab will be independent of the slab width. The diagram can be used to get the appropriate taper in terms of the variation of width at meniscus and bottom of the mold for a given casting condition (speed, width etc.). Knowing the surface temperature of the slab at casting speed in consideration, the associated shrinkage can be obtained by moving vertically in the diagram. Then the width variation can be obtained by moving horizontally on the diagram until reaching line for the appropriate slab width. For example, casting at 1.01 m/min, a 1.38 % shrinkage at the mold exit for a 900 mm slab amounts to 12.4 mm of width variation. This corresponds to about 6.2 mm shrinkage per face and is very close to the natural shrinkage of 6.7 mm of the slab (914 x 203 mm size) corner at mold exit under the same casting conditions as seen in Figure 8.3. Thus, this kind of a diagram could be a useful tool for the mold operator for setting appropriate taper for the given casting condition. Similar diagrams can be generated for various steel grades and casting conditions. Using this diagram, one can design the most appropriate concave mold or multi-taper molds. Diagrams similar to this have been routinely used in Europe for mold design in conventional continuous casting of billets, blooms and slabs including the most familiar new concept of two slope mold^[13].

8.5 CONCLUSIONS

The finite element model CONCAST has been successfully applied to obtain the shrinkage of the solidifying steel shell of a continuously cast slab. Model results suggest that shrinkage at the narrowface of the slab mold is mostly governed by the heat transfer characteristics of the wideface. A simple 1-D thermal analysis of the center of the wideface can reasonably predict shrinkage of the corner region. Based on this 1-D model, a taper diagram was developed to predict the taper necessary to compensate for the shrinkage of the shell as a function of casting speed and width. Diagrams such as these can be useful tools for the casting engineer to set ideal mold taper for different casting conditions.

The present model has confirmed that the shell shrinks more in the top of the mold than in the bottom. Problems arise if the taper is either too large or too small. Shrinkage of steel depends on the grade, low carbon steels having larger shrinkage than the stainless steels. At present, a well-chosen linear taper appears reasonable for stainless steel grades, while for low carbon steels such tapers are not optimum. Further work for a detailed parametric study of all process variables is recommended before non-linear multiple tapers or contoured end-wall designs are implemented.

8.6 REFERENCES

1. R.D. Pehlke: *Summer Conferences*, University of Michigan, Ann Arbor, 1976.
2. M. Larrecq: IRSID, Report No. 941, 1982.
3. R.J. Dippenaar, I.V. Samarasekera and J.K. Brimacombe: "Mold Taper in Coninous Casting Billet Machines", *Transactions of Iron & Steel Society of AIME*, 1986, vol. 7, pp. 31,43.
4. W.R. Storkman and B.G. Thomas: "Heat Flow and Stress Models of Continuous Casting to Predict Slab Shape", *Modeling of Casting and Welding Processes*, TMS/AIME, April, 14-17, Palm Coast, FL, 1988.
5. D.A. Dyudkin, S.V. Khokhlov and A.M. Kondraty: *translated from Metallurg*, 1985, vol. 7, pp. 22-23.
6. S. Deshimaru, S. Omiya and H. Mizota: *Transactions of the Iron and Steel Institute Japan*, 1984, vol. 24 (10), pp. B339.
7. K. Harste: *Investigation of the shrinkage and the origin of mechanical tension during the solidification and successive cooling of cylindrical bars of Fe-C alloys.*, Dissertation (German) Thesis, Technical University of Clausthal, 1989.
8. A. Grill, K. Sorimachi and J.K. Brimacombe: "Heat Flow, Gap Formation and Break-Outs in the Continuous Casting of Steel Slabs", *Metallurgical Transactions*, 1976, vol. 7B, pp. 177-189.
9. K. Takemoto, M. Tatenno, S. Nakayama and K. Ebina: "Optimum Design of Mold Shape by Solidification-Deformation Coupled Analysis", *9th Process Technology Conference Proceedings*, ISS-AIME, Detroit, MI, 1990, Vol. 9.
10. K. Okamura and K. Yamamoto: "Coupled Analysis Between Thermal Deformation and Heat Transfer of Solidifying Shell in Continuous Casting Mold", *Modeling of Casting, Welding and Advanced Solidification Processes VI*, T.S. Pivonka, V. Voller and L. Katgerman, eds., TMS-AIME, Warrendale, PA, Palm Beach, FL, 1993, pp. 535-541.

11. W. Emling and G. Lawson: LTV Steel, private communication, 1993.
12. R. Alberny, A. Leclercq, D. Amory and M. Lahousse: *La Revue de Metallurgie - CIT*, 1976, vol. 73, pp. 545-557.
13. J.P. Birat, M. Larrecq, J.Y. Lamant and J. Petegnief. *The Continuous Casting Mold : A Basic Tool for Surface Quality and Strand Productivity*. Mold Operation for Quality and Productivity. 3-14, 1991.

CHAPTER 9

BULGING BELOW MOLD

In continuous casting a partially solidified steel strand is continuously being extracted from the water cooled copper mold. The strand shell exiting the mold is weak and usually too thin and hot to support the internal liquid pressure. Rolls, positioned at various elevations below the mold provide additional containment. This intermittent containment provided by the rolls, prevents the total failure of the strand by total rupture (breakout) and also limits the shell deformation. In between rolls the shell deforms considerably and bulges out causing internal strains in the shell. The quality of the continuously cast steel is determined by the conditions existing during solidification between rolls and during straightening of the strand. Together with roll misalignment and roll bending, bulging causes internal defects as a result of internal cracking and segregation. While this bulging is small in billets it can be significant in slabs. Therefore, casting machines should be designed to limit inter-roll bulging and bulging strains to acceptable levels.

It has been observed that bulging of shell well below those levels that lead to breakouts, have been found to result in internal cracking in strand cast steel^[1]. Steels have a low ductility region just below the solidus^[2]. Studies have shown that internal cracks can occur when the tensile strain in this sub-solidus region of the strand shell exceeds certain critical value. Although these strains can result from a variety of both thermal and mechanical causes, the deformation of the shell by internal ferrostatic pressure is of primary concern, especially at high casting speed.

Prediction of strand bulging between rollers was of prime importance to the steel manufacturers. Several models^[3-8] have been developed to study the bulging of the slab and its implications on the strains generated at the solidification front. They range from simple analytical models based on elementary theory of beam bending^[9, 10] to complicated elasto-plastic models^[1, 6] and elasto-visco-plastic models^[4, 5, 7, 8, 11]. Most of these works model the shell deformation using either 3D or 2D longitudinal section at the center of the wideface of the slab between rollers

far down in the mold, near unbending. However, there is practically no work available in the literature on slab deformation just below the mold. Furthermore, most of these models cannot predict the slab behavior in the transverse section, especially in the corner region. Figure 9.1 shows schematically the bulging of slab at the center of the wideface.

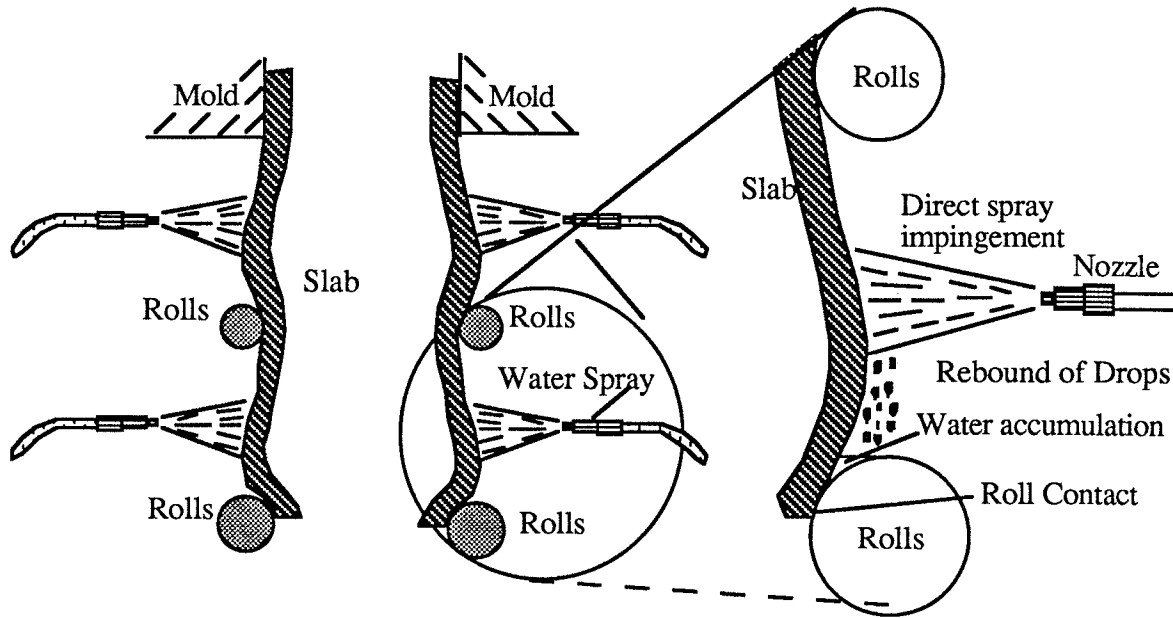


Figure 9.1 Schematic representation of interaction between the shell and the rolls

9.1 SPRAY COOLING BELOW MOLD

It is well known that spray cooling practices have a significant effect on the quality of continuously cast steel slabs. In the spray zone of a slab caster, which consists of spray nozzles positioned between support rolls, as shown in Figure 9.1, thermal stresses are generated in the slab owing to surface cooling and reheating between successive spray nozzles, while mechanical stresses arise from roll misalignment and bulging due to ferrostatic pressure, between the rolls creates further stresses. If the stresses are of sufficient magnitude, internal or surface cracks result. Studies have shown that among the factors that are known to influence crack formation,

bulging is the major cause of defects in continuously cast slabs^[12]. The tendency of the slab to bulge is affected by spray cooling practice because it determines the temperature distribution in the solidifying shell, and hence its strength to withstand ferrostatic pressure.

Extensive research has been done to characterize the heat transfer in the spray cooling zone and a summary of these works can be found in Brimacombe et al.^[13] and Hibbins and Brimacombe^[12]. Cooling of the slab surface in each segment of the spray zone can be categorized as a) Direct spray cooling zone, b) Roll and residual water cooling zone and c) Radiational cooling zone. Although the heat transfer is different in these regions, most of the previous work aimed at obtaining an effective heat transfer coefficient as function of spray water flux and slab surface temperature for the entire region between rolls. Table 9.1 lists the location and size of rolls and the water flow rate in the spray nozzles for a typical slab caster^[14]. The location of the sprays are assumed to be halfway between the rolls. The heat transfer through the rolls is expressed as a fraction of the heat transfer in the sprays as reported by Hibbins^[12].

9.2 SIMULATION BELOW MOLD

The results presented in chapters 7 and 8, were for the simulations in the mold. Further simulations were carried out incorporating the bulging of the slab in between rolls, and cooling by water sprays. As described in chapter 3, the stress analysis below mold is carried out by fixing the wideface surface to an assumed bulge shape. The simulation below mold is done by taking the slice through the strand up to the distance of two roll spacings. The main objective here is to study the effects of slab bulging on the deformation of the transverse section and its implications on the longitudinal surface depressions. The simulation starts with the initial shape, temperature and stress distribution of that at mold exit. The outside of the shell is cooled by water spray cooling. The heat transfer coefficient for the spray cooling is given by Eq. 3.15 and the heat transfer coefficient for the rollers is taken from the calculations of Haeghele^[14] based on the fraction of heat extraction at rolls^[12] given in Table 9.1. The basis of the calculation of the average heat transfer

coefficient between the strand and the rolls is shown in Appendix H. As shown schematically in Figure 9.1, the shell bulges out in between rollers and is pushed back to the position of the rollers. The position of the two rollers used in this simulation is taken from Table 9.1. The maximum bulging and its shape is shown in Figure 3.9. This contour at the center of the wideface provides the rigid constraint for the entire wideface as a function of distance between rolls. The narrowface is left unconstrained, as it usually is not supported other than by a few of foot rolls at the bottom of the mold.

Table 9.1 Location and size of rolls in a typical slab caster along with spray conditions.

| Zone No | Zone starts at (mm below top) | No. of rolls in zone | Roll radius (m) | Water flux (l/m ²) | Fraction of q through roll ^[12] |
|---------|----------------------------------|-------------------------|--------------------|-----------------------------------|---|
| 1 | 815.000 | 1 | 0.064 | 8.090 | 0.010 |
| 2 | 940.000 | 9 | 0.086 | 3.110 | 0.080 |
| 3 | 2710.000 | 20 | 0.127 | 1.760 | 0.220 |
| 4 | 8700.000 | 13 | 0.162 | 1.320 | 0.200 |
| 5 | 36400.000 | 30 | 0.222 | 0.950 | 0.360 |

9.3 RESULTS AND DISCUSSION

The temperature history at various location on the surface and the inside of the shell is shown in Figure 9.2. The strand in the process of casting is intermittently cooled by spray water in the secondary cooling range. As the slab comes out of the mold its surface temperature starts increasing in absence of any cooling, until it approaches the spray, whence it starts cooling again. As the slab passes below the spray, its temperature starts increasing again until it approaches the

second spray and a similar cycle is repeated. The sequence is repeated about 50 times in a conventional continuous caster before the strand is completely solidified. Notice that the

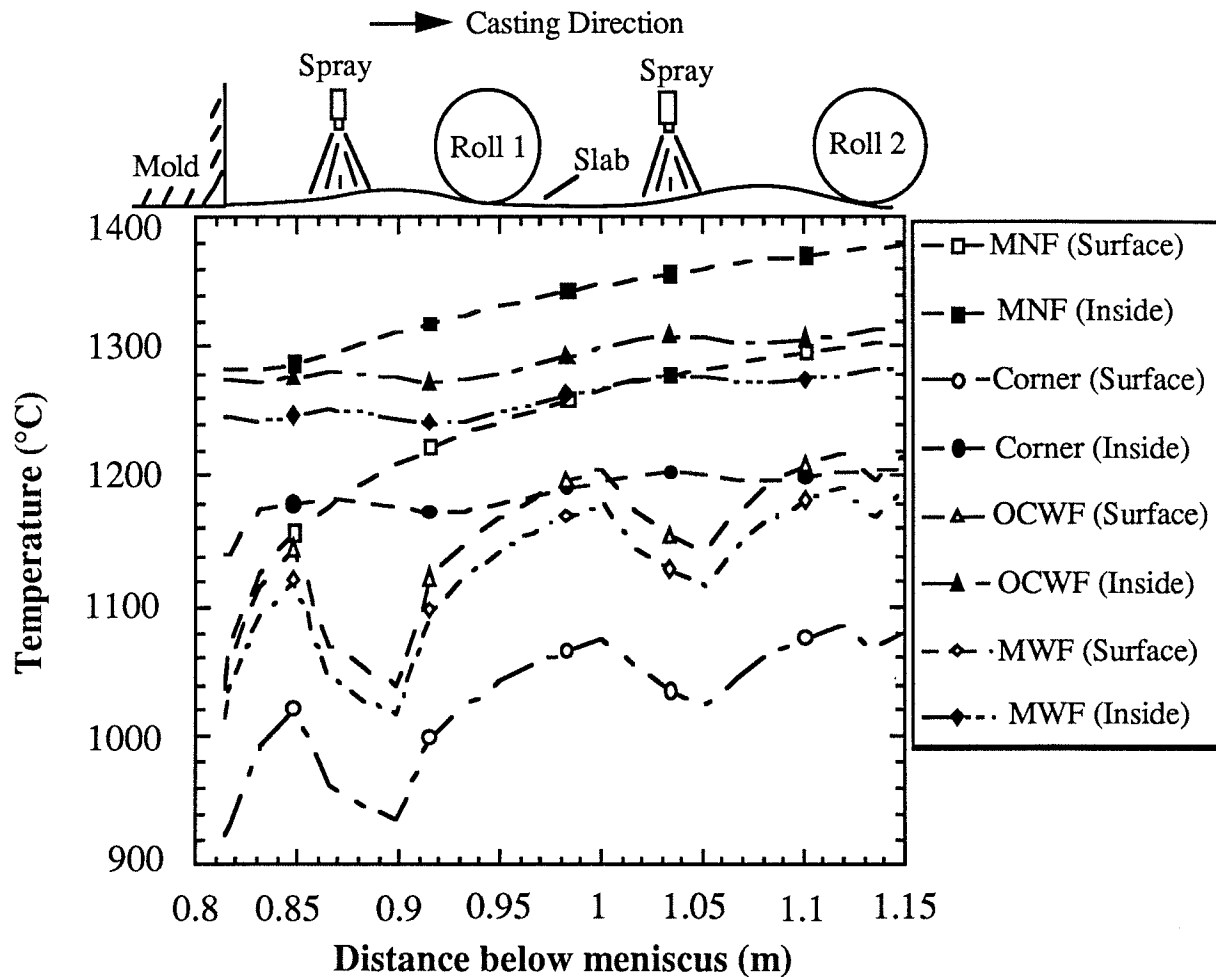


Figure 9.2 Temperature history at various point on the surface and inside (16 mm below surface) of the shell as it moves down the strand with no narrowface cooling.

narrowface surface temperature increases monotonically over the first several rolls in absence of any sprays. Many casting machines employ soft narrowface cooling near the foot rolls. It can be seen that the surface temperature amplitude caused by spray cooling is about 100 ~ 160 °C while the interior temperature at 16 mm below slab surface oscillates about 20 ~ 30 °C. Similar results have been reported by Kojima et al.^[15] using a finite difference heat transfer calculation of the spray zone. These fluctuations in the slab temperature causes important variations in stresses.

The stress history at the mid-wideface (MWF) generated by the model for the simulations below the mold is shown in Figure 9.3. The surface stresses reach a maxima near the points of peak bulging, at the same time the interior goes to compression. As the slice approaches the rollers, it is pushed back to its original position and a stress reversal occurs; the surface goes to compression and the interior to tension. This behavior is caused primarily by simple plate bending, as illustrated at the top of Figure 9.3. These tensions at the solidification front at the rollers are of big concern as they are capable of generating internal cracks. It is therefore, necessary to minimize the tensile stresses generated at the solidification front.

The stress history at some other locations generated by the model for the simulations below the mold is shown in Figure 9.4. The mechanical behavior of the slab is slightly different on the narrowface. The narrowface, which has no roll support, remains bulged out all through, keeping the surface in tension at the mid-face (MNF), except at the off-corner (OCNF) location, where the bending of the shell about the rigid corner produces compression on the surface and tension in the inside. The corner being the coldest, goes into maximum tension and compression during each cycle. The off-corner wideface (OCWF) behaves in a similar manner as the mid-wideface with slightly lower stresses on the surface but slightly higher stress in the interior due to the bending about the corner for this case with a uniformly thick shell. The behavior of this location changes, however, when the wideface shell thickness is not uniform.

The overall picture of the longitudinal effects of slab bulging is shown in Figure 9.5. The effects can be easily understood looking at the transverse slices of the slab deformation and stresses. Figure 9.5 shows the deformed shape of the slab (magnified 5 times), at five locations of interest, namely mold exit, peak bulge and at the rollers. Also plotted in the same figure are the principal stresses in the domain, which can be used to know the stress state of the slab. As seen in the figure, near the peak bulge, both the narrow and widefaces bulge out producing tensile stresses

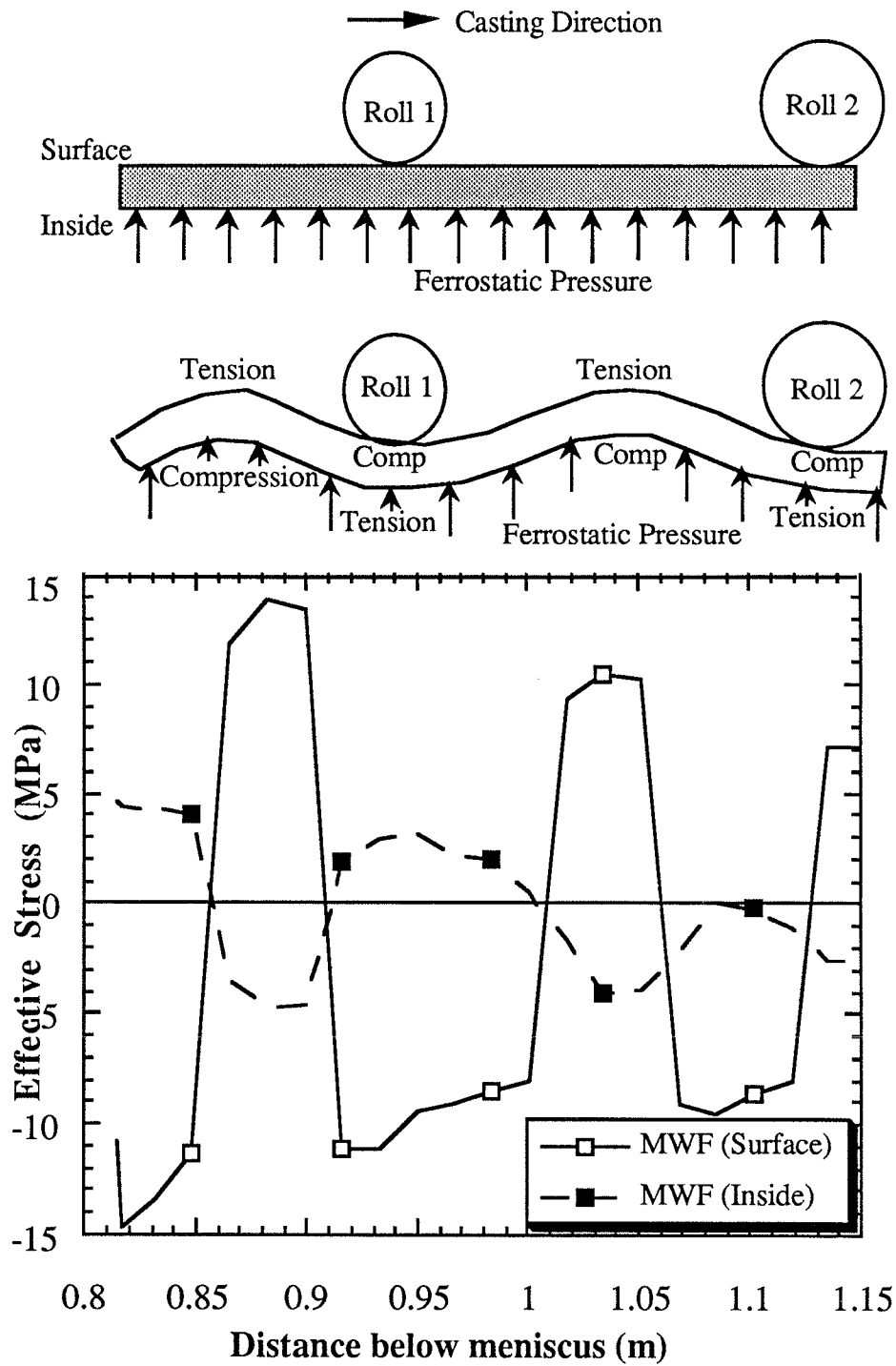


Figure 9.3 Effective stress history at the mid-widface (MWF) on the surface and inside (16mm below surface) of the shell as it moves down the strand with no narrowface cooling.

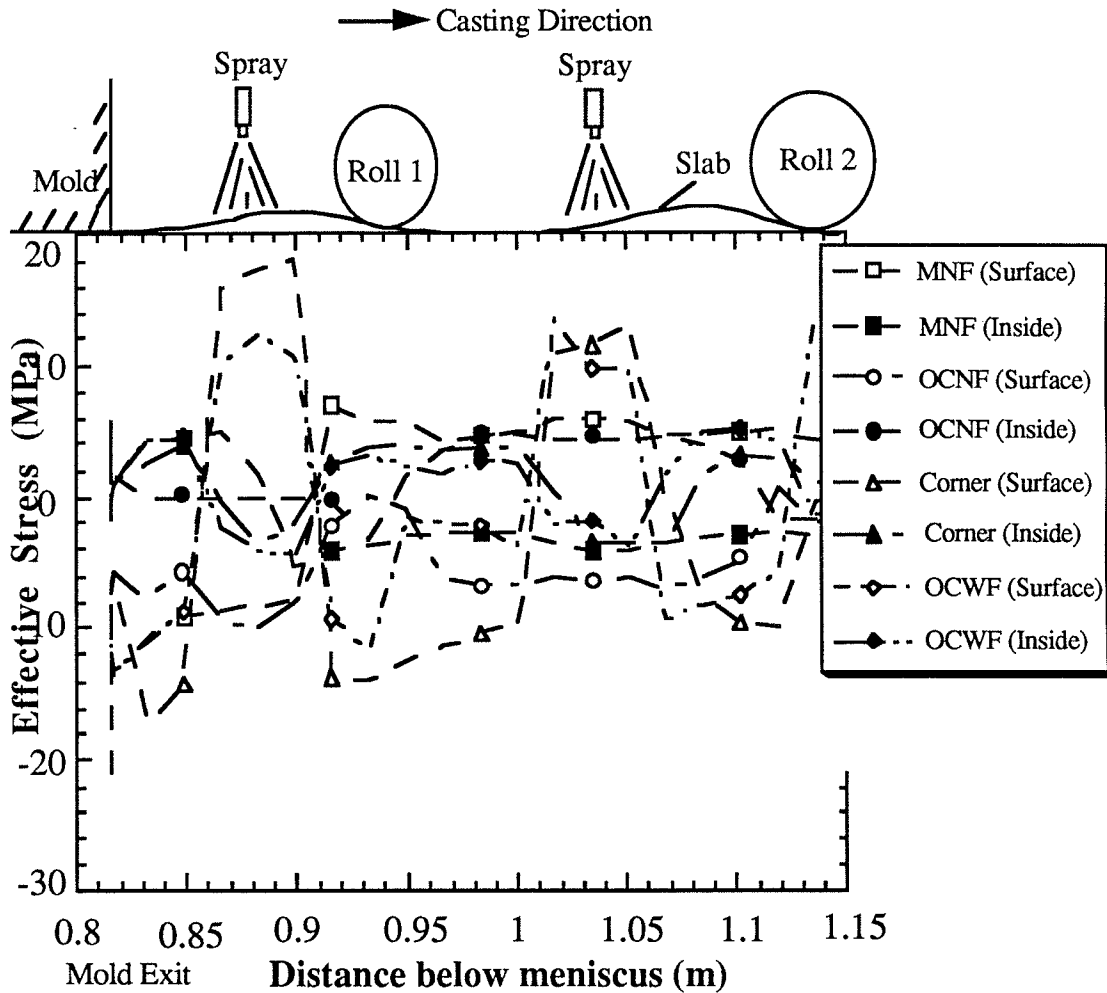


Figure 9.4 Stress history at different locations on the surface and 16 mm inside of the shell as it moves down the strand.

on the surface. While the majority of the wideface surface gets tensile stress due to bulging in between the rolls, the narrowface produces tension at the center, but the surface near the off-corner gets compression due to bending about the rigid corner. The off-corner narrowface being already hot, thin and weak due to too little taper in the mold, is vulnerable to the stress cycling below. Under extreme circumstances this can generate cracks in this off-corner region and a possible breakout below mold. It can also be seen from the figure that as the shell is pushed back near the rollers the corner tends to rotate producing a very slight depression on the wideface. Since the

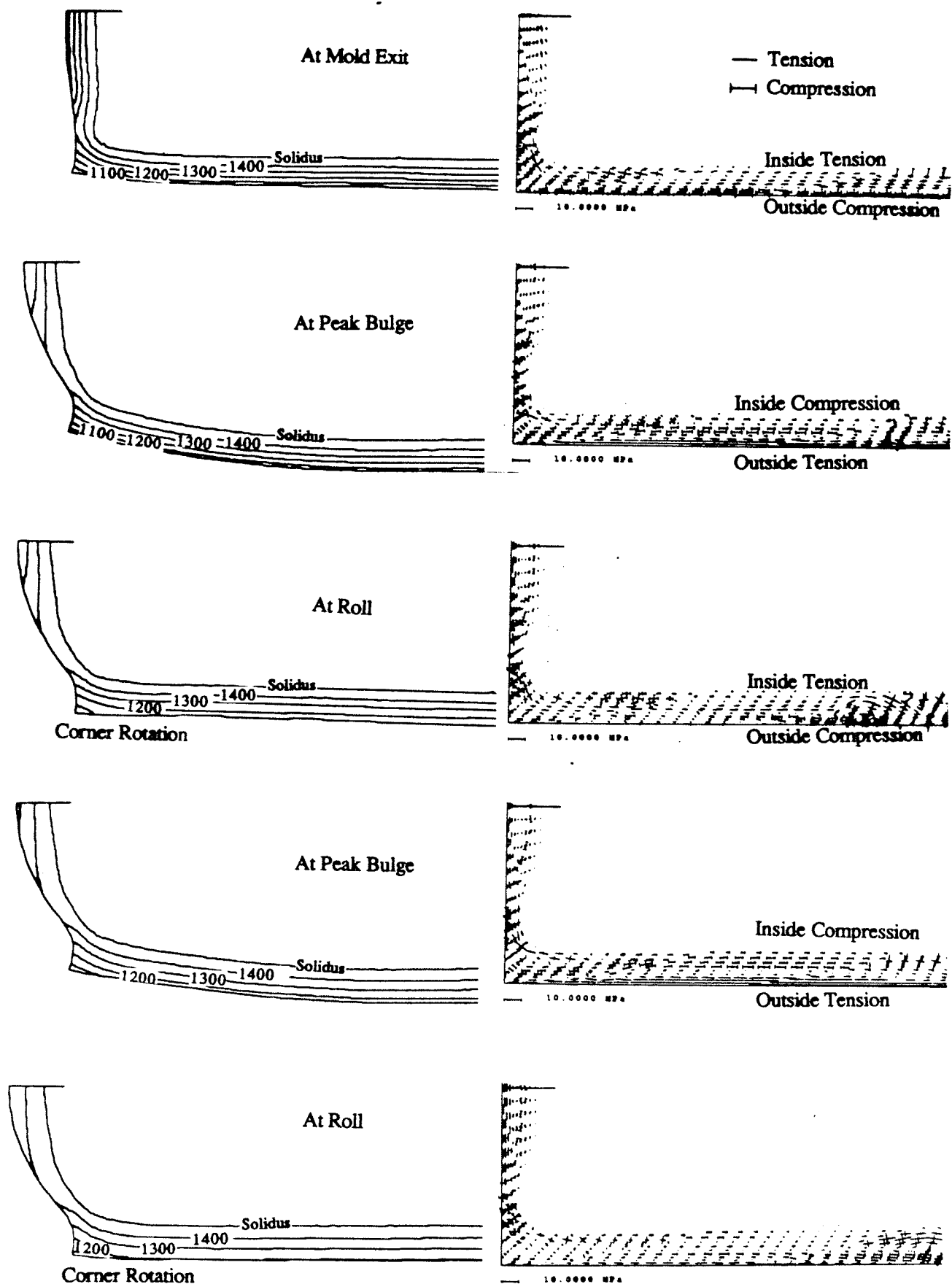


Figure 9.5 Temperature contours and principal stresses in the shell during bulging below mold.

wideface is uniformly thick and strong this corner rotation has no effect on the shape of the slab. This corner rotation has important implications when shell thickness is not uniform which will be discussed in the next section.

9.4 OFF-CORNER DEPRESSIONS

Longitudinal depressions, 2 to 5 mm deep, have been observed on the broad face of conventionally cast 304 stainless steel steels at the off corner region as shown in Figure 1.4. Similar off-corner depressions or "gutters" have been reported by Yamamoto et al.^[16] and Mahapatra et al.^[17] in plain carbon steel. Plain carbon steels often show cracks underneath these depressions at depths ranging from 16.0 to 20.0 mm^[17]. It has been proposed that these depressions are associated with bulging of the narrowface along with rotation of the corner inside the mold or are caused by buckling of the thin and weak shell in the off-corner region resulting from squeezing of the end plates against the narrowfaces^[17, 18]. By this mechanism of formation of off-corner depressions, tensile strain is generated close to the solidification front in the solid shell at the off-corner region of the broad faces, and the formation of subsurface cracks due to this tensile strain below or at the base of the surface depressions can be explained.

Industrial experiences suggest that off-corner gutters are mostly formed at lower casting speed and high superheat practices^[19]. Convex narrowface usually accompanies these gutters on the wideface. However, concave narrowface sometimes accompany gutter, believed due to excessive water spray just below the mold. Gutters are mostly found on the inside radius in curved mold machines^[20]. At this point it is not clear how or where, the gutter is formed or what measures influences it.

Based on these industrial experiences of gutter formation the model was run to simulate some of the conditions that lead to the formation of gutters to understand the mechanism of formation of these defects. The formation of these defects is often attributed to heat transfer in the off-corner region. The possibilities of the abnormalities in heat transfer in the off-corner region are numerous and include :

- i) Non-uniform mold powder distribution (due to meniscus solidification effects, mold powder properties, surface turbulence, effects of flow pattern, non uniform mold wall thickness due to mold curvature etc.)
- ii) Non-uniform air gaps (due to mold distortion and wear, Improper taper on the wideface, Misaligned footroll(s) creating larger airgaps in oneside than the other)
- iii) High or nonuniform superheat due to nozzle misalignment or higher casting speed.

In the present case non-uniformity in the flux distribution was chosen to reproduce this abnormality. In one case the heat transfer in the off-corner region was enhanced by artificially decreasing the mold powder layer thickness and in the other case the resistance to heat flow was decreased by increasing the powder layer thickness. The resulting change in heat transfer had an effect on the thickness of the shell in the off-corner region. Assuming such a condition prevailed in the mold, which led to non-uniform shell thickness at mold exit, simulations were extended below mold using the results at mold exit. The results are summarized in Table 9.2 in terms of the size and location of the depressions. The significant depressions inside the mold were only observed in the case with enhanced localized heat transfer near the off-corner region in the mold. A similar mechanism of locally enhanced heat transfer in the mold has been suggested by Wolf for the formation of transverse depressions in stainless steel slabs^[21].

Wolf^[21] has attributed the formation of transverse depressions in austenitic stainless steels and plain carbon steels to local overcooling of the strand during initial solidification that is followed by contraction due to 'plastic hinge effect' and rebending. According to Wolf, the frequency of these depressions can be reduced by ensuring a low heat flux near the meniscus, and suggested that this can be achieved by operating at higher casting speeds, higher super heats and an optimum slag and an optimum slag-film stability corresponding to minimum heat flux and friction^[21].

For slabs with a thin off corner region, depressions are not usually formed in the mold. Significant depressions at this thin off corner regions start forming below the mold. Figure 9.6 shows the evolution of an off-corner surface depression as the slice travels between the rolls for

the simulation with 25° superheat, 1.35 %/m narrowface taper in mold and 1.02 m/min casting speed for stainless steel properties. The nodal displacement of the surface nodes at three different locations are plotted as a function of distance through the strand in Figure 9.6. As seen in the figure, the mid-widface follows the bulged contour of Figure 3.9 imposed as the constraint. The displacement of the off-corner node with respect to the corner node is increasing, implying a depression being formed on the surface at that location of the slab. It can be noticed that the off-corner displacement increases sharply just below each point of peak bulging between rolls. The phenomena is repeated at the peak bulge in between the first and the second roll with further increase in the size of the depression. This confirms that the depressions are formed below the mold by the combined effect of pushing on the shell by the rollers and the rotation of the corner. It is expected that the depressions would continue to grow below the second roll, but at a reduced rate, as shell thickness increases and bulging will tend to decrease with decreasing shell surface temperature.

From the various simulations carried out in this work, it has been observed that as long as the heat transfer is adequate in the off-corner region and a uniform shell comes out of the mold, the off-corner depressions are not usually formed. However, simulations with the same slice below mold (Figure 9.5) has suggested that depressions are not formed at least within the first few rolls when the wideface shell is uniformly thick. With further distance down the strand, shell thickens and becomes even less likely to form gutters or alter surface shape. This led to the belief that the depressions must be associated with non uniform cooling of the wideface leading to thinning of the off corner region.

9.5 MECHANISM OF OFF-CORNER DEPRESSIONS

Based on the findings of the model simulations a mechanism of formation of the off-corner depressions can be postulated. The depressions appear to be forming in two steps. First of all, it seems that thinning of the off-corner wideface region of the slab in the mold is a critical step in the

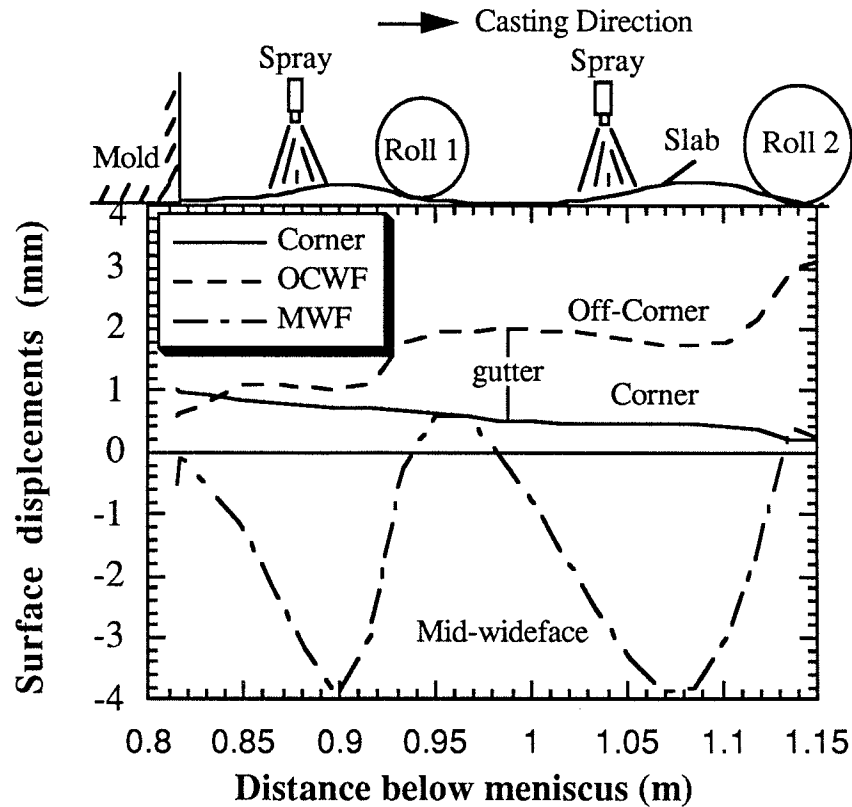


Figure 9.6 Evolution of off-corner gutters below the mold for conditions C with high taper in Table 9.2.

formation of depressions in this region. This thinning might happen for a number of conditions listed in section 9.4.

The second step is bulging of the shell below the mold. As the slab bulges outward below the mold, both the center of the wideface and narrowface bends about the rigid corner. As the rolls are approached the wideface gets pushed back beyond its original position because of negative bulging, while the hot narrowface remains bulged out in absence of any support. Pushing of the wideface by the rolls makes the rigid corner to rotate by a few degrees to accommodate some of the strains due to bulging as shown in Figure 9.7. The weak off-corner region cannot withstand this corner rotation and buckles producing a depression in the off-corner region. Evidence of compressive stresses at the root of the depressions strengthens this buckling mechanism. Figure

9.7 shows the section at different locations in the mold, and furnishes evidence in support of the above mechanism. Based on this mechanism, gutters are formed primarily below the mold. However, gutters were observed to form inside the mold when low narrowface taper allowed some corner rotation..

Alternate mechanisms for depressions formation is buckling of thick shell in the off-corner region. However it is difficult to understand how such localized high heat transfer conditions could prevail in the mold in the presence of gap or depression. Further work is necessary to identify if such heat transfer conditions could prevail through a better understanding of the flux behavior in the gap.

9.6 EFFECT OF SPRAY COOLING

The simulation results presented above assumed uniform wideface cooling with no spray cooling on the narrowface. Some mold designs allow cooling on the narrowface up to few roll segments. To study the effect of spray cooling the heat transfer coefficients for the spray region were increased by a factor of 2 than the normal cooling given by Eq. 3.15. Three different cases were studied :

- i) No Cooling on the narrowface and normal cooling on the wideface,
- ii) Normal cooling on the narrowface and normal cooling on the wideface,
- iii) Harder cooling (2 times normal) on the narrowface and normal cooling on the wideface,
- iv) Harder cooling on both narrowface and the wideface.

Table 9.2 summarizes the results on the effect of spray cooling on the formation of off-corner depressions. As evident from the table, cooling on the narrowface seems beneficial in reducing the amount of depressions. With increasing cooling on the narrowface the amount of surface depressions can be reduced. It is expected that even higher cooling extended further below mold would further reduce off-corner depressions. They are expected to always persist, so long as there is significant off-corner shell thinning at mold exit. However, the calculations show that

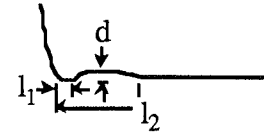


Table 9.2 Location and size of depression for different mechanisms

| Mechanism of depression | Location of depression (l_1 - l_2) | | Size of Maximum depression (d) | |
|--|--|-------------------------|--------------------------------|-------------------------|
| | Low Taper (0.65%/m) | High Taper (1.35%/m) | Low Taper (0.65%/m) | High Taper (1.35%/m) |
| A. Case with uniform shell | | | | |
| a) In mold | 5-15 mm | | 0.02 mm | 0 mm |
| b) Below mold | 5-96 mm | 5-15 mm | 0.25 mm | 0.06 mm |
| B. Case with off-corner thick shell | | | | |
| a) In mold | 5-75 mm | 5-80 mm | 2.27 mm | 4.08 mm |
| b) Below mold | 5-80 mm | 5-96 mm | 2.37 mm | 5.06 mm |
| C. Case with Off-corner thins shell | | | | |
| a) In mold | 5-70 mm | | 0.98 mm | 0.0 mm |
| b) Below mold | 5-109 mm | 5-150 mm | 3.83 mm | 2.96 mm |
| Effect of Spray Cooling Below Mold | | | | |
| Case C with normal NF* cooling and normal WF cooling | 5-229 mm | | 3.40 mm | |
| Case C with hard NF cooling and normal WF cooling | 5-200 mm | | 2.90 mm | |
| Case C with hard NF cooling and hard WF cooling | 5-200 mm | | 2.2 mm | |

* NF = Narrowface, WF = Wideface.

depressions cannot be totally removed. Doubling the cooling on the narrowface reduces the depressions by about 25 %.

9.7 CONCLUSION

The model described in this work was successfully extended below the mold by taking the transverse slice of the slab through the rolls with an imposed bulged shape of the center of the wideface. Model simulation suggest that cyclic thermo-mechanical loading of the slab below mold can generate tension on the surface as well as in the interior of the shell. Bulging of the strand in between rolls is responsible for off-corner depressions when the off-corner region of the shell exiting the mold is relatively thin. A mechanism of the formation of these off-corner depressions is proposed. Cooling on the narrowface is beneficial and high spray cooling on both the narrowface and the wideface can reduce the off-corner depressions. Model results suggest that primary way to prevent gutter is to achieve uniform, reasonably thick shell at mold exit, followed by uniform sprays and proper roll alignment. Proper mold practice to keep uniform mold powder distribution to prevent off-corner wideface shell thinning. This means that surface turbulence, flow characteristics and powder properties are important. Also adequate taper should be provided to prevent off-corner air gap formation. It seems that superheat and spray cooling is not as important as the other factors contributing off-corner shell thinning.

9.8 REFERENCES

1. S.S. Daniel: "Roll-containment model for strand-cast slabs and blooms", *Ironmaking and Steelmaking*, 1982, vol. 1, pp. 16-24.
2. F. Weinberg: "The Ductility of Continuously-Cast Steel Near the Melting Point - Hot Tearing", *Metallurgical Transactions*, 1979, vol. 10B (June), pp. 219-227.
3. A. Grill, J.K. Brimacombe and F. Weinberg: "Mathematical analysis of stresses in continuous casting of steel", *Ironmaking and Steelmaking*, 1976, vol. 3 (1), pp. 38-47.
4. B.A. Lewis, B. Barber and N.J. Hill: "Boundary Condition Difficulties Encountered in the Simulation of Bulging during the Continuous Casting of Steel", *App. Math. Model*, 1983, vol. 7 (August), pp. 274-277.
5. B. Barber, B.A. Lewis and B.M. Leckenby: "Finite-element Analysis of Strand Deformation and Strain Distribution in Solidifying Shell During Continuous Slab Casting", *Ironmaking and Steelmaking*, 1985, vol. 12 (4), pp. 171-175.
6. M. Uehera, I.V. Samarasekera and J.K. Brimacombe: "Mathematical Modeling of Unbending of Continuously cast Steel Slabs", *Ironmaking and Steelmaking*, 1986, vol. 13 (3), pp. 138-153.
7. K. Okamura and H. Kawashima: "Three-dimensional Elasto-Plastic and Creep Analysis of Bulging in Continuously Cast Slabs", *ISIJ International*, 1989, vol. 29 (8), pp. 666-672.
8. B. Barber and A. Perkins: "Strand Deformation in Continuous Casting", *Ironmaking and Steelmaking*, 1989, vol. 16 (6), pp. 406-411.
9. A. Palmaers, A. Etienne and J. Mignon: "Calculation of the Mechanical and Thermal Stresses in Continuously Cast Strands, in german", *Stahl und Eisen*, 1979, vol. 99 (19), pp. 1039-1050.
10. K. Miyazawa and K. Schwerdtfeger: *Ironmaking and Steelmaking*, 1985, vol. 6, pp. 68.

11. A. Grill and K. Schwerdtfeger: "Finite-element analysis of Bulging Produced by Creep in Continuously Cast Steel Slabs", *Ironmaking and Steelmaking*, 1979, vol. 6 (3), pp. 131-135.
12. S.G. Hibbins and J.K. Brimacombe. *Characterization of Heat Transfer in the Secondary Cooling System of a Continuous Slab Caster*. Continuous Casting - Heat Flow, Solidification and Crack Formation. 2: 139-151, 1984.
13. J.K. Brimacombe, P.K. Aggarwal, S. Hibbins, B. Prabhaker and L.A. Baptista. *Spray Cooling in the Continuous Casting of Steel*. Continuous Casting - Vol. 2. Heat Flow, Solidification and Crack Formation. 2: 109-123, 1984.
14. G. Haegele: *Application of Mathematical Models to Investigate Defect Formation During Hot Charging of Continuously Cast Steel Slabs*, Masters Thesis, University of Illinois at Urbana, Champaign, 1988.
15. S. Kojima, T. Matsukawa and T. Kodama: "Condition of Internal Cracks in Continuous Casting of Steel Slabs", *8th Process Technology Conference Proceedings*, ISS-AIME, 1990, Vol. 8, pp. 255-262.
16. H. Yamamoto, Y. Nuri and Ohashi: *Transactions of the Iron and Steel Institute of Japan*, 1982, vol. 22, pp. B-336.
17. R.B. Mahapatra, J.K. Brimacombe and I.V. Samarasekera: "Mold Behavior and its Influence on Product Quality in the Continuous Casting Slabs : Part II. Mold Heat Transfer, Mold Flux Behavior, Formation of Oscillation Marks, Longitudinal Off-corner Depressions, and Subsurface Cracks", *Metallurgical Transactions*, 1991, vol. 22B (December), pp. 875-888.
18. B.G. Thomas: "Application of Mathematical Models to the Continuous Slab Casting Mold.", *ISS Transactions*, 1989, vol. 16 (12), pp. 53-66.
19. R. Omalley: Armco Inc. Butler, PA, private communication, 1993.
20. E.S. Szekeres: Casting Consultants Inc., Pittsburg, PA, private communication, 1993.
21. M. Wolf: "Strand Surface Quality of Austenitic Steels: Part I. Macroscopic Shell Growth and Ferrite Distribution", *Ironmaking and Steelmaking*, 1986, vol. 13, pp. 248-257.

CHAPTER 10

APPLICATION TO CRACK FORMATION

Cracks in the slab form due to the combined effects of tensile stresses and metallurgical embrittlement. At high temperatures, steels have three distinct zones of reduced ductility as shown in Figure 10.1. These are often referred to as high (30-70 °C below solidus), intermediate (800 °C to 1200 °C) and low (600 °C to 900 °C) temperature low-ductility zones. At temperatures just below solidus the ductility is reduced by microsegregation of S and P to the interdendritic liquid, which lowers the local solidus temperature. Relatively small strains (1-2 %) can separate grains surrounded by the low melting liquid, as a result cracks can propagate outward from the solidification front between dendrites. This zone of reduced ductility produces what is called the

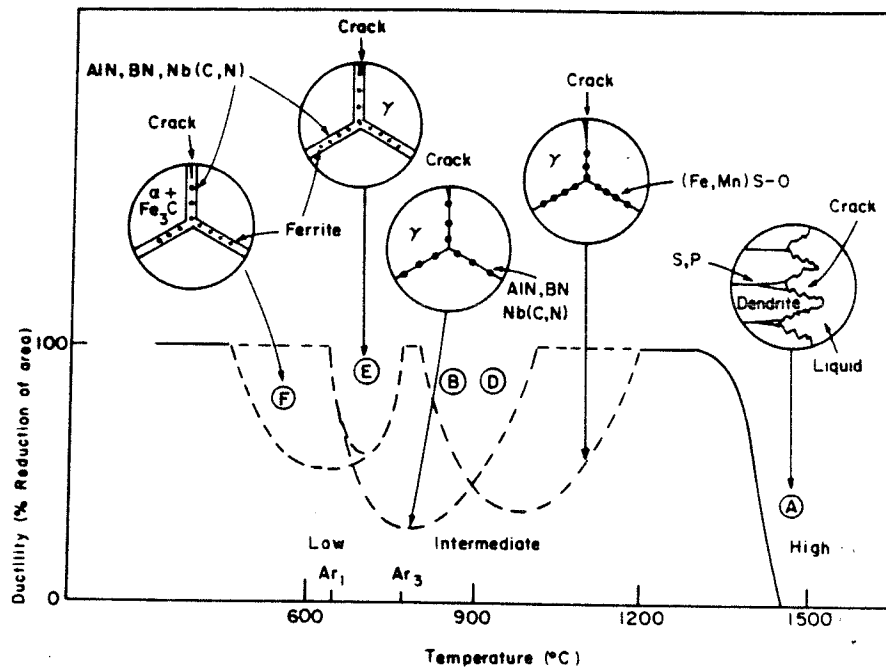


Figure 10.1 Schematic representation of temperature zones of low hot ductility of steel^[1].

"hot tears" and is responsible for most internal cracks in continuous casting. Other embrittlements are caused by mechanisms such as segregation, precipitation of sulphides and nitrides along prior austenite grain boundaries, dynamic recrystallization and coalescence of microvoids at grain boundaries, which are difficult to model with macro-models such as the present one.

Therefore, using the model to understand the formation of various cracks requires a valid fracture criterion to link the calculated mechanical behavior with the microstructural phenomena that control crack initiation and propagation. This criterion can be developed independently to the macro stress model, based on metallurgical understanding. However, extensive experimental verification are needed to use such cracking criterion. Thus, stress models should be used in conjunction with experiments to determine the fracture criteria empirically [2]. In the next section a general description of the various cracks in continuous slab casting and their mechanisms of formation are provided.

10.1 HOT TEARS

A Possible mechanisms of hot tearing is outlined by Nederberg^[3] which suggest that : hot tearing is initiated at temperatures close to the solidus temperature by excessive relative displacements of the grains surrounded by thin liquid films of segregated alloying elements. The associated relative displacements takes place by sliding along the grain boundaries or simply pulling them apart. Metal near the solidification front is very sensitive to strain and tensile stress, depending on steel composition. In the past, several stress based [4-6] and critical strain based [7-9] cracking criteria have been proposed.

First, the maximum normalized stress based on effective stress divided by the yield strength of the alloy at the particular temperature in question has been used as a criterion for cracking.^[6, 10] In the context of unified constitutive law, where no initial yield limit exists, the calculation of such normalized stresses is dubious. Recently Fjaer^[11] has used a hot tearing criterion based on the ratio of the effective viscoplastic strain rate ($\dot{\epsilon}$) to the cooling rate (\dot{T}) to

identify casting conditions that lead to hot tearing by comparison of results with industrial experience.

Criteria to predict cracks need a critical temperature range. For hot tearing, this may be characterized better by a critical range of liquid fraction, f_L , such as $0.01 < f_L < 0.1$ ^[12] or $0.01 < f_L < 0.2$ ^[9]. For other types of cracks the critical low ductility temperature range can be used in conjunction with a mechanical fracture criteria. To supplement this, several different mechanical criteria for cracking have been developed and used.

A critical stress criterion has been used in early stress models for steel, (e.g. 20 MPa for $T > 1340\text{ }^{\circ}\text{C}$)^[5, 13] but was later judged to be insufficient^[7, 9] Tensile stress still appears to be a requirement for crack formation^[9]. The maximum tensile stress occurs just before formation of a critical flaw^[14]. However, tension is usually unavoidable in the susceptible inner portion of the shell, as discussed in the next section.

A critical strain criterion appears to have more potential for predicting hot tears^[7, 9] Careful strain measurements during bending of solidifying steel ingots with a liquid core have led to estimates of the critical strain under continuous casting conditions^[9, 15] The critical values range from 1.0 to 3.8%,^[8, 9, 15, 16] with the lowest values found at high strain rate and in sensitive grades (e.g. high S peritectic steel). For the same strain, low strain rates favor fewer, longer cracks, relative to high strain rates, since more time is available for the cracks to grow^[9, 15] In aluminum rich Al-Cu alloys, critical strains were reported from 0.09% to 1.6% and were relatively independent of strain rate^[14, 17].

The ductility of steel at elevated temperature has been studied extensively and reviewed^[18, 19]. Although this work has contributed to understanding cracking mechanisms and composition effects, it is difficult to extract quantitative fracture criteria beyond the critical temperature ranges. Yamanaka has deduced that strain damage leading to cracks can accumulate over successive loading periods^[9]. Thus, it appears to be important to model the entire mechanical history of the

slab, rather than simply to search for a peak stress or strain. There is still much work to be done in fracture criteria, despite significant progress in recent years.

10.2 TRANSVERSE CRACKS

Transverse cracks specially at oscillation marks are also believed to initiate in the mold, because of the presence of mold powders in them. These cracks are believed to occur because of grain coarsening due to reduced cooling rates at these places ^[20] as well as contact and friction between the mold and the weak shell in the upper region of the mold^[21]. Transverse stresses which forms at the root of excessively deep meniscus marks (caused by poor oscillation practice, surface turbulence, meniscus freezing due to fluid arriving too cold etc.) open up later in the low temperature ductility zones under the action of large tensile tresses. Thus a stress criterion seems adequate in developing an understanding of these types of cracks. Model predicted transverse stress history should be used to study the mechanism of formation of these cracks and their possible locations.

The sources of tensile stresses in the continuous casting machine are numerous such as : creep bulging due to ferrostatic pressure both in mold (for insufficient taper) and below, unbending, roll misalignment and withdrawal forces, friction against oscillating mold, reheating below mold etc.. Surface cracks originate from deviations from this classic behavior, which produce tension at the surface. These deviations can arise from reheating of the surface, friction with the mold walls, phase transformations, bulging between rolls and multidimensional effects. Cracking of steel is very much composition dependent. Certain steel compositions, such as peritectic grades, are susceptible to surface and subsurface cracks, leading to slivers and other problems in the final product. The model presented in this work is an ideal tool to investigate this type of problem.

10.3 LONGITUDINAL CRACKS

Longitudinal cracks are observed along the mid-face and corner region of the slabs. These cracks are believed to have generated due to tensile strains generated in the mold due to mold disorders such as alignment, taper, oscillation, lubrication and in the upper spray zones due to overcooling.^[22] In slabs longitudinal cracks in the off-corner region are caused by bulging of the narrowface in the mold due to poor support conditions (i.e. low taper). The role of mold lubrication in the generation of this quality problem is significant. The model presented here can be used to study the generation of the longitudinal stresses in the slab.

10.4 RESULTS AND DISCUSSION

The present model predictions of the stress distribution through a typical unconstrained (i.e. frictionless) solidifying shell is illustrated in Figure 10.2. Note that to maintain force equilibrium, the average stress (represented by the area under each curve) should always be zero. The solidifying and shrinking shell generates a compressive stress on its cold outer surface and tension in its hot inner surface. The interior tensile region contributes to sub-surface *hot tears* when accompanied by metallurgical embrittlement. The nature of this moving stress distribution suggests that these cracks can originate early in the mold and grow inward as the solidification proceeds.

Figure 10.2 also shows how the effects of the δ - γ transformation incorporated into the model, are manifested as small, sharp tensile peaks in the stress distribution. The superimposed temperatures through the shell show that this 5.5 MPa peak clearly corresponds to the δ -ferrite region as dictated by the phase diagram. The sudden shrinkage from the δ to γ phase produces these tensile peaks. This sub-surface peak is not seen in high carbon or stainless steels which do not have this transformation as shown in Figure 10.3. It should be mentioned here the tensile peaks were obtained using the constitutive equation of the δ -phase same as that of the γ -phase. Explicit methods are suitable for using the composite function in the mixed range. Wray^[23]

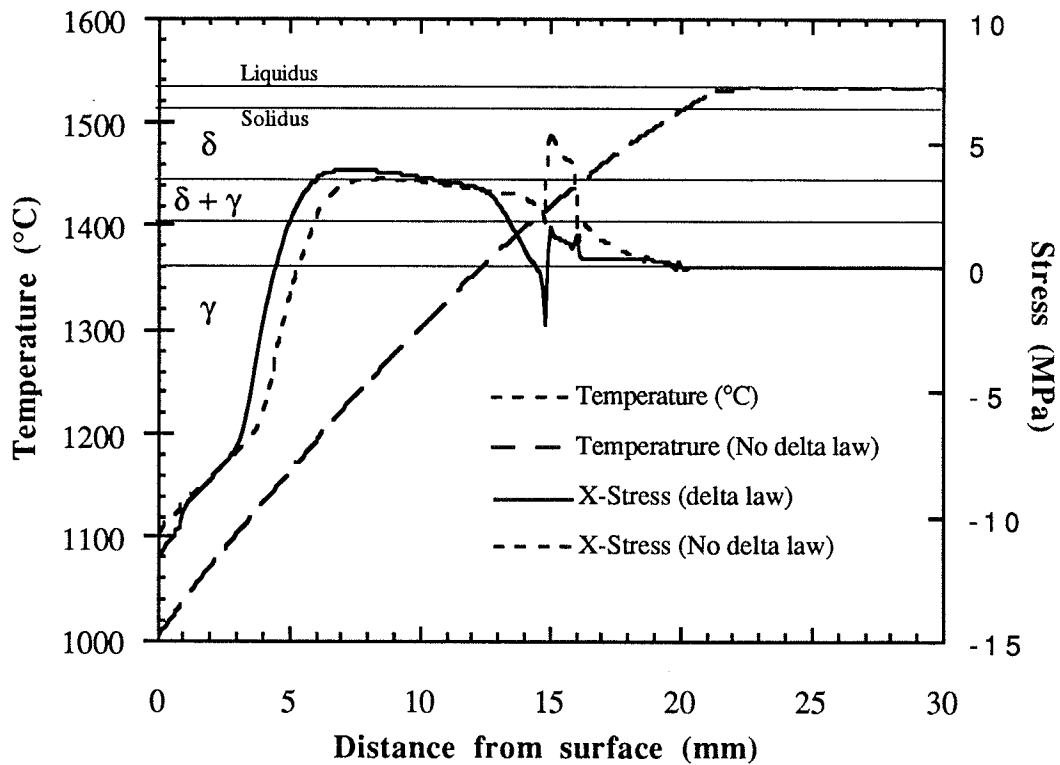


Figure 10.2 Comparison of transverse stress profile through the shell with and without the constitutive law for the δ -phase at mold exit.

has measured the creep strength of the δ -phase as a function of strain-rate and temperature. According to Wray, δ -phase is about 4-9 times weaker than the γ -phase depending on the strain rate. Next the equation proposed by Wray^[23] used to describe the behavior in both δ and $\delta+\gamma$ phases were incorporated in the model. The results shown in Figure 10.3 compares the stress distribution through the shell. It can be seen that the tensile peaks observed in Figure 10.2 were greatly reduced by incorporating the constitutive equation of the δ -phase. Since δ -phase is weaker than the γ -phase^[23], it is expected that strain will concentrate in this phase and the stress peak will disappear. This lower tensile peak is unlikely to cause cracks in low carbon steels, which have reasonable hot ductility. However, in steels where metallurgical embrittlement is a problem, such as caused by microsegregation, this tensile stress may cause subsurface cracks.

Similar stress distribution through the shell can also be obtained for austenitic stainless steel as shown in Figure 10.3. Figure 10.3 compares the stresses through the shell at mold exit between stainless steel and low-carbon steels. The stress magnitudes are of the same order, except that the stainless steel does not have the sub-solidus tensile peak as does the low-carbon steel. Thus the low-carbon steels should be more prone to internal cracks than the stainless steels. This is in agreement with the practice. However, other stainless steel grades such as ferritic, which has the δ - γ transformation are prone to sub-surface cracks. The effects of transformation plasticity will also affect this stress distribution. Moreover, steels have good ductility in the temperature range of 1200 °C and 1350 °C and as such stress alone should not be sufficient to cause cracks. This again calls for a strain based fracture criterion for the hot tears and further work is necessary to quantify the limit on the strain accumulation in the delta phase before cracks can form.

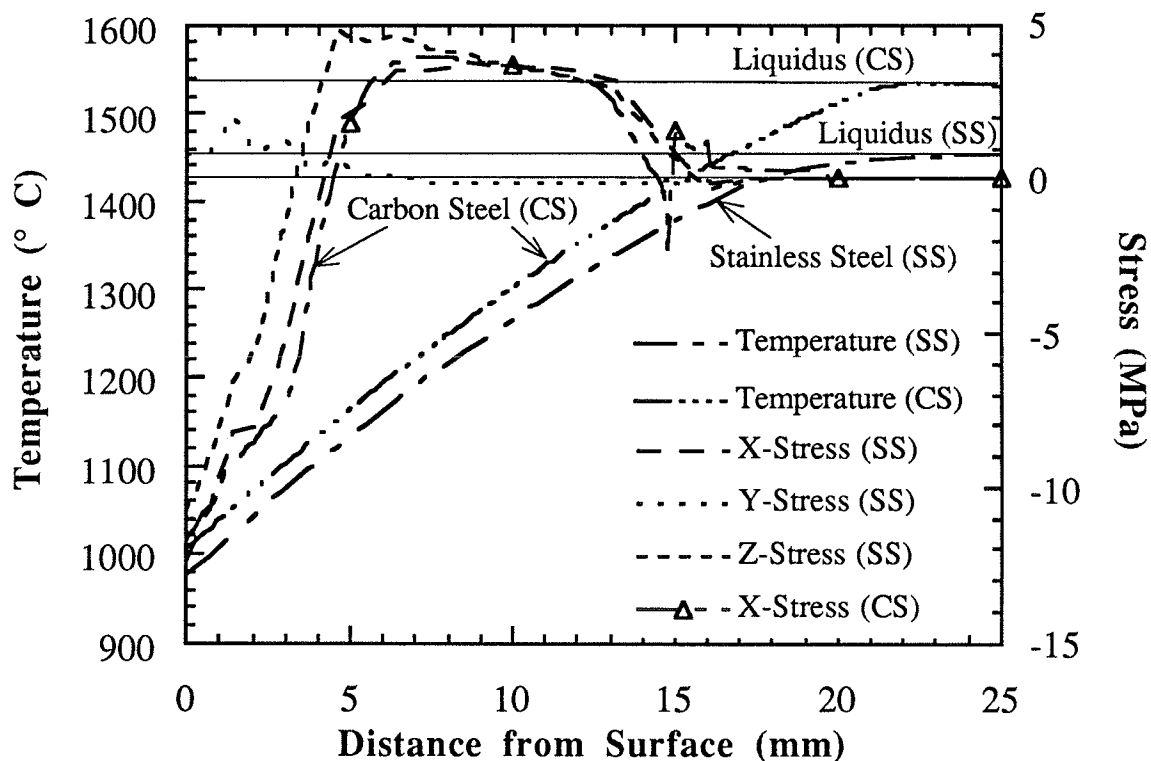


Figure 10.3 Comparison of transverse and longitudinal stresses between stainless steel and low-carbon steel.

Comparison of different stresses in Figure 10.3 suggest that the stresses are mostly longitudinal (σ_x) and transverse (σ_z) in nature, the normal stress (σ_y) being negligible. This suggest cracks parallel to the slab surface are less likely and in practice the cracks are mostly transverse and longitudinal in nature. The model presented here can be used to understand the formation of both of these types of cracks through carefully analyzing the evolution of the σ_x , for longitudinal cracks and σ_z , for transverse cracks.

It has been observed in the previous chapters that hot spots can generate on the slab surface due to either in sufficient taper or non-uniform mold flux film. When the hot spots are formed on the shell surface tensile stresses are generated in theses regions as the hotter regions are surrounded by relatively colder region as shown in Figure 10.4. These local thermal gradients produce tensile stresses on the shell. We have seen that when the shell cools uniformly the stresses are usually compressive on the surface. However bulging below mold introduces tensile stresses and the already existing tensile regions might be prone to cracking under the cyclic loading below the mold

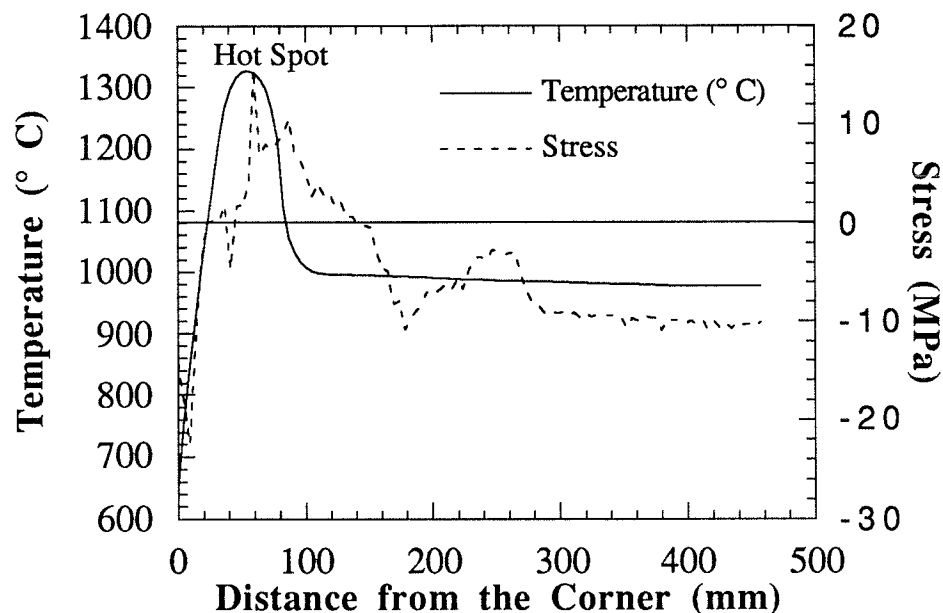


Figure 10.4 Variation of temperature and x-stress along the wideface surface at mold exit with a hot spot.

and could propagate a sub-surface crack from corner through to the surface. Tensile strength of plain carbon steels have been reported in the range of 30 MPa at 800 °C and 10 MPa at 1400 °C.^[24] Thus the off-corner region of the slab is more prone to cracking when hot spots exist in this region. The thin shell formed in this region due to reduced heat transfer makes it more vulnerable to large tensile stresses.

It has been established that the slabs are susceptible to cracks when the mechanical strains due to unbending or roll misalignment exceeds a certain critical value (usually 0.1-0.2%). Large surface tensile stresses are generated during slab bulging below the mold. Figure 10.5 shows the stress distribution through the shell at two different locations below the mold. Near the first peak

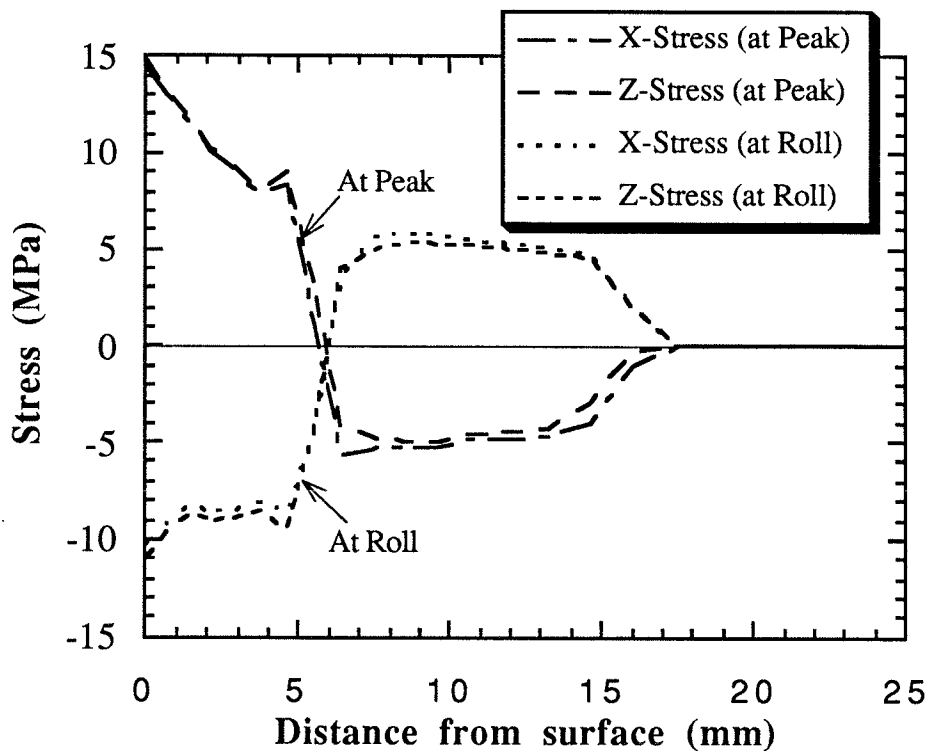


Figure 10.5 Stress through the shell below the mold (MWF) showing high surface tensile stress in between rolls.

bulge, the large tensile stresses on the surface are produced by a combination of surface reheating and bulging due to ferrostatic pressure. The interior goes into compression from its original state

of tension at mold exit. As the rolls are approached the stresses are reversed again. This severe mechanical cycling continues over a number of roll segments in addition to other mechanical effects of bending, roll misalignment. In absence of a proper stress criterion, it is difficult to conclude how the shell will react to this load cycling. However, choice of proper spray cooling below the mold to minimize the generation of any tensile stress should be beneficial.

The effective inelastic strain histories below the mold on the surface and the interior of the shell at the off-corner wideface is shown in Figure 10.7. It can be seen that the plastic strains for the surface nodes gradually decrease, while that for the interior nodes the plastic strain gradually increases. Notice that the interior plastic strains are in tension and are considerably higher compared to that at the surface. These values are relatively higher than the critical strains at which cracks form. This further strengthens the theory of internal crack formation during bulging below the mold.

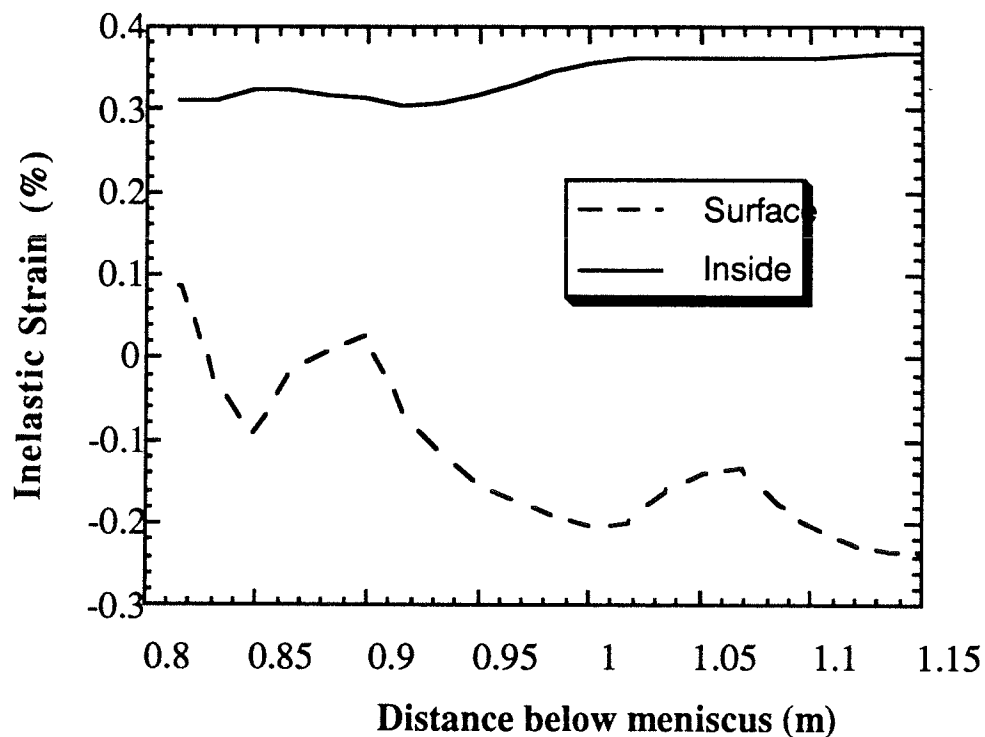


Figure 10.6 Effective inelastic strain history during bulging below mold in the off-corner region of the slab.

10.5 TRANSVERSE CORNER CRACKS

Steel slabs often exhibit transverse cracks at the corner. These cracks are often attributed to large surface gradients in the spray zone^[22] and also to friction with the mold due to excessive taper^[21]. Figure 10.7 shows the evolution of the transverse stress at various location in the slab for the simulations with stainless steel properties for the casting conditions of 25° superheat, 0.65%/m taper and 1.02m/min casting speed. The transverse slices through the slab taken at 3 different locations in the mold is show in Figure 10.7(a). As can be seen in the figure, the high tensile transfer stresses mostly concentrate in the corner region. The stress history plotted in the Figure 10.7(b) shows that, while most the surface has compressive stress in the mold, the corner which starts with compressive stress (σ_z) reverses to tension some where halfway in the mold. The temperature history plot in the same figure suggests that initially the corner cools much faster than its surrounding region, generating tension. Further below the mold the corner temperature stabilizes and brings the corner to compression again. It can also be seen from Figure 10.7(a) that maximum tensile peak shifts from the corner at the mid-height to a slightly off corner region at mold exit. The peak also shifts from surface in the upper region of the mold to an off-corner sub-surface (about 8 mm from surface) region at mold exit. These results suggest that corner cracks can form in the mold when the cooling rate in the corner region of the mold is very high. The model results can thus be used to gain confidence in the qualitative understanding of various defects in continuous slab casting.

10.6 CONCLUSIONS

The model has been used to predict the stress-state at various locations in the slab to help understand the formation of various cracks. Models results suggest that the low-carbon steels are more prone to internal cracks than austenitic stainless steel due to sub-surface tensile stresses generated as a result of the d-g transformation . Bulging below mold enhances the chances of such crack formation. The stresses in the steel are mostly transverse and longitudinal in nature and

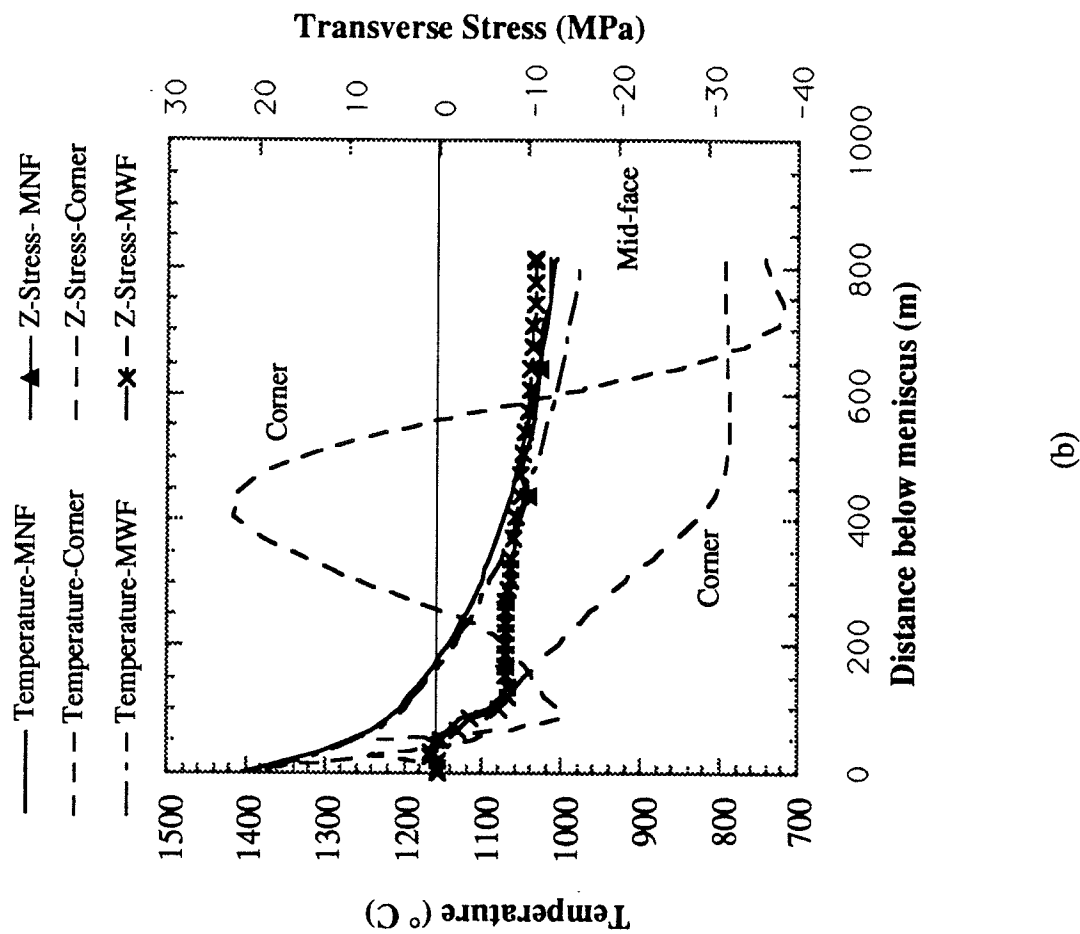
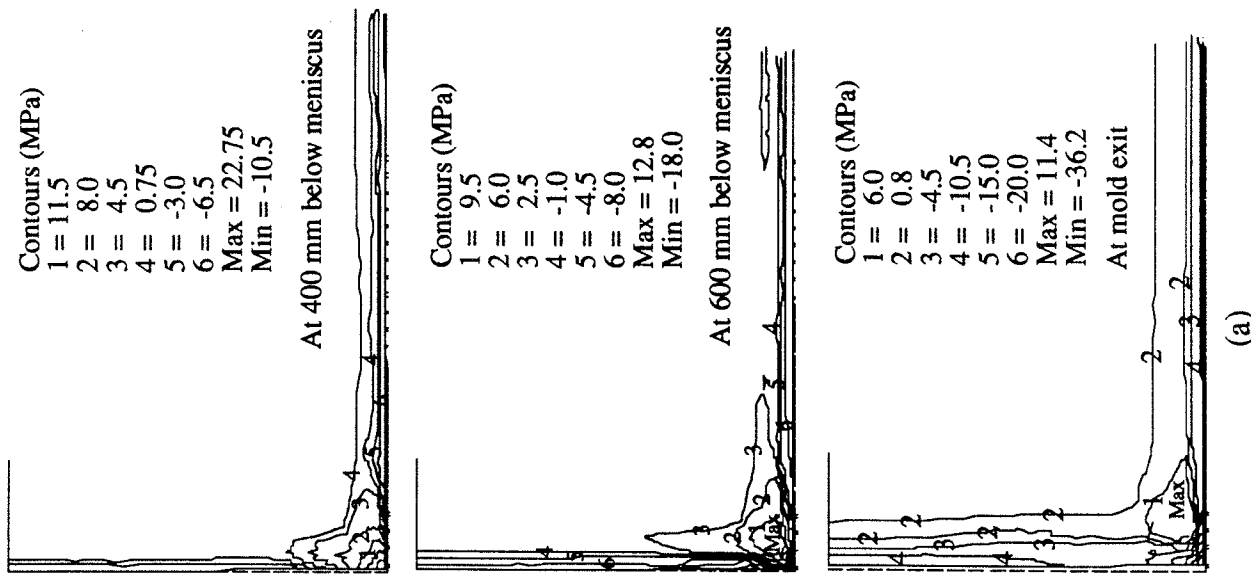


Figure 10.7 History of transverse (σ_z) stress in the shell, a) σ_z contours at three different locations in the mold
 (b) Transverse stress and temperature history at three different locations on the slab surface.

normal stresses are negligible. In absence of valid fracture criteria the model predictions are mostly qualitative and can provide an understanding of the complex interaction of various thermo-mechanical phenomena that govern the process.

10.7 REFERENCES

1. B.G. Thomas, J.K. Brimacombe and I.V. Samarasekara: "The Formation of Panel Cracks in Steel Ingots : A State-of-the-Art Review : I. Hot ductility of Steel ; II. Mid-face and Off-corner cracks.", *Transactions of the Iron and Steel Institute of AIME*, 1986, vol. 7, pp. 7-29.
2. B.G. Thomas: "Stress Modeling of Casting Processes : An Overview", *Modeling of Casting, Welding and Advanced Solidification Process VI*, TMS-AIME, Palm Coast, FL, March 21-26, 1993.
3. M.L. Nedreberg: *Thermal Stress and the Hot Tearing during the DC Casting of AlMgSi Billets*, PhD. Thesis, University of Oslo, Department of Physics, 1991.
4. J. Mathew and H.D. Brody: "Simulation of thermal stresses in continuous casting using a finite element method", *Nuclear metallurgy*, 1976, vol. 20 (2), pp. 978-990.
5. A. Grill, J.K. Brimacombe and F. Weinberg: "Mathematical analysis of stresses in continuous casting of steel", *Ironmaking and Steelmaking*, 1976, vol. 3 (1), pp. 38-47.
6. J.E. Kelly, K.P. Michalek, T.G. O'Connor, B.G. Thomas and J.A. Dantzig: "Initial Development of Thermal and Stress Fields in Continuously Cast Steel Billets", *Metallurgical Transactions A*, 1988, vol. 19A (10), pp. 2589-2602.
7. K. Sorimachi and J.K. Brimacombe: "Improvements in Mathematical Modelling of Stresses in Continuous Casting of Steel", *Ironmaking and Steelmaking*, 1977, vol. 4, pp. 240-245.
8. K. Wunnenberg and R. Flender: "Investigation of Internal-Crack Formation in Continuous Casting using a Hot Model", *Ironmaking and Steelmaking*, 1985, vol. 12 (1), pp. 22-29.
9. A. Yamanaka, K. Nakajima, K. Yasumoto, H. Kawashima and K. Nakai: "Measurement of Critical Strain for Solidification Cracking", *Modelling of Casting, Welding, and Advanced Solidification Processes - V*, M. Rappaz, M.R. Ozgu and K.W. Mahin, eds., TMS, Warrendale, PA, Davos, SW, 1990, Vol. V, pp. 279-284.

10. J. Mathew and H.D. Brody: "Simulation of heat flow and thermal stresses in axisymmetric continuous casting", *Proc. Int. Conf. on Solidification*, A. Nicholson, eds., TMS, 1979, Vol. 192, pp. 244-249.
11. H.G. Fjaer, E.K. Jensen and A. Mo: "Mathematical Modeling of Heat Transfer and Thermal Stresses in Aluminium Billet Casting : Influence of Direct Water Cooling Conditions", *Proceedings of 5th International Aluminum Extrusion Technology Seminar*, R.L.W.a.V.R. Bird, eds., The Aluminum Association, 1992, Vol. I, pp. 113-120.
12. T.W. Clyne and G.J. Davies: "The influence of composition on solidification cracking susceptibility in binary alloy systems", *Br. Foundrymen*, 1981, vol. 74 (4), pp. 65-73.
13. *MARC Users Manual*, MARC Analysis Research Corp., Palo Alto, CA, 1991.
14. P. Wisniewski and H.D. Brody: "Tensile Behavior of Solidifying Aluminum Alloys", *Modelling of Casting, Welding, and Advanced Solidification Processes - V*, M. Rappaz, M.R. Ozgu and K.W. Mahin, eds., TMS, Warrendale, PA, Davos, SW, 1990, Vol. V, pp. 273-278.
15. G. Carlsson, B. Brolund and R. Nystrom: "Measurements of Mould Distortion and Mold Heat Flux in Industrial Casters", *Journées Siderurgiques ATS*, Paris, Dec. 6-7, 1989.
16. D. Bammann and R.D. Krieg: "Summary and Critique", in *Unified Constitutive Equations for Creep and Plasticity*, A. Miller, eds., Elsevier Applied Science Publishers Ltd., Essex, United Kingdom, 1987, pp. 325.
17. T. Hashimoto, K. Ohnishi, M. Yamaguchi, M. Kinugawa and M. Ueda: "An Analysis of the Thermal Load of Mold Plates in a Continuous Casting Plant", *The Hitachi Zosen Technical Review*, 1982, vol. 43 (3),
18. B. Mintz, S. Yue and J.J. Jonas: "Hot ductility of steels and its relationship to the problem of transverse cracking during continuous casting", *International Materials Reviews*, 1991, vol. 36 (5), pp. 187-217.
19. B.G. Thomas, J.K. Brimacombe and I.V. Samarasekera: "The Formation of Panel Cracks in Steel Ingots, A State of the Art Review, Part I--Hot Ductility of Steel", *Transactions of the Iron and Steel Society*, 1986, vol. 7, pp. 7-20.

20. M. Wolf: "Estimation Method of Crack Susceptibility for new steel grades", *1St European Conference on Continuous Casting*, 23-25 September, Florence, Italy, 1991.
21. K. Takemoto, M. Tateno, S. Nakayama and K. Ebina: "Optimum Design of Mold Shape by Solidification-Deformation Coupled Analysis", *9th Process Technology Conference Proceedings*, ISS-AIME, Detroit, MI, 1990, Vol. 9.
22. J.K. Brimacombe and K. Sorimachi: "Crack Formation in the Continuous Casting of Steel", *Metallurgical Transactions B*, 1977, vol. 8B, pp. 489-505.
23. P.J. Wray: "Plastic Deformation of Delta-Ferrite Iron at Intermediate Strain Rates", *Metall. Trans.*, 1976, vol. 7A, pp. 1621-1627.
24. H.B. Rahamatalla and A.-S.T. M.: "Brittle Behavior and Crack Formation in Continuously Cast Steels", *Steel Times International*, 1988, vol. 12 (3), pp. 54-58.

CHAPTER 11

SUMMARY AND FUTURE WORK

1. A two-dimensional stepwise-coupled transient thermo-mechanical finite-element model has been developed to simulate the behavior of the solidifying steel shell in the mold region of a continuous slab casting machine and below. The model can predict the coupled evolution of temperature, shape, stress and strain distributions in the shell. The boundary conditions incorporate the results of other models, specifically including the effects of non-uniform superheat delivery to the solidifying shell due to turbulent fluid flow and the effects of thermal distortion of the mold.
2. Internal consistency of the numerical procedures, including the elastic-viscoplastic algorithm for incremental plasticity has been validated with several test problems with known solutions. Furthermore, the model has been verified with measurements on a cast breakout shell.
3. A 3D thermal-elastic finite-element model has been developed of a continuous slab casting mold and support structure using ABAQUS. The mold plates distort inward with maximum distortion found near center of wide face. Mold distortions on the order of a millimeter have been predicted and is sufficient to alter the effective taper of the narrow face, and may partially compensate for non-linear shrinkage of shell. It could have a significant effect on heat transfer and growth of the shell also, particularly in the corners where the largest gaps form. Increasing heat input (from higher casting speed, more taper, changing mold flux, etc.) increases mold temperatures and distortion. Stress calculations on the hotface suggest that residual distortion may be possible in some low strength copper alloys and can be prevented through proper material selection and design.
4. The non-uniform dissipation of superheat produces slower shell growth on the narrow face than on the wide face.

5. The model has been applied to understand the factors contributing to breakout formation due to inadequate heat transfer and shell thinning on the narrow face which are :

- a) inadequate narrow face taper, such as may occur from an accidental loss of taper or during a widening width change.
- b) excessive shell erosion of the off-corner region of the narrow face due to jet impingement from a misaligned or a blocked bifurcated nozzle, higher superheat or higher casting speed.
- c) inadequate powder feeding at the meniscus, leading to larger average air gaps

6) The present model has confirmed that the shell shrinks more in the top of the mold than in the bottom. Problems arise if the taper is either too large or too small. A continuous, ideal taper that compensates for this is proposed. However, when variable casting speed, mold distortion, and other uncertainties such as fluid flow and mold flux build-up are considered, at present, a well-chosen linear taper appears reasonable for stainless steel grades, while for low carbon steels such tapers are not optimum.

7. Model simulation suggest that cyclic thermo-mechanical loading of the slab below mold can generate tension on the surface as well as in the interior of the shell. Bulging of the strand in between rolls is responsible for off-corner depressions when the off-corner region of the shell exiting the mold is relatively thin. Model results suggest that primary way to prevent gutter is to achieve uniform, reasonably thick shell at mold exit, followed by uniform sprays and proper roll alignment.

8. The δ - γ transformation produces tensile stress peaks in the sub-surface region which might contribute to sub-surface cracks. Models results suggest that the low-carbon steels are more prone to internal cracks than austenitic stainless steel due to δ - γ transformation . Bulging below mold enhances the chances of such crack formation.

9. This model is a powerful tool which can be applied to investigate the influence of process parameters on the shell behavior and to understand the various problems which affect slab casting.

RECOMMENDATIONS FOR FUTURE WORK

Based on the findings of this present work, several recommendations can be made to enhance the capability of the model especially in terms of quantitative predictions of crack formation.

First of all an experimentally valid fracture criteria in the form of an evolving damage parameter that can be embedded in the model to predict evolution of cracks in the slab. In absence of any such fracture criteria stress models can only give a qualitative information about the formation of various types defects mentioned in this work.

There is a need for the development of constitutive equation for the δ -phase to study the effects of steel composition (especially the carbon content) and phase transformation on the thermo-mechanical behavior of the steel. Perhaps, fitting the available experimental data reported in the literature in to integrable differential equations could be the first step forward in this direction. In order to correctly quantify the effects of phase transformation in the constitutive equation, experimental validations are necessary through empirical data on cracks from the steel companies and correlate these data with model calculations to understand origin of defects. In addition, to completing material behavior during phase change detailed parametric study is needed to examine the problems of defect (cracks, surface depression) formation in order to recommend proper casting practices that can alleviate these problems.

To avoid generating unnecessary stresses in the liquid, the model currently forces the elastic strains in the liquid to be zero. This can be avoided by using separate constitutive law for the liquid that can reduces the stresses in the liquid to near zero by producing enough viscoplastic strains.

Better understanding of heat transfer through the gap, how mold powder consumption and distribution affects the thermomechanical behavior needs further investigation..

APPENDIX A

CONSTANT-TEMPERATURE GRADIENT TRIANGLES FOR HEAT FLOW MODEL

For constant-gradient triangles the temperature variation across the element is defined by a linear equation as given by

$$T = a_0 + a_1x + a_2y \quad (\text{A.1})$$

As the name suggests, this implies a constant temperature gradient or heat flux across the element. The temperature at any point in the element is given as

$$T(x,y) = \sum_{i=1}^3 N_i(x,y) T_i \quad (\text{A.2})$$

The nodal temperatures are defined as

$$\{T\} = \{T_1 \ T_2 \ T_3\}^T \quad (\text{A.3})$$

The temperature gradient across the element can then be expressed as

$$\begin{Bmatrix} \frac{\partial T}{\partial x} \\ \frac{\partial T}{\partial y} \end{Bmatrix} = \begin{bmatrix} \frac{\partial N_1}{\partial x} & \frac{\partial N_2}{\partial x} & \frac{\partial N_3}{\partial x} \\ \frac{\partial N_1}{\partial y} & \frac{\partial N_2}{\partial y} & \frac{\partial N_3}{\partial y} \end{bmatrix} \begin{Bmatrix} T_1 \\ T_2 \\ T_3 \end{Bmatrix} \quad (\text{A.4})$$

The [B] matrix for this element can be written in terms of the nodal coordinates, as

$$[B] = \frac{1}{2A} \begin{bmatrix} b_i & b_j & b_k \\ c_i & c_j & c_k \end{bmatrix} \quad (\text{A.5})$$

where

$$\begin{aligned} b_i &= x_j - x_k \\ c_i &= y_k - y_j \end{aligned} \quad (\text{A.6})$$

Finally, for these elements the conductance and capacitance matrices can be directly evaluated using the following equations without using numerical integration. The terms in the conductance matrix [K] are written as

$$K_{ij} = \int_A B^T k(T) B dA = \frac{k(T)}{4A} (b_i b_j + c_i c_j) \quad (A.8)$$

where $k(T)$ is the temperature dependent thermal conductivity and the terms in the capacitance matrix [C] are written as

$$C_{ij} = \int_A N^T C_p(T) N dA = \frac{A}{12} \frac{\partial H(T)}{\partial T} (1 + \delta_{ij}) \quad (A.9)$$

where $H(T)$ is the temperature dependent enthalpy function, the $\frac{\partial H(T)}{\partial T}$ term is defined in Eq. 3.5 and δ_{ij} is the Kronecker delta function. A consistent formulation was used for the capacitance matrix [C] as given by Eq. A.9. The thermal force vector {Q} was formed as :

$$\{Q\} = \int N^T q'' dL = \frac{q'' L_{ij}}{2} \quad (A.10)$$

where q'' is the heat flux represented by Eq. 3.8 or 3.12 and L_{ij} is the length of the boundary between node i,j. The material properties are evaluated at the centroid of the element where the temperature is given

$$T^e = \sum_{i=1}^3 T_i N_i = \frac{1}{3} (T_1 + T_2 + T_3) \quad N_i = \frac{1}{3} \quad (A.11)$$

APPENDIX B

LINEAR STRAIN TRIANGLES FOR STRESS MODEL

For the linear strain triangles the displacement function is quadratic across the element and as such the strain in the element is a linear function of the spatial coordinates. Although the linear displacement assumption is the most economical and performs very well for heat transfer solidification problems, the more sophisticated “quadratic displacement” elements offer better accuracy for solidification stress problems^[1]. The matrices of these formulations are given below in the notation of Figure A.2. The equations are based on plane strain formulation and the modifications for generalized-plane-strain formulation are given in Appendix C.

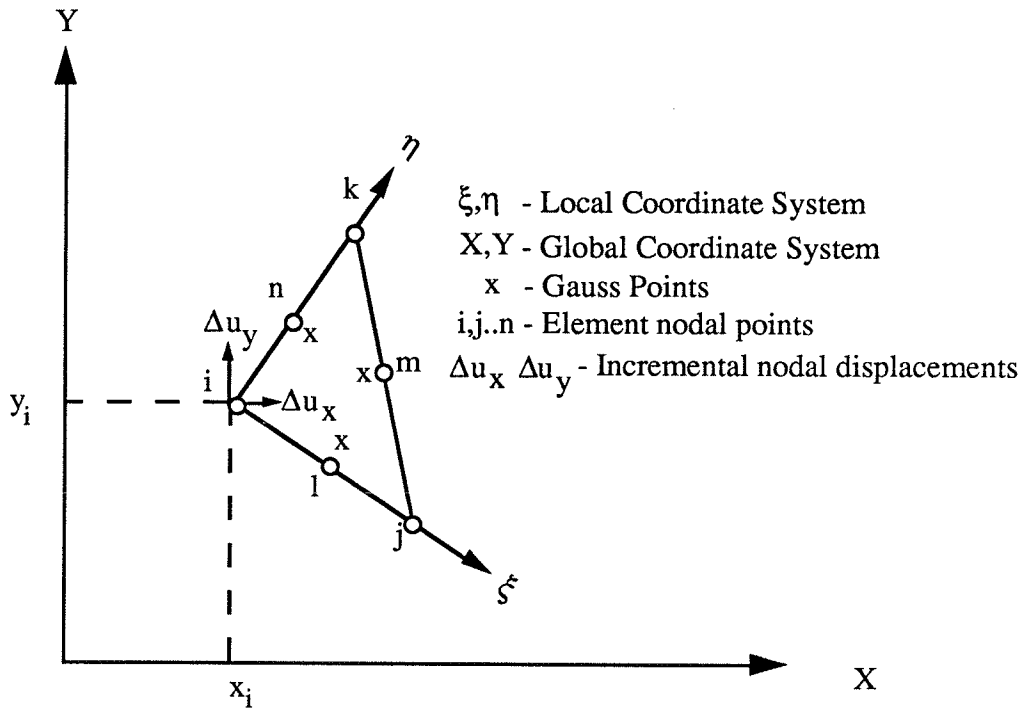


Figure B.1 Linear Strain Triangular element in local and global coordinate system.

The position $\{X\}$, in global coordinates of a point inside an element is given by

$$\begin{Bmatrix} x^{(e)} \\ y^{(e)} \end{Bmatrix} = \sum_{i=1}^6 \begin{bmatrix} N_i^{(e)} & 0 \\ 0 & N_i^{(e)} \end{bmatrix} \begin{bmatrix} x_i^{(e)} \\ y_i^{(e)} \end{bmatrix} \quad (B.1)$$

where $[N]$ is the matrix of shape functions in local coordinate system. The nodal displacements can be written as

$$u(x,y) = \sum_{i=1}^6 N_i(x,y) u_i \quad (B.2)$$

Also, within the element the displacement in global coordinate is written as

$$\begin{bmatrix} x^{(e)} \\ y^{(e)} \end{bmatrix} = \sum_{i=1}^6 \begin{bmatrix} N_i^{(e)} & 0 \\ 0 & N_i^{(e)} \end{bmatrix} \begin{bmatrix} x_i^{(e)} \\ y_i^{(e)} \end{bmatrix} \quad (B.3)$$

For isoparametric formulation a coordinate transformation is required. The Jacobian matrix for the transformation is written as

$$[J] = \begin{bmatrix} \frac{\partial x}{\partial \xi} & \frac{\partial y}{\partial \xi} \\ \frac{\partial x}{\partial \eta} & \frac{\partial y}{\partial \eta} \end{bmatrix} = \begin{bmatrix} \sum_{i=1}^6 \frac{\partial N_i^{(e)}}{\partial \xi} x_i^{(e)} & \sum_{i=1}^6 \frac{\partial N_i^{(e)}}{\partial \xi} y_i^{(e)} \\ \sum_{i=1}^6 \frac{\partial N_i^{(e)}}{\partial \eta} x_i^{(e)} & \sum_{i=1}^6 \frac{\partial N_i^{(e)}}{\partial \eta} y_i^{(e)} \end{bmatrix} \quad (B.4)$$

$$\frac{\partial N_i^{(e)}}{\partial x} = \frac{\partial N_i^{(e)}}{\partial \xi} \frac{\partial \xi}{\partial x} + \frac{\partial N_i^{(e)}}{\partial \eta} \frac{\partial \eta}{\partial x} \quad (B.5)$$

$$\frac{\partial N_i^{(e)}}{\partial y} = \frac{\partial N_i^{(e)}}{\partial \xi} \frac{\partial \xi}{\partial y} + \frac{\partial N_i^{(e)}}{\partial \eta} \frac{\partial \eta}{\partial y} \quad (B.6)$$

where

$$[N_i^{(e)}] = [(2\xi-1)\xi \quad (2\eta-1)\eta \quad (2(1-\xi-\eta)-1)(1-\xi-\eta) \quad 4\xi\eta \quad 4(1-\xi-\eta)\eta \quad 4(1-\xi-\eta)\xi] \quad (B.7)$$

The strain displacement relations for the plane-strain or plane stress are given by

$$\epsilon^{(e)} = \sum_{i=1}^6 B_i^{(e)} u_i^{(e)} \quad (B.8)$$

where the strain-displacement transformation matrix $[B_i^{(e)}]$ is given by Eq. B.9.

$$[B_i^{(e)}]_{3 \times 12} = \begin{bmatrix} \frac{\partial N_i^{(e)}}{\partial x} & 0 \\ 0 & \frac{\partial N_i^{(e)}}{\partial y} \\ \frac{\partial N_i^{(e)}}{\partial y} & \frac{\partial N_i^{(e)}}{\partial x} \end{bmatrix} \quad (B.9)$$

For the force equilibrium within each element

$$\int_{\Omega} [B_i^{(e)}]^T \sigma \, d\Omega = \sum_{j=1}^6 K_{\sigma_{ij}} u_j^{(e)} = \int_{\Omega^{(e)}} [B_i^{(e)}]_{12 \times 3}^T [D]_{3 \times 3} \left(\sum_{j=1}^6 [B_j^{(e)}]_{3 \times 12} u_j^{(e)} \right) d\Omega \quad (B.10)$$

where $K_{\sigma_{ij}}$ are the components of the element stiffness matrix $[K]$ and $[D]$ is the Elasticity matrix given by

$$[D]_{3 \times 3} = \frac{E(T)}{(1+\nu)(1-2\nu)} \begin{bmatrix} (1-\nu) & \nu & 0 \\ \nu & (1-\nu) & 0 \\ 0 & 0 & \frac{(1-2\nu)}{2} \end{bmatrix} \quad \text{for Plane-strain} \quad (B.11)$$

$$[D]_{3 \times 3} = \frac{E(T)}{(1-\nu^2)} \begin{bmatrix} 1 & \nu & 0 \\ \nu & 1 & 0 \\ 0 & 0 & \frac{(1-\nu)}{2} \end{bmatrix} \quad \text{for Plane-stress} \quad (B.12)$$

Finally the terms in the element stiffness matrix $[K_{\sigma}]$ are written as

$$K_{\sigma_{ij}} = \sum_{i=1}^{ng} \Gamma_{ij}(\xi_{ng}, \eta_{ng}) W_{ng} \cdot 0.5 \quad (B.13)$$

where $\Gamma_{ij}(\xi_{ng}, \eta_{ng})$ is given by

$$\Gamma_{ij}(\xi_{ng}, \eta_{ng}) = \int_{\Omega^{(e)}} [B_i^{(e)}]^T [D] [B_j^{(e)}] \, d\Omega \quad (B.14)$$

and $d\Omega = \det J d\xi d\eta$.

Similarly the terms for the element force vector can be written as

$$\{\Delta F_{\epsilon T}\} = \int [B]^T [D] \{\Delta \epsilon_T\} d\Omega \quad (B.15)$$

$$\{\Delta F_{\epsilon p}\} = \int [B]^T [D] \{\Delta \epsilon_p\} d\Omega \quad (B.16)$$

$$\{F_{TP}\} = \int [N]^T \{P\} d\Gamma \quad (B.17)$$

$$\{F_{el}\} = \int [B]^T [D] \{\epsilon_{el}\} d\Omega \quad (B.18)$$

where $P = h\rho g$ is the internal ferro-static pressure acting at the solid/liquid interface. Components of $\{\Delta \epsilon_T\}$, are calculated from the scalar values, $\Delta \epsilon_T$, in Eq. 3.23 by:

$$\{\Delta \epsilon_T\} = \begin{Bmatrix} TLE(T_{t+\Delta t}) - TLE(T_t) \\ TLE(T_{t+\Delta t}) - TLE(T_t) \\ 0 \\ TLE(T_{t+\Delta t}) - TLE(T_t) \end{Bmatrix} \quad (B.19)$$

Components of $\{\Delta \epsilon_p\}$, are calculated from the scalar values, $\Delta \epsilon_p$, in Eq. 27 using the Prandtl - Reuss equations:

$$\begin{aligned} \Delta \epsilon_{px} &= \frac{\Delta \epsilon_p}{2\sigma} (2\sigma_x - \sigma_y - \sigma_z) \\ \Delta \epsilon_{py} &= \frac{\Delta \epsilon_p}{2\sigma} (2\sigma_y - \sigma_x - \sigma_z) \\ \Delta \epsilon_{pz} &= \frac{\Delta \epsilon_p}{2\sigma} (2\sigma_z - \sigma_x - \sigma_y) \\ \Delta \epsilon_{p_{xy}} &= \frac{3}{2} \frac{\Delta \epsilon_p}{2\sigma} \tau_{xy} \end{aligned} \quad (B.20)$$

and σ is defined in Eq. 3.29. For 6-node isoparametric element as shown in Figure B.1, $n_g = 3$, $\xi_1 = \eta_1 = 0.5$; $\xi_2 = 0.5$, $\eta_2 = 0.0$; $\xi_3 = 0.0$ $\eta_3 = 0.5$ and $W_1 = W_2 = W_3 = 0.333333333333$

APPENDIX C

EQUATIONS FOR GENERALIZED PLANE STRAIN FORMULATION BY DIRECT METHOD

Here the same shape functions are used for the in-plane displacements as in plane stress or plane strain but different strain displacement relations are used. The components of the strain tensor are expressed in Eqs. 3.16-3.19. The strain-displacement relation can be written as

$$\begin{bmatrix} \{\Delta\epsilon\} \\ \{\Delta\epsilon_z\} \end{bmatrix} = \underset{4 \times 15}{[B']} \{\delta\} \quad (C.1)$$

where $\{\Delta\epsilon\}$ are the in plane strains given by Eq. 3.16-3.18

$$\{\Delta\epsilon\} = \begin{Bmatrix} \Delta\epsilon_x \\ \Delta\epsilon_y \\ \Delta\epsilon_{xy} \end{Bmatrix} \quad (C.2)$$

and $\{\Delta\epsilon_z\}$ is the out-of-plane incremental strain. The unknown vector $\{\delta\}$ consists of the in-plane displacements and the unknowns in Eq. 3.22

$$\{\delta\} = \begin{Bmatrix} \{u\} \\ a \\ b \\ c \end{Bmatrix} \quad (C.3)$$

The new strain-displacement relation can be written as

$$\underset{4 \times 15}{[B']} = \begin{bmatrix} & & & 0 & 0 & 0 \\ & \underset{3 \times 12}{[B]} & & 0 & 0 & 0 \\ & & & 0 & 0 & 0 \\ 0 & 0 & 0 & 1 & x & y \end{bmatrix} \quad (C.4)$$

where $[B]$ is the strain displacement matrix for 2-D plane strain formulation as given by Eq. B.9.

Finally the stress strain relations can be written as

$$\begin{Bmatrix} \{\Delta\sigma\} \\ \{\Delta\sigma_z\} \end{Bmatrix} = [D'] \begin{Bmatrix} \{\Delta\epsilon\} \\ \{\Delta\epsilon_z\} \end{Bmatrix} - [D'] \{\Delta\epsilon_T\} - [D'] \begin{Bmatrix} \{\Delta\epsilon_p\} \\ \{\Delta\epsilon_{pz}\} \end{Bmatrix} \quad (C.5)$$

where the subscript p and T denotes plastic strain and thermal strains given by Eq. A.29 and A.30 respectively and $[D']$ is defined in Eq. 3.20.

Finally applying Galerkin formulation to the governing equilibrium equation and associated boundary condition one can write the final form of the finite element equations as

$$[K'_{\sigma}]_{15 \times 15} \{\delta\} = \{\Delta F_{th}\} + \{\Delta F_{pl}\} + \{F_{IP}\} - \{F_{el}\} \quad (C.6)$$

Eq. A.15 can be written as

$$\begin{bmatrix} [K_{\sigma}]_{12 \times 12} & [K_1]_{12 \times 3} \\ [K_1']_{3 \times 12} & [K_2]_{3 \times 3} \end{bmatrix} \begin{Bmatrix} \{\delta\}_{12 \times 1} \\ a \\ b \\ c \end{Bmatrix} = \begin{Bmatrix} \{S\} \\ \{G\} \end{Bmatrix} \quad (C.7)$$

where $[K]_{12 \times 12}$ is the plane strain stiffness matrix given by Eq. B.13.

$$[K_1]_{12 \times 3} = \frac{\nu E(T)}{\lambda} \int [B]^T \begin{bmatrix} 1 & x & y \\ 1 & x & y \\ 0 & 0 & 0 \end{bmatrix} d\Omega \quad (C.8)$$

and

$$[K_1']_{3 \times 12} = [K_1]_{12 \times 3}^T \quad (C.9)$$

$$[K_2]_{3 \times 3} = \frac{(1-\nu)E(T)}{\lambda} \int \begin{bmatrix} x & x^2 & xy \\ y & xy & y^2 \\ 1 & x & y \end{bmatrix} d\Omega \quad (C.10)$$

$$[S]_{12 \times 1} = \int [B]^T \frac{\nu E(T)}{\lambda} (\Delta\epsilon_T) d\Omega + \int [B]^T \frac{\nu E(T)}{\lambda} \{\Delta\epsilon_p\} d\Omega + \int [N]^T \{P\} d\Gamma \quad (C.11)$$

$$[G]_{3 \times 1} = \int (1-\nu) \frac{(1-\nu)E(T)}{\lambda} (\Delta\epsilon_T) \begin{pmatrix} 1 \\ x \\ y \end{pmatrix} d\Omega + \int \begin{pmatrix} 1 \\ x \\ y \end{pmatrix} \frac{(1-\nu)E(T)}{\lambda} \{\Delta\epsilon_{pz}\} d\Omega + \begin{pmatrix} F \\ M_y \\ M_x \end{pmatrix} \quad (C.12)$$

For the special case of generalized plane strain for which $b=c=0$ (i.e. no rotation of the plane in the 2-d simulation) the element matrices $[B']$ and $[K']$, can be reduced to 4×13 and 13×13 respectively because the two-fold symmetry assumption does not allow any rotation or bending of the section.

The structure of the stiffness matrix does not remain banded any longer and the overall bandwidth becomes equal to the system size (number of total degrees of freedom). The last three rows contain information for all nodal points, thus making the shape of the stiffness matrix as shown in Figure C.1. Each element of the domain contributes to the last three lines of the stiffness matrix. Thus the total number of equations solved is $(ndf+3)$ where ndf is the total number of degrees of freedom, which is equal to number of nodes times 2 (degrees of freedom for each node). For the present case where $b=c=0$, the number of equations solved is $(ndf+1)$.

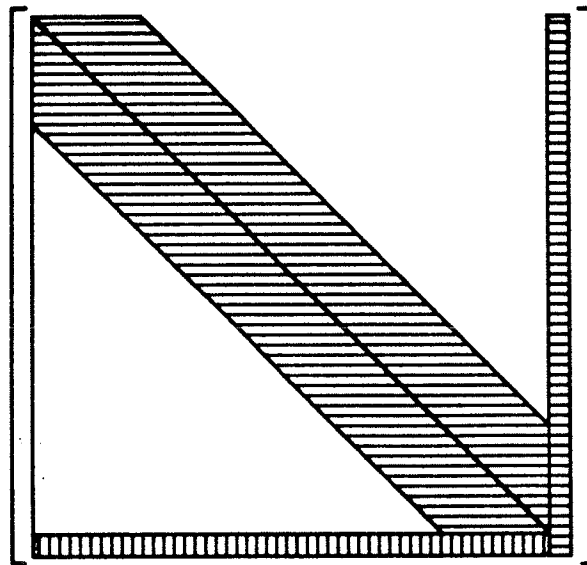


Figure C.1 Shape of the stiffness matrix for the generalized plane strain formulation.

APPENDIX D

ITERATIVE METHOD OF GENERALIZED PLANE STRAIN FORMULATION

In finite elements, the generalized plane strain calculations can be achieved in two ways: They can be classified as (1) iterative methods and (2) direct methods. The formulation for the direct method was described in APPENDIX C and iterative method is described below.

Iterative method:

In the Iterative method, the strain in the Z-direction is applied as a pseudo load vector in a similar way as to how the plastic strain is treated. The stiffness matrix is formulated as in the plane strain. The strain in the Z-direction are evaluated, such that the net force in the Z-direction over the entire domain is zero, i.e. $\int \Delta \sigma_z dA = 0$. Iterations are performed until convergence, i.e. until strains in Z-direction in successive iterations are close enough. The computational scheme is outlined below.

```

-----
= .....loop on time steps
=           Initialize  $\Delta \epsilon_{z0}^{n+1} = \Delta \epsilon_z^n$ 
=.....loop on iterations (from i=0 until convergence)
=            $\{\Delta F_{\epsilon z}\}_{i+1}^{n+1} = \int [B]^T [D] \{\Delta \epsilon_z\}_i^{n+1} dV$ 
=           solve  $\{\Delta u\}_{i+1}^{n+1}$  by Choleski method
=            $[K] \{\Delta u\}_{i+1}^{n+1} = \{\Delta F_{th}\}^{n+1} + \{\Delta F_{pl}\}^{n+1} + \{\Delta F_{\epsilon z}\}_{i+1}^{n+1}$ 
=           calculate total strain  $\{\Delta \epsilon\} = [B] \{\Delta u\}$ 
=           calculate total incremental stress  $\Delta \sigma = [D] (\{\Delta \epsilon\} - \{\Delta \epsilon_{th}\} - \{\Delta \epsilon_{pl}\})$ 

```

$$= \text{calculate } \Delta \epsilon_{z_{i+1}}^{n+1} = \frac{\int \left(\text{se0} - \text{svp} - \frac{E\nu}{\lambda} (\Delta \epsilon_x + \Delta \epsilon_y) \right) dA}{\int \frac{E(1-\nu)}{\lambda} dA}$$

$$= \text{convergence verification } | \Delta \epsilon_{z_{i+1}}^{n+1} - \Delta \epsilon_{z_i}^{n+1} | < \text{TOL}$$

=..... next time step

APPENDIX E

FINITE ELEMENT EQUATIONS FOR MOLD DISTORTION ANALYSIS

The basic governing differential equations for the stress model are the mechanical equilibrium equations:

$$[L]^T \{\sigma\} = \{F\} \quad (E.1)$$

which relate the total vector, $\{\sigma\} = \{\sigma_x, \sigma_y, \sigma_z, \tau_{xy}, \tau_{yz}, \tau_{zx}\}^T$ to total external forces, $\{F\} = \{F_x, F_y, F_z\}^T$, and the compatibility equations which relate total strain, $\{\epsilon\} = \{\epsilon_x, \epsilon_y, \epsilon_z, \gamma_{xy}, \gamma_{yz}, \gamma_{zx}\}^T$ to total displacement, $u = \{u, v, w\}^T$:

$$\{\epsilon\} = [L] \{u\} \quad (E.2)$$

where differential operators are contained in matrix, $[L] =$

$$\begin{bmatrix} \partial/\partial x & 0 & 0 \\ 0 & \partial/\partial y & 0 \\ 0 & 0 & \partial/\partial z \\ \partial/\partial y & \partial/\partial x & 0 \\ 0 & \partial/\partial z & \partial/\partial y \\ \partial/\partial z & 0 & \partial/\partial x \end{bmatrix} \quad (E.3)$$

Additional equations are needed to relate stresses and strains, called the “constitutive equations”:

$$\{\sigma\} = [D] \{\epsilon\}_e \quad (E.4)$$

where $[D]$ contains the elastic constants, which depend only upon the material properties of elastic modulus, E and Poisson's ratio, ν , for an isotropic material:

$$[D] = \frac{E}{(1+\nu)(1-2\nu)} \begin{bmatrix} 1-\nu & \nu & \nu & 0 & 0 & 0 \\ \nu & 1-\nu & \nu & 0 & 0 & 0 \\ \nu & \nu & 1-\nu & 0 & 0 & 0 \\ 0 & 0 & 0 & (1-2\nu)/2 & 0 & 0 \\ 0 & 0 & 0 & 0 & (1-2\nu)/2 & 0 \\ 0 & 0 & 0 & 0 & 0 & (1-2\nu)/2 \end{bmatrix} \quad (E.5)$$

Equation (E.4) states that stresses are caused only by elastic strains. The total strain vector, $\{\epsilon\}$, is composed of elastic and thermal strain components:

$$\{\epsilon\} = \{\epsilon\}_e + \{\epsilon\}_T \quad (E.6)$$

where $\{\epsilon\}_e$ is the elastic strain $\{\epsilon\}_T$ is the thermal strain. The finite element form of the governing equation (1) along with appropriate boundary conditions are expressed as

$$[K_{3D}] \{u\} = \{F\} \quad (E.7)$$

where $[K_{3D}] = \int_V [B_{3D}]^e T D [B_{3D}]^e dV$ is the stiffness matrix, $\{F\}$ is the force vector and $[B_{3D}]^e$

$= [L] \{N_{3D}\}$, $\{N_{3D}\}$ being the shape function. The algebraic equations in (7) are solved for the displacements which are then used to calculate the strain and stress as per equation (2) and (4).

APPENDIX F

CALCULATION OF BOLT PRE-STRESS

Each bolt is tightened with 110 ft.lb (145 N.m) of torque which corresponds to 44 kN axial force in each bolt. The area of each bolt $A = \pi (19/2 \text{ mm})^2 = 283.5 \text{ mm}^2 = .000284 \text{ m}^2$ and length of each bolt $L = 280\text{mm}$ or 0.28m .

Assuming Modulus for steel as $E = 210 \text{ GPa}$, the stress in the bolts can be calculated as

$$s = E \frac{\Delta L}{L} = \frac{F}{A}$$
$$\therefore \text{Stress} = \frac{F}{A} = 44000 / .000284 = \underline{155.2 \text{ MPa}}$$

The elastic extension then can be calculated as

$$\Delta L = \frac{F L}{A E} = 1000 * \frac{44000 * .28}{.000284 * 210 \times 10^9} = 0.21 \text{ mm}$$

Thus, bolt prestress will reduce mold distortion by a measurable amount, but will not prevent it entirely!

APPENDIX G

CORRECTION TO SIMULATION TIME FOR DRAINAGE DURING A BREAKOUT

To compare the section of the model simulation with that of a breakout shell, a correction for the position of the section is needed to account for the solidification time that occurred while the liquid metal was draining during the breakout. Thus, the time in the simulation corresponds to the distance down the breakout shell according to the relation:

$$t = \frac{Z}{V_c} + t_d \quad (G1)$$

where:

t = time in the simulation (i.e. time below meniscus that corresponds to the breakout slice being considered),

Z = position down the breakout shell of the slice considered (m)

V_c = casting speed (m/s).

The "drainage time", t_d , represents the time for the metal level to drop from the meniscus (top of the breakout shell) to the distance down the breakout shell to the breakout slice of interest, Z . It is calculated using the following equation,

$$t_d = \frac{\sqrt{Z_b} - \sqrt{Z_b - Z}}{C_D \frac{\pi d_b^2}{4NW} \sqrt{\frac{g}{2}}} \quad (G2)$$

where :

Z_b = position of the breakout hole from the top of the shell (m),

C_D = drag coefficient = 1.0,

g = gravity = 9.81 m/s²,

d_b = diameter of the breakout hole (m),

N = thickness of the slab (m),

W = width of the slab (m).

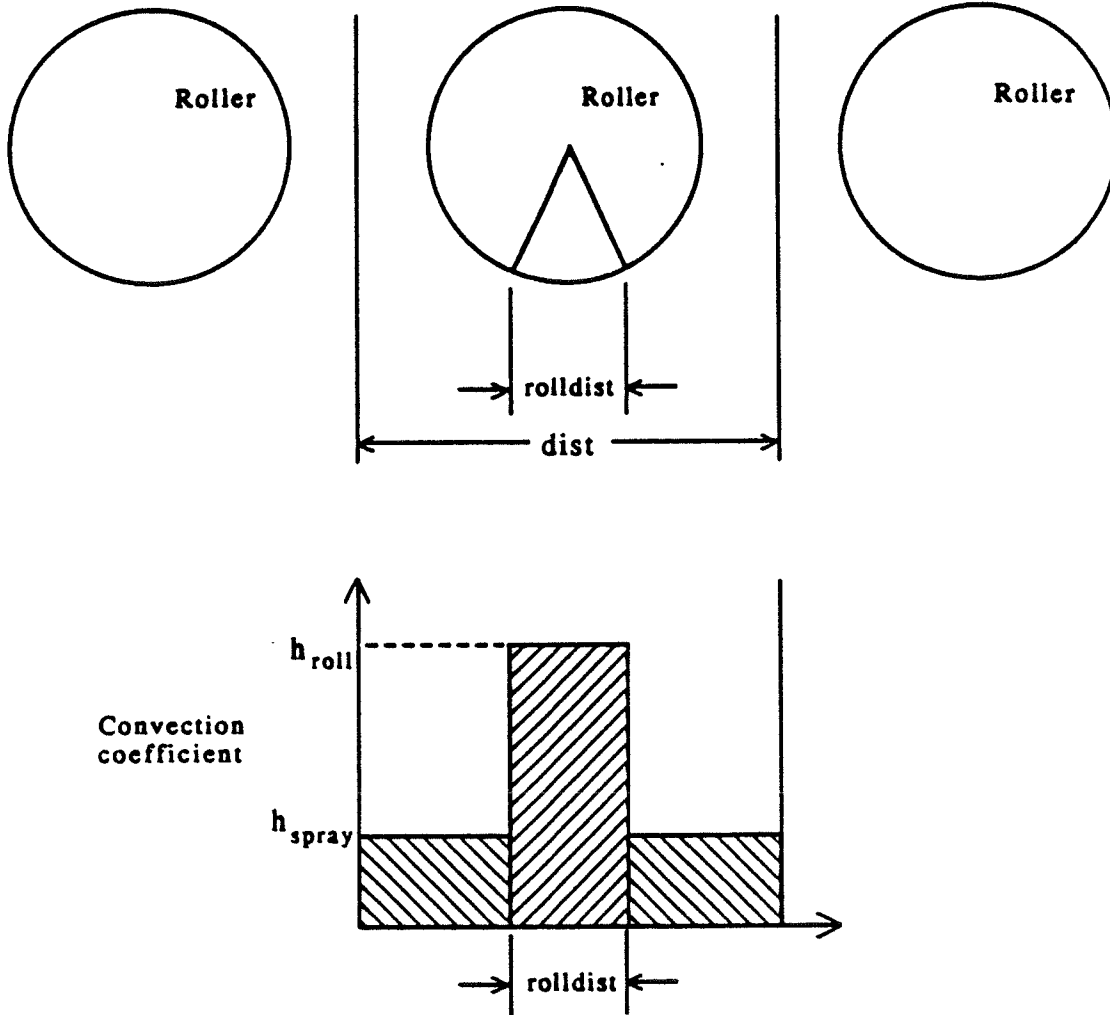
The above equation was derived based on the relation in Gaskel^[2] corrected for a rectangular slab. It is assumed here, that the metal flow to the mold is shut off simultaneously with the metal level starting to drop below meniscus and that the hole growth is complete.

For the present example, $Z_b = 1524$ mm (60"), $Z = 228.6$ mm (9"), $N = 229$ mm (9"), $W = 1016$ mm (40"), and $V_c = 0.0169$ m/s were used. Although the exact size of the hole was not measured, its diameter was estimated to fall between 50 mm and 100 mm, which produces upper and lower limits on t_d of 3.8 s and 1.0 s respectively. A correction time of 1.5 sec was used, although there is very little difference in results for these small times.

APPENDIX H

Calculation of heat transfer coefficients for the rolls

The following calculations are taken from Haegele^[3] based on the fraction of heat extraction data from Hibbins.^[4]



where

$$\text{dist} = \frac{\text{Total Length of zone}}{\text{Number of rolls in zone}}$$

$$\text{rolldist} = 2 \pi (\text{Roll radius}) \left(\frac{\text{degree of contact}}{360^\circ} \right)$$

h_{roll} = Average heat transfer coefficient for rolls

h_{spray} = Average heat transfer coefficient for sprays

Performing a heat balance in one roll "cycle",

$$h_{\text{spray}} (\text{dist} - \text{rolldist}) + h_{\text{roll}} (\text{rolldist}) = h_{\text{ave}} (\text{dist})$$

$$\begin{array}{ccc} \text{A (spray part)} & \text{B (roll part)} & \text{C (total)} \end{array}$$

But we know from the percentages of heat removed by the rollers and by the sprays from the literature [19]:

$$B = (\text{fracroll}) C$$

$$A = (1 - \text{fracroll}) C$$

$$C = A + B$$

where fracroll is the fraction of heat removed by the roller. By manipulating these equations, this yields:

$$A = (1 - \text{fracroll})(A + B)$$

$$A - A(1 - \text{fracroll}) = B(1 - \text{fracroll})$$

$$A(\text{fracroll}) = B(1 - \text{fracroll})$$

$$B = A \left(\frac{\text{fracroll}}{1 - \text{fracroll}} \right)$$

Plugging in:

$$(h_{\text{roll}})(\text{rolldist}) = (h_{\text{spray}})(\text{dist} - \text{rolldist}) \left(\frac{\text{fracroll}}{1 - \text{fracroll}} \right)$$

$$\therefore h_{\text{roll}} = (h_{\text{spray}}) \left(\frac{\text{dist} - \text{rolldist}}{\text{rolldist}} \right) \left(\frac{\text{fracroll}}{1 - \text{fracroll}} \right)$$

REFERENCES

1. A. Moitra, H. Zhu and B.G. Thomas: *unpublished research*, University of Illinois, Report, 1992.
2. D.R. Gaskell: *An Introduction to Transport Phenomena in Materials Engineering*, Macmillan Publishing Company, New York, 1992.
3. G. Haegele: *Application of Mathematical Models to Investigate Defect Formation During Hot Charging of Continuously Cast Steel Slabs*, Masters Thesis, University of Illinois at Urbana, Champaign, 1988.
4. S.G. Hibbins and J.K. Brimacombe. *Characterization of Heat Transfer in the Secondary Cooling System of a Continuous Slab Caster*. Continuous Casting - Heat Flow, Solidification and Crack Formation. 2: 139-151, 1984.

VITA

Avijit Moitra was born on 30th August 1960, to Mrs. Ira Maitra and Mr. Bisweswar Maitra, in Calcutta India. He was raised in the city of Calcutta and finished his last year in high school in the year 1979. He then joined the Indian Institute of Technology, Kharagpur where he completed his Bachelor of Technology Degree with Honors in Metallurgical Engineering in 1984. Avijit was a recipient of the Govt. of India merit scholarship and IIT merit award during the course of his undergraduate study. Upon graduation he worked for two and half years in a metal forming company in India. He moved to University of Alabama at Tuscaloosa, Alabama and received his MS degree in Materials Engineering in May 1989. He joined the Mechanical and Industrial Engineering at the University of Illinois in the Fall of 1989 in the doctoral program. During the course of the study at Illinois he has held a research assistantship from the department of mechanical engineering.

He was married to Chitralkha Moitra on December 15, 1986 in Calcutta, India and was blessed with a son Reet on June 19, 1992. He has accepted a position as a Group Design Engineer in the Advanced Engineering Technology division of Associated Springs Barnes Group Inc. at Bristol, Connecticut.

